

DIGITAL ACCESS TO SCHOLARSHIP AT HARVARD
DASH.HARVARD.EDU

HARVARD LIBRARY


Gravitational Wave Astronomy in the LSST Era

Link
http://nrs.harvard.edu/urn-3:HUL.InstRepos:37944940

Terms of use
This article was downloaded from Harvard University's DASH repository, and is made available under the terms and conditions applicable to Other Posted Material (LAA), as set forth at
https://harvardwiki.atlassian.net/wiki/external/NGY5NDE4ZjgzNTc5NDQzMGIzZWZhMGFlOWI2M2EwYTg

Accessibility
https://accessibility.huit.harvard.edu/digital-accessibility-policy

Share Your Story
The Harvard community has made this article openly available.
Please share how this access benefits you. Submit a story

©2016 – Michael W. Coughlin
all rights reserved.

Thesis advisor: Professor Christopher W. Stubbs Michael W. Coughlin

Gravitational wave astronomy in the LSST era

Abstract

Optimizing the science of astronomical observatories such as gravitational-wave detectors and large telescopes maximizes their potential science output. In this thesis, I present the results from a number of analyses related to this endeavor. The first is a method to detect gravitational-wave transients. I cast this search as a pattern recognition problem, where the goal is to identify statistically significant clusters in spectrograms of strain power when the precise signal morphology is unknown. The second set of analyses uses Earth and Moon seismic data to place upper limits on an isotropic stochastic gravitational wave background. I use two different response models, which cover the frequency band 0.3 mHz – 1 Hz. I find that because the Moon's ambient noise background is much quieter than that of the Earth, using the Moon's data allows for a significantly improved upper limit on a background. The third analysis relates to noise sources that will limit gravitational-wave detectors in the near future, which include Newtonian noise and global magnetic noise from the Schumann resonances. For both of these cases, I show prospects for the optimal subtraction of these noise sources using arrays of seismometers and magnetometers respectively. I further discuss calibration and site characterization studies for the Large Synoptic Survey Telescope, a wide-field survey likely to detect electromagnetic counterparts to gravitational-wave events. In particular, I discuss the design and implementation of a prototype calibration system tested on current telescopes, as well as perform sky brightness measurements which can be used for telescope scheduler optimization.

Contents

0 Introduction **1**

1 Upper Limit on a Stochastic Background of Gravitational Waves from Seismic Measurements in the Range 0.05 Hz to 1 Hz **14**

2 Constraining the gravitational wave energy density of the Universe in the Range 0.1 Hz to 1 Hz using the Apollo Seismic Array **26**

2.1 Formalism 30
2.2 Moon-Moon Correlation 34
2.3 Earth-Moon Correlation 37
2.4 Conclusion 42

3 Constraining the gravitational wave energy density of the Universe using Earth's ring **44**

3.1 Earth's normal-mode oscillations 46
3.2 Theory of Earth's response to gravitational waves 52
3.3 Gravimeter data 57
3.4 Search for a stationary gravitational-wave background 59
3.5 Conclusion 63

4 Detecting compact binary coalescences with seedless clustering **65**

4.1 Seedless clustering for chirps 71
4.2 Sensitivity study 75
4.3 Results 77
4.4 Conclusions 79

5 The detectability of eccentric compact binary coalescences with advanced gravitational-wave detectors **85**
5.1 Seedless clustering for chirps 90
5.2 Sensitivity study 94
5.3 Results 95
5.4 Computational requirements 98
5.5 Astrophysical implications 98
5.6 Discussion 101
5.7 Appendix: Eccentric template derivation 102

6 Prospects for searches for long-duration gravitational-waves without time slides **106**
6.1 Formalism 112
6.2 Background Study 117
6.3 Uncertainties: Statistical and systematic 120
6.4 Conclusions and Future Work 123

7 Wiener filtering with a seismic underground array at the Sanford Underground Research Facility **128**
7.1 Data Quality 134
7.2 Wiener Filtering 136
7.3 Filter Results 140
7.4 Conclusion 150

8 Towards a first design of a Newtonian-noise cancellation system for Advanced LIGO **157**
8.1 Newtonian Noise Cancellation 159
8.2 LIGO Hanford Array 164
8.3 Array Optimization 168
8.4 Results 170
8.5 Conclusion 175

9 Subtraction of correlated noise in global networks of gravitational-wave interferometers **180**

10 Real-time earthquake warning for astronomical observatories **201**
10.1 Earthquake Properties and Identification 206
10.2 Hazard Assessment 209
10.3 Early Earthquake Warning 215
10.4 Seismic network optimization 218
10.5 Conclusion 220

11 Maximizing the Probability of Detecting an Electromagnetic Counterpart of Gravitational-wave Events **229**
11.1 Formalism 233
11.2 Optimization 241
11.3 Conclusion 245

12 A Daytime Measurement of the Lunar Contribution to the Night Sky Brightness in LSST's *ugrizy* Bands– Initial Results **248**
12.1 Apparatus 252
12.2 Results 260
12.3 Conclusion 269

13 A collimated beam projector for precise telescope calibration **272**
13.1 Goals 275
13.2 Apparatus 279
13.3 Demonstration 284
13.4 Conclusion 288

14 Conclusion **291**

References **326**

Listing of figures

1 Gravitational-wave polarizations. 4

1.1 Seismic SGWB upper limits. 15
1.2 Seismic ORF. 20
1.3 Location of seismometers. 22
1.4 Seismic spectra histogram. 23

2.1 Lunar SGWB upper limits. 28
2.2 Lunar velocity profiles. 31
2.3 Lunar seismic spectra histogram. 36
2.4 SGWB point estimate. 37
2.5 Earth-Moon system. 38
2.6 Earth-Moon ORF. 42

3.1 Normal modes SGWB upper limits. 47
3.2 Simulated spectrum of spheroidal normal modes around ${}_6S_2$. 51
3.3 Earth quadrupole oscillation. 56
3.4 Medians of gravimeter spectra measured in 2012. 58
3.5 Coherence of signals from two levitated spheres in the same gravimeter at Wettzell, Germany. 60
3.6 Point estimates of GW energy density and errors. 62

4.1 Simulated BNS injection and recovery. 81
4.2 BNS injections into real data. 83
4.3 Omega scan comparison. 84

5.1 Simulated eccentric BNS injections. 104
5.2 Eccentric parameterization. 105

6.1 Seedless clustering probability distributions. 124

6.2 Simulated seedless clustering background distributions. 125
6.3 Simulated seedless clustering p-value distributions. 126
6.4 Comparing p-value distributions. 127

7.1 Homestake seismic spectra. 141
7.2 Homestake coherence. 143
7.3 Wiener filter variation over the course of a day. 153
7.4 Wiener filter subtraction residuals. 154
7.5 Wiener filter residuals as a function of filter order. 154
7.6 Histogram of residual spectra. 155
7.7 The MANGO GW detector target spectrum. 156

8.1 Layout of the instrument floor at the Y-end station of the LIGO Hanford Observatory. 165
8.2 Histograms of seismic speed measurements using LHO array data at 10, 15, and 20 Hz. 166
8.3 Measured correlation function for the LIGO Hanford site at 15 Hz. . . . 167
8.4 IPW, Gaussian, and APW models for the seismic fields. 177
8.5 Sensor Locations. 178
8.6 Subtraction residuals vs frequency and number of sensors. 179

9.1 Power spectral density of magnetometers. 190
9.2 Coherence between magnetometer pairs. 198
9.3 Time-frequency coherence between magnetometer pairs. 199
9.4 Success of the Wiener filtering procedure under two metrics. 200

10.1 Earthquake time-series data. 208
10.2 Effect of strong ground motion on the observatories. 223
10.3 Earthquake parameter distributions. 224
10.4 Predicted peak ground acceleration. 224
10.5 Earthquake time delays. 225
10.6 Map of the probability distribution for regional Chilean earthquakes. . 226
10.7 Potential gain in warning time with low-latency earthquake networks. . 227
10.8 Optimal seismometer distances for the EEW seismic network. 228

11.1 Relative variance in the number of galaxies. 236

11.2 Gravitational-wave likelihood skymap. 244
11.3 Optimization of telescope time allocations. 247

12.1 Sketch of the photodiode portion of the apparatus. 253
12.2 Photon sensitivity function curves. 254
12.3 Fit to the photodiode fluxes. 263
12.4 Variation Δm_5 in the point source magnitudes. 266
12.5 u, g, and r-band flux as a function of time. 270

13.1 Sketch of the apparatus. 280
13.2 Collimated beam projector throughput. 285
13.3 Collimated beam projector example image. 290

List of Tables

3.1 Normal mode summary. 50

4.1 Relative duty cycles for chirp-like templates 74
4.2 Sensitive distances for different waveforms (assuming optimal sky location and source orientation) given the design sensitivity of Advanced LIGO. 82

5.1 Sensitive distances for different waveforms (assuming optimal sky location and source orientation) given the design sensitivity of advanced LIGO. 96
5.2 Potential detection rates of eccentric compact binary coalescences for both matched filtering and seedless clustering. 99

7.1 Table detailing station information, including station names, type of seismometer, and position relative to Yates shaft of the former Homestake mine.135

12.1 System throughput values. 256
12.2 Irradiance attenuation due to lunar scattering, in the LSST bands, at various lunar phase angles. 259
12.3 Dark current measurement for all six filters. 260
12.4 Daytime sky brightness values as function of angle between the point on sky and sun, altitude of the point on the sky, and altitude of sun fit to a plane of the form $a + bx + cy + dz$ in electrons/s. 262
12.5 Zenith daytime sky brightness values, converted to expected LSST lunar sky backgrounds at zenith at full moon. 268

13.1 Masks and filters available for the collimated beam projector. 282

To my parents.

Acknowledgments

I owe a huge thank you to many people. First of all, Christopher Stubbs was kind enough to take me into his group and help out with many of my projects. Peter Doherty provided so much practical lab knowledge that saved me literally months of work. Nelson Christensen gave me my start in the field of gravitational waves and has completely shaped my trajectory in science. Jan Harms and Eric Thrane, from their time as post-docs at the University of Minnesota up until now, have continued to push my research in directions I never would have imagined. My labmates, Nicholas Mondrik and Kairn Brannon, have been invaluable colleagues helping make the Collimated Beam Projector a success. Fellow graduate students Patrick Meyers and Tanner Prestegard have been closely involved in many of my projects and they helped keep me sane. My brothers, Scott and Eric Coughlin, have been huge helps in various gravitional-wave projects; it truly is a family affair. Last but not least, my parents, Bill and Lisa Coughlin, deserve a lot of credit for giving me all the support I have needed to be successful.

I'd love to be able to see Einstein's face right now!

Rainer Weiss

0 Introduction

Einstein's theory of general relativity predicts that all accelerating objects with non-symmetric mass distributions produce oscillations in the space-time metric, known as gravitational waves (GWs)[230]. GWs were a purely theoretical prediction until the discovery of the binary pulsar system PSR 1913+16. The orbit of this neutron star pair has been shown to be slowly losing energy at the rate predicted by General Relativity for GW emission[319]. This has served as indirect evidence for the existence of GWs.

The first discovery of a gravitational wave signal has been announced[24]. The signal, known as GW150914, was announced on 14 September 2015, to the broad network of follow-up facilities who signed confidential Memoranda of Understanding with the aLIGO/adVirgo team. As discussed in[24], it is a compact binary merger of two

black holes with chirp mass $M_c = 31.7 M_\odot$ and asymmetric mass ratio $q = 0.8$. From this event, the estimated local rate of BBH coalescences is $R_{local} = 0.016$ Mpc^{-3}Myr^{-1} with a factor of 5 uncertainty in either direction. GW150914 was found with a network signal to noise ratio of 25.3 corresponding to an $\approx 5\sigma$ detection. The initial LIGO skymaps returned by the unmodeled pipelines returned sky-areas with 90% confidence levels of ≈ 150 square degrees, with the final LIGO skymaps corresponding to compact binary coalescences returning skymaps about 50% smaller.

A number of gravitational wave detectors have been designed and implemented over the past fifty years. Joseph Weber built and published results from the first such detector. It looked for strains induced in an aluminum bar by GWs passing through the bar[317]. Although he published that he succeeded in GW detection, these "detections" are thought to be only noise sources. Many detectors similar to Weber's exist today, although they are seismically isolated and cryogenically cooled in order to reduce the natural vibrations in the bars and increase their sensitivity[28].

Interferometric gravitational-wave detectors include ground-based detectors, such as LIGO[23], Virgo[26], and GEO600[151], proposed underground detectors, such as the Einstein Telescope (ET)[131], and proposed space-based detectors, such as LISA[107]. These experiments seek to directly detect GWs and use them to study astrophysical sources. They are sensitive to the coalescence of massive binary systems containing massive objects such as a neutron stars or black holes. Other possible sources include the core collapse of a massive star into a Type II supernova, as well as processes from the time of the Big Bang that produce a stochastic background of GWs[78].

GWs are difficult to directly detect, mainly due to their extremely small amplitudes. Their space displacements are on the order of 10^{-18} m. To achieve this sensitivity, LIGO and Virgo use special interferometry techniques, state-of-the-art optics,

highly stable lasers, and multiple layers of vibration isolation[23].

Similar to light, gravitational effects do not propagate with infinite speed. Whenever the mass distribution in the universe changes (for example, when one drops a pencil), the gravitational field throughout the universe adapts to this new mass distribution. The amount of time the field takes to adapt at any given point in the universe is equal to the amount of time it takes for light to travel to that point. This propagating disturbance in the gravitational field is a GW.

GWs are a consequence of any theory which demands that gravitational effects propagate at finite speed. The strength and type of GW signal depends on the theory, so a characterization of any signal seen would serve as a test of general relativity. Further, studies of GW signals from exotic objects such as black holes, gamma ray bursts, and cosmic strings would give insight into their mechanics more than current electromagnetic followups[230].

As GWs pass through space, space-time is contracted and expanded in directions orthogonal to the direction of propogation. This oscillation can be written as a linear combination of two polarizations, one of which occurs in the x and y-directions, and the other along the two diagonals. Figure 1 shows these polarizations. It is this property of GWs that is exploited in order to detect them with interferometric detectors.

The interferometric ground-based detectors are Michelson interferometers with Fabry-Perot cavities. This type of interferometer consists of a monochromatic light source, which today is almost exclusively a laser. Its light is sent to a beam splitter and sent down two orthogonal arms. At the end of each of these arms is a reflective mirror. The beams reflect off of these mirrors and recombine at the beam splitter, thereby sending a portion of the light toward a photodiode, and the remaining back towards the laser. This photodiode outputs a current proportional to the average pho-

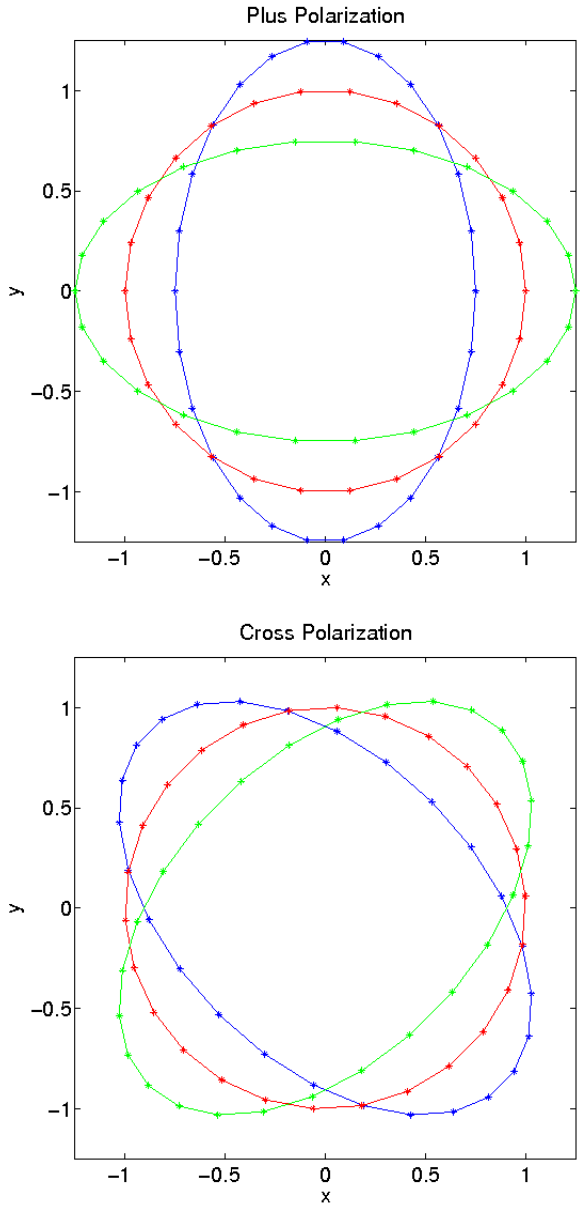


Figure 1: On the left is the deformation of space in the x and y-directions by a GW with plus polarization. On the right is the deformation of space in the x and y-directions by a GW with cross polarization

ton flux at the detector[28]. Any variation in the lengths of either arm will change the power seen at the photodetector. If a GW passes through an interferometer perpendicular to its arms, space orthogonal to the direction of its motion will expand and contract. This will change the length of both arms, causing the power to modulate as a function of time.

The binary coalescence of compact objects (CBCs), which include black holes (BHs) and neutron stars (NSs), are a likely source of gravitational-waves (GWs)[125,126]. As a CBC passes through its inspiral and merger stage, it generates GWs which sweep upward in frequency and amplitude through the sensitive band of GW detectors. The detection of GWs from CBCs will provide information about the populations of compact objects in the universe and a way to test general relativity. It is predicted that the advanced detectors could detect between 0.4-100 binary NS signals per year[123].

Estimating the parameters of the CBC objects is interesting for a number of reasons. Accurately estimating the sky location of the objects will allow for electromagnetic follow-up with telescopes[14]. The hope is that some fraction of the energetics released during CBC events will be in the form of electromagnetic waves. Short-hard gamma-ray bursts (GRBs) are thought to be the result of NS-NS or NS-BH mergers[124]. As optical afterglows have been observed for a few seconds to a few days after the GRB trigger, telescopes may be able to capture the afterglow from these events after GW detection. If multiple detections are available for analysis, inference about the distribution of the population of CBCs will allow for probing the astrophysics of binary evolution and dynamics of dense stellar environments[15]. Obtaining information about the CBC objects may also lead to unexpected discoveries for individual events.

Due to the large error boxes on sky localizations from the gravitational-wave detec-

tors, wide-field survey telescopes will most likely be required to make an electromagnetic followup detection. One such telescope is the Large Synoptic Survey Telescope (LSST), which is a wide-field 8.4 meter telescope that over a 10 year time period will repeatedly survey the southern sky in 6 passbands[212]. The telescope is in the process of being built on the El Pen peak of Cerro Pachon, a 2682 metre high mountain in Coquimbo Region, in northern Chile, alongside the existing Gemini South and Southern Astrophysical Research Telescopes. It is scheduled to be operational in 2022. Each LSST "visit" will consist of 2 back-to-back 15-second exposures before repointing to the next sky position. Each patch of sky will be visited 1000 times. LSST will provide a new time-domain window into the deep optical universe, exploring the transient optical sky and probing dark energy and dark matter.

This thesis explores a variety of topics related to GW astronomy. It is organized as follows. Chapters 1 through 3 are on how to use seismic data to search for gravitational waves. Chapters 4 through 6 are on how to detect long-duration gravitational-wave transients, including compact binary coalescences. Chapters 7 through 10 are on seismic and magnetic noise, including how to use seismic and magnetic data to reduce the effect on detectors. Chapters 11 through 13 are on characterization of the future LSST site and potential improvements to its efficiency.

In chapter 1, we present an upper limit of $\Omega_{\mathrm{GW}} < 1.2 \times 10^{8}$ on an isotropic stochastic gravitational-wave (GW) background integrated over a year in the frequency range $0.05\,\mathrm{Hz} - 1\,\mathrm{Hz}$, which improves current upper limits from high-precision laboratory experiments by about 9 orders of magnitude. The limit is obtained using the response of Earth itself to GWs via a free-surface effect described more than 40 years ago by F. J. Dyson. The response was measured by a global network of broadband seismometers selected to maximize the sensitivity. Publication information can be found in[88].

In chapter 2, we describe an analysis of Apollo era lunar seismic data that places an upper limit on an isotropic stochastic gravitational-wave background integrated over a year in the frequency range 0.1 Hz – 1 Hz. We find that because the Moon's ambient noise background is much quieter than that of the Earth, significant improvements over an Earth based analysis were made. We find an upper limit of $\Omega_{\rm GW} < 1.2\times10^5$, which is three orders of magnitude smaller than a similar analysis of a global network of broadband seismometers on Earth and the best limits in this band to date. We also discuss the benefits of a potential Earth-Moon correlation search and compute the time-dependent overlap reduction function required for such an analysis. For this search, we also find an upper limit an order of magnitude larger than the Moon-Moon search. Publication information can be found in[86].

Chapter 3 places limits on a mHz frequency band GW background. A gravitational wave can interact with matter by exciting vibrations of elastic bodies. Earth itself is a large elastic body whose so-called normal-mode oscillations ring up when a gravitational wave passes. Therefore, precise measurement of vibration amplitudes can be used to search for the elusive gravitational-wave signals. Earth's free oscillations that can be observed after high-magnitude earthquakes have been studied extensively with gravimeters and low-frequency seismometers over many decades leading to invaluable insight into Earth's structure. Making use of our detailed understanding of Earth's normal modes, numerical models are employed for the first time to accurately calculate Earth's gravitational-wave response, and thereby turn a network of sensors that so far has served to improve our understanding of Earth, into an astrophysical observatory exploring our Universe. In this work, we constrain the energy density of gravitational waves to values in the range 0.035 – 0.15 normalized by the critical energy density of the Universe at frequencies between 0.3 mHz and 5 mHz, using 10 years of

data from the gravimeter network of the Global Geodynamics Project that continuously monitors Earth's oscillations. This work is the first step towards a systematic investigation of the sensitivity of gravimeter networks to gravitational waves. Further advance in gravimeter technology could improve sensitivity of these networks and possibly lead to gravitational-wave detection. Publication information can be found in[87].

In chapter 4, we show how seedless clustering can be used to search for compact binary coalescences, which are a promising source of gravitational waves for second-generation interferometric gravitational-wave detectors. Although matched filtering is the optimal search method for well-modeled systems, alternative detection strategies can be used to guard against theoretical errors (e.g., involving new physics and/or assumptions about spin/eccentricity) while providing a measure of redundancy. In this chapter, we apply seedless clustering to the problem of low-mass ($M_{\rm total} \leq 10 M_{\odot}$) compact binary coalescences for both spinning and eccentric systems. We show that seedless clustering provides a robust and computationally efficient method for detecting low-mass compact binaries. Publication information can be found in[95].

In chapter 5, we show how seedless clustering can be used to search for eccentric compact binary coalescences. While most binaries are expected to possess circular orbits, some may be eccentric, for example, if they are formed through dynamical capture. Eccentric orbits can create difficulty for matched filtering searches due to the challenges of creating effective template banks to detect these signals. Here, we describe a parameterization that is designed to maximize sensitivity to low-eccentricity ($0 \leq \epsilon \leq 0.6$) systems, derived from the analytic equations. We show that this parameterization provides a robust and computationally efficient method for detecting eccentric low-mass compact binaries. Based on these results, we conclude that advanced detectors will have a chance of detecting eccentric binaries if optimistic models

prove true. However, a null observation is unlikely to firmly rule out models of eccentric binary populations. Publication information can be found in[91].

In chapter 6, we discuss how in previous work, we have introduced a clustering algorithm referred to as seedless clustering, and shown that it is a powerful tool for detecting weak and long-lived ($\sim$10–1000 s) gravitational-wave transients. However, as the algorithm is currently conceived, in order to carry out a search on approximately a year of data, significant computational resources may be required for estimating background events. Currently, the use of the algorithm is limited by the computational resources required for performing background studies to assign significance to events identified by the algorithm. In this work, we present an analytic method for estimating the background generated by the seedless clustering algorithm and compare the performance to both Monte Carlo Gaussian noise and time-shifted gravitational-wave data from a week of LIGO's 5th Science Run. We demonstrate qualitative agreement between the model and measured distributions and argue that the approximation will be useful to supplement conventional background estimation techniques for advanced detector searches for long-duration gravitational-wave transients. Publication information can be found in[90].

In chapter 7, we use a seismic array that has been deployed at the Sanford Underground Research Facility in the former Homestake mine, South Dakota, to study the underground seismic environment. This includes exploring the advantages of constructing a third-generation gravitational-wave detector underground. A major noise source for these detectors would be Newtonian noise, which is induced by fluctuations in the local gravitational field. The hope is that a combination of a low-noise seismic environment and coherent noise subtraction using seismometers in the vicinity of the detector could suppress the Newtonian noise to below the projected noise

floor for future gravitational-wave detectors. In this work, certain properties of the Newtonian-noise subtraction problem are studied by applying similar techniques to data of a seismic array. We use Wiener filtering techniques to subtract coherent noise in a seismic array in the frequency band 0.05 – 1 Hz. This achieves more than an order of magnitude noise cancellation over a majority of this band. The variation in the Wiener-filter coefficients over the course of the day, including how local activities impact the filter, is analyzed. We also study the variation in coefficients over the course of a month, showing the stability of the filter with time. How varying the filter order affects the subtraction performance is also explored. It is shown that optimizing filter order can significantly improve subtraction of seismic noise. Publication information can be found in[89].

In chapter 8, we discuss how Newtonian gravitational noise from seismic fields is predicted to be a limiting noise source at low frequency for second generation gravitational-wave detectors. Mitigation of this noise will be achieved by Wiener filtering using arrays of seismometers deployed in the vicinity of all test masses. In this work, we present optimized configurations of seismometer arrays using a variety of simplified models of the seismic field based on seismic observations at LIGO Hanford. The model that best fits the seismic measurements leads to noise reduction limited predominantly by seismometer self-noise. A first simplified design of seismic arrays for Newtonian-noise cancellation at the LIGO sites is presented, which suggests that it will be sufficient to monitor surface displacement inside the buildings. This paper has been submitted to Classical and Quantum Gravity.

In chapter 9, we point out that the recent discovery of merging black holes suggests that a stochastic gravitational-wave background is within reach of the advanced detector network operating at design sensitivity. However, correlated magnetic noise

from Schumann resonances threatens to contaminate observation of a stochastic background. In this work, we report on the first effort to eliminate intercontinental correlated noise from Schumann resonances using Wiener filtering. Using magnetometers as proxies for gravitational-wave detectors, we demonstrate as much as a factor of two reduction in the coherence between magnetometers on different continents. While much work remains to be performed, our results constitute a proof-of-principle and motivate follow-up studies with a dedicated array of magnetometers. This paper has been submitted to Classical and Quantum Gravity.

In chapter 10, we describe how early earthquake warning is a rapidly developing capability that has significant ramifications for many fields, including astronomical observatories. In this chapter, we discuss the susceptibility of astronomical facilities to seismic events, including large telescopes as well as second-generation ground-based gravitational-wave interferometers. We describe the potential warning times for observatories from current seismic networks and propose locations for future seismometers to maximize warning times. Publication information can be found in[93].

In chapter 11, we discuss how compact binary coalescences are a promising source of gravitational waves for second-generation interferometric gravitational-wave detectors such as advanced LIGO and advanced Virgo. These are among the most promising sources for joint detection of electromagnetic (EM) and gravitational-wave (GW) emission. To maximize the science performed with these objects, it is essential to undertake a follow-up observing strategy that maximizes the likelihood of detecting the EM counterpart. We present a follow-up strategy that maximizes the counterpart detection probability, given a fixed investment of telescope time. We show how the prior assumption on the luminosity function of the electro-magnetic counterpart impacts the optimized followup strategy. Our results suggest that if the goal is to detect an

EM counterpart from among a succession of GW triggers, the optimal strategy is to perform long integrations in the highest likelihood regions, with a time investment that is proportional to the 2/3 power of the surface density of the GW location probability on the sky. In the future, this analytical framework will benefit significantly from the 3-dimensional localization probability. This paper has been submitted to Experimental Astronomy.

In chapter 12, we determine the spatial structure of the lunar contribution to night sky brightness, taken at the LSST site on Cerro Pachon in Chile. We use an array of six photodiodes with filters that approximate the Large Synoptic Survey Telescope's *u, g, r, i, z,* and *y* bands. We also use the sun as a proxy for the moon, and measure sky brightness as a function of zenith angle of the point on sky, zenith angle of the sun, and angular distance between the sun and the point on sky. We make a correction for the difference between the illumination spectrum of the sun and the moon. Because scattered sunlight totally dominates the daytime sky brightness, this technique allows us to cleanly determine the contribution to the (cloudless) night sky from backscattered moonlight, without contamination from other sources of night sky brightness. We estimate our uncertainty in the relative lunar night sky brightness vs. zenith and lunar angle to be between 0.3-0.7 mags depending on the passband. This information is useful in planning the optimal execution of the LSST survey, and perhaps for other astronomical observations as well. Although our primary objective is to map out the angular structure and spectrum of the scattered light from the atmosphere and particulates, we also make an estimate of the expected number of scattered lunar photons per pixel per second in LSST, and find values that are in overall agreement with previous estimates. Publication information can be found in[94].

In chapter 13, we discuss how the precise determination of the instrumental re-

sponse function versus wavelength is a central ingredient in contemporary photometric calibration strategies. This typically entails propagating narrowband illumination through the system pupil, and comparing the detected photon rate across the focal plane to the amount of incident light as measured by a calibrated photodiode. However, stray light effects and reflections/ghosting (especially on the edges of filter passbands) in the optical train constitute a major source of systematic uncertainty when using a flat-field screen as the illumination source. A collimated beam projector that projects a mask onto the focal plane of the instrument can distinguish focusing light paths from stray and scattered light, allowing for a precise determination of instrumental throughput. This work describes the conceptual design of such a system, outlines its merits, and presents results from a prototype system used with the Dark Energy Camera wide field imager on the 4-meter Blanco telescope. A calibration scheme that blends results from flat-field images with collimated beam projector data to obtain the equivalent of an illumination correction at high spectral and angular resolution is also presented. In addition to providing a precise system throughput calibration, by monitoring the evolution of the intensity and behaviour of the ghosts in the optical system, the collimated beam projector can be used to track the evolution of the filter transmission properties and various anti-reflective coatings in the optical system. This paper has been submitted to the conference proceedings of SPIE 2016.

Chapter 14 presents the thesis summary.

One man's noise is another man's signal.

Edward W. Ng

1

Upper Limit on a Stochastic Background of Gravitational Waves from Seismic Measurements in the Range 0.05 Hz to 1 Hz

The idea to use Earth itself as response body to GWs is occasionally discussed among GW scientists, but quickly refuted since back-of-the-envelop calculations show that achievable strain sensitivities lie far below what is commonly considered as scientifi-

cally interesting. In fact, past attempts to find GW signals of known frequency from pulsars in seismic data were either unsuccessful[326,217] or even led to false detection claims[259]. As illuminating as these publications are from today's perspective, it will be shown in this paper that analyzing data from a network of modern global broadband seismometers with near optimal search pipelines can nonetheless lead to upper limits on GW amplitudes that beat previous high-precision gravity-strain measurements in certain frequency bands by many orders of magnitude. More specifically, we set a new upper limit on a frequency-independent energy density of a stationary stochastic GW background in the frequency range 0.05 Hz – 1 Hz that is about 9 orders of magnitude below the previous upper limit. The currently valid upper limits are summarized in Figure 1.1.

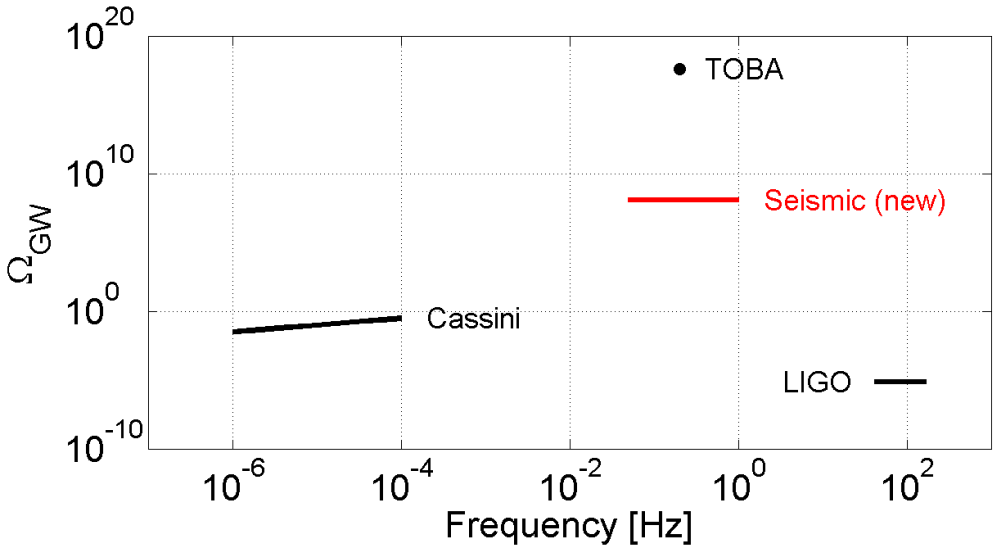


Figure 1.1: Currently valid upper limits on a stochastic GW background. Further details about these limits can be found in[275].

The response mechanism exploited here was first described by Dyson[116]. In the following, we repeat the most important part of his calculation mainly to present it in

a modern form. Dyson derives a boundary condition at a free flat surface that links surface displacement associated with seismic waves to the strain tensor of a GW. This equation can readily be written as

$$\begin{aligned}\lambda(\nabla \cdot \vec{\xi}(\vec{r},t))\vec{e}_z + \mu((\vec{e}_z \cdot \nabla)\vec{\xi}(\vec{r},t) + \nabla(\vec{e}_z \cdot \vec{\xi}(\vec{r},t))) \\ = \mu\, \vec{e}_z^{\top} \cdot h(\vec{r},t)\end{aligned} \tag{1.1}$$

Here λ, μ are the Lamé constants, $\vec{\xi}(\vec{r},t)$ ground displacement, $\vec{e}_z$ the normal vector to the surface ($\vec{e}_z^{\top}$ denotes its transpose), and $h(\vec{r},t)$ the spatial part of the GW strain tensor (i. e. a 3×3 matrix). This equation can be used to derive a GW response measured in horizontal and vertical surface displacement, but since seismic noise in vertical direction is typically weaker than in horizontal direction, we will focus on vertical displacement ξ_z from here on.

In this case, the response to GWs can be obtained by first projecting equation (1.1) onto the z-direction:

$$\lambda(\nabla \cdot \vec{\xi}(\vec{r},t)) + 2\mu\partial_z\xi_z(\vec{r},t) = \mu\, \vec{e}_z^{\top} \cdot h(\vec{r},t) \cdot \vec{e}_z \tag{1.2}$$

As pointed out in[116], boundary conditions demand that the horizontal wavevector of the GW and the generated seismic waves are the same. This means that since GWs travel at much higher speed than seismic waves, seismic waves generated by a GW propagate almost vertically with respect to the surface. In this case, all vertical seismic displacement is produced by longitudinal (compressional) waves, and all horizontal displacement by transverse (shear) waves. With these conclusions, we can solve equation (1.2) via Fourier transform with respect to $\vec{r}$ and t, using the following ap-

proximations

$$\begin{aligned} \nabla \cdot \vec{\xi}(\vec{r}\,,t) &\rightarrow i\vec{k} \cdot \vec{\xi}(\vec{k}\,,\omega) \approx i\omega/\alpha\, \xi_z(\vec{k}\,,\omega) \\ \partial_z \xi_z(\vec{r}\,,t) &\rightarrow ik_z \xi_z(\vec{k}\,,\omega) \approx i\omega/\alpha\, \xi_z(\vec{k}\,,\omega) \end{aligned} \tag{1.3}$$

where α is the speed of compressional waves, and $\vec{k}, \omega$ are the Fourier frequencies associated with $\vec{r}$, t. Transforming back into $\vec{r}$, t space, equation (1.2) finally simplifies to

$$\dot{\xi}_z(\vec{r}\,,t) \approx -\frac{\beta^2}{\alpha} \vec{e}_z^{\,\top} \cdot h(\vec{r}\,,t) \cdot \vec{e}_z \tag{1.4}$$

where β is the speed of shear waves. The fact that the natural readout variable is ground velocity rather than ground displacement simplifies the analysis as it is directly proportional to the data output by most commercial broadband seismometers, and also seismic noise has favorable properties in these units as shown below.

Applying equation (1.4) in real-world GW searches requires further assumptions and simplifications. First, seismic waves generated by a GW at one location can travel to the other side of the Earth interfering with counter-propagating seismic waves from the same GW and thereby modifying the GW response measured as surface displacement. However, above 0.05 Hz, seismic waves that have passed Earth have significantly smaller amplitude, which means that the flat free surface GW response is a good approximation to a more refined model that also takes Earth's spherical shape into account[321,53]. More significantly, systematic errors need to be considered with respect to the calibration of data into GW strain according to equation (1.4). The first calibration step is to convert raw data of seismometers into ground velocity. This is relatively easy to achieve in the targeted frequency range and it has also been confirmed in many dedicated experiments that relative calibration errors of broadband

seismometers between 0.05 Hz – 1 Hz lie well below 0.1 [135]. In addition, spectral histograms have been calculated for a full year to exclude that any of the seismic stations are subject to major technical issues.

The second calibration step from ground velocity to GW strain leads to the dominant systematic error. For an accurate calibration, one needs global surface maps of compressional and shear wave speeds α, β, which are not directly available. They can however be estimated from other parameters. The most accurate method that we found is to use the Poisson's ratio ν in combination with a global map of Rayleigh-wave phase velocities c_{R}. A global map of the Poisson's ratio was not available, but its value is constrained by measurements to be in the range $\nu \in [0.25, 0.29]$ [335]. Therefore, a mean value of $\nu_0 = 0.27$ is used and an estimate of the calibration error related to global variations $\Delta\nu$ of the Poisson's ratio is obtained from

$$\beta^2/\alpha \approx 0.5682 c_{\mathrm{R}} \cdot (1 - 1.5377 \Delta\nu) \tag{1.5}$$

The phase velocity map of c_{R} used in this paper was published by Ekström [121]. Since Rayleigh waves show significant dispersion, the maps were evaluated at several frequencies up to 0.04 Hz. Below 0.04 Hz, dispersion leads to minor relative changes in velocity of less than 0.1 [302,121]. However, Rayleigh-wave velocities decrease rapidly towards higher frequencies [68,72]. We exploit this general trend to minimize the calibration error by linearly interpolating between c_{R} at 0.05 Hz to $0.5 c_{\mathrm{R}}$ at 0.5 Hz. We estimate the remaining relative calibration error associated with wave dispersion to be about 0.3. Adding this error in quadrature to the relative calibration error associated with variations in Poisson's ratio, which is 0.03, and to the calibration error of the seismometer response to ground motion, leads to an overall calibration error of 0.32.

Our search for a stochastic GW background is based on the correlation of data from pairs of detectors similar to a recently published work[273]. An upper limit on a GW energy density Ω_{GW} is obtained from point estimates of

$$Y = 2 \int_0^\infty df\, \Re[\tilde{s}_1^*(f)\tilde{s}_2(f)]\tilde{Q}_{12}(f) \tag{1.6}$$

with $\langle Y \rangle = \Omega_{\mathrm{GW}}$ provided that noise contributing to the data $\tilde{s}_1(f)$, $\tilde{s}_2(f)$ is perfectly uncorrelated between seismometers. The signal-to-noise ratio (SNR) can be enhanced by filtering the data[69,33]. The optimal filter spectrum $\tilde{Q}_{12}(f)$ depends on the so-called overlap-reduction function (ORF) $\gamma_{12}(f)$[141], the noise spectral densities $S_1(f)$, $S_2(f)$ of the two seismometers, and also takes into account the relation between the GW spectral density and Ω_{GW}:

$$\tilde{Q}_{12}(f) = \mathcal{N} \frac{\gamma_{12}(f)}{f^3 S_1(f) S_2(f)} \tag{1.7}$$

where $\mathcal{N}$ is a normalization constant[10]. In this form, the filter is optimized for a frequency independent energy density Ω_{GW}. The ORF incorporates the dependence of the optimal filter on the relative positions and alignments of detector pairs. In the case of the free-surface GW response measured in vertical surface velocity, the alignment is fully determined by the detector location. Therefore, the ORF is simply a function of the seismometer positions, which is shown in Figure 1.2 as a function of the latitude λ_2 and longitude ϕ_2 of seismometer 2 with the seismometer 1 at $\lambda_1 = \phi_1 = 0$. For the free-surface response of eq. (1.4), an explicit expression of the

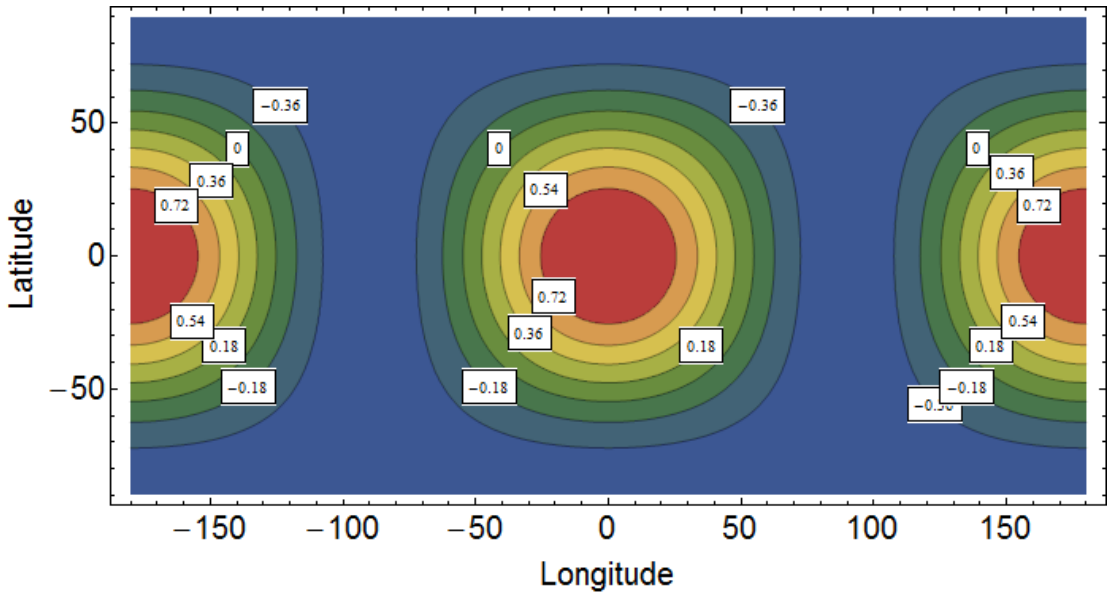


Figure 1.2: ORF at frequency $f = 0.5\,\mathrm{Hz}$ between seismometers as a function of the latitude and longitude of seismometer 2. Seismometer 1 is located at $\lambda_1 = \phi_1 = 0$.

ORF can be obtained:

$$\begin{aligned} \gamma_{12}(f) &= \frac{15((3-\Phi^2)\sin(\Phi) - 3\Phi\cos(\Phi))(1+3\cos(2\delta))}{4\Phi^5} \\ \Phi &\equiv \frac{4\pi f R_\oplus}{c}\sin(\delta/2) \\ \sin^2(\delta/2) &= \sin^2(\Delta\lambda/2) + \cos(\lambda_1)\cos(\lambda_2)\sin^2(\Delta\phi/2) \end{aligned} \tag{1.8}$$

where f is the frequency, c the speed of light, $R_\oplus$ Earth's radius, and $\Delta\lambda = \lambda_2 - \lambda_1$, $\Delta\phi = \phi_2 - \phi_1$. Here the result is given in terms of the angle δ subtended by the great circle between the two seismometers, and Φ is the phase accumulated by a GW that propagates along the line connecting the two seismometers.

Ideally, the locations of seismometers forming a correlation pair should be chosen to maximize the ORF. This is obviously the case for seismometers close to each other (coincident seismometers have $\gamma_{12}(f) = 1$). However, choosing seismometers close

to each other means that seismic noise is highly correlated, which strongly limits the SNR of the search for a stochastic GW signal. As can be seen in Figure 1.2, the ORF of a pair of antipodal stations is also high, $\gamma_{12}(0.5\,\mathrm{Hz}) \approx 0.996$, so that GW signals in the two seismometers are highly correlated, and at the same time, one can expect a great reduction in correlation of seismic noise. Therefore, as a first step, we selected seismometers that form antipodal pairs.

It is found that among seismometers forming antipodal pairs, many still show high seismic correlations. These correlations are generated by teleseismic events that produce significant ground motion on the entire globe. For this reason, times of strong ground motion are excluded in our analysis: two hours following earthquakes with magnitude $M > 6$ and a full day after earthquakes with $M > 8$. This greatly reduces seismic correlation between stations, but residual correlations can still be significant (i. e. much greater than the statistical error). Therefore, instead of using all available seismometer pairs, we select pairs with the lowest seismic correlation observed over an entire year. The final selection of 20 seismometer pairs is shown in Figure 1.3. Seismic data from 2012 were used for this study provided by the Data Management Center of the Incorporated Research Institutions for Seismology (IRIS). These stations were equipped with STS-1, STS-2, KS-36000-I, or KS-54000 broadband instruments. Their amplitude and phase response are approximately flat in the frequency range 0.05 Hz – 1 Hz.

As explained in the following, vetoes were applied to data stretches according to different criteria with the goal to restore stationarity of seismic data. The vetoed data are excluded from any of the presented results. As a first step, we give a simple characterization of the seismic data in terms of observed seismic spectra. Measuring a seismic spectrum every 128 s for each seismometer used in the analysis, and combining

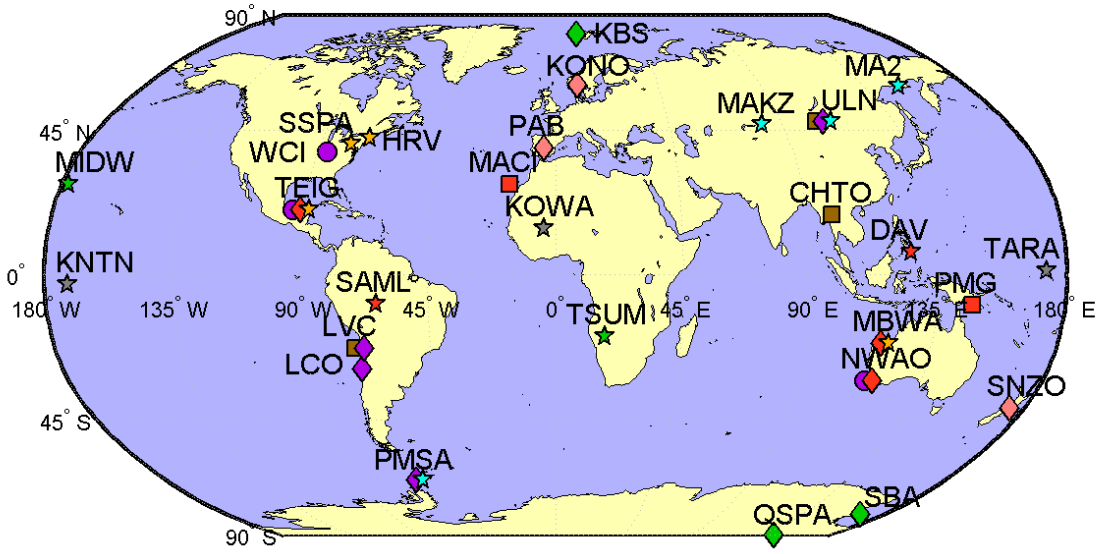


Figure 1.3: Location of seismometers used in this study. Markers are identical for seismometers that form an antipodal pair. Overlapping markers belong to the same seismic station.

all these spectra into one histogram, one obtains the result shown in Figure 1.4. The histogram does not only provide a complete view on the instrument sensitivity (limited by ambient seismic noise), but was also used to identify stations subject to strong disturbances (either by operators that made changes to the system, or by unknown local seismic events). These stations were further analyzed in time-frequency plots and the affected data stretches were vetoed for further analyses. The resulting distribution of seismic spectra extends well beyond the global low- and high-noise models that are shown as black curves, but the 10th and 90th percentiles lie mostly within this range, which are shown as white curves together with the median consistent with modern definitions of global noise models[97].

Another veto was applied based on time series to improve stationarity of the data.

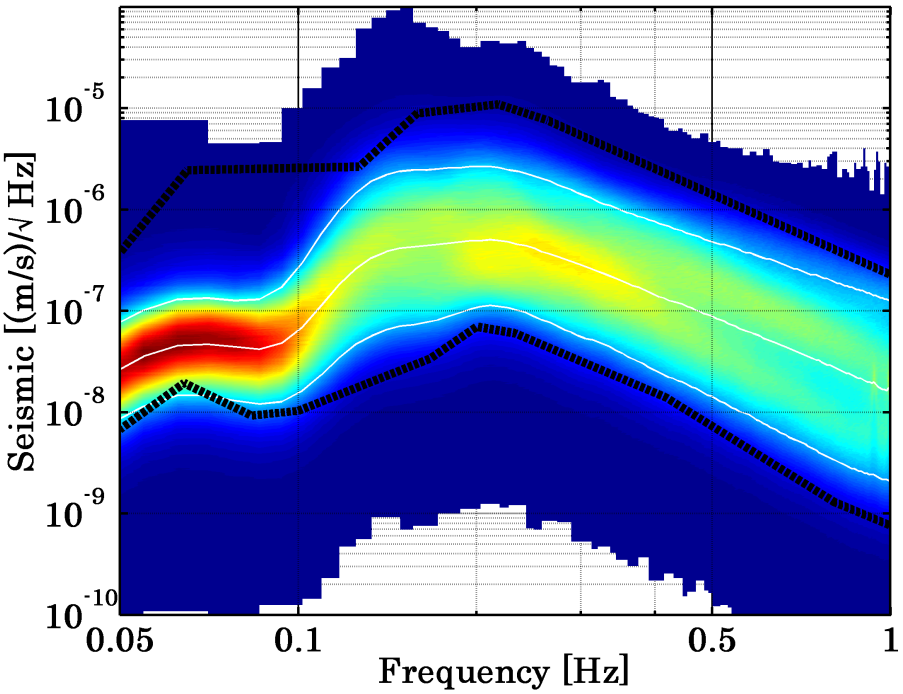


Figure 1.4: Combined histogram of 128 s seismic spectra from all stations used in our analysis accumulated over one year excluding vetoed data stretches. The three white curves are the 10th, 50th and 90th percentile of the distribution, whereas the two black lines represent the global low-noise and high-noise models as defined in [240].

What is meant by stationarity of seismic data needs clarification. Any ground motion in the frequency range 0.05 Hz – 1 Hz is produced by some kind of event, be it a storm, earthquake, anthropogenic noise, etc. The distribution of seismic displacement observed over long periods of time and therefore summing the contribution of many thousands of these events is what can be tested for stationarity. It follows that the observation time is an important parameter in the assessment of stationarity. For example, there can be stations in seismically active regions where a background of $M < 4$ earthquakes follows a stationary distribution over the course of a year. Since we are ultimately interested in the stationarity of the distribution of Ω_{GW} point es-

timates and associated errors, we used the distribution of one of these, the errors, to define a non-stationarity veto of data. This was done by calculating the histogram of errors for each month and station based on 100 s Hann windowed data segments with 50% overlap. Data that led to significant variations of these histograms from month to month were vetoed. Ultimately, these vetoes were exclusively related to strong events that contributed to the high-energy tail of the distribution.

After applying all vetoes, which amounted to excluding up to 5% of data, the resulting combined upper limit using all seismometer pairs, and the upper limit obtained from the single best pair including calibration errors are

$$\Omega_{\mathrm{GW}}^{\mathrm{tot}} < 1.2 \times 10^{8},\ \Omega_{\mathrm{GW}}^{\mathrm{sgl}} < 2.7 \times 10^{8} \tag{1.9}$$

We assumed a value $H_0 = 67.8\,\mathrm{km/s/Mpc}$ of the Hubble constant[77]. Using $S_{\mathrm{GW}}(f) = 3H_0^2\Omega_{\mathrm{GW}}/(10\pi^2 f^3)$, this translates into a strain sensitivity of about $1.3 \times 10^{-13}\,\mathrm{Hz}^{-1/2}$ at 0.1 Hz. The strongest conceivable upper limit on a stochastic background in the frequency range 0.05 Hz – 1 Hz set by a single seismometer pair can be calculated by assuming that seismic noise is uncorrelated between seismometers and stationary with spectrum given by the global low-noise model, and seismic data is perfectly calibrated into units of GW strain:

$$\Omega_{\mathrm{GW}}^{\mathrm{opt}} < 2.4 \times 10^{7} \left(\frac{1\,\mathrm{yr}}{T}\right)^{1/2} \left(\frac{1.9\,\mathrm{km/s}}{\beta^2/\alpha}\right)^{2} \tag{1.10}$$

where T is the correlation time, and here seismic speeds are assumed to be frequency independent.

The previous upper limit $\Omega_{\mathrm{GW}} < 4.3 \times 10^{17}$ was set by a high-precision gravity

strain measurement[175]. The main reasons for which it was possible to improve this upper limit by so many orders of magnitude are that only modest seismic isolation has been achieved at low frequencies so far. At the same time, the effective baseline of the free-surface response corresponds to the length of seismic shear waves in the range 0.05 Hz to 1 Hz, which is about 4–5 orders of magnitude larger than the baseline realized in past experiments. Finally, the global network of broadband seismometers records data reliably, with some stations providing data over periods of several years allowing us to carry out long integrations of the strain signal.

As can be concluded from eq. (1.10), future improvements on the upper limit by more than an order of magnitude using seismic measurements should not be expected, but it may be possible to achieve a better result by (1) identifying seismometer pairs with unusually low ambient seismic noise at both sites (Moon?), (2) integrating for much longer than 1 yr, (3) finding locations where the fraction β^2/α has an unusually high value, (4) optimizing data selection so that a larger number of seismometer pairs significantly contribute to lowering the upper limit, or (5) narrowing the band of the search and make use of structural resonances in the strain response[183].

2

Constraining the gravitational wave energy density of the Universe in the Range 0.1 Hz to 1 Hz using the Apollo Seismic Array

The use of astrophysical bodies, such as the Earth, Moon, Sun, and other stars, as detectors of GWs is well-motivated. Siegel and Roth[275] recently used high-precision radial velocity data for the Sun to place upperlimits on a stochastic gravitational-

wave (GW) background in the millihertz band. We recently used data from a network of modern global broadband seismometers to set upper limits on a stochastic background of GWs in the 0.05-1 Hz frequency range, which bested previous limits by 9 orders of magnitude[88]. These studies complement GW detectors such as LIGO[17] and torsion-bar antennas[273]. There are currently few dedicated GW experiments in the frequency range 10^{-4} Hz - 10 Hz. In this band, compact binaries in their inspiral and merger phase are strong possibilities. Although interesting in their own right, these would be a foreground for the potential detection of primordial GWs. GWs were recently possibly detected in the B-mode polarization of the CMB background, providing confirmation of the theory of inflation[76]. Assuming a slow roll inflationary model, this signal would correspond to a GW energy density spectrum $\Omega_{\rm GW} \approx 10^{-15}$ in the 0.1 Hz to 1 Hz band. There are a number of GW experiments which could probe this background. Space-based GW detectors will target the frequency band 10^{-4} Hz - 1 Hz[310]. There are also concepts for a number of future low-frequency terrestial GW detectors with sensitivity goals better than $10^{-19}/\sqrt{\rm Hz}$ in the 0.1 Hz to 10 Hz band[160]. The currently valid upper limits are summarized in Figure 2.1.

One of the lessons from the previous study was that a quieter seismic environment would increase the sensitivity of the analysis. For this reason, we analyze Lunar seismic data taken during the Apollo missions. The Moon is the only cosmic body in the Solar system (apart from the Earth), for which seismic data are available. These seismometers were placed on the Moon by the Apollo 12, 14, 15 and 16 missions from 1969 through 1972 and were functional until they were switched off in September 1977. The network was placed on the front center of the Moon in an (approximately) equilateral triangle with 1100-km spacing between stations. Each seismic station consisted of three long-period seismometers aligned orthogonally to measure the three

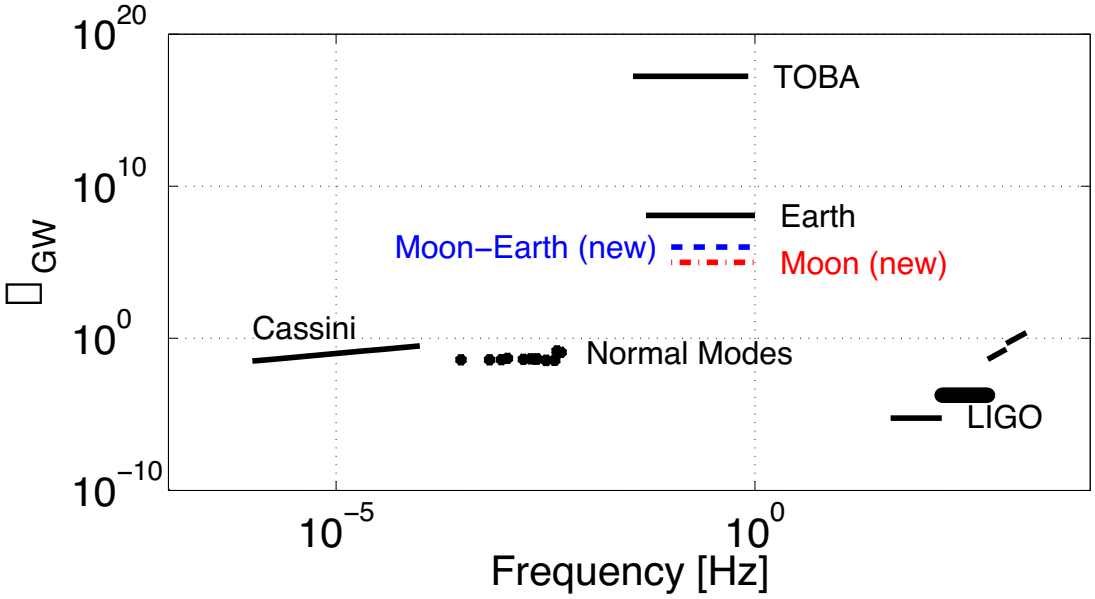


Figure 2.1: Currently valid upper limits on GW energy density. These limits were set by correlating data from torsion-bar antennas[273], Doppler-tracking measurements of the Cassini spacecraft[41], monitoring Earth's free-surface response with seismometers[88], measuring the normal modes of the Earth[87] and correlating data from the first-generation, large-scale GW detectors LIGO[3].

directions of motion. It also included a single-axis short-period seismometer sensitive to vertical motion at higher frequencies. Many important analyses have been performed using this data set, including generation of the first models of the Moon (for a review of the differences between the structures of the Earth, Moon, and Mars, please see[210]).

The main sources of ambient noise on the Earth are active tectonics as well as ocean microseisms and atmospheric fluctuations. As the Moon has none of these, the ambient noise background is quite different. Instead, the Moon's seismic noise is predominantly due to tidal forces, thermal stresses, and impacts from asteroids[269]. Thermal stresses are due to energy from the Sun, and thus their amplitude is strongly correlated to the lunation period of 29.5 Earth days. They increase after the lunar

sunrise and gradually decrease after the sunset.

More than 12,000 moonquake events have been discovered[331]. About 7,050 of these events have been positively identified as deep moonquakes, 1,743 are meteoroid impacts, 28 are shallow moonquakes, and there are some other events, such as thermal moonquakes and artificial impacts, and unclassified events. The deep moonquakes are believed to be caused by tidal forces between Earth and the Moon, unlike earthquakes, which are due to tectonic plate movement. The energy loss due to both the deep and shallow moonquake events has been analyzed[149]. Deep moonquakes release several orders of magnitude less energy than shallow moonquakes. The moonquakes were analyzed in detail in order to study the shallow seismic velocity structure under the seismometers[80,167,224,206,268]. More recently, analyses of these data suggested a presence of a solid inner and fluid outer core, overlain by a partially molten boundary layer[318]. There are proposals to place a seismic array on the Moon to improve on these analyses[144].

In this paper, we report on searches for an isotropic stochastic background using Apollo lunar seismometers from 1976. We perform two such analyses, a Moon-Moon correlation search and an Earth-Moon correlation search. The idea is to use the Moon and Earth as response bodies to GWs. We analyze data from a network of seismometers with near optimal search pipelines. For the Moon-Moon case, we find an upper limit approximately three orders of magnitude smaller than the previous best limits in the frequency range of interest. For the Earth-Moon case, the upper limit is approximately an order of magnitude larger. These are likely to remain the best limits in this frequency band until second-generation torsion bar antennas[175]. In section 2.1, we outline the search pipeline. We describe the Moon-Moon analysis and results in section 2.2. In section 2.3, we describe the time-dependent overlap reduction function for

an Earth-Moon search and perform a similar analysis. We conclude with a discussion of topics for further study in section 2.4.

2.1 Formalism

The response mechanism used here was first described by Dyson[116]. A rederivation in modern terms was presented in[88]. The idea is to measure displacement at the surface due to GWs, given by

$$\dot{\xi}_z(\vec{r},t) \approx -\frac{\beta^2}{\alpha}\vec{e}_z^{\top}\cdot h(\vec{r},t)\cdot\vec{e}_z, \tag{2.1}$$

where $\vec{\xi}(\vec{r},t)$ is ground displacement, $\vec{e}_z$ the normal vector to the surface, and $h(\vec{r},t)$ the spatial part of the GW strain tensor (i. e. a 3×3 matrix), β is the speed of shear waves, and α is the speed of compressional waves.

There are two calibration steps required to calibrate raw seismometer data into GW strain. The first is to calibrate raw data of seismometers into ground velocity. Apollo lunar data are sampled in displacement, and so a derivative is first taken to convert to velocity. The second is to calibrate from ground velocity into GW strain. From, Eq. (2.1), this requires calculation of β^2/α. To do so, we use a combination of the Poisson's ratio ν and Rayleigh-wave velocities $c_{\rm R}$ calculated from Weber's Lunar seismic speed model[318]. Between 1 km - 15 km, ν assumes values between 0.24 – 0.27 calculated from the estimates of seismic speeds in each layer. The reason why we do not directly calculate the calibration factor from estimates of α, β is that these parameters vary with depths, and therefore one needs an effective value of β^2/α characterizing the coupling to a surface source (the GW excitation) in a specific frequency range. The corresponding averaging over near surface layers is equivalent to calculating the Rayleigh-wave velocity as a function of frequency. The Rayleigh-wave dis-

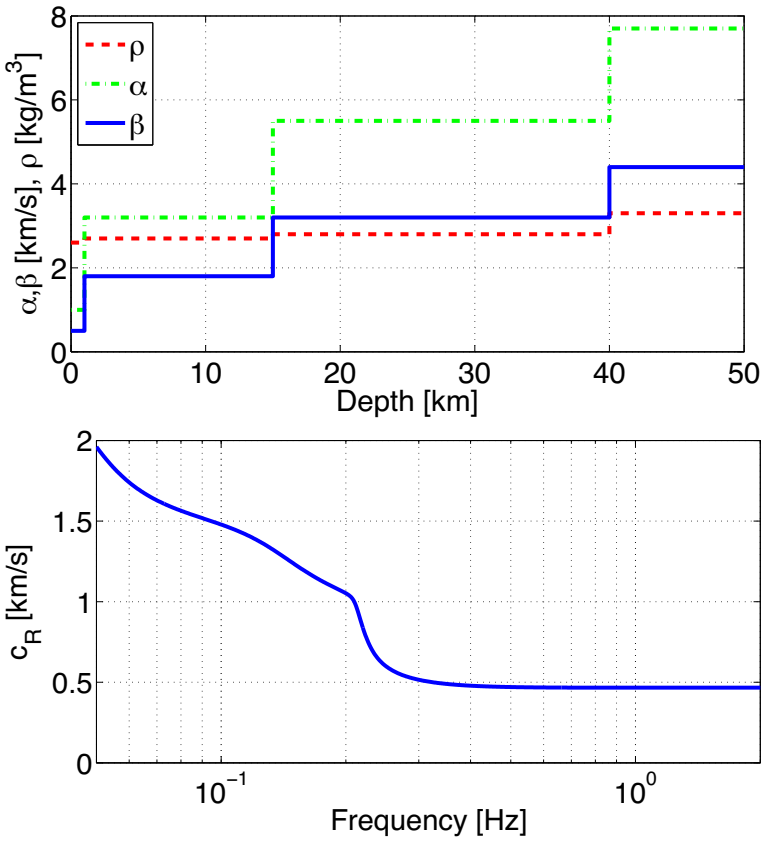


Figure 2.2: On the left is the P-, S-wave velocity and density structure for the whole-Moon model displayed for the near-surface layers (0 km-50 km)[318]. On the right is the dispersion curve calculated using Geopsy's gplivemodel for this layered model.

persion curve is obtained using Geopsy's gplivemodel[316], which computes dispersion curves from a layered model, and is plotted on the right of Figure 2.2. From 0.05 Hz to 0.2 Hz, the velocities decrease approximately linearly by a factor of 2. From 0.2 Hz to 0.3 Hz, the velocities decrease rapidly by another factor of 2. Above 0.3 Hz, the dispersion is minor. As was argued in[88], only a rough independent estimate of the Poisson's ratio is required to obtain the calibration factor since variations $\Delta\nu$ of the Poisson's ratio are expected to be minor (as seems to be the case as well for the Moon given the range of values obtained from all Moon layers). Expanding the calibration

term into linear order of the variation around a reference value of $\nu_0 = 0.27$, one can estimate the systematic calibration error according to

$$\beta^2/\alpha \approx 0.5682 c_{\mathrm{R}} \cdot (1 - 1.5377\Delta\nu) \tag{2.2}$$

Since the Rayleigh-wave speed varies with frequency, the calibration factor is a function of frequency. The gravitational-wave energy density spectrum is defined as

$$\Omega_{\mathrm{GW}}(f) = \frac{1}{\rho_c}\frac{d\rho_c}{dlnf} \tag{2.3}$$

where the critical density of the universe is $\rho_c = 3H_0^2/8\pi G$. Expressing in terms of the one-sided power spectral density, $S_h(f)$,

$$\Omega_{\mathrm{GW}}(f) = \left(\frac{2\pi^2}{3H_0^2}\right) f^3 S_h(f) \tag{2.4}$$

We use a cross-correlation method optimized for detecting an isotropic SGWB using pairs of detectors[33]. This method defines a cross-correlation estimator:

$$\hat{Y} = \int_{-\infty}^{\infty} df \int_{-\infty}^{\infty} df' \delta_T(f - f') \tilde{s}_1^*(f) \tilde{s}_2(f') \tilde{Q}(f') \tag{2.5}$$

and its variance:

$$\sigma_Y^2 \approx \frac{T}{2} \int_0^{\infty} df P_1(f) P_2(f) |\tilde{Q}(f)|^2, \tag{2.6}$$

where $\delta_T(f - f')$ is the finite-time approximation to the Dirac delta function, $\tilde{s}_1$ and $\tilde{s}_2$ are Fourier transforms of time-series strain data from two seismometers, T is the coincident observation time, and P_1 and P_2 are one-sided strain power spectral densities from the two seismometers. The signal-to-noise ratio (SNR) can be enhanced

by filtering the data[69,33]. The optimal filter spectrum $\tilde{Q}_{12}(f)$ depends on the overlap-reduction function (ORF) $\gamma_{12}(f)$[141], the noise spectral densities $S_1(f)$, $S_2(f)$ of the two seismometers, and also takes into account the relation between the GW spectral density and $\Omega_{\rm GW}$:

$$\tilde{Q}_{12}(f) = \mathcal{N}\frac{\gamma_{12}(f)}{f^3 S_1(f) S_2(f)} \tag{2.7}$$

where $\mathcal{N}$ is a normalization constant[10]. In this form, the filter is optimized for a frequency independent energy density $\Omega_{\rm GW}$. The ORF incorporates the dependence of the optimal filter on the relative positions and alignments of detector pairs. In our case, the ORF is determined by the relative locations of the seismometers and is given by

$$\gamma_{12}(f) = \frac{15((3-\Phi^2)\sin(\Phi) - 3\Phi\cos(\Phi))(1+3\cos(2\delta))}{4\Phi^5} \tag{2.8}$$

with

$$\Phi \equiv \frac{2\pi f D}{c} \tag{2.9}$$

where D is the distance between the seismometers, f is the GW frequency, c the speed of light. The angle δ denotes the relative orientation of two vertical sensors. In the Moon-Moon case, the distance depends on the location of the seismometers on the Moon

$$\begin{aligned} D &\equiv 2\sin(\delta/2) R_\circ \\ \sin^2(\delta/2) &= \sin^2(\Delta\lambda/2) + \cos(\lambda_1)\cos(\lambda_2)\sin^2(\Delta\phi/2) \end{aligned} \tag{2.10}$$

where $R_\circ$ is the Moon's radius, and $\Delta\lambda = \lambda_2 - \lambda_1$, $\Delta\phi = \phi_2 - \phi_1$ are the differences in latitude and longitude. The distance between a seismometer on Earth and on the Moon is well approximated by the distance between the centers of Earth and

Moon, and so that distance is used in the analysis. The change in distance between the Earth and Moon as a function of time is predominantly due to the eccentricity of the Moon's orbit. It is calculated from an implementation of the method described in[220]. The relative orientation angle δ needs to be calculated as a function of time for the Moon-Earth analysis as outlined in section 2.3.

2.2 Moon-Moon Correlation

Long-period Apollo PSE ALSEP seismometers were run in two modes of data acquisition. The "peak" mode has a peak sensitivity at about 0.5 Hz. The "flat-response" mode is about flat from 0.1-1 Hz in units of ground displacement. There were four seismometers taking data during this period. Three of the seismometers took coincident broadband data from July 1975 to March 1977. These seismometers form an approximately 1100 km equilateral triangle. From this period, we took a year of data from 1976. The original data were converted into MiniSEED and supplied by GEOSCOPE. During the conversion process, a constant, nominal sample rate was assumed, when in reality the sample rate varied with time because the timing oscillator on board the central station was not temperature controlled. This generates a small timing error and increases the correlation between stations with a 24 hour periodicity slightly. ALSEP seismometer data was also binned in 54 s records. Blocking of the entire ALSEP data into 54 s blocks affected the reference voltage of the analog-to-digital converter through the power supply. This is the likely cause of the small spectral line at about 0.81 Hz, which is about half the period of a logical record of the ALSEP data ($64/106 \approx 0.604$ seconds).

For the analysis, we divide the strain time series data into 50% overlapping 100 s

segments that are Hann-windowed. It is found that the seismometers show high seismic correlations due to transient events. These are likely predominantly due to moonquakes and asteroids hitting the Moon. For this reason, we remove the data surrounding all known moonquakes. This removes about 13% of the original data and greatly reduces seismic correlation between stations. To minimize remaining correlations, we apply stationarity cuts to the data. We calculate the signal-to-noise ratio of each 100 s segment and find the signal-to-noise ratio threshold required to bring the point estimate to half of the sigma error bars. We then remove the segments with signal-to-noise ratios that exceed this limit. This removes about 1% of the data. Ultimately, these vetoes were exclusively related to strong events that contributed to the high-energy tail of the distribution.

The vetoed data are excluded from any of the presented results. As a first step, we give a simple characterization of the seismic data in terms of observed seismic spectra. Measuring a seismic spectrum every 128 s for each seismometer used in the analysis, and combining all these spectra into one histogram, one obtains the result shown in Figure 2.3. This demonstrates the sensitivity of the Lunar seismometers. One can see that the median of the spectra is well below the global new low-noise model[240]. This low-noise floor of the Earth's ambient noise determined the ultimate noise limit for the Earth analysis. This demonstrates the significant benefit of a lunar search.

To combine the measured $\hat{Y}$ for each of the seismometer pairs, we follow[33] and average results from detector pairs weighted by their variances. The optimal estimator is given by

$$\hat{Y}_{\rm tot} = \frac{\sum_l \hat{Y}_l \sigma_l^{-2}}{\sum_l \sigma_l^{-2}} \tag{2.11}$$

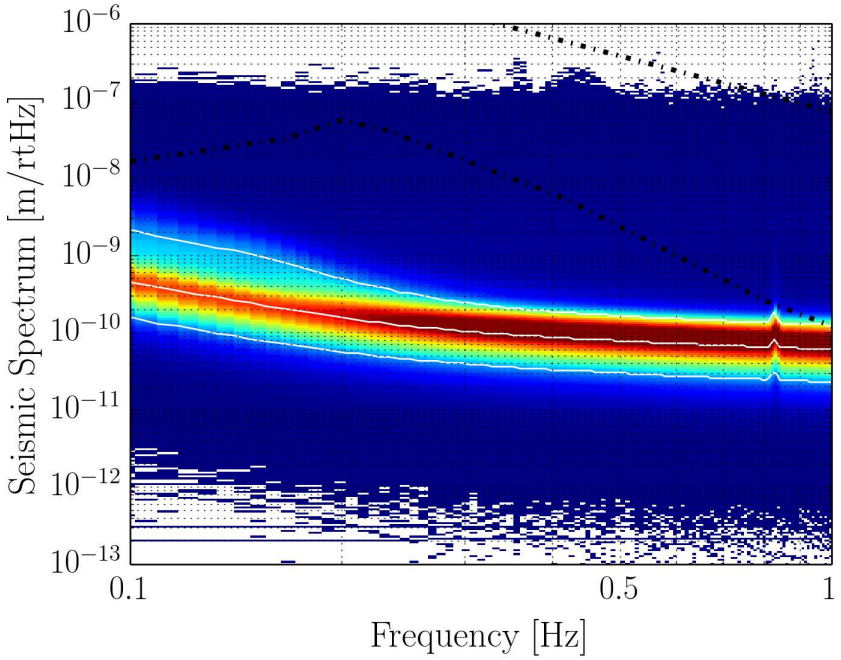


Figure 2.3: Spectral variation of combined lunar seismic spectra. The dash-dotted lines in black represent the global new low- and high-noise models[240].

where l sums over detector pairs. The total variance, $\sigma^2_{\rm tot}$, is

$$\sigma^{-2}_{\rm tot} = \sum_l \sigma_l^{-2}. \tag{2.12}$$

The resulting combined upper limit of a frequency-independent energy density using the three seismometer pairs, and integrating over frequencies between 0.1 Hz and 1 Hz, including calibration errors is

$$\Omega_{\rm GW} < 1.2 \times 10^5 \tag{2.13}$$

We assumed a value $H_0 = 67.8\,{\rm km/s/Mpc}$ of the Hubble constant[77]. Using $S_{\rm GW}(f) = 3H_0^2\Omega_{\rm GW}/(10\pi^2 f^3)$, this translates into a strain sensitivity of about $4.1 \times 10^{-15}\,{\rm Hz}^{-1/2}$

at 0.1 Hz.

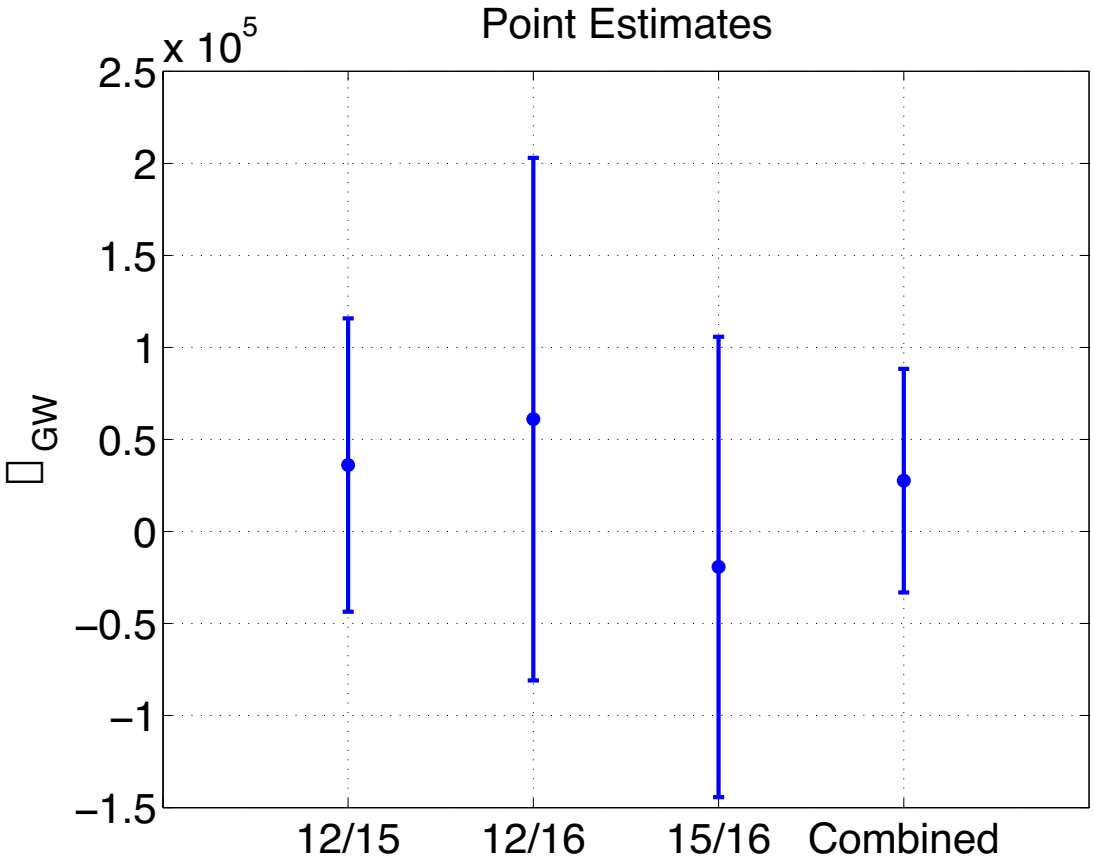


Figure 2.4: Point estimate and error bars for the three seismometer pairs, as well as for the combination of the three pairs.

2.3 Earth-Moon Correlation

In the analyses that have been performed thus far, first on the Earth and now with the Lunar seismometers, the relative orientation of the seismometers analyzed were in a constant orientation. These studies have benefited from the years of seismic data available, both from the vast seismic arrays on Earth as well as the Lunar seismic ar-

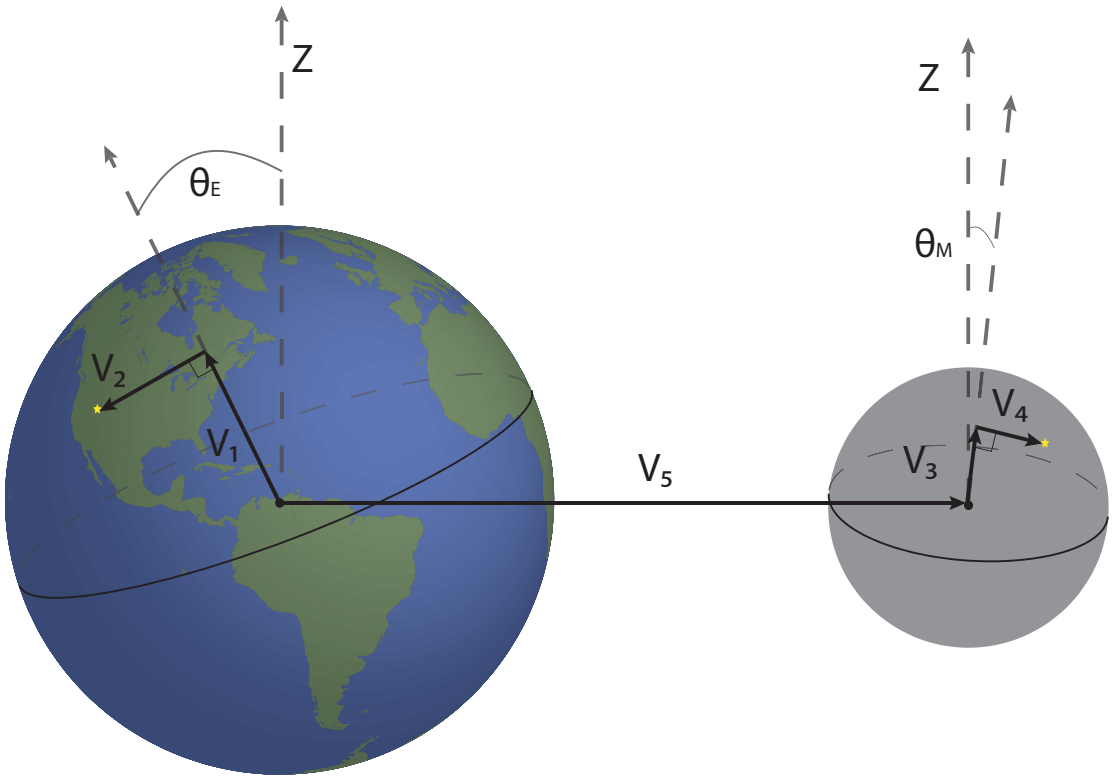


Figure 2.5: Geometry of the Earth-Moon correlation derivation. The sum of $\vec{v_1}$ and $\vec{v_2}$ correspond to the Earth seismometer, while the sum of $\vec{v_3}$ and $\vec{v_4}$ correspond to the Moon seismometer.

ray. A short-coming of these analyses are the potential for residual seismic correlation due to seismic activity present at both seismometers.

A potential way around this is to correlate seismometers from the Moon and the Earth. First, we calculate the relative orientation of seismometers on the Earth and the Moon, accounting for the rotation of the bodies. We will then use these orientations to calculate a time-dependent ORF using Eq. (2.8). This calculation will be useful for any situation where detectors have a time-dependent orientation. We begin with the geometry shown in Figure 2.5 and define the coordinate system we will work in. A convenient coordinate system to work in is known as the EME2000 sys-

tem, which is an Earth-centered frame. It defines its epoch to be January 1, 2000, 12 hours Terrestrial Time, which has a Julian Date of 2451545.0. Its z-axis is orthogonal to the Earth's mean equator at this epoch, the x-axis aligned with the mean vernal equinox, and the y-axis is orthogonal to both, rotated 90° about the celestial equator. The orientation of the Moon as a function of time is well-known in this system, and therefore provides an ideal coordinate system on which to base these calculations. We make the approximation that the Earth rotation axis has changed negligably between 1970 and 2000, which is reasonable because the Earth's precession has a period of 26,000 years.

We compute each seismometer location as the sum of two orthogonal vectors. For convenience, we will denote three dimensional rotations by $R(\theta, \vec{v})$, where θ is the angle of rotation and $\vec{v}$ is the vector being rotated around. We denote the longitudes of the Earth and Moon seismometers by ϕ_{E} and ϕ_{M} respectively, and the latitudes by λ_{E} and λ_{M}. We begin with the vectors for the Earth seismometer, $\vec{v}_1$ and $\vec{v}_2$. The first vector, $\vec{v}_1$, is orthogonal to the Earth's equatorial plane. Because the coordinate system is fixed such that the equator is always in the $x - y$ plane, this vector is a constant in the Z direction with a length of $\sin(\lambda_{\mathrm{E}})$. The second vector, $\vec{v}_2$, points from the tip of $\vec{v}_1$ to the seismometer. Because of the Earth's axial rotation, this vector is time-dependent and traces out a circle in the $x - y$ plane, with a radius equal to $\cos(\lambda_{\mathrm{E}})$. The vector's angle in this plane can be computed as the sidereal time at the longitude of the seismometer, which corresponds to the seismometer's right ascension in this system. We denote this angle by $\alpha(\phi_{\mathrm{E}}, t)$. Therefore, $\vec{v}_2$ results from a rotation of a vector in the x-direction around the z-axis by this angle, $R(\alpha(\phi_{\mathrm{E}}, \mathrm{t}), \vec{Z})$, where $\vec{Z}$ denotes the unit vector pointing in the direction of the z-axis.

We now perform the same calculation for the Lunar seismometer vectors, $\vec{v}_3$ and

$\vec{v}_4$. In this system, the axis orthogonal to the Moon's equator is slightly more complicated than that of the Earth. There are equations describing the right ascension, α_{M}, and declination, δ_{M}, of the Lunar pole as a function of time in the EME2000 coordinate system[40]. We denote the vector normal to the Moon's equator, computed from these coordinates using the usual spherical to Cartesian conversion, as $\vec{Z}_{\mathrm{M}}(t)$. $\vec{v}_3$ is then in the direction of $\vec{Z}_{\mathrm{M}}(t)$ with a length $\sin(\lambda_{\mathrm{M}})$. To calculate $\vec{v}_4$, we first compute the vector known as the IAU node, which is the vector orthogonal to $\vec{Z}_{\mathrm{M}}$ and the z-axis, $\vec{Z}_{\mathrm{M}}(t) \times \vec{Z}$. There are also equations describing the angle $W(t)$ between the prime meridian of the Moon and the IAU node vector[40]. We use the code in[118], which provides α_{M}, δ_{M}, and W, to compute these quantities. To account for the difference between the prime meridian and the longitude, we add the Lunar seismometer's longitude to $W(t)$. $\vec{v}_4$ is then computed by rotating the IAU node by this angle, $R(W(t) + \phi_{\mathrm{M}}, \vec{Z}_{\mathrm{M}}(t))$. It has a length of $\cos(\lambda_{\mathrm{M}})$.

We can now succinctly summarize the computation of the four vectors in equation form:

$$\begin{aligned}
\vec{v}_1 &= \sin(\lambda_{\mathrm{E}})\vec{Z} \\
\vec{v}_2 &= \cos(\lambda_{\mathrm{E}})R(\alpha(\phi_{\mathrm{E}}, t), \vec{Z}) \cdot \vec{X} \\
\vec{v}_3 &= \sin(\lambda_{\mathrm{M}})\vec{Z}_{\mathrm{M}}(t) \\
\vec{v}_4 &= \cos(\lambda_{\mathrm{M}})R(W(t) + \phi_{\mathrm{M}}, \vec{Z}_{\mathrm{M}}(t)) \cdot \frac{\vec{Z}_{\mathrm{M}}(t) \times \vec{Z}}{\|\vec{Z}_{\mathrm{M}}(t) \times \vec{Z}\|}
\end{aligned} \tag{2.14}$$

where the Moon rotation axis vector is given in terms of the time-dependent right-ascension and declination angles according to

$$\vec{Z}_{\mathrm{M}} = [\cos(\alpha_{\mathrm{M}})\cos(\delta_{\mathrm{M}}), \sin(\alpha_{\mathrm{M}})\cos(\delta_{\mathrm{M}}), \sin(\delta_{\mathrm{M}})] \tag{2.15}$$

We now have the required quantities to calculate the angle δ in Eq. (2.8) between the two seismometers. This corresponds to finding the angle between $\vec{v}_1 + \vec{v}_2$ and $\vec{v}_3 + \vec{v}_4$. Figure 2.6 shows the ORF between example Earth and Moon seismometers as a function of time at 0.1 Hz. The ORF displays both a daily cycle, due to the rotation of the Earth, as well as a monthly cycle, due to the Moon's libration, which has a 28 day period. Due to tidal locking, the Moon has only one face pointing towards the Earth at all times. The face pointing towards the Earth oscillates slightly with time, and this effect is called libration. Slightly more than half of the Moon's surface can be seen from Earth. Libration in longitude results from the eccentricity of the Moon's orbit around Earth, while libration in latitude results from the inclination between the Moon's axis of rotation and the normal of its orbital plane.

We perform an analysis as described above using the Lunar seismic array and seismometers on Earth. The Earth seismometers used are Geotech KS-36000 Borehole seismometers located in Albuquerque, New Mexico, USA (ANMO), Guam, Marianas Islands (GUMO), and Mashhad, Iran (MAIO). To calibrate these data, we convert from displacement to velocity by first taking a derivative. Following[88], we use a global phase velocity map of c_{R} to calculate β^2/α for the Earth seismometers[121]. We perform the analysis on the coincident data from 1976 for all nine possible pairs, which yields the following upper limits for all pairs and the single best pair:

$$\Omega_{\mathrm{GW}}^{\mathrm{tot}} < 1.1 \times 10^6, \; \Omega_{\mathrm{GW}}^{\mathrm{sgl}} < 1.9 \times 10^6 \tag{2.16}$$

Although this is an order of magnitude higher than that obtained for the Moon-Moon analysis, it is in some sense a more robust upper limit since correlation between seismometers can only exist due to a GW signal.

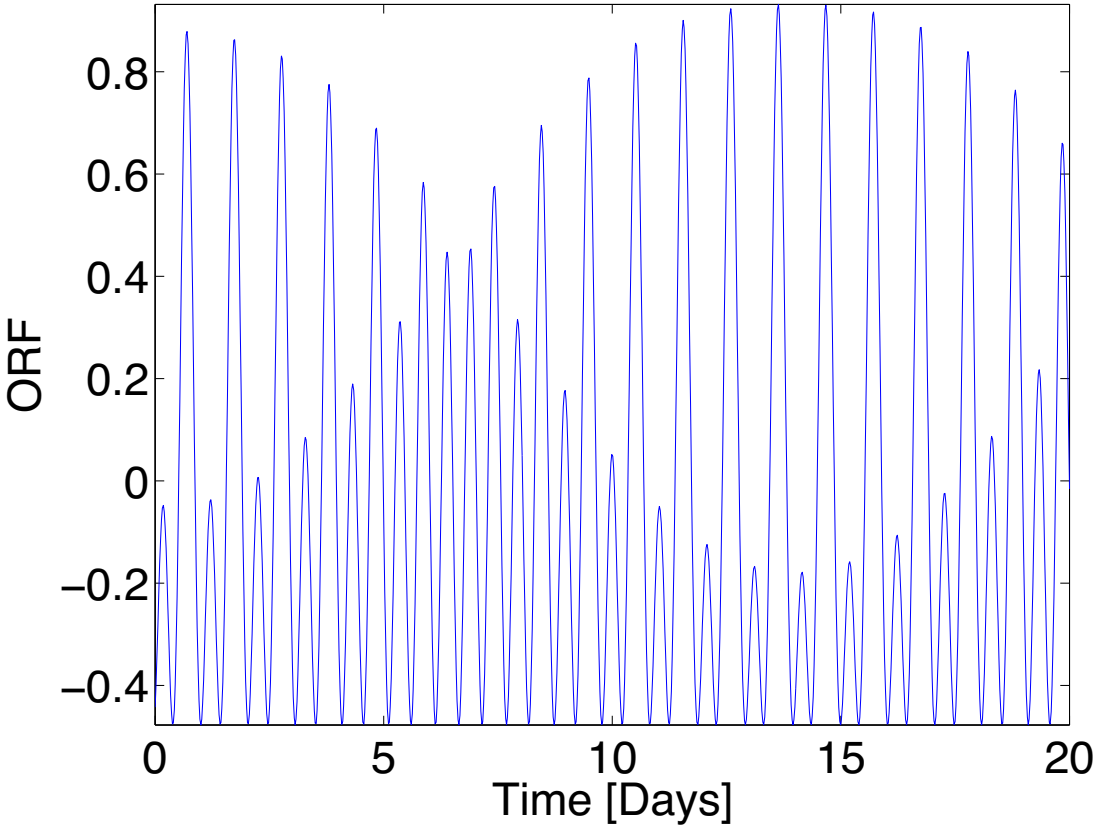


Figure 2.6: Overlap reduction function between example Earth and Moon seismometers as a function of time at 0.1 Hz. This is computed for the S12 Lunar station and Albuquerque, New Mexico, USA (ANMO) seismic stations at the beginning of 1976. It displays a daily variation due to the rotation of the earth, as well as a monthly cycle, due to the libration of the Moon.

2.4 Conclusion

The results presented in this paper using the Apollo Lunar seismometers are likely the best upper limits that can currently be achieved with seismometers in the frequency range 0.1 Hz – 1 Hz. As the Moon has the lowest ambient seismic noise currently measured, future improvements on this upper limit using seismic measurements should not be expected. For this reason, these constraints are likely to remain the best in this frequency band until second-generation torsion bar antennas[175]. Unlike indirect

limits that exist on cosmological backgrounds, our method directly constrains the astrophysical and cosmological components of the stochastic GW background. This complements the direct upper limits in other frequency bands and the integrated, indirect upper limits in the same frequency regime.

There are proposals to create a network of lunar geophysical stations, such as SELENE2[294], and the development of a network of broadband seismometers on the surface of the Moon[332]. These are in conjunction with space missions being planned to create a lunar station as well as to do fundamental science, including constructing a theory of the formation of the Earth, and its initial state and evolution. The use of an array of modern seismometers placed in an anti-podal network array would likely improve the result, although not likely more than an order of magnitude.

3

Constraining the gravitational wave energy density of the Universe using Earth's ring

So far, the strongest evidence for the existence of gravitational waves (GWs) comes from the observation of the binary pulsar PSR B1913+16[320]. The shrinking of its orbit observed over three decades can be fully explained by the emission of GWs and associated energy loss according to the General Theory of Relativity. Dedicated experiments attempt to measure these waves as phase modulation of laser beams

(GEO600[213], LIGO[161], Virgo[25], KAGRA[42], eLISA[34], TOBA[36]), or through their imprint on the polarization of the cosmic microwave background (BICEP2[59], EBEX[234]). Furthermore, GWs can be searched in data of other high-precision experiments including Doppler tracking of satellites[41], monitoring arrival times of pulsar signals[165], or using the Global Positioning System[39]. Gravitational waves can also excite oscillations of elastic bodies. This principle is exploited for example in the design of spherical resonant GW detectors (MiniGRAIL[109], Mario Schenberg[30]). Also oscillations of stars can be excited, and therefore observation of these modes can be used to detect GWs[275]. All these experiments combined monitor a wide range of GW frequencies starting from waves that have oscillated only a few times since the beginning of the Universe, up to a few 1000 Hz.

Recently, the authors of this article have presented results from an observation of the free, flat surface response of Earth to GWs[88]. As was explained there, the method cannot be extended to frequencies below about 50 mHz since seismic motion starts to be globally coherent at lower frequencies, and the GW response is strongly affected by Earth's spherical shape. The low-frequency GW response is best described in terms of Earth's normal-mode oscillations[53]. These oscillations are continuously monitored by a global network of low-frequency seismometers and gravimeters. Especially the superconducting gravimeters of the Global Geodynamics Project (GGP), which were used in this paper, provide excellent sensitivity below 10 mHz with data records reaching back more than 10 years[100]. As will be shown, the stationary noise background is almost the same for all gravimeters and uncorrelated between different instruments, which makes it possible to use a large fraction of the data of the entire network to search for GW signals that are significantly weaker than the stationary noise level by means of a near-optimal correlation method. Whereas previous GW searches using

Earth's normal modes only tried to explain excess energy in normal modes[321,304], the work in this article is the first to combine a near-optimal analysis of gravimeter data with a detailed GW response model, which makes it possible to accurately calibrate normal-mode amplitudes into GW strain.

The limits obtained in this study through normal-mode observations are plotted in Figure 3.1 together with upper limits set in other frequency bands. The previous upper limits in the frequency range 0.3 mHz to 5 mHz are improved by 2 to 5 orders of magnitude. A brief summary of normal-mode oscillations is given in section 3.1. In section 3.2, we outline the theory of Earth's resonant (normal-mode) response to GWs. A characterization of gravimeter data is presented in section 3.3. Finally, the GW search algorithm is discussed in section 3.4, and new constraints are presented on the energy density of GWs averaged over directions and wave polarizations.

3.1 Earth's normal-mode oscillations

Earth's free oscillations, called normal modes, can be excited by gravitational waves. Earth's slowest normal-mode oscillation occurs at about 0.3 mHz, and distinct modes can still be identified up to a few millihertz. At higher frequencies, the discrete vibrational spectrum transforms into a quasi-continuous spectrum of seismic vibrations that are increasingly dominated by local sources. The data used in this study were sampled once per minute, and low-pass filtered suppressing signal response above about 5 mHz depending on the gravimeter. In addition, a few gravimeters show resonant features above 5 mHz in their response. Therefore, the upper frequency bound of the GW search was chosen to be 5 mHz to guarantee accurate calibration of the data.

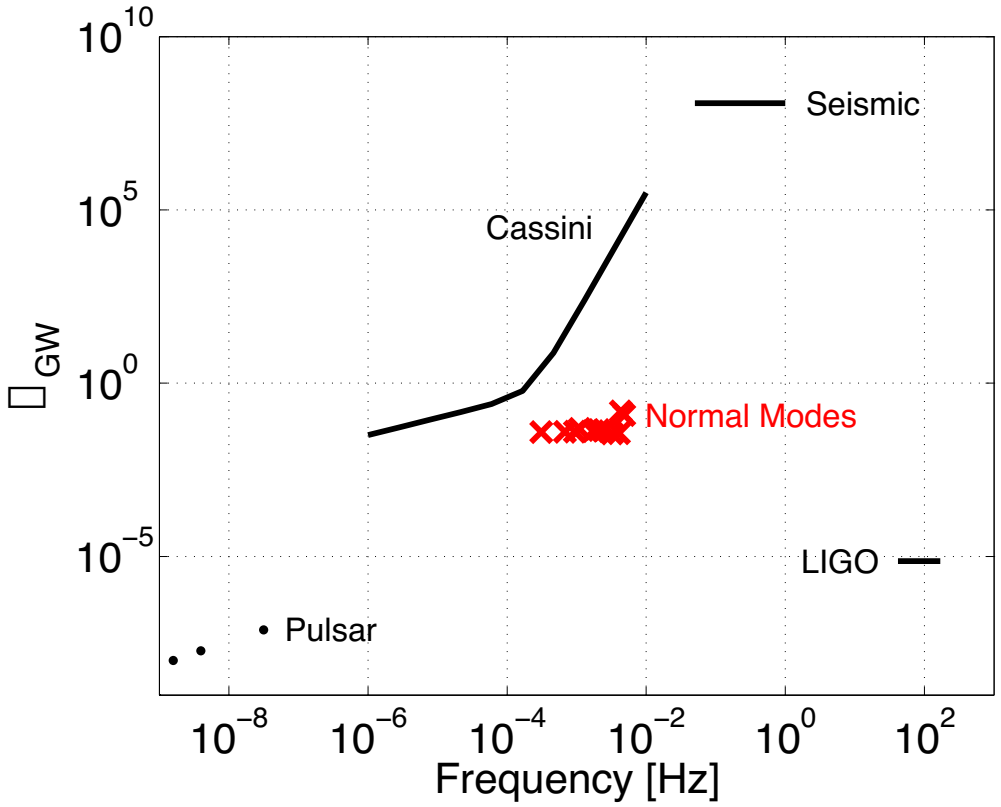


Figure 3.1: Current upper limits on GW energy density. These limits were set by pulsar timing observations[182], Doppler-tracking measurements of the Cassini spacecraft[41], monitoring Earth's free-surface response with seismometers ("Seismic")[88], and correlating data from the first-generation, large-scale GW detectors LIGO[17]. The new limits resulting from normal-mode measurements are shown as crosses.

At frequencies below 5 mHz, the diameter of Earth is much smaller than the length of GWs. In this so-called long-wavelength regime, a GW can effectively be represented by a quadrupole-force field that excites Earth's normal modes. Normal modes are divided into toroidal ${}_nT_l$ and spheroidal ${}_nS_l$ modes, where n, l are non-negative integers that determine the radial and angular mode shape respectively. The toroidal modes only produce tangential displacement. Spheroidal modes show tangential and radial displacement, and they also perturb Earth's gravity field. Not all normal modes are equally responsive to a quadrupole force. In fact, only the quadrupole modes with $l = 2$ show significant GW response in the long-wavelength regime[53]. The coupling mechanism of a GW to oscillations of elastic bodies is governed by variations of the shear modulus, including the shear-modulus change across the free surface. Earth shows strong internal variations of the shear modulus. In the liquid outer core, the shear modulus vanishes, and therefore significant internal contributions to Earth's GW response can be expected at the inner-core boundary, as well as at the core-mantle boundary. Due to the complex internal structure of Earth, normal modes also show a complex radial dependence of their amplitudes. Modes with the high amplitudes at the inner-core boundary, core-mantle boundary, and free surface couple strongly to GWs.

In order to calculate the response of Earth to GWs, normal-mode amplitudes as a function of radius need to be modelled numerically. For superconducting gravimeters, three contributions need to be modelled and added coherently: seismic acceleration, perturbation of the gravity potential, and lift against a static gravity gradient. For this work, normal-mode solutions were generated with the numerical simulation tool Minos[328]. These solutions are valid for a spherical, non-rotating, laterally homogeneous Earth, and here are based on the Earth model PREM[117] that describes vari-

ations of mass density, seismic speeds, and damping parameters from Earth's center to its surface. The gravimeters are designed to measure radial ground motion and gravity changes, which are caused only by spheroidal modes. Therefore, one can focus on these modes for the GW search. Of all spheroidal quadrupole modes ${}_nS_2$, only 14 have frequencies f_n below 5 mHz as shown in Table 3.1. Even though Earth also responds to GWs off these 14 mode frequencies, the best sensitivity is obtained at normal-mode frequencies making use of the resonant signal amplification. The GW response at normal-mode frequencies needs to take into account the damping experienced by each mode in order to obtain the correct signal amplification. The damping is quantified by a mode's quality factor, which corresponds to the ratio of a mode frequency to its natural spectral linewidth. The quality factors of the 14 modes lie between about $Q = 100$ and 900. The mode frequencies and quality factors used here were all taken from the numerical simulation, but it should be emphasized that numerical estimates of the mode frequencies are very accurate, at least for the purpose of this paper, and also the quality factors agree well with observation[148,105].

The coupling strength α_n of a mode to a GW can be expressed by a dimensionless quantity. Its values for the 14 quadrupole modes below 5 mHz are summarized in Table 3.1. They depend on the radial as well as tangential displacement of each mode, and also on shear-modulus changes and mass density as functions of the distance to Earth's center. The coupling strength varies by more than an order of magnitude without clear pattern. This is owed to the complexity of mode solutions, which have greatly varying sensitivity to shear-modulus changes at different depths.

In addition to the coupling strengths, the second important parameter characterizing each mode is its vertical displacement u_n and gravity potential perturbation p_n at the surface, which govern the gravimeter signal. These amplitudes are also summa-

${}_nS_2$	0	1	2	3	4	5	6	7	8	9	10	11	12	13
f_n [mHz]	0.309	0.679	0.938	1.11	1.72	2.09	2.41	2.52	3.21	3.23	4.03	4.06	4.33	4.84
Q_n	510	310	95.9	365	433	317	92.9	340	316	445	203	126	229	878
α_n	-0.65	-18.3	-1.78	-0.70	-18.9	13.3	4.31	-34.5	-3.97	-6.54	15.8	-16.9	12.7	3.12
u_n	0.74	-0.14	-0.06	-0.19	-0.18	-0.11	-0.02	-0.09	-0.05	0.13	0.073	0.057	-0.02	0.086
p_n	-0.43	0.028	6e-5	-5e-4	2e-4	5e-5	-3e-6	2e-5	5e-6	4e-6	2e-7	7e-7	1e-6	2e-8
Ω_{GW}	0.039	0.039	0.040	0.048	0.041	0.045	0.042	0.044	0.035		0.036		0.15	0.12

Table 3.1: Summary of mode parameters: mode frequencies f_n, quality factors Q_n, coupling strengths α_n, radial surface displacement u_n, perturbation of gravity surface potential p_n (both normalized to the same, but arbitrary unit). The last row shows the upper limits on the energy density Ω_{GW} as plotted in Figure 3.6.

rized in Table 3.1. The amplitudes of displacement and gravity potential are normalized such that their relative contribution to the gravimeter signal can be compared. It can be seen that the gravity perturbation is significant only for the two modes ${}_0S_2$ and ${}_1S_2$.

A feature of normal modes that is not captured by the Minos simulation is mode coupling due to Earth's ellipticity, rotation, and lateral heterogeneity. One effect is the so-called self coupling, in which a quadrupole ($l = 2$) multiplet can split into up to 5 resolvable modes, which are labelled by a third integer $m = -2, \ldots, 2$[162]. Since each mode can therefore potentially respond to a different GW, mode splitting influences the overall GW response. Another possibility is that two modes that happen to be very close in frequency can couple and exchange energy. The latter situation is depicted in Figure 3.2 taking the mode ${}_6S_2$ as example. Whereas the next highest quadrupole mode ${}_7S_2$ is well isolated, mode ${}_6S_2$ lies very close to other spheroidal modes, which can couple and exchange energy. Although the effect is minor on normal-mode frequencies and Q-values[106,174], a consequence is that one cannot design the GW search into too narrow frequency bands only relying on simulation predictions. An extreme narrow-band search needs to be based on a detailed characterization of the quadrupole modes taking into account observed mode (self-)coupling, which has not been done in the work presented here. Concerning energy transfer be-

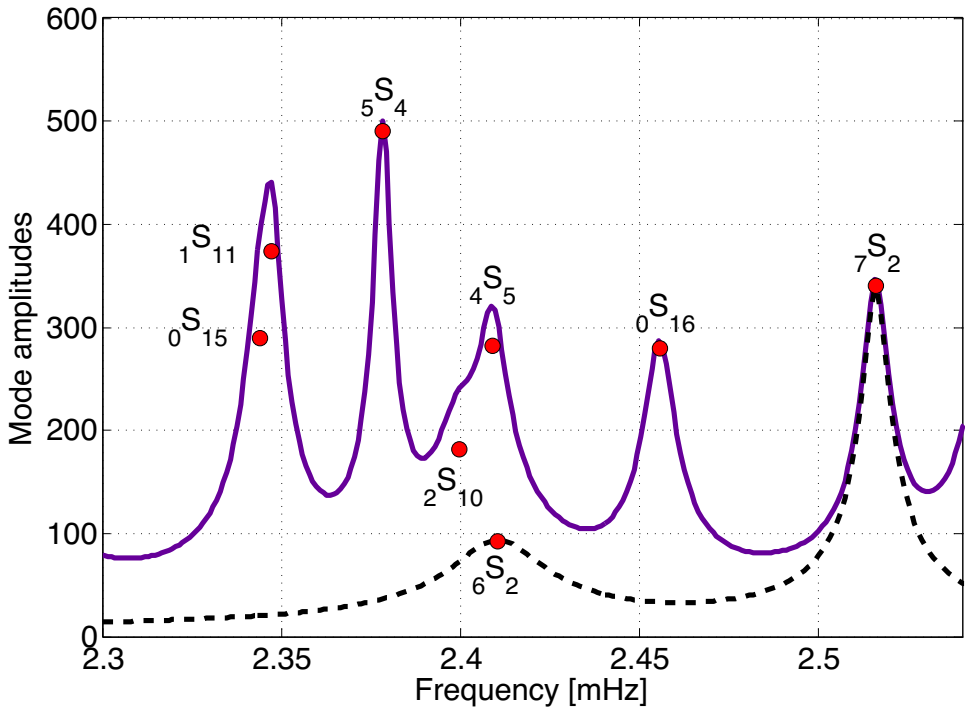


Figure 3.2: Simulated spectrum of spheroidal normal modes around ${}_6S_2$. The values of the red markers correspond to the modes' Q-factors.

tween coupled modes, the effect would generally lead to a decrease in GW response of a quadrupole mode independent of the Q-values of the coupled modes. However, estimating the change in GW response that is consistent with observed shifts of normal-mode frequencies (based on a simple coupled harmonic oscillator model), it can be concluded that the energy lost into other modes through coupling is negligible. Therefore, the main issue with mode coupling is that the GW search needs to be designed with sufficient bandwidth around each mode frequency so that it is guaranteed that the peak response of the entire quadrupole multiplet lies within this band. Further details about the impact of mode coupling on GW sensitivity are given in section 3.4.

3.2 Theory of Earth's response to gravitational waves

Two response mechanisms of an elastic body to GWs have been described in detail in past publications. First, Dyson calculated the amplitude of seismic waves produced by GWs incident on a free, flat surface[116]. He found that the first time derivative of vertical surface displacement is given by

$$\dot{\xi}_z(\vec{r},t) \approx -\frac{\beta^2}{\alpha}\vec{e}_z^{\top} \cdot h(\vec{r},t) \cdot \vec{e}_z \tag{3.1}$$

Here, $\vec{e}_z$ denotes the normal vector of the surface, h the spatial part of the GW strain tensor, and α, β are the compressional and shear-wave speed. It can already be seen that the shear modulus μ plays an important role in the elastic-body response since

$$\beta^2 = \frac{\mu}{\rho}. \tag{3.2}$$

Accordingly, the GW response vanishes for vanishing shear modulus. One has to keep in mind though that the equations of elastic deformation used to derive this result are neglecting contributions that can become important when the shear modulus is sufficiently small. For example, the GW response model of a spherical body with vanishing shear modulus has been used by Siegel and Roth[275] to propose GW measurements by monitoring oscillations of the Sun.

The role of the shear modulus is also evident in the GW response of an elastic spherical body. This case was studied by Ben-Menahem[53], and is used here to calculate Earth's resonant GW response. In the following, we will present the most important results of his work with minor reformulations. In terms of the amplitudes of radial displacement $u_{n2m}(r)$, and tangential displacement $v_{n2m}(r)$, the coupling strength of a GW to a normal quadrupole mode can be defined as

$$\alpha_{n2m} \equiv -\frac{R}{\beta_c^2} \frac{\int_0^{R+} \mathrm{d}r\, r^2 \mu'(r)(u_{n2m}(r) + 3v_{n2m}(r))}{\int_0^R \mathrm{d}r\, r^2 \rho(r)(u_{n2m}^2(r) + 6v_{n2m}^2(r))}, \tag{3.3}$$

where R is Earth's radius, β_c is the shear-wave speed at Earth's center, $\mu'(r)$ the derivative of the shear modulus, and $\rho(r)$ the mass density. The upper integration limit $R+$ signifies that the shear-modulus change across the free surface needs to be included. In the following, only the radial order n will be used to specify a quadrupole mode whose properties are independent of the index m neglecting mode coupling. The mode amplitudes $u_n(r)$, $v_n(r)$ have arbitrary units, since units of the mode variables cancel in the final result. They are considered unitless in this work. It is only necessary that all mode variables including the amplitude $\phi_n(r)$ of the gravity potential are normalized consistently.

The complete solution for the GW response also needs to take into account the

angular dependence of excited oscillations. A simple first step is to consider the response to a single, plus-polarized GW. For a spherical, laterally homogeneous Earth, the acceleration a_{n2m} measured by a gravimeter in the long-wavelength regime can be written

$$\begin{aligned} a_{n2m}(f_n;\theta,\phi) = \frac{\sqrt{24\pi}}{15}\frac{\beta_c^2}{R}Q_n\alpha_n h(f_n)\delta_{|m|,2}Y_2^{m\,*}(\theta,\phi) \\ \cdot\left(u_n(R)+3\frac{\phi_n(R)}{R(2\pi f_n)^2}+2\frac{g}{R(2\pi f_n)^2}u_n(R)\right), \end{aligned} \tag{3.4}$$

where $h(f_n)$ is the GW strain amplitude, $g = 9.81\,\mathrm{m/s^2}$, and δ_{kl} the Kronecker delta. For a quadrupole mode with $l = 2$, the angular parameter can take the values $m = -2,\ldots,2$. The expression in the brackets comprises the three contributions to the gravimeter signal: radial surface displacement, perturbation of the gravity potential, and lift against a static gravity gradient[101]. The second contribution corresponds to the parameter p_n in Table 3.1: $p_n \equiv 3\phi_n(R)/(R(2\pi f_n)^2)$. The angle θ denotes the relative angle between the direction of propagation of the GW and the location of the gravimeter on Earth's surface in a coordinate system with origin at the center of the Earth. The angle ϕ describes the rotation of this coordinate system with respect to the polarization frame of the GW. Accordingly, two modes, $m = \pm 2$, of the quadrupole multiplet are excited by each GW in this choice of coordinate system.

For the GW search carried out in this study, we also need to know the correlation between two gravimeters due to an isotropic GW background. Each GW that couples to quadrupole normal modes produces an angular surface vibration pattern that can, in an arbitrarily oriented Earth-centered coordinate system, be represented by a linear combination of quadrupole spherical harmonics $Y_2^m(\theta,\phi)$ with $m = -2,\ldots,2$[255]. The situation is illustrated in Figure 3.3. A plus-polarized GW propagates parallel

to the north–south axis. The red and blue colored shapes represent Earth's induced quadrupole oscillation at its two maxima separated by half an oscillation period. Since the signal amplitude measured by gravimeters depends on their location, coherence between two gravimeters also depends on location. For symmetry reasons, it is clear that for an isotropic GW field, coherence integrated over all polarizations and propagation directions only depends on the relative position of the two gravimeters. This correlation function is known as overlap-reduction function, and normalized such that it is unity for collocated gravimeters[69]. In order to calculate it, the response as given by equation (3.4) needs to be calculated in a rotated coordinate system for one of the gravimeters. Since the GW correlation also depends on the nature of the GW field, a specific model needs to be chosen. Results in this paper are calculated for an isotropic, stationary field of GWs. Integration over all GW propagation directions and polarizations yields the overlap-reduction function:

$$\gamma_{12}(\sigma) = \sqrt{4\pi/5}\, Y_2^0(\sigma, 0), \tag{3.5}$$

where σ is the angle subtended by the great circle that connects the two gravimeters. All else being equal, the gravimeter pairs that contribute most significantly to the estimate of a GW energy density are either close to each other or antipodal. Note that the overlap-reduction function can be approximated as frequency independent since the Earth is orders of magnitude smaller than the length of a GW at mHz frequencies.



Figure 3.3: Earth quadrupole oscillation. The red and blue shapes correspond to the maxima of a quadrupole oscillation separated by half an oscillation period. The green balls mark locations of some of the gravimeters of the GGP network. Here the oscillation is induced by a GW propagating along the north-south axis.

3.3 Gravimeter data

In addition to disturbances from large earthquakes including the subsequent ringdown of the normal modes[330], or local short-duration disturbances, gravimeter data also contain a stationary noise background consisting of instrumental noise, hydrological, and atmospheric disturbances[101]. The stationary noise level is very similar in almost all instruments, with a median of a few $(\mathrm{nm/s^2})/\mathrm{Hz^{1/2}}$ at 1 mHz. The medians of gravimeter spectra recorded during the year 2012 are plotted in Figure 3.4. Four gravimeters show elevated medians, but in all these cases it is not the stationary background being higher, but instead the four instruments are frequently perturbed by strong local events, which therefore contribute significantly to the medians. A detailed study of gravimeter noise for most of these sites can be found in[256].

A local disturbance can produce strong broadband noise in gravimeters. Consequently, noise amplitudes at different frequencies show partial correlation. This property was exploited to subtract some of the background noise that adds to the normal-mode signals, and thereby improve sensitivity to GWs. In this way, it was possible to suppress the background noise at normal modes up to a factor 3 (varying in time, and with different success for each normal mode). Using off-resonance amplitudes for noise subtraction, it is possible to ensure that an insignificant amount of GW signal is subtracted with the noise. Additional noise reduction can be achieved in some gravimeters by direct subtraction of gravity noise of atmospheric origin[228]. For this purpose, each superconducting gravimeter is equipped with a pressure sensor. The idea is that the pressure data contain direct information about corresponding atmospheric density and therefore gravity perturbations. It is found that the correlation between pressure and gravimeter data is significant below about 1 mHz and weakly frequency-

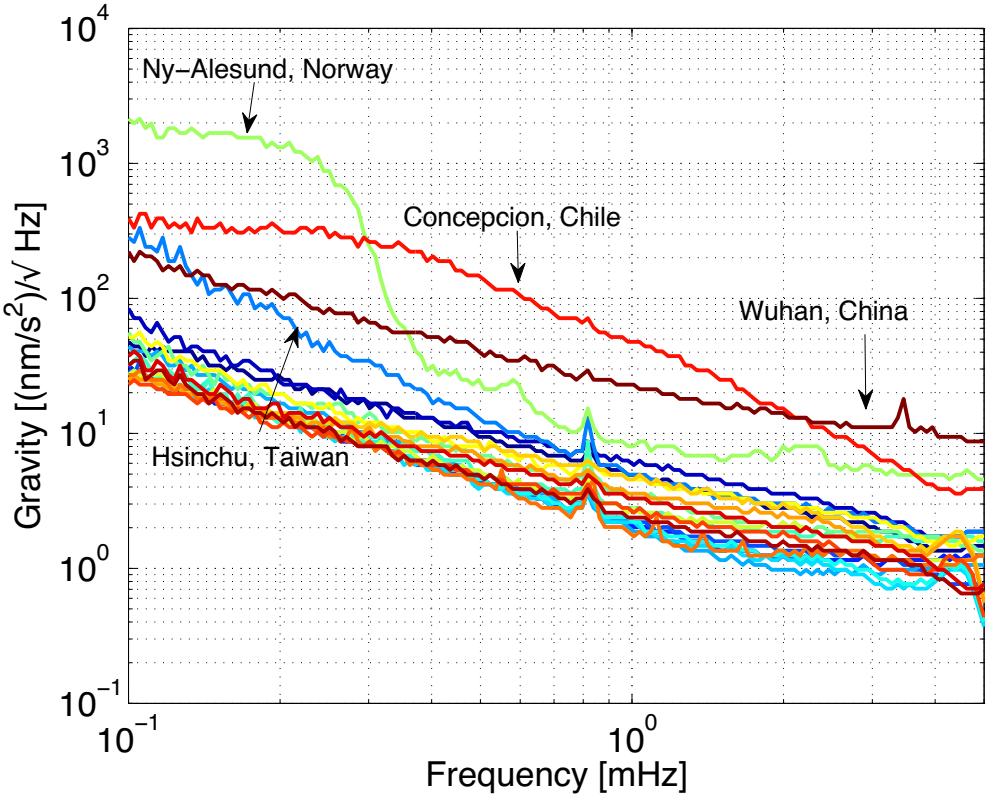


Figure 3.4: Medians of gravimeter spectra measured in 2012. All gravimeters used in this study show a comparable level of stationary background noise represented by their spectral medians, except for the 4 gravimeters highlighted in the plot.

dependent. This can be exploited to coherently subtract gravity noise with a conversion factor around $-0.35\,\mu$gal/hPa, which needs to be optimized for each gravimeter. The quality of pressure data is poor at some gravimeter sites so that good noise reduction cannot be generally achieved.

At should be emphasized that environmental disturbances can show strong correlation well below 0.3 mHz. Another important property of gravimeter data is that coherence between any two gravimeters of the GGP network at frequencies between 0.3 mHz and 5 mHz produced by environmental disturbances is insignificant provided that times of high-magnitude earthquakes are excluded. Even for superconducting gravimeters that contain two levitated spheres, strong coherence is only observed below about 2 mHz after removing the highest 10th percentile of loud events as shown in Figure 3.5. The lack of environmental coherence is an important feature of the gravimeter network, which makes it a very efficient tool to search for GWs, since significant correlations of environmental origin would greatly limit the network sensitivity.

3.4 Search for a stationary gravitational-wave background

In this section, we outline the GW search method based on correlation measurements between gravimeter pairs. Depending on the relative position of two gravimeters on Earth's surface, correlation of gravimeter signals arising from GWs is described by the overlap-reduction function in equation (3.5). Once the expected correlation of GW signals between different gravimeters is calculated, the measured correlations are used to obtain an estimate of the energy density of GWs following the method described in[33]. The upper limit on the GW energy density presented in this paper

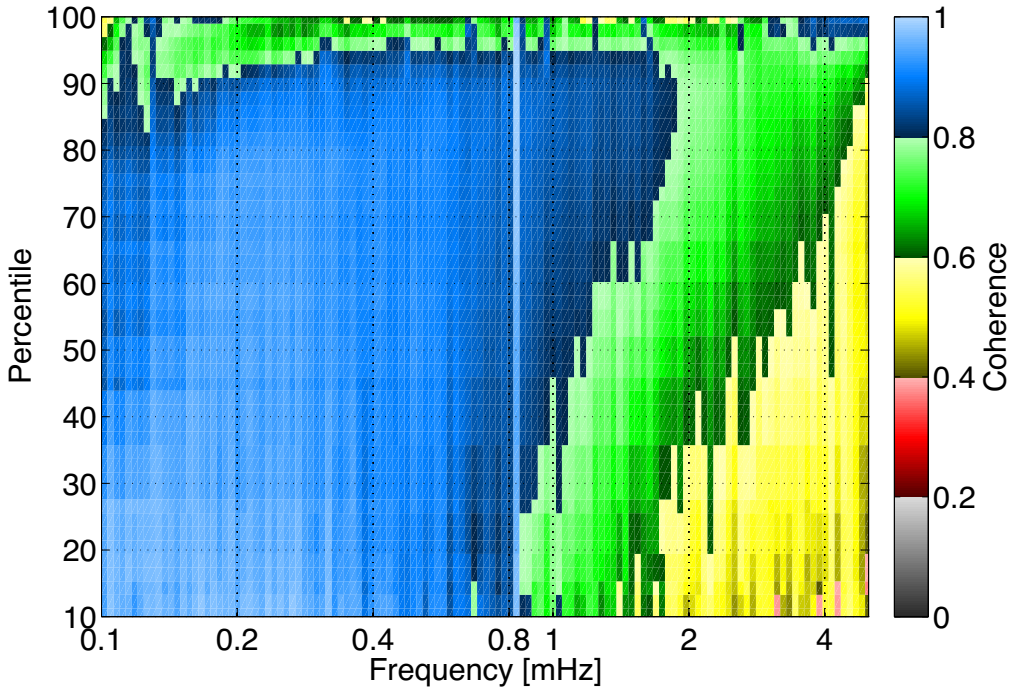


Figure 3.5: Coherence of signals from two levitated spheres in the same gravimeter at Wettzell, Germany. The result is shown as a function of percentile of gravimeter noise excluded from the coherence measurement. A percentile of 90 means that 10% of the loudest spectra were excluded from the coherence measurement. Only the high-Q radial normal mode ${}_0S_0$ at about 0.81 mHz contributes significantly to coherence for all times.

was obtained as a near-optimal combination of measured correlations using 10 years of data, forming pairs with gravimeters of the GGP network. The total amount of data is divided into stretches short enough so that the spectral resolution is wider than the frequency spread of a quadrupole multiplet as discussed in section 3.1. The length of data stretches obtained in this way is different for each normal mode. Each data stretch leads to a point estimate of the GW energy density according to

$$\hat{\Omega}_{\mathrm{GW}}(f_n) = \frac{4\pi^2}{3H_0^2} \frac{\hat{S}_{12}(f_n) f_n^3}{\gamma_{12}} \tag{3.6}$$

Here, $\hat{S}_{12}(f_n)$ is the measured cross-spectral density between two gravimeters in units of GW strain spectral density. As pointed out before, the overlap-reduction function γ_{12} can be approximated as frequency independent for normal-mode observations.

Based on the conservative assumption that the $l = 2$ quadrupole mode splits into 5 distinct isolated modes ($m = -2, \ldots, 2$) that all respond incoherently to GWs, the GW response of a quadrupole mode is obtained by adding contributions from different values of m incoherently. Furthermore, two pairs of the 14 quadrupole modes are too close in frequency to be resolvable with the chosen frequency resolution ($n = 8, 9$ and $n = 10, 11$, see Table 3.1). This means that in addition to the incoherent sum over a multiplet, contributions from the two quadrupole modes in each of these pairs need to be summed incoherently leading to a combined point estimate.

The final results will be presented as constraints on the energy density in GWs separately for each mode. Figure 3.6 shows the point estimates of the GW energy density with error bars. All point estimates are consistent with a non-detection, and the resulting energy constraints are mostly determined by the error bars. The values are listed in Table 3.1. Energy densities can be translated into strain spectral den-

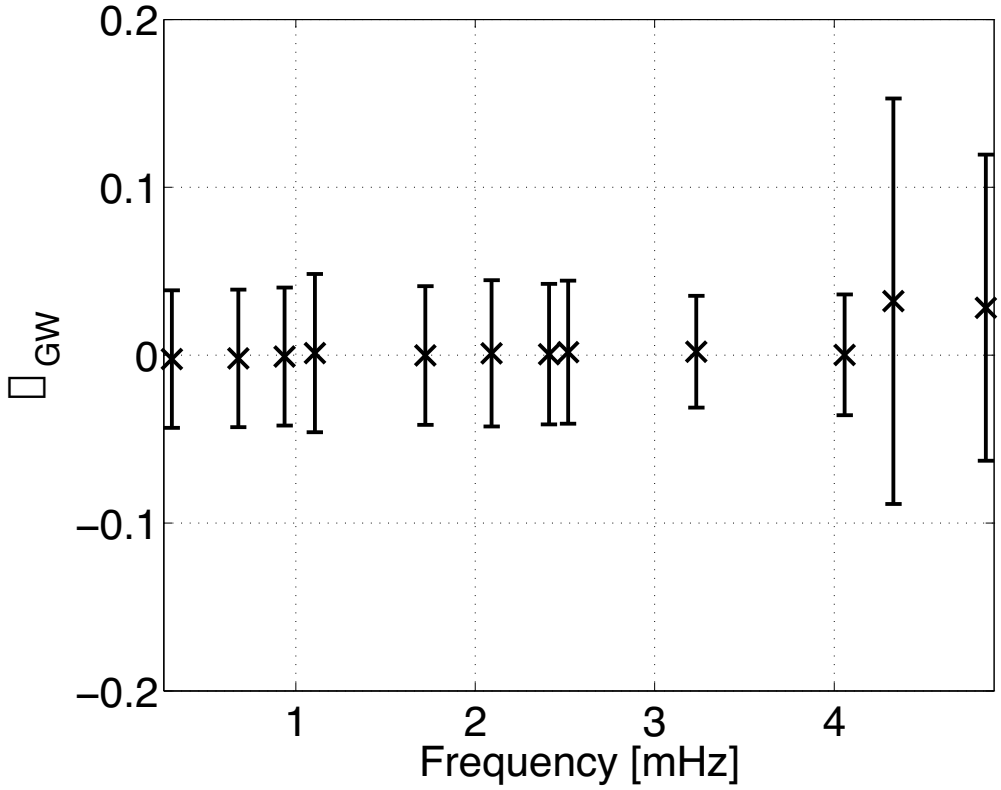


Figure 3.6: Point estimates of GW energy density and errors. Of the 14 original modes, only 12 are plotted here since two pairs, $n = 8, 9$, and $n = 10, 11$, have been merged to one value each since the chosen frequency resolution cannot resolve them.

sities, which lie between $h_{\mathrm{GW}} \leq 2.2 \times 10^{-14}\,\mathrm{Hz}^{-1/2}$ for the mode ${}_0S_2$ and $h_{\mathrm{GW}} \leq 6.2 \times 10^{-16}\,\mathrm{Hz}^{-1/2}$ for ${}_0S_{13}$. Even though these results demonstrate an improvement in sensitivity by a few orders of magnitude over previous searches in this frequency band (see Figure 3.1), the new upper limits are still not stringent enough to constrain cosmological models of GW backgrounds. A conservative estimate of the energy density of GWs from inflation predicts a value of order $\Omega_{\mathrm{GW}} \sim 10^{-15}$, and a GW background from cosmic strings is predicted at $\Omega_{\mathrm{GW}} \sim 10^{-7}$, both at normal-mode frequencies[17]. Also a GW background from a cosmological distribution of unresolved compact binary stars such as white dwarfs and neutron stars is predicted at lower values, $\Omega_{\mathrm{GW}} \sim 10^{-12}$, at normal-mode frequencies[140]. Therefore, with achieved upper limits between $\Omega_{\mathrm{GW}} = 0.035 - 0.15$, the stationary gravimeter noise as plotted in Figure 3.4 has to be lowered by 2 to 3 orders of magnitude to be able to place first constraints on cosmological models.

3.5 Conclusion

In this paper we showed that today's understanding of Earth's interior can be used to accurately calculate Earth's resonant GW response. In this way, it was possible to calibrate gravimeter data into units of GW strain, and directly obtain new upper limits on the GW energy density in the range $0.035 - 0.15$ at frequencies between 0.3 mHz and 5 mHz. This was achieved by correlating data of gravimeter pairs recorded over the past 10 years.

Alternatively, one could make use of the same response mechanism to search for individual astrophysical signals such as galactic white-dwarf binaries. Millions of binaries are predicted to radiate quasi-monochromatic waves in this frequency band[102]

including already discovered systems (see for example Roelofs et al[253]). Again, about 3 orders of magnitude sensitivity improvement are required to make a detection likely. The integrated gravitational-wave signal should be distinguishable from terrestrial sources since it is modulated due to Earth's rotation. The additional challenge here is that a continuous integration of the signal, as would be favorable for this search, results in an extremely narrow frequency resolution, which requires a more detailed investigation of mode-coupling effects. The diversity in nature of Earth's oscillations also makes it possible to test alternative theories of gravity. For example, a scalar component of the GW field could be searched in monopole modes ${}_nS_0$ as has already been attempted by Weiss and Block[321].

Further improvement in GW sensitivity may be achieved with a new generation of gravimeters. Especially atom-interferometric gravimeters are currently under active development[113]. The open question is if there will be some form of environmental noise limiting the sensitivity of gravimeters irrespective of their intrinsic acceleration sensitivity, and whether methods can be developed to mitigate this noise if necessary. Nonetheless, we have demonstrated that gravimeter technology is a viable option to detect GWs, and that ground-based GW detection seems to be a possibility at frequencies, which are generally considered accessible only for space-borne detectors.

God does not care about our mathematical difficulties. He integrates empirically.

Albert Einstein

4

Detecting compact binary coalescences with seedless clustering

Compact binary coalescences (CBCs) of black holes (BHs) and/or neutron stars (NSs) are a likely source of gravitational waves (GWs)[125,126,13]. CBC events include binary neutron stars (BNSs), neutron-star black holes (NSBHs), and binary black holes (BBHs). As a CBC passes through its inspiral and merger stage, it generates GWs which sweep upward in frequency and strain amplitude through the sensitive band of GW detectors. The detection of GWs from CBCs will provide information about the populations of compact objects in the universe[260], elucidate the properties of strong

field gravity, and provide a means to test general relativity[29].

Here, we focus on relatively low-mass binaries ($M_{\rm total} \leq 10 M_\odot$). There are two reasons for restricting our attention to this region of parameter space. First, the rate of low-mass CBCs is less subject to theoretical uncertainty than high stellar-mass binary BHs and intermediate-mass BBH[13]. Second, we are interested in long-lived signals ($\approx$ 54–270 s), which appear as curved tracks in spectrograms of GW strain power, and therefore provide an appealing target for seedless clustering[298,300] (described in greater detail below).

Searches for CBCs often use matched filtering, which requires precise knowledge of astrophysical waveforms. (Excess power searches are also used, especially for high-mass systems associated with shorter signals; see, e.g.,[192,12].) Since CBCs are, for the most part, well-modeled systems, matched filtering provides an essentially optimal strategy for detecting compact binaries. However, there are several reasons why it is useful to consider alternative detection strategies.

Verification. Alternative methods can provide verification of detections by matched filter pipelines, thereby increasing confidence in the veracity of a result. Of course, because seedless clustering will be less sensitive than matched filtering searches in most cases, non-detection by seedless clustering is not a concern either. On the other hand, in the case of a significantly eccentric signal, where matched filtering and seedless clustering have competitive sensitivities as seen below and the detection confidences will be smaller than for a non-eccentric signal, using multiple pipelines is useful. Although there is some redundancy provided by the multiple implementations of matched filtering used in current searches, seedless clustering provides a very different approach to gravitational-wave detection and detection by both methods potentially indicates the robustness of the result.

Visualization of the GW signal. In general, advanced detector CBC events are expected to be buried in noise to the extent that it will be difficult to see by eye their signature in a time series or strain auto-power spectrogram. Here we show that, by coherently combining the output of multiple detectors, CBCs can be visualized as faint but visible arcs on "radiometric spectrograms"—especially when the eye is guided by the reconstructed track of a search algorithm. (The curious reader is encouraged to skip ahead to Figure 4.1 for an example of a radiometric spectrogram.)

Visualizing the signal helps confirm that the detected signal looks like one expects. The coherent combination also allows for confirmation that the parameter estimation of the signals, including the direction, chirp mass, and time of coalescence, are all consistent with the radiometric spectrogram. For example, an error in the reconstructed CBC direction creates characteristic stripes; see[300]. If, on the other hand, the chirp mass is incorrect, the reconstructed track will have the wrong frequency evolution as a function of time. Of course, this is a qualitative check, as seedless clustering does not measure these parameters.

Based on the results presented below, $\approx$ 8% of the events detected by matched filtering will produce a signature with false alarm probability less than 0.1% when followed up with seedless clustering. For visualizations purposes, seedless clustering can be used to help interpret spectrograms, even if the (seedless) significance is marginal, and the detection is due entirely to matched filtering.

Data processing corner cases. Real-world GW searches require design choices, which take into account the complicated nature of GW detectors. Detector performance is non-stationary, the noise contains non-Gaussian "glitches," and data-taking is sometimes interrupted by lock-loss, just to name a few relevant effects. As a result, workarounds are employed, e.g., to estimate background, to discard noisy data, and to handle gaps.

Matched filtering[45] and seedless clustering[246] have different ways of performing these tasks. In general, these technical details are (by design) not important factors in determining the average sensitivity of a search. However, by employing multiple search methods we can guard against individual events falling between the cracks. Although the authors do not know of any examples where data quality cuts have caused a potential signal to be missed, different technical pipeline details in handling poor data quality and data gaps can create differences in what data is analyzed and how it is treated.

An example of a possible data processing corner case is shown in Figure 4.2. This event was identified correctly by both matched filtering and seedless clustering. The left-hand panel shows $\rho(t; f)$ obtained using "engineering-run" data*, in which data from a LIGO sub-system, in this case the pre-stabilized laser, is recolored to match the Advanced LIGO noise curve. Such engineering run data does not contain astrophysically useful strain measurements, but is nonetheless useful for its non-Gaussian noise characteristics. The data contains five segments consistent with non-Gaussian noise and would be removed in a search. Nonetheless, despite these noise artifacts, it is still possible to detect a simulated binary neutron star signal. The right-hand panel shows the reconstructed signal, obtained with the seedless clustering algorithm we describe below.

Waveform uncertainties. Theoretical errors in matched filter waveforms can arise from the computational limitations and/or imperfect approximations. Due to computational limitations, most CBC searches so far use template banks composed of non-spinning, non-eccentric waveforms, which are less computationally challenging than search with spin and eccentricity. High-spin systems take longer to simulate

*The data in question are from LIGO Engineering Run 5, collected during 2014.

with numerical relativity and the addition of extra spin parameters creates larger, more unwieldy template banks. Searches that ignore spin can suffer significant losses in sensitivity[66]; the cases considered here have between a 23-36% match, which is maximized over time and phase, between the spinning and non-spinning waveforms; these numbers increase to at least 97% when maximized over mass as well. When spin is included, it is often assumed that the spins are aligned in order to make the calculation more tractable. Even so, the inclusion spin effects can lead to a factor of two increase in sensitive volume[247]; see also[60,248]. Main sequence binaries circularize by the time they enter the sensitive frequency band of terrestrial detectors[62]. However, dynamical capture may produce gravitational waves from highly eccentric binaries[231,62,281,164,150]. Samsing et al.[261] show how eccentric binaries can be generated from interactions between compact binaries and single object, inducing chaotic resonances in the binary system. O'Leary et al. present a model where the scattering of stellar mass BHs in galactic cores which contain a super-massive black hole can lead to CBCs with high eccentricities[231]. They expect that 90% of such systems would have eccentricity $\epsilon > 0.9$ when entering the sensitive band. As part of ongoing work, we are estimating the rate of detections likely given O'Leary et al.'s model. The cases considered here have a less than 1% match between the eccentric and circular waveforms of equivalent mass. These numbers increase to between 20-60% when maximized over mass. Huerta and Brown showed how matched filtering template banks have less than 95% match for compact binaries with $\epsilon > 0.02$, with matches of about 50% and 20% for BNS systems of 0.2 and 0.4 respectively[170]. We show in section 4.3 that sensitivity distances of matched filtering and seedless clustering are comparable at these eccentricities. This highlights the difficulty of detecting them using a template bank composed of circular templates. Imperfect assumptions about eccentricity

and spin may therefore create openings for ostensibly sub-optimal detection strategies.

New physics. One can also imagine significant waveform errors due to the existence of new or unforeseen physics. For example, Piro raised concerns about the effects of magnetic interactions in BNS[245]. While these magnetic interactions were subsequently shown to be ignorable[204] for GW astronomy, one can imagine a comparable source of theoretical error. More speculatively, non-standard theories of gravitation can lead to modifications of the waveform[272,47]. These theories in particular show that the inspiral and merger stage of scalarized binaries can deviate from general relativity, although the similarity of the inspiral stage to general relativity means that they will still be detected by matched filtering.

Thus, there are many reasons why it is worth considering alternatives to matched filtering. One common alternative technique for detection of GW transients is to search for excess power in spectrograms (also called frequency-time ft-maps) of GW detector data[291,193,132]. This method casts GW searches as pattern recognition problems.

Previous work has shown how "seedless clustering" can be used to perform sensitive searches for long-lived transients[298,300]. The idea of seedless clustering is to integrate the signal power along spectrogram tracks chosen to capture the salient features of a wide class of signal models. Seedless clustering calculations are embarrassingly parallel, and so the technique benefits from the recent proliferation of highly parallel computing processors including graphical processor units and multi-core central processing units. Previous papers[298,300] have pointed out that seedless clustering algorithms might be useful for CBC detection/confirmation.

In this work, we apply the seedless clustering formalism to efficiently search for CBC signals. In section 4.1, we review the basics of seedless clustering. We show how

the formalism of[298,300] can be tuned to more sensitively detect CBC signals. In section 4.3, we determine the sensitivity of seedless clustering algorithms (with different levels of tuning) to CBC waveforms. We conclude with a discussion of topics for further study in section 4.4.

4.1 Seedless clustering for chirps

Searches for unmodeled GW transients typically begin with spectrograms proportional to GW strain power. The pixels of these spectrograms are computed by dividing detector strain time series in segments and computing Fourier transform of the segments. The Fourier transform of the strain data from detector I for the segment with a mid-time of t is denoted $\tilde{s}_I(t;f)$. For the results presented here, we use 50%-overlapping, Hann-windowed segments with duration of 1 s. The frequency resolution is 1 Hz.

Searches for long-duration GW transients in particular use the cross-correlation of two GW strain channels from spatially separated detectors to construct ft-maps of cross-power signal-to-noise ratio[132]:

$$\rho(t;f|\hat{\Omega}) = \mathrm{Re}\left[\lambda(t;f)e^{2\pi i f\Delta\vec{x}\cdot\hat{\Omega}/c}\tilde{s}_I^*(t;f)\tilde{s}_J(t;f)\right]. \tag{4.1}$$

Here, $\hat{\Omega}$ is the direction of the GW source, $\Delta\vec{x}$ is a vector describing the relative displacement of the two detectors, c is the speed of light, and $e^{2\pi i f\Delta\vec{x}\cdot\hat{\Omega}/c}$ is a direction-dependent phase factor, which takes into account the time delay between the two detectors. The $\lambda(t;f)$ term is a normalization factor, which employs data from neigh-

boring segments to estimate the background at time t:

$$\lambda(t;f) = \frac{1}{\mathcal{N}}\sqrt{\frac{2}{P'_I(t;f)P'_J(t;f)}}. \tag{4.2}$$

$P'_I(t;f)$ and $P'_J(t;f)$ are the auto-power spectral densities for detectors I and J in the segments neighboring t. For additional details, see[132,298,300]

GWs appear as tracks or blobs in the ft-maps. The morphology of the the GWs are dependent on the signal. CBC signals appear as chirps of increasing frequency. Clustering algorithms are used to identify clusters of pixels Γ likely to be associated with a GW signal. The total signal-to-noise ratio for a cluster of pixels can be written as a sum of over $\rho(t;f|\hat{\Omega})$:

$$\mathrm{SNR}_{\mathrm{tot}} \equiv \frac{1}{N^{1/2}} \sum_{\{t;f\}\in\Gamma} \rho(t;f|\hat{\Omega}), \tag{4.3}$$

where N is the number of pixels in Γ.

Different clustering algorithms employ different methods for choosing Γ. Seed-based algorithms connect statistically significant seed pixels to form clusters[298,292]. In seedless clustering algorithms[298], Γ is chosen from a bank of parametrized frequency-time tracks. Each such track is referred to as a "template." Calculations for many templates can be carried in parallel, which facilitates rapid calculations on multi-core devices such as graphical processor units (GPUs).

It must be noted that our templates are different from matched-filtering templates. Seedless clustering templates describe the morphology of a power spectrogram track whereas matched filter templates describe the phase evolution of a signal appearing in just one detector. Matched filter templates contain all the available information

about the signal, whereas seedless clustering templates are a lossy, binned representation of the signal. By throwing away information, the seedless clustering search is less sensitive than a matched filter search, but by throwing away information, it can simultaneously become more robust against waveform uncertainties and new physics.

A very general search with minimal assumptions may employ, e.g., a template bank of randomly generated Bézier curves[139], which have been shown to do a reasonably good job of mimicking long-lived narrowband gravitational-wave signals[300]. However, one may equally well carry out a more specialized search, targeting a specific class of signals. Given our present interest in CBC signals, we opt to work with a more specialized template bank consisting of parametrized chirps:

$$f(t) = \frac{1}{2\pi}\frac{c^3}{4GM_{\rm total}}\sum_{k=0}^{7} p_k \tau^{-(3+k)/8}, \tag{4.4}$$

where

$$\tau = \frac{\eta c^3 (t_c - t)}{5GM}. \tag{4.5}$$

Here, G is the gravitational constant and $M_{\rm total}$ is the total mass of the binary. The expansion coefficients p_k can be found in[57]. Each chirp template is parametrized by two numbers: the coalescence time and the chirp mass. (This is in contrast to Bézier curves, which are parametrized by six numbers.) While technically, the waveform depends on the individual component masses, the main features of the signal can be well-approximated by only the chirp mass. Therefore, to reduce the parameter space by one variable, we employ the approximation that the individual component masses are equal.

The space of arbitrary long-lived gravitational-wave signals is very large, and so general algorithms, employing Bézier templates, use randomly generated numbers

hardware	targeted duty cycle	all-sky duty cycle
CPU	2%	7%
GPU	7%	7%

Table 4.1: Relative duty cycles for chirp-like templates running on different architectures for the targeted and all-sky versions.

to span as much of the signal space as possible. The space of CBC chirp signals is much smaller. A search for binary neutron star signals with component masses of 1.4–$3M_\odot$ plateaus in sensitivity using just 50 chirp mass bins. The same search requires 825 time bins for 660 s of data—a typical on-source window (in which the signal is assumed to exist) for a GW search triggered by a gamma-ray burst[16]. Thus, the template density for a targeted CBC search is $\approx 6.3 \times 10^4\,\mathrm{ks}^{-1}$ whereas a Bézier bank might require $\approx 8 \times 10^8\,\mathrm{ks}^{-1}$ [300]; (1 ks = 1000 s). Since there are so many fewer templates in a chirp-template search (about four orders of magnitude fewer), it is computationally feasible to employ every template.

Of course, the previous calculation was for a targeted search in which the source location is previously determined, e.g., by an electromagnetic trigger or by a different search algorithm. In[300], we showed how the introduction of a phase factor can be used to allow to carry out an efficient all-sky search with seedless clustering. This formalism is straightforwardly applied to our chirping templates. For the CBCs detected by the LIGO Hanford-Livingston detector pair, it is sufficient to consider 40 time delays, each corresponding to a ring on the sky. Thus, even an all-sky search using seedless clustering to detect CBC signals can employ a relatively modest template density: $\approx 2.5 \times 10^6\,\mathrm{ks}^{-1}$.

To estimate the computational cost of an all-sky seedless clustering search (with chirp-like templates), we carried out a benchmark study using a Kepler GK104s GPU

and an 8-core Intel Xeon E5-4650 CPU. Each job was allotted 8 g of memory. The GPU was able to analyze 660 s of data in 48 s, corresponding to a duty cycle of $\approx 7\%$. Using all eight cores, the CPU duty cycle was comparable; the job-by-job variability in run time is greater than the difference between GPUs and 8-core CPUs on average.

If we require background estimation at the level of FAP $= 1\%$, it follows that a continuously running seedless clustering search with chirp-like templates can be carried out with just 8 GPUs (or 8-core CPUs). (Background estimation at the level of FAP $= 0.1\%$ would require 74 GPUs / 8-core CPUs.) In reality, the duty cycle from coincident GW detectors may be $\approx 50\%$, in which case these computing requirements are conservative by a factor of two. Repeating the test for a targeted search (for which the source location is known), we obtained an 8-core CPU duty cycle of 2%, a factor of 3 speed-up. The targeted search run on GPUs does not run appreciably faster than the all-sky version. These results are summarized in table 4.1.

In addition to improved computational efficiency, there is another important advantage to be gained through the use of CBC templates compared to Bézier templates. In[300], we showed that quadratic Bézier curves do a mediocre job approximating CBC signals. By adopting the chirping templates described in Eq. 4.4, we expect to capture more signal-to-noise ratio, and thereby extend the sensitive distance of the search. An example of a weak BNS signal recovered with a seedless chirping template is shown in Figure 4.1.

4.2 Sensitivity study

In order to determine the sensitivity of seedless clustering with chirp templates, we perform a sensitivity study with Monte Carlo noise. We assume Gaussian noise con-

sistent with the design sensitivity of Advanced LIGO. Following[16], we assume that an external trigger has predicted that the signal exists in a 660 s on-source window (we note that GRB-triggered CBC searches use 6 s). For each trial, we search for a chirp signal four different ways: using Bézier curves and a known sky location (BK), using Bézier with unknown sky location (BU), using chirp templates with a known sky location (CK), and using chirp templates with an unknown sky location (CU).

The first step of the sensitivity study is background estimation. We perform many trials to estimate the distribution of $\mathrm{SNR}_{\mathrm{tot}}$ for noise. We generate separate noise distributions for all four search variations (BK, BU, CK, CU). Using these noise distributions, we determine the value of $\mathrm{SNR}_{\mathrm{tot}}$ (for each search variation), which corresponds to a false alarm probability (FAP) of 0.1%.

The next step is to determine the distance to which different signals can be detected with $\mathrm{SNR}_{\mathrm{tot}}$ sufficient for a detection with FAP $< 0.1\%$. We view FAP $< 0.1\%$ as the minimum level to be considered interesting. In the case an event exceeds this threshold, more time-slides can be performed for the particular event to estimate its significance. We add GW signals to realizations of detector noise. Each injected signal is injected with an optimal sky location and an optimal source orientation. We define the "sensitive distance" as the distance at which 50% of the signals are recovered with FAP $< 0.1\%$. We consider 15 CBC waveforms with component masses ranging from 1.4–10$M_{\odot}$. Of these waveforms, eight characterize eccentric systems and three characterize systems where one or more object has a large dimensionless spin:

$$a \equiv cJ/Gm^2. \tag{4.6}$$

Here J is the angular momentum and m is the component mass.

Non-eccentric waveforms are generated using a SpinTaylorT4 approximation. Eccentric waveforms are generated using `CBWaves`, which employs all the contributions that have been worked out for generic eccentric orbits up to 2PN order[103]. The parameters for each waveform are give in Table 4.2.

4.3 Results

The results of our sensitivity study are summarized in Table 4.2. There are a number of interesting trends. First, while all of the (known direction) seedless clustering distances are astrophysically interesting, the chirping templates perform consistently better than the Bézier templates. The ratio of detection distance for chirping templates / Bézier templates ranges from 120–261% with a mean of 131%. The average ratio of sensitive volumes is 480%. This is comparable to the gain in sensitivity for a matched filter search to be had through the inclusion of spin[247], indicating that while it is certainly advantageous to use chirping templates, the Bézier templates do surprisingly well.

We find no significant difference in the chirping-template detection distance between systems that do or do not contain spin. The similarity in the sensitivity distances between the non-spinning and spinning cases indicates that the spins do not effect the signal morphology in a significant enough way to deviate from the non-spinning track. The advantage of chirping templates appears to increase slightly for spinning systems. Finally, we observe no loss in sensitivity going from the targeted CK search to the all-sky CU search. Evidently, the increase in signal space from the additional parameter of sky location is not sufficient to meaningfully affect the background distribution.

Highly eccentric signals generally have a longer duration than than those with low or no eccentricity. The sensitivity (using both Bézier templates and chirp-like templates) decreases with eccentricity. There is a similar advantage in distance of the chirp-like templates over the Bézier templates at low eccentricity. This benefit decreases slightly as eccentricity increases. This is due to the breakdown of the circular binary approximation. The breakdown becomes more pronounced at higher eccentricities, as one would expect.

Using matched filtering, Advanced LIGO, operating at design sensitivity, is expected to reliably detect BNS (with optimal orientation and sky location) out to distances of 450 Mpc[4], 2.4× further than the seedless clustering detection distance quoted here. It follows that $\approx$ 8% of the events detected by matched filtering will produce a FAP $< 0.1\%$ signature when followed up with seedless clustering. Given a realistic astrophysical rate of $40\,\mathrm{yr}^{-1}$ BNS detections by Advanced LIGO[9], this implies that we can expect to confirm ≈ 3 events per year of science data using seedless clustering. The use of expanded template banks that include waveforms with spin will allow matched filtering searches to observe to comparable distances as the non-spinning case[60]; therefore the follow-up numbers will be similar to the above.

In the event that circular template banks are used to search for eccentric signals, there will be a non-negligible loss in sensitivity for these searches. Huerta and Brown estimate signal-to-noise ratio loss factors of about 0.5 and 0.2 for BNS systems with eccentricities of 0.2 and 0.4 respectively[170]. This would bring the matched filtering sensitivity distances of these signals to 225 Mpc and 90 Mpc, compared to 180 Mpc and 160 Mpc for seedless clustering; therefore seedless clustering may provide further opportunities for observing these types of signals.

In addition to providing confirmation of these loudest CBC events, seedless cluster-

ing will provide a safety net by potentially detecting events missed due to waveform error, data-processing subtleties, and/or new physics.

4.4 Conclusions

Seedless clustering provides a computationally efficient tool for the follow-up and detection of compact binary coalescences. While seedless clustering is expected to be less sensitive than matched filtering, it provides a number of useful features including verification, visualization of the gravitational-wave signal, the ability to catch corner-case signals, and robustness to both waveform uncertainty and existence of new physics.

We compared a specially tuned implementation of seedless clustering, optimized for compact binary coalescences, to a more generic search using Bézier curves. We find that the CBC-tuned search can expand the sensitive volume by as much as a factor of 4.2× depending on the waveform (a factor of two on average) compared to the generic Bézier search. Perhaps more importantly, the tuned search requires 10^4 fewer templates per unit of time, allowing for a significantly faster search.

There are a number of potential improvements to the algorithm worth exploring. It may be possible to improve the implementation of seedless clustering described here by more optimally weighting different time-frequency bins based on the known waveform. It is also worth exploring the effect of only using equal mass templates to recover potentially non-equal mass signals. It is possible that for cases with larger mass ratios than those considered here, it may be necessary to relax this assumption in order to reconstruct a majority of the signal. Another possibility for improvement is the implementation of a better parametrization for the eccentric waveforms. Unlike for

circular binaries, there is, at present, no closed expression for the phase evolution of a binary with arbitrary eccentricity. A more effective parametrization is likely to capture more signal-to-noise ratio, thereby extending the sensitive range. Finally, it will be useful to carry out a systematic comparison of seedless clustering with matched filtering pipelines and using non-Gaussian noise. Mock data challenges with injected compact binary signals are currently being performed, and the results of these will be useful for a one-to-one comparison of methods.

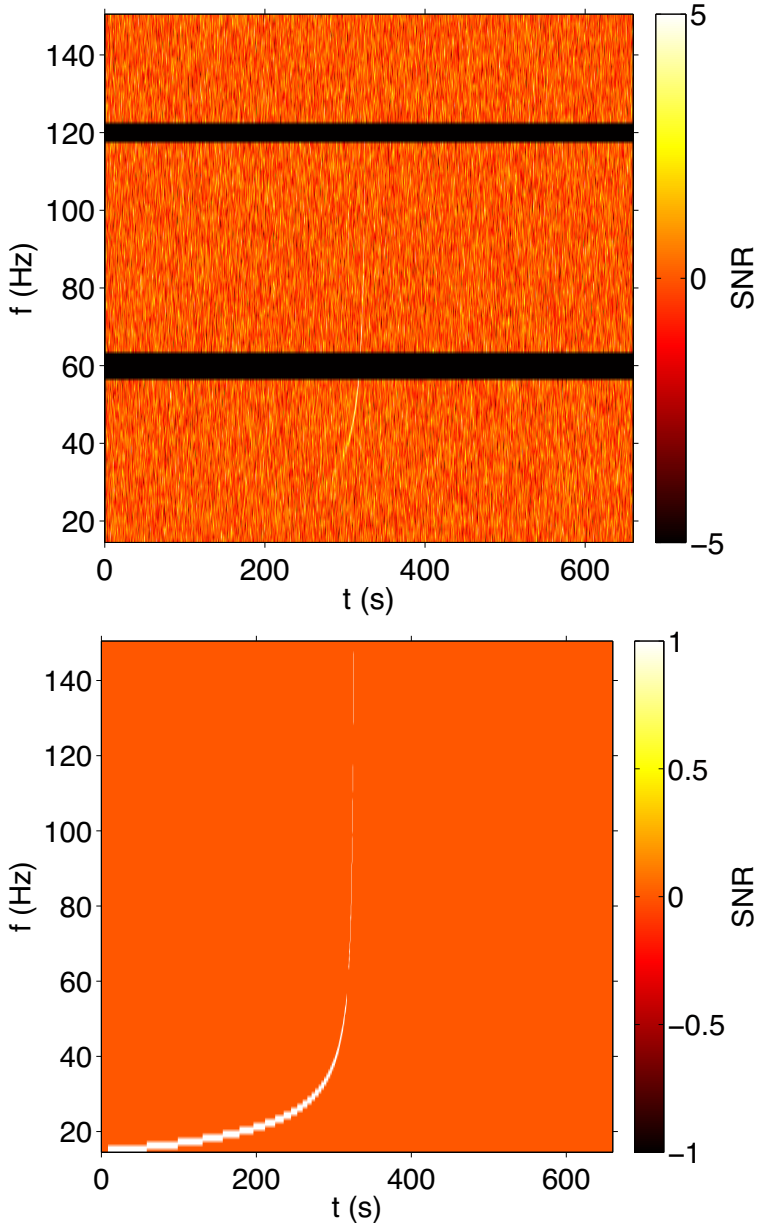


Figure 4.1: The plot on the left shows $\rho(t; f)$ for a simulated eccentric ($\epsilon = 0.2$) BNS signal injected on top of Monte Carlo detector noise. The component masses are $1.4M_{\odot}$. The chirping signal appears as a faintly-visible track of lighter-than-average pixels. The horizontal lines are frequency notches to remove instrumental artifacts. On the right is the recovery obtained with seedless clustering. The signal is recovered with a FAP $< 0.1\%$.

Waveform	m_1	m_2	a_1	a_2	ϵ	$t_{\rm dur}$ (s)	$D_{\rm BK}$	$D_{\rm BU}$	$D_{\rm CK}$	$D_{\rm CU}$
BNS 1	1.4	1.4	0	0	0	170	160	130	190	190
NSBH 1	3.0	1.4	0	0	0	96	200	200	290	290
NSBH 2	3.0	1.4	0.95	0	0	97	220	180	320	320
NSBH 3	10.0	1.4	0	0	0	77	280	260	680	680
BBH 1	3.0	3.0	0	0	0	54	330	330	470	470
BBH 2	3.0	3.0	0.95	0	0	55	320	270	470	470
BBH 3	3.0	3.0	0.95	0.95	0	55	320	260	470	470
BBH 4	5.0	5.0	0	0	0	42	620	560	750	750
BBH 5	5.0	5.0	0.95	0	0	42	680	680	750	750
BBH 6	5.0	5.0	0.95	0.95	0	43	750	680	830	830
EBNS 1	1.4	1.4	0	0	0.2	120	150	120	180	180
EBNS 2	1.4	1.4	0	0	0.4	224	150	120	160	160
ENSBH 1	3.0	1.4	0	0	0.2	69	180	180	290	290
ENSBH 2	3.0	1.4	0	0	0.4	127	180	160	240	240
ENSBH 3	3.0	1.4	0	0	0.6	237	180	160	240	240
EBBH 1	3.0	3.0	0	0	0.2	40	270	220	320	320
EBBH 2	3.0	3.0	0	0	0.4	70	220	200	240	240
EBBH 3	3.0	3.0	0	0	0.6	128	220	180	220	220

Table 4.2: Sensitive distances for different waveforms (assuming optimal sky location and source orientation) given the design sensitivity of Advanced LIGO[4]. Each row represents a different waveform: BNS="binary neutron star," NSBH="neutron star black hole binary," BBH="binary black hole. A waveform beginning with an "E" is eccentric. The columns marked m_1 and m_2 give the component masses in units of $M_\odot$. The columns marked a_1 and a_2 give the component spins; see Eq. 4.6. The next columns list the ellipticity ϵ and the waveform duration in seconds. The final four columns list the (FAP = 0.1%, FDP = 50%) detection distance (in Mpc) for Bézier templates with known sky location (BK), Bézier templates with unknown sky location (BU), chirp-like templates with known sky location (CK), and chirp-like templates with unknown sky location (CU).

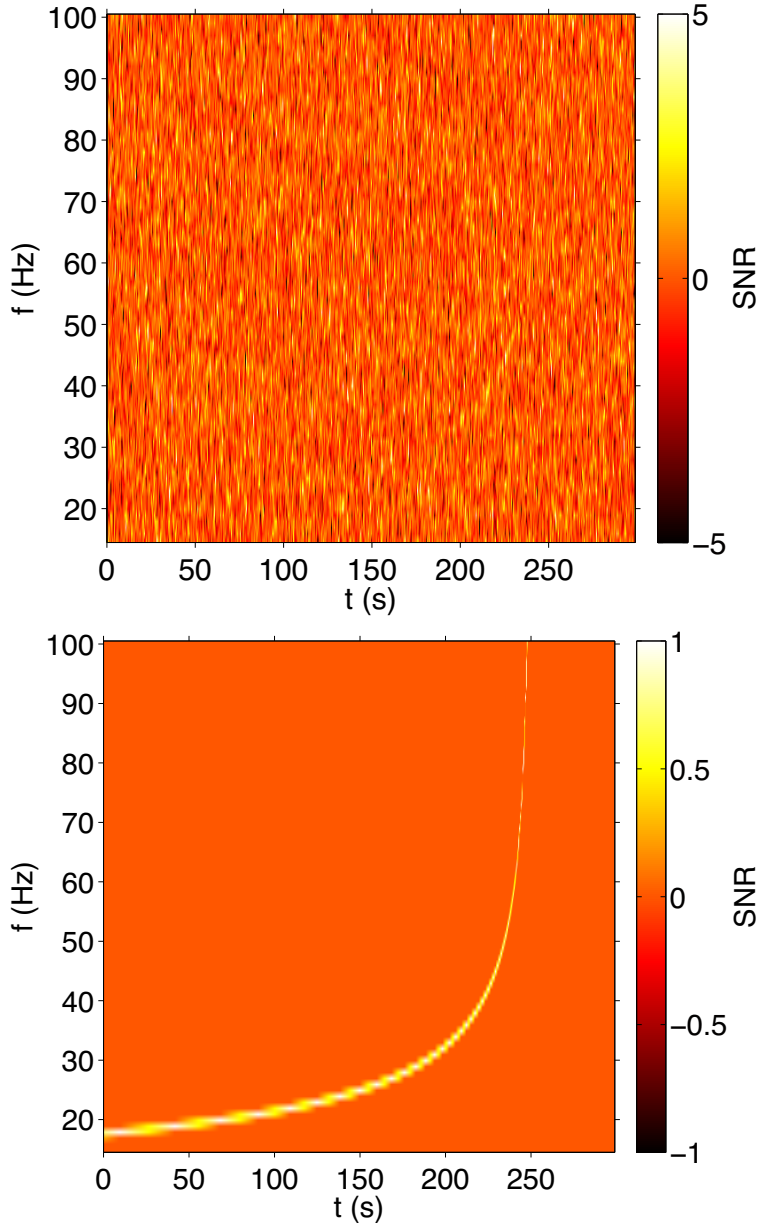


Figure 4.2: The plot on the left shows $\rho(t; f)$ during a recent LIGO engineering run, in which data from a LIGO subsystem—not sensitive to GW strain—is recolored to produce semi-realistic detector noise. On the right is the seedless clustering recovery, which is able to to detect the injected signal with high confidence FAP $< 0.1\%$, despite the relatively poor data quality. (Though it is not immediately apparent from these plots, five segments are identified as characteristic of non-stationary noise[246].) The signal is recovered with FAP $< 0.1\%$.

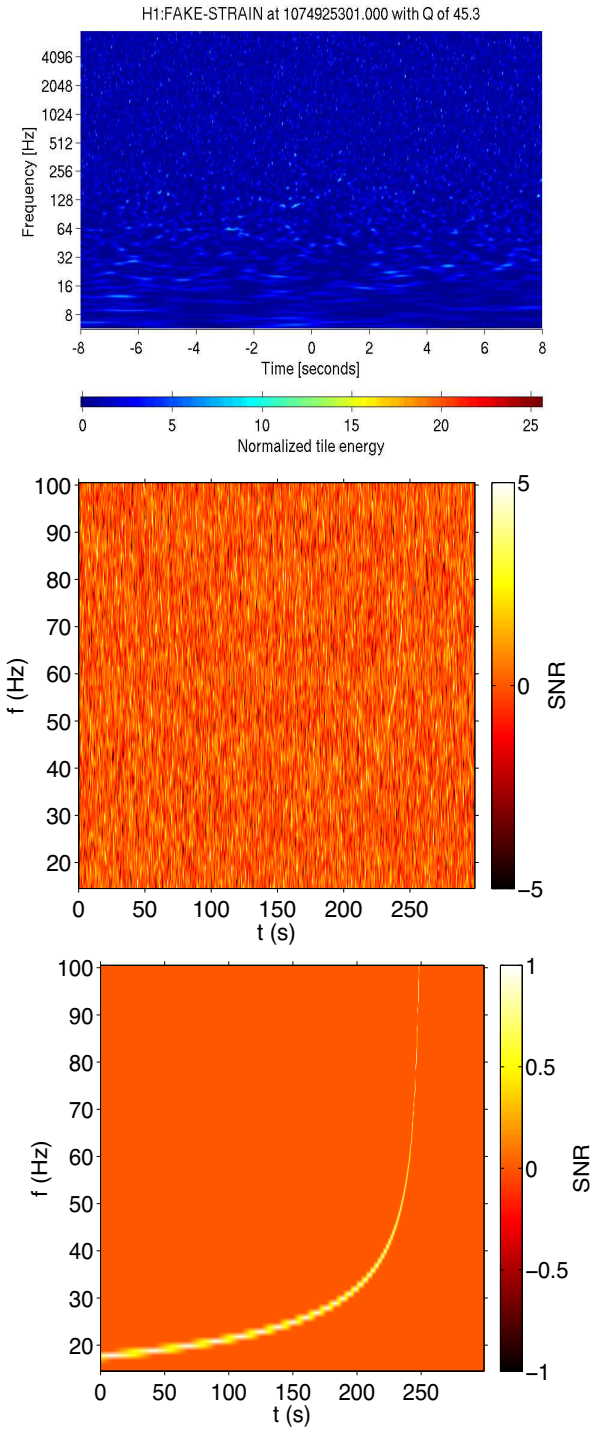


Figure 4.3: Data from a recent LIGO engineering run, in which data from a LIGO subsystem—not sensitive to GW strain—is recolored to produce semi-realistic detector noise. A simulated binary neutron star signal has been added to the data. The top plot shows a wavelet transform of single-detector auto-power[254], currently in wide use for diagnostics. The injected waveform, which ends at $t = 250$, is difficult to make out by eye. The middle plot shows a spectrogram of $\rho(t; f)$. The injection, though faint, is visible between 200-250 s. The bottom plot shows the reconstructed track using seedless clustering; FAP $< 0.1\%$.

5

The detectability of eccentric compact binary coalescences with advanced gravitational-wave detectors

Compact binary coalescences (CBCs) of black holes and/or neutron stars are a likely source of gravitational waves (GWs)[125,126,13]. The GWs generated by CBCs, such as binary neutron stars (BNSs), neutron-star black holes (NSBHs), and binary black holes (BBHs), sweep upward in frequency and strain amplitude through the sensitive band of GW detectors such as LIGO[180], Virgo[26], GEO[151], and KAGRA[280]. The de-

tection of GWs from CBCs will provide information about the populations of compact objects in the universe[260], elucidate the properties of strong field gravity, and provide a means to test general relativity[29].

Searches for CBCs almost entirely use matched filtering, which requires precise knowledge of astrophysical waveforms. Excess power searches are also used, especially for high-mass systems associated with shorter signals; see, e.g.,[12]. Because CBCs are, for the most part, well-modeled systems, matched filtering provides an essentially optimal strategy for detecting compact binaries. Due to computational limitations, most CBC searches use template banks composed of non-spinning, non-eccentric waveforms, which are less computationally challenging to implement than searches with complications such as spin and eccentricity. Up until now, there have been no dedicated matched filtering searches for low mass binaries with low to moderate eccentricities. Huerta and Brown have shown that searches using waveforms that assume no eccentricity are significantly sub-optimal above $\epsilon > 0.05$[170]. They conclude that in order to detect and study the rate of eccentric stellar-mass compact binaries in aLIGO, a search specifically targeting these systems will need to be constructed. Matched filtering searches would require eccentric template banks to avoid being significantly sub-optimal. One method for overcoming these difficulties is building larger (and smarter) template banks to perform searches. This is, of course, computationally expensive, and in some cases, intractable.

There have been a number of recent developments that potentially enable searches for eccentric binaries. Huerta et al.[171] recently developed a purely analytic, frequency-domain model for gravitational waves emitted by compact binaries on orbits with small eccentricity. This model reduces to the quasi-circular post-Newtonian approximant TaylorF2 at zero eccentricity and to the post-circular approximation of Yunes et

al.[333] at small eccentricity. A computationally-tractable, matched filtering search using these templates is possible. Matched filtering searches rely on knowing the phase of the gravitational-wave signal being searched for. This is powerful for limiting the noise background of detector data but also is subject to modeling errors, especially in highly eccentric cases where perturbative waveform generation methods are not yet sufficiently accurate to be used as templates. Another proposed method for detecting highly eccentric binaries is the search for the "repeated bursts" created by the many passes of the eccentric binary[194,293]. Tai et al.[293] applied a single-detector power stacking algorithm, developed in[188] to search for gravitational-wave bursts associated with soft gamma ray repeater events, to the case of eccentric binary mergers. They use a time-frequency signature informed by an eccentric model developed in[119] to sum up power in Q-transform pixels, which is a multi-resolution basis of windowed complex exponentials. Excess power methods, like those from[293] and those presented below, do not have the same issues as matched filtering, as phase information is not used in these analyses. In the work that follows, we will differ from[293] in the use of a coherent multi-detector statistic with a generic eccentric frequency-time track with the assumption of low-to-moderate eccentricity CBCs.

There is significant astrophysical motivation for designing searches for eccentric CBCs. Main sequence evolution binaries will be circularized by the time they enter the sensitive frequency band for ground-based detectors[239,238]. On the other hand, models exist which could result in highly eccentric CBCs in the sensitive band. O'Leary et al. present a model where the scattering of stellar mass black holes in galactic cores containing a super-massive black hole can lead to CBCs with high eccentricities[231]. They expect that 90% of such systems would have eccentricity $\epsilon > 0.9$ when twice their orbital frequency, likely the dominant frequency of gravitational-wave emission,

enters the sensitive band.

Assuming a highly idealized pipeline, and ignoring complications such as template bank trial factors, they found the expected rate of coalescence detectable by aLIGO to be $1 - 10^2$ per year. This rate estimate is dominated by intermediate-mass black hole binaries, which coalesce with a greater cross section, and which produce a louder signal than stellar mass binaries. In our analysis, we focus on low-mass binaries, where the method presented below is likely to give the greatest improvement over other methods. In this work, we argue that the detection rate in realistic pipelines is probably closer to 0.001–0.5 per year.

Samsing et al.[261] show how eccentric binaries can be generated from interactions between compact binaries and single objects, inducing chaotic resonances in the binary system. Although the number of BBHs in the galactic center is not well constrained, there may be more than 10^3 black holes in central 0.1 pc of our galaxy[166]. Binary-binary interactions in globular clusters can also result in non-zero eccentricity. If the orbital planes of the inner and outer binary are highly inclined with respect to one another, Kozai resonances increase the eccentricity of the inner binary[322,38,271]. Antonini and Perets[38] estimate that 0.5% of binaries formed in this way will have eccentricities $\epsilon > 0.5$ when they enter the sensitive band. Eccentric binary black hole mergers have also been studied[281,164]. Numerical relativity simulations have shown that highly eccentric BNS systems can exhibit interesting features, including f-modes and disks resulting from the merger[150]. Simulations of NSBH mergers show varying amounts of mass transfer and accretion disk size[120,283]. Therefore, there is significant motivation to design searches for eccentric CBCs as GW sources. Another potential mechanism for forming eccentric neutron star binaries is tidal capture[207].

In situations where the GW is either difficult to accurately model or the parame-

ter space too large to easily create template banks to accurately span the parameter space, a potential alternative is to search for excess power in spectrograms (also called frequency-time ft-maps) of GW detector data[291,193,132]. In these searches, the goal is to design pattern recognition algorithms that can identify the presence of GW signals across the parameter space of interest (in our case, low mass, low-to-moderate eccentricity CBCs). A strategy that has been shown to be effective in searches for long-lived transients is known as "seedless clustering," which integrates the signal power along spectrogram tracks using pre-defined "templates" chosen to capture the salient features of a wide class of signal models[298,300,96]. Examples of both nearby and near-detection threshold eccentric BNS signals recovered with a seedless chirping template are shown in Figure 5.1.

In previous work [96], the authors have shown how seedless clustering can be applied to searches for low-mass CBC signals ($M_{\rm total} \leq 10 M_{\odot}$). A shortcoming of the previous analysis was the use of a circular PN expansion when performing the search for the CBC signals, which is sub-optimal for binaries with even low to moderate eccentricities. In this paper, we show how to apply seedless clustering formalism to efficiently search for eccentric CBC signals. In section 5.1, we review the basics of seedless clustering and show how the formalism of[298,300,96] can be tuned to more sensitively detect eccentric CBC signals. In section 5.3, we determine the sensitivity of seedless clustering algorithms to eccentric CBC signals. In section 5.4, we describe the computational resources required for realistic searches and compare the algorithms' performance on CPUs and GPUs. In section 5.5, we discuss the implications of the results to the detectability of O'Leary et al.[231], Samsing et al.[261] and Antonini and Perets[38] models. We conclude with a discussion of topics for further study in section 5.6.

5.1 Seedless clustering for chirps

Spectrograms proportional to GW strain power are the starting point for most searches for unmodeled GW transients. Pixels are computed by dividing detector strain time series in segments and computing the Fourier transform of the segments. We denote the Fourier transform of strain data from detector I for the segment with a mid-time of t by $\tilde{s}_I(t;f)$. The time and frequency resolution is typically optimized based on the signal morphology. Following[96], we use 50%-overlapping, Hann-windowed segments with duration of 1 s and a frequency resolution is 1 Hz.

Searches for long-duration GW transients construct spectrograms of ft-maps of cross-power signal-to-noise ratio using the cross-correlation of two GW strain channels[132]:

$$\rho(t;f|\hat{\Omega}) = \frac{2\sqrt{2}}{\mathcal{N}}\mathrm{Re}\left[e^{2\pi i f \Delta\vec{x}\cdot\hat{\Omega}/c}\frac{\tilde{s}_I^*(t;f)\tilde{s}_J(t;f)}{\sqrt{P_I'(t;f)P_J'(t;f)}}\right]. \tag{5.1}$$

Here, $\hat{\Omega}$ is the direction of the GW source, $\Delta\vec{x}$ is a vector describing the relative displacement of the two detectors, c is the speed of light, and $e^{2\pi i f \Delta\vec{x}\cdot\hat{\Omega}/c}$ is a direction-dependent phase factor, which takes into account the time delay between the two detectors. $P_I'(t;f)$ and $P_J'(t;f)$ are the auto-power spectral densities for detectors I and J in the segments neighboring t. $\mathcal{N}$ is a FFT normalization factor, $L \times Fs$, where L is the number of samples and Fs is the sampling frequency. For additional details, see[132,298,300,96].

Pattern recognition algorithms are used to find signals present in the ft-maps. The specific form of the potential GW in the ft-map depends on the signal. Low mass, low-to-moderate eccentricity CBCs appear as chirps of increasing frequency. For highly eccentric signals, the signal also includes distinct and repeated "pre-bursts"

that last from minutes to days as the binary evolves from the initial very eccentric phase towards the less eccentric phase[194].

As described above, seedless clustering identifies clusters of pixels, denoted Γ, likely to be associated with a GW signal by integrating along tracks of pre-defined templates. The total signal-to-noise ratio for a cluster of pixels can be written as a sum of over $\rho(t; f|\hat{\Omega})$:

$$\mathrm{SNR}_{\mathrm{tot}} \equiv \frac{1}{N^{1/2}} \sum_{\{t;f\}\in\Gamma} \rho(t; f|\hat{\Omega}), \tag{5.2}$$

where N is the number of pixels in Γ.

While seed-based algorithms connect statistically significant seed pixels to form clusters[298,292], seedless clustering uses banks of parametrized frequency-time tracks. Because of their parameterization, calculations for many templates can be carried in parallel, which facilitates rapid calculations on multi-core devices such as graphical processor units (GPUs). Because these banks do not use phase and GW waveform amplitude, searches utilizing them are less sensitive than traditional matched filtering searches. On the other hand, for this same reason, they can be more robust when searching for GWs that do not fit the signal model exactly.

There are a number of seedless clustering parameterizations at this point in the literature[139,300,96]. One of the most robust is a template bank of randomly generated Bézier curves[139], which have been shown to be sensitive to a number of long-lived narrowband GW signals[300]. In the case of circular CBC signals, the most appropriate choice is a PN expansion of the form:

$$f(t) = \frac{1}{2\pi} \frac{c^3}{4GM_{\mathrm{total}}} \sum_{k=0}^{7} p_k \tau^{-(3+k)/8}, \tag{5.3}$$

where

$$\tau = \frac{\eta c^3 (t_c - t)}{5GM}. \tag{5.4}$$

Here, G is the gravitational constant, M_{total} is the total mass of the binary, η is the symmetric mass ratio and t_c is the coalescence time. The definition should be provided. The expansion coefficients p_k can be found in[57]. In[96], these were shown to fit the frequency evolution of the circular CBCs very well. On the other hand, the fits for eccentric CBCs were less precise. This motivates the derivation presented below.

To derive an expression for eccentric CBC signals, we use the lowest-order, quadrupole formula for eccentric binaries[239,238]. The derivation can be found in Appendix 5.7 and the frequency evolution in equation 5.15. One characteristic of seedless clustering is the use of a single track across the ft-map. This is suboptimal for eccentric signals as some power is present in harmonics of the orbital frequency of the binary, as can be seen in Figure 5.1. Yunes et al.[333] show that for small eccentricities, the power is dominated by components oscillating at once, twice and three times the orbital frequency. In the limit $\epsilon \ll 1$, the dominant term is the second harmonic. It is consistent with the assumptions above then that we search for a single, dominant harmonic with our algorithm.

In[96], circularized CBC waveforms are parameterized by two numbers: the coalescence time and the chirp mass. (In[96], we showed how approximating the individual component masses as equal led to excellent track fits, allowing for a significant reduction in the number of templates required to span the space.) The inclusion of eccentricity expands the chirp parameter space by an additional dimension. In the analysis below, we conservatively use a minimum componenent mass of $1M_{\odot}$.

By searching over 40 different time-delays, corresponding to 40 different sky rings,

a computationally efficient all-sky search can be performed. This was demonstrated in[96] to be sufficient to recover CBC signals in arbitrary directions. The assumption of low-to-moderate eccentricities here leads to a small increase in the number of templates required to span the space of interest. At eccentricities of 0.5 or above, contributions from the neglected terms in the derivation become significant at the 10% level. Also, the assumption that most of the power is in a single harmonic begins to break down. Therefore, we search from $0 \leq \epsilon \leq 0.5$. This leads to an increase in templates by a factor of 6 (using steps of 0.1 in eccentricity). The sensitivity does not improve appreciably with a higher resolution scan over eccentricity bins.

In order to justify expanding the parameter space, which not only requires more templates but also increases the noise background distribution (requiring higher signal-to-noise ratio to make detections), the fit of the templates must improve. We show below that there is a portion of the parameter space where the eccentric templates have more overlap with the signals and consequently capture more signal-to-noise ratio (SNR), and thereby extend the sensitive distance of the search. A simple metric for determining the efficacy of the fits is the overlap between the true track h and the template track s

$$O(s,h) = \frac{\frac{1}{N_s^{1/2}} \sum_{i=1}^{N_s} \rho_s}{\frac{1}{N_h^{1/2}} \sum_{i=1}^{N_h} \rho_h} \tag{5.5}$$

where N_s and N_h are the number of pixels in the s and h tracks respectively. The overlap corresponds to the sum over the true track h by the template track s, as in Eq. 5.2. $O(s,h) = 1$ corresponds to perfect overlap whereas $O(s,h) = 0$ corresponds to zero overlap. It is important to note that this definition of overlap is only *analogous* to the standard definition for matched filter searches—see, e.g.,[62,60]—as this definition is designed for spectrographic excess power searches. The fitting factor, FF,

gives the loss in SNR due to non-optimal templates. FF is computed by maximizing the overlap function over the template bank

$$FF(h) = \max_s \left(O(s,h)\right). \tag{5.6}$$

Like our expression for $O(s,h)$, $FF(s,h)$ is analogous (but not directly comparable to) definitions from matched filtering; see, e.g.,[62,60]. $FF = 1$ means that the fit in templates is perfect, while $FF = 0$ means that there is no overlap.

5.2 Sensitivity study

The design of the sensitivity study is as follows. We use Monte Carlo Gaussian noise consistent with the design sensitivity of advanced LIGO. We perform an untriggered search over a week of data. Following[96], we create 660 s non-overlapping spectrograms. To estimate background, we perform 100 time-slides of a week of data. For each trial, we search for a chirp signal using circular templates and using eccentric templates.

We begin our study by determining our background. Using many noise realizations, we estimate the the distribution of $\mathrm{SNR}_{\mathrm{tot}}$ for the two search variations corresponding to circular and eccentric templates. Using these noise distributions, we determine the value of $\mathrm{SNR}_{\mathrm{tot}}$ (for each search variation). This corresponds to a false alarm probability (FAP) of 1% for the untriggered searches.

We then determine the distance at which the signals can be detected with $\mathrm{SNR}_{\mathrm{tot}}$ sufficient for a FAP $< 1\%$. To do so, we inject GW signals into many noise realizations, with optimal sky location and an optimal source orientation, and recover them with the two search variations. We define the "sensitive distance" as the distance at

which 50% of the signals are recovered with FAP $< 1\%$ for each pipeline. Following[96], we use 15 CBC waveforms with component masses ranging from 1.4–5$M_\odot$ and eccentricities ranging from $0 - 0.6$. "Eccentricity" here is taken to mean the eccentricity of the binary when twice its orbital frequency enters the sensitive band. Non-eccentric waveforms are generated using a SpinTaylorT4 approximation. Eccentric waveforms are generated using `CBWaves`, which employs all the contributions that have been worked out for generic eccentric orbits up to 2PN order[103]. The parameters for each waveform are give in Table 5.1.

5.3 Results

We summarize the results of our sensitivity study in Table 5.1. First, we evaluate the improvement in sensitivity gained by using eccentric templates. Then, for the sake of completeness, we consider the (small) *loss* in sensitivity for circular signals due to the expanded search space.

5.3.1 Recovery of eccentric signals

We begin with an analysis of the fitting factors. The fitting factors for the eccentric templates range from $0.55 - 1$, while the fitting factors for the circular templates range from $0.25 - 1$. In general, the fitting factors for the circular and eccentric templates are similar for the non-eccentric cases considered here. This is to be expected as the eccentric templates should converge to the circular ones in the limit of small eccentricities. The performance at low eccentricities for the low-mass systems shows a slightly better fitting factor for the circular templates. As eccentricity and mass increase, the fitting factors for eccentric systems become significantly higher than that

Waveform	m_1	m_2	ϵ	$t_{\rm dur}$ (s)	$FF_{\rm Circular}$	$FF_{\rm Eccentric}$	$D_{\rm Circular}$	$D_{\rm Eccentric}$
BNS 1	1.4	1.4	0	170	0.95	0.95	160	160
NSBH 1	3.0	1.4	0	96	0.9	0.9	270	270
BBH 1	3.0	3.0	0	54	0.95	0.95	420	390
BBH 2	5.0	5.0	0	42	0.75	0.75	620	560
EBNS 1	1.4	1.4	0.2	120	0.85	0.85	150	160
EBNS 2	1.4	1.4	0.4	224	0.65	0.85	150	160
ENSBH 1	3.0	1.4	0.2	69	0.95	0.95	240	240
ENSBH 2	3.0	1.4	0.4	127	0.6	0.9	220	240
ENSBH 3	3.0	1.4	0.6	237	0.65	0.75	220	240
EBBH 1	3.0	3.0	0.2	40	0.3	0.75	240	360
EBBH 2	3.0	3.0	0.4	70	0.25	0.7	180	290
EBBH 3	3.0	3.0	0.6	128	0.3	0.6	200	350
EBBH 4	5.0	5.0	0.2	14	0.45	0.85	350	420
EBBH 5	5.0	5.0	0.4	26	0.3	0.65	290	390
EBBH 6	5.0	5.0	0.6	51	0.4	0.55	240	390

Table 5.1: Sensitive distances for different waveforms (assuming optimal sky location and source orientation) given the design sensitivity of advanced LIGO[4]. Each row represents a different waveform: BNS="binary neutron star," NSBH="neutron star black hole binary," BBH="binary black hole. A waveform beginning with an "E" is eccentric. The columns marked m_1 and m_2 give the component masses in units of $M_\odot$. The next columns list the eccentricity ϵ and the waveform duration in seconds. The next two columns list the fitting factors (FF) for both chirp-like templates and eccentric templates. The final two columns list the (FAP = 1%, FDP = 50%) detection distance (in Mpc) for circular templates and eccentric templates.

for the circular templates. For some of the systems considered here, the fitting factors for the eccentric templates can be more than a factor of two higher than for the circular templates. This means that the signal-to-noise ratio recovered for these tracks will be more than a factor of two higher for the eccentric bank. Figure 5.2 shows an example of the improvement of eccentric waveform fits from using the eccentric templates. The main reason that the fitting factors become relatively poor as mass increases is the breakdown of the assumption that the signals being searched for are narrowband. For systems with non-zero eccentricity, there is a broad spectrum of frequencies rather

than an identifiable $f(t)$.

The ratio of detection distance for eccentric templates to circular templates ranges from 100–175% with a mean of 130%. This corresponds to an average ratio of sensitive volumes, which corresponds to distance cubed, is 250%. This is comparable to the gain in sensitivity when going from Bézier curves to circular templates[96]. The sensitivity distances for eccentric waveforms decreases as eccentricity increases. The fall-off is significantly slower for the eccentric templates. This is due to the breakdown of the circular binary approximation. The breakdown becomes more pronounced at higher eccentricities, as one would expect. The increase in sensitivity when going from an all-sky search to a triggered search is between 10–20% for both circular and eccentric templates.

Table 5.1 shows that the sensitive distances are not always monotonically decreasing functions of the eccentricity for either eccentric or circular templates. This is because the sensitive distances are determined both by the fitting factors as well as the waveforms themselves. Because the fitting factors are maximized over the parameter space, some of the waveforms will be better fit than others. In addition, the waveforms will have different amounts of available "power" to be fit. Therefore, it is not necessarily surprising that the sensitive distances are not monotonically decreasing.

5.3.2 Recovery of circular signals

We now turn our attention to the sensitivity distances. The trends in the sensitivity distances are similar to those seen in the fitting factors. In general, the sensitivity to the circular waveforms for the eccentric templates is slightly worse than the circular waveforms. This is predominantly due to the increased background distribution from the expansion of the parameter space. The ratio of detection distance for eccentric

templates / circular templates ranges from 90–100% with a mean of 95%. The average ratio of sensitive volumes is 88%.

5.4 Computational requirements

To estimate the computational cost of an all-sky seedless clustering search (with eccentric chirp-like templates), we carried out a benchmark study using a Kepler GK104s GPU and an 8-core Intel Xeon E5-4650 CPU. Each job was allotted 8 g of memory. The GPU was able to analyze 660 s of data in 106 s, corresponding to a duty cycle of $\approx 16\%$. This is about a factor of two slower than the circular-template search. Using all eight cores, the CPU duty cycle was comparable; the job-by-job variability in run time is greater than the difference between GPUs and 8-core CPUs on average.

If we require background estimation at the level of FAP = 1%, which corresponds to performing 100 time-slides, it follows that a continuously running seedless clustering search with chirp-like templates can be carried out with just 32 continuously-running GPUs (or 8-core CPUs). Here, we have taken into account an additional factor of two needed to implement overlapping spectrograms to ensure that signals do not fall on the boundary. (Background estimation at the level of FAP = 0.1% would require 320 GPUs / 8-core CPUs.) In reality, the duty cycle from coincident GW detectors may be $\approx 50\%$, in which case these computing requirements are conservative by a factor of two.

5.5 Astrophysical implications

O'Leary et al. present a model where the scattering of stellar mass black holes in galactic cores which contain a super-massive black hole can lead to CBCs with high

Model	Source	Algorithm	Low Rate	Realistic Rate	High Rate
Scattering in galactic cores[231]	BBH	MF	0.008	0.02	0.5
		SC	0.001	0.002	0.06
Binary-single stellar encounters[261]	BNS	MF	0.004	0.4	4
		SC	0.0005	0.05	0.5
	NSBH	MF	0.002	0.1	3
		SC	0.0003	0.01	0.4
	BBH	MF	0.004	0.2	10
		SC	0.0005	0.03	1
Kozai resonances[38]	BNS	MF	-	0.002	-
		SC	-	0.0002	-
	BBH	MF	-	0.01	-
		SC	-	0.001	-

Table 5.2: Potential detection rates of eccentric compact binary coalescences for both matched filtering and seedless clustering. The rates combine results for eccentric binaries given by O'Leary et al.[231], Samsing et al.[261] and Antonini and Perets[38], as well as aLIGO detection rates. The matched filtering line assume a dedicated eccentric binary matched filtering pipeline, which does not currently exist. The seedless clustering algorithm is the one presented in this paper. Please see the text of section 5.5 for further details.

eccentricities, corresponding to eccentricities near to 1[231]. We discuss here the potential for detecting such systems given the rates presented in the paper. Table I of[231] presents the Merger Rate per Milky Way Equivalent Galaxy (MWEG) for the models considered. We can straightforwardly convert from the rates in this paper to what we expect in the advanced detector era. The most optimistic scenario, given by model F-1, predicts $1.5 \times 10^{-2}\,\mathrm{MWEG}^{-1}\,\mathrm{Myr}^{-1}$. The median scenario, given by the median of the models considered, predicts $3.3 \times 10^{-4}\,\mathrm{MWEG}^{-1}\mathrm{Myr}^{-1}$. The pessimistic scenario, given by model Aβ3, predicts $2.0 \times 10^{-4}\,\mathrm{MWEG}^{-1}\mathrm{Myr}^{-1}$. We now find the rates of CBCs given by Table II of[9]. The low, realistic, and high rates for BBHs are $0.01\,\mathrm{MWEG}^{-1}\mathrm{Myr}^{-1}$, $0.4\,\mathrm{MWEG}^{-1}\mathrm{Myr}^{-1}$, and $30\,\mathrm{MWEG}^{-1}\mathrm{Myr}^{-1}$ respectively. The matched filter detection rates of CBCs for advanced LIGO are given by Table IV of[9]. The low, realistic, and high detection rates for BBHs are 0.4, 20, and 1000 respectively.

Using these estimates, we can compute the expected rates of eccentric detections by a matched filtering pipeline using the ratio of the O'Leary et al. and aLIGO detection rates, multiplied by the BBH detection rate. These are: 0.008, 0.02, and 0.5 for the low, realistic, and high detection rates for BBHs. We can convert between matched filter and seedless clustering detection rates by dividing through by 8 (as the distances differ by about a factor of 2)[96]. These are given by 0.001, 0.002, and 0.06 for the low, realistic, and high detection rates for BBHs. Table 5.2 summarizes these results. We note here that the matched filtering results stated here would require a dedicated eccentric binary matched filtering pipeline, which does not currently exist. A matched filtering pipeline using circular templates would have rates similar in order of magnitude to that of seedless clustering. We describe in section 5.3 where seedless clustering is most competitive. The relatively low detection rates are due to the significantly fewer eccentric binaries expected relative to circular binaries, at least in the O'Leary et al. model.

Samsing et al.[261] estimate that eccentric binaries formed from interactions between compact binaries and single objects are about 1% of the anticipated total compact object merger rate. Therefore, we can scale the matched filter detection rates of CBCs for advanced LIGO from Table IV of[9] for the BNS, NSBH, and BBH systems by 0.01. This results in 0.004, 0.4, and 4 for the low, realistic, and high detection rates for BNS, 0.002, 0.1, and 3 for NSBH, and 0.004, 0.2, and 10 for BBH. Performing the same scaling as above for seedless clustering, we find 0.0005, 0.05, and 0.5 for the low, realistic, and high detection rates for BNS, 0.0003, 0.01, and 0.4 for NSBH, and 0.0005, 0.03, and 1 for BBH.

Antonini and Perets[38] estimate that eccentric binaries formed from Kozai resonances have rates of 1% and 10% of the realistic detection rates of circular binaries

for BNS and BBH systems respectively. About 0.5% of these binaries will enter the sensitive band with significant eccentricities ($\epsilon \geq 0.5$). Therefore, we can scale the realistic rates from Table IV of[9] for the BNS and BBH systems by 0.00005 and 0.0005 respectively. This results in 0.002 and 0.01 for BNS and BBH respectively. Performing the same scaling as above for seedless clustering, we find 0.0003 and 0.001.

5.6 Discussion

We have described an analytic expression for the frequency evolution of low-mass, low-to-moderate eccentricity waveforms. We showed how an implementation of this evolution for seedless clustering, optimized for compact binary coalescences, can improve searches for eccentric signals significantly. We find that the eccentric search can expand the sensitive volume by as much as a factor of 3× depending on the waveform (a factor of 1.4 on average) compared to a comparable circular search.

In the event that circular template banks are used by matched filtering to search for eccentric signals[61], there will be a non-negligable loss in sensitivity for these searches. Huerta and Brown estimate signal-to-noise ratio loss factors of about 0.5 and 0.2 for BNS systems with eccentricities of 0.2 and 0.4 respectively[170]. This would bring the matched filtering sensitivity distances of these signals to 225 Mpc and 90 Mpc, compared to 160 Mpc for these two eccentricity values when using seedless clustering; therefore seedless clustering with eccentric template banks may provide further opportunities for observing these types of signals.

In the future, we intend to explore the possibility that including amplitude information in the track recoveries improves the detection sensitivities. This is beneficial especially for compact binaries, where the amplitude information is known. Therefore,

the spectrogram pixels predicted to contain a higher amplitude of SNR are weighted more strongly than those predicted to contain less. This would help account for the relatively low-SNR contribution at low frequency and not overweight the pixels in that band, which will increases the background SNR distribution. Also, it will be useful to carry out a systematic comparison of seedless clustering with matched filtering pipelines using non-Gaussian noise. Mock data challenges with injected compact binary signals are currently being performed, and the results of these will be useful for a one-to-one comparison of methods. Finally, we intend to use this algorithm on future data from advanced LIGO and advanced Virgo.

5.7 Appendix: Eccentric template derivation

To derive an expression for eccentric CBC signals, we use the lowest-order, quadrupole formula for eccentric binaries (for simplicity, we will set $G = c = 1$)[239,238]. We write our equations in terms of eccentricity ϵ and a new variable $x = (M_{\rm total} \times \omega)^{2/3}$, where w is the angular velocity of the compact object. To derive an analytic solution, we keep the lowest order terms in x for both the x and ϵ evolution. Because we are fitting the frequency evolution of the inspiral, the fact that the PN calculations tend to slowly converge at late inspiral are less important here. The differential equations are[164]:

$$\dot{x} = \frac{2\eta}{15(1-\epsilon^2)^{7/2}}(96 + 292\epsilon^2 + 37\epsilon^4)x^5 + \mathcal{O}(x^6) \tag{5.7}$$

$$\dot{\epsilon} = \frac{-\epsilon\eta}{15(1-\epsilon^2)^{5/2}}(304 + 121\epsilon^2)x^4 + \mathcal{O}(x^5). \tag{5.8}$$

Taking the ratio of these equations, we obtain

$$\frac{dx}{d\epsilon} = \frac{-2}{\epsilon}\left(\frac{1}{1-\epsilon^2}\right)\left(\frac{96+292\epsilon^2+37\epsilon^4}{304+121\epsilon^2}\right)x. \tag{5.9}$$

We integrate this equation, yielding

$$x(\epsilon) = C_0\left[\frac{1-\epsilon^2}{\epsilon^{12/19}(304+121\epsilon^2)^{870/2299}}\right]. \tag{5.10}$$

Plugging this equation back into the original differential equation and expanding to fourth order in epsilon, results in

$$\epsilon(t) = \left(\frac{B-t}{A\times M}\right)^{19/48}, \tag{5.11}$$

where

$$A = \frac{5\times 31046}{172\times 2^{2173/2299}\times 19^{1118/229}\eta C_0^4} \tag{5.12}$$

$$C_0 = (2\pi M f_0)^{2/3}\left[\frac{1-\epsilon_0^2}{\epsilon_0^{12/19}(304+121\epsilon_0^2)^{870/2299}}\right]^{-1} \tag{5.13}$$

$$B = AM\epsilon_0^{48/19}. \tag{5.14}$$

Combining these together,

$$f(t) = \frac{1}{2\pi M}\left[\frac{C_0(1-\epsilon^2)}{\epsilon^{12/19}(304+121\epsilon^2)^{870/2299}}\right]^{3/2}, \tag{5.15}$$

where f_0 is the initial frequency of the binary, and ϵ_0 is the initial eccentricity.

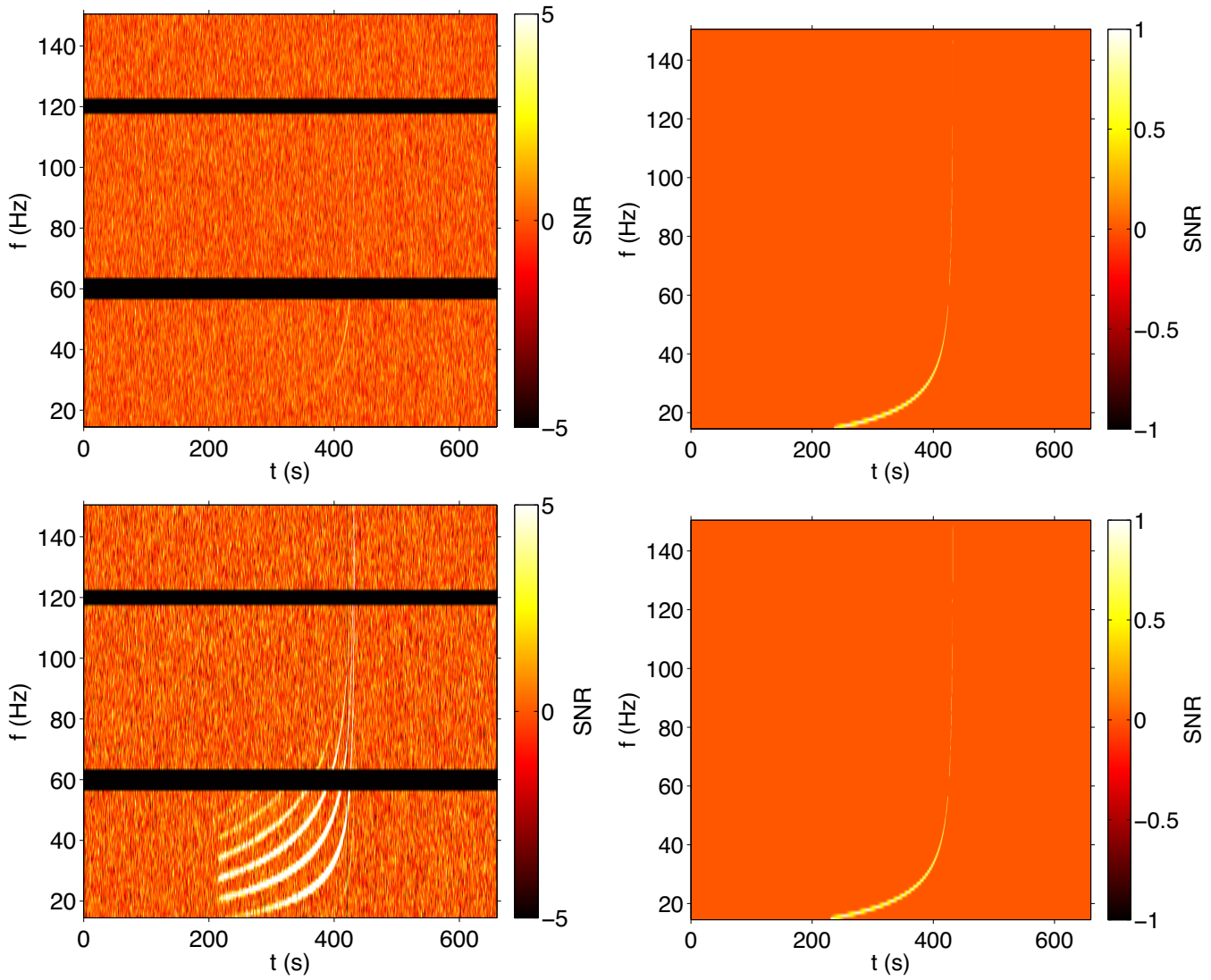


Figure 5.1: The plot on the top left shows $\rho(t; f)$ for a simulated eccentric ($\epsilon = 0.4$) BNS signal injected on top of Monte Carlo detector noise. The simulated noise is created for the advanced LIGO Hanford and Livingston Observatories operating at design sensitivity. The component masses are $1.4M_{\odot}$ and the distance is 100 Mpc. The chirping signal appears as a faintly-visible track of lighter-than-average pixels. The horizontal lines are frequency notches to remove instrumental artifacts. On the top right is the recovery obtained with seedless clustering. The signal is recovered with a FAP $< 0.1\%$. The plot on the bottom left shows $\rho(t; f)$ for the same system but an order of magnitude nearer at 10 Mpc. The harmonics are visible at this distance. The bottom right shows the recovery obtained with seedless clustering.

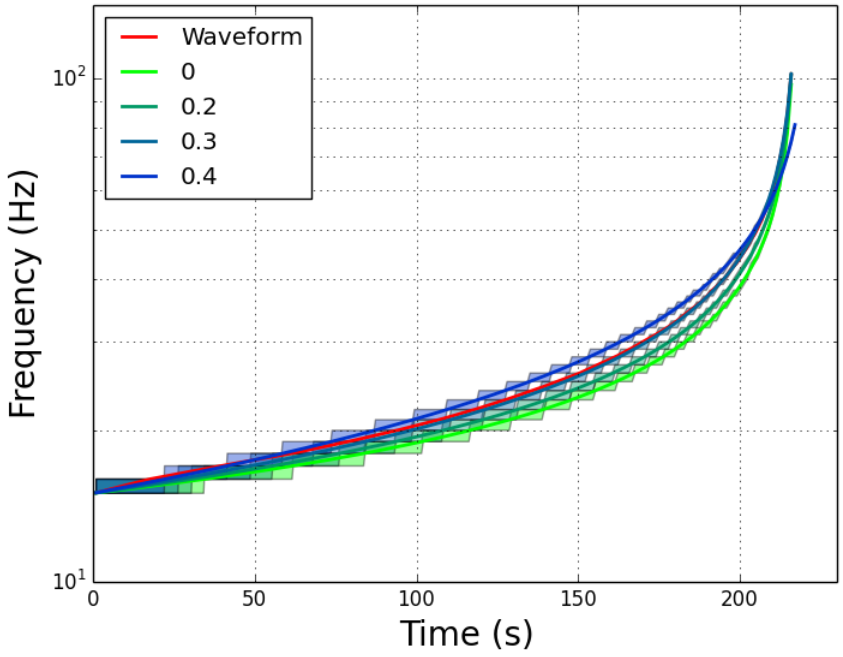


Figure 5.2: This plot shows a BNS waveform (red) with $\epsilon = 0.4$ and $m_1 = m_2 = 1.4\,\mathrm{M}_\odot$ compared to eccentric templates using Equation 5.15 with eccentricities ranging from $\epsilon = 0$ (light green) through $\epsilon = 0.4$ (blue). The shaded regions represent a nominal 1 Hz band around the track. Ideally, the shaded region for a track would overlap with the red waveform. While the best fit (which happens for $\epsilon = 0.3$) is not associated with the correct eccentricity, it is nonetheless a reasonable fit to the waveform that is better than could be obtained using only a circular parameterization ($\epsilon = 0$). This exhibits the superiority of the shape of the eccentric parameterization in fitting eccentric waveforms.

6

Prospects for searches for long-duration gravitational-waves without time slides

Second-generation gravitational-wave detectors such as Advanced LIGO[180] and Advanced Virgo[295] will be coming online in the coming months and years. Some searches for gravitational-wave transients seek to detect gravitational-wave transients lasting ∼10–1000 s. Compact binary coalescences of black holes (and/or neutron stars) are one example of long-lived gravitational-wave sources[125,126,123]. Uncertain models exist for more exotic sources of long-lived transients, including emission from rotational instabilities in protoneutron stars[244,242,243,83] and black-hole accretion disk instabil-

ities[191,307,308]. When a matched filter search is not possible, searches for unmodeled long-lived transients[5,132,299,300,96,92] can be employed.

Searches for compact binary coalescences typically rely on performing time-slides of single detector *triggers*, generated by performing a matched filter (in the compact binary coalescence case) on single-detector time series data. Time-slides are the shift of either time-series data or triggers from one detector against those of another, and are designed to eliminate potential gravitational-wave content contaminating the background estimation. Burst searches use clustering algorithms, as opposed to matched filtering techniques, on single detector time-frequency maps[35] or multi-detector coherent maps[291,193,132]. Calculating the coherent statistic takes significant computational resources because the triggers are inherently multi-detector and so the time-slides must be done on the time-series data itself, rather than the single-detector triggers. Because detector noise is generally non-Gaussian, it is difficult to know if an event in one detector is signal or noise. For this reason, multiple detectors are required to perform gravitational-wave searches. To estimate background, these searches time-shift the data of each detector with respect to the other(s), by some unphysical delay which is larger than the light travel time between the detectors. The coherent statistics are then computed between the time-shifted data in the same way as the original search algorithm, and in this way, false alarm rates can be estimated. Current searches use thousands of time-slides or more[181,126,124]. The main limitation on the number of time-slides that can be performed is limited computational resources, although the short-duration coherent burst pipelines have now been tested in the ten-thousand time-slides regime. Currently, they are moving towards the hundred-thousand time-slide regime, while the compact binary matched filtering pipelines have successfully generated 5σ background distributions. 5σ means that the event has a

SNR exceeding a significance threshold that corresponds to a 1 in 1,744,278 occurrence, after accounting for trials factors. For a single event, therefore, 1,744,278 time-slides must be performed to determine whether an event has an SNR exceeding a 5σ threshold. The difficulty in reaching these levels is due to computationally intensive calculations like the matched filter used in compact binary coalescence[31], calculation of the coherent SNR[324] used in burst searches, and potentially seedless clustering[299,300,96,92] in a long-duration transient search.

Was et al. demonstrated the limitation of using time-slides to perform background estimation in the single-detector trigger case[314,313]. Although coherent analyses do not use single-detector time-slides, background estimation for coherent searches rely on estimating the properties of the noise with finite measurements and therefore have error bars on their background estimation as well. They showed that the precision on the background estimation using time-slides of trigger streams is in fact limited and that the variance associated with their use saturates at some point. The computational limitations and the potential problems with time-slides motivate a search for potential alternative forms of background estimation in gravitational-wave searches. Gravitational-wave searches for isotropic stochastic gravitational wave backgrounds[18,6] and directional searches towards Sco X-1, the galactic center, and SN1987A[11] have assumed that the detection statistic is normally distributed with a known mean and variance that can be calculated from first principles when performing the searches. These searches sum up data from long stretches of time, and combined with the use of long time segments (60 s) and Gaussianity cuts, these statistics are Gaussian by the Central Limit Theorem. This has the significant computational cost-saving benefit of not requiring time-slides to perform the search, although limited time-shift analyses are used as sanity checks and to ensure that particularly non-Gaussian frequency bins

can be removed from the analysis.

Some searches for long-duration gravitational-wave transients use the same cross-correlation technique as stochastic searches[132], although other methods exist[291,193]. They utilize cross-power spectrograms, computed from the cross-correlation of two gravitational-wave detectors, and use pattern recognition algorithms to search for clusters of excess strain cross-power[132]. One algorithm used to search for long-duration gravitational waves is *seedless clustering*, which integrate along many different paths in spectrograms. This algorithm is sensitive to signals that can be well-approximated by parameterized curves, and the advantage of seedless clustering is most pronounced for long and weak signals[299,300,96,92]. We have previously shown how seedless clustering algorithms can be used to significantly enhance the sensitivity of searches for signals of this type[299]. Although seedless clustering algorithms are *embarrassingly parallel*[143], and therefore computations can be performed on graphical processor units, seedless clustering searches are still limited by computation of the noise background.

Cannon et al. [65] recently proposed a method to estimate the false alarm probability of compact binary coalescences without time-slides. They are able to approximate compact binary events as a Poisson process in order to convert the calculated false alarm probability into a false alarm rate. This in particular allows for a statistical detection of a population of events, which could be collectively more significant than the single most significant event alone. The method proposed in our paper is similar in that we measure events based on the data and then use a statistical approximation to the distribution of the measured tracks to make approximations to the noise background. There are also a number of notable differences. Because long-duration transient gravitational waves are typically searched for using a coherent combination of detector data, the trigger distributions no longer obey Poisson statistics. Instead,

we will exploit the fact that seedless clustering sums many approximately statistically independent pixels to use Gaussian statistics to estimate the background. In this paper, we demonstrate a semi-analytical approximation to the seedless clustering output from cross-correlation spectrograms. One potential criticism of the analysis that follows is the fact that we compare the approximation with data from time-slide analyses out to $\approx 3\sigma$, not to the 5σ distributions we present at the end of the paper. It would be necessary to perform 5σ worth of time-slides to verify the approximation. This calculation is currently very difficult to do computationally, and of course, if we could perform 5σ worth of time-slides, we would not need an approximation in the first place. Moreover, as we perform the analysis using a relatively clean week-long stretch of data, different sets of data could result in different results. Therefore, we consider the analysis that follows as a first test for the feasibility of an approximate method. As argued above, we expect the background distributions to be better behaved in long-duration analyses than in short-duration searches, and therefore perhaps less susceptible to significant deviations from empirical distributions. In the future, we can use distributions generated by future analyses that perform more time-slides and over longer periods to compare against the approximation to test its utility. Therefore, although time-slides are likely required to create confidence in a detection due to the problem just described, we now summarize several reasons why it is useful to consider alternative significance-estimation strategies.

Algorithm Verification. The semi-analytic method provides a verification for the pipeline in multiple ways. In the case where data-quality work is being performed correctly, in general, the data should be generally well-approximated by Gaussian noise, outside of some data transients which pass the data quality cuts. Therefore, background estimation should approximately follow the distribution if it is assumed that

the data is Gaussian. Also, this provides a sanity check that the algorithm performs as expected on the data. By performing a limited number of time-slides or performing a simulated analysis on Gaussian noise, it should be clear that the model for the algorithm is correct, which can provide confidence that the algorithm is performing as expected (or not).

Sensitivity to waveform models. There are a number of papers contained in the literature about the sensitivity of gravitational-wave detectors to long-duration gravitational waves[299,300,244,96,92]. In general, the sensitivity studies have been performed by running the analysis on 1,000 ft-maps to reach a FAP of 0.1%, and the sensitivity to various waveform models are computed relative to this number. For a year of data, assuming ft-maps of 250 s with 50% overlap, and a desirable FAP of $\approx 3\,\sigma$ or FAP = 0.27%, there will be more than 10^8 maps analyzed. Before any analysis, either a search for gravitational-waves or a waveform sensitivity study, is performed, it is desirable to be able to estimate the background quickly. This estimate informs expectations of potential results as well as how to setup the analysis. Using the method described in this paper, we can analytically compute what we expect a threshold based on this number of maps, without needing to perform an analysis with many time-slides.

Event follow-up and electromagnetic alerts. There are preparations for joint electromagnetic and gravitational-wave observations in the advanced detector era[276]. Low-latency gravitational-wave searches are aiming for run-times ≤ 1 min. For significance estimates on this time-scale, rapid background estimation techniques are required. The method described in this paper is able to give an approximate FAR for any event on this time-scale. In the case where there is eventually interest in joint electromagnetic and gravitational-wave observations for generic long-duration transients, this

method may be useful for making that happen.

The remainder of the paper is organized as follows. In Sec. 6.1, we describe the formalism of an all-sky transient search and seedless clustering. In Sec. 6.2, we present the results of a Monte Carlo and time-shifted study comparing the semi-analytical model to seedless clustering. In Sec. 6.3, we explore the errors, both systematic and statistical, with our method. In Sec. 6.4, we discuss our conclusions and suggest directions for future research.

6.1 Formalism

We use the cross-correlation of two GW strain channels from spatially separated detectors to perform searches for long-duration GW transients. We construct ft-maps of cross-power signal-to-noise ratio. We divide detector strain time series into segments and compute Fourier transforms of the segments to create the pixels, which we denote as $\tilde{s}_I(t;f)$, where we take strain data from detector I for the segment with a mid-time of t. Following[299,300,96,92], the segments are 50%-overlapping and Hann-windowed with duration of 1 s and a frequency resolution of 1 Hz.

The expression for the cross-power signal-to-noise ratio is as follows[132]:

$$\rho(t;f|\hat{\Omega}) = \frac{2\sqrt{2}}{\mathcal{N}}\mathrm{Re}\left[e^{2\pi i f \Delta\vec{x}\cdot\hat{\Omega}/c}\frac{\tilde{s}_I^*(t;f)\tilde{s}_J(t;f)}{\sqrt{P_I'(t;f)P_J'(t;f)}}\right]. \tag{6.1}$$

where $\Delta\vec{x}$ is a vector describing the relative displacement of the two detectors, $\hat{\Omega}$ is the direction of the GW source, and c is the speed of light. The time delay between the two detectors, which is a direction-dependent phase factor, is in the $e^{2\pi i f \Delta\vec{x}\cdot\hat{\Omega}/c}$ term. $P_I'(t;f)$ and $P_J'(t;f)$ are the auto-power spectral densities for detectors I and J in the segments neighboring t. $\mathcal{N}$ is a FFT normalization factor, $L \times Fs$, where L is

the length of data in seconds and Fs is the sampling frequency. Additional details can be found in[132,299,300,96,92]

We write the total signal-to-noise ratio for a cluster of pixels as a sum over $\rho(t; f|\hat{\Omega})$:

$$\mathrm{SNR}_{\mathrm{tot}}(\Gamma) \equiv \frac{1}{N^{1/2}} \sum_{\{t;f\}\in\Gamma} \rho(t; f|\hat{\Omega}), \tag{6.2}$$

where N is the number of pixels in Γ, which is chosen from a bank of parametrized frequency-time tracks, and each track is referred to as a *template*.

To modify the above algorithm to perform an all-sky search[300,96,92], we use complex signal-to-noise ratio:

$$\mathfrak{p}(t; f) = \frac{2\sqrt{2}}{\mathcal{N}} \left[\frac{\tilde{s}_I^*(t; f)\tilde{s}_J(t; f)}{\sqrt{P_I'(t; f)P_J'(t; f)}} \right]. \tag{6.3}$$

This statistic preserves the complex phase information, which encodes the direction of the source. As a proxy for the sky location, which is unknown, we add an additional variable $\Delta\tau$ which corresponds to the time delay between the detectors[300]. Therefore, we rewrite Eq. 6.2 as

$$\mathrm{SNR}_{\mathrm{tot}}(\Gamma) \equiv \frac{1}{N^{1/2}} \sum_{\{t;f\}\in\Gamma} \mathrm{Re}\left[e^{2\pi i f \Delta\tau} \mathfrak{p}(t; f) \right], \tag{6.4}$$

and this sum is carried out for many randomly selected clusters Γ. We finally define $\mathrm{Max}[\mathrm{SNR}_{\mathrm{tot}}]$ as the maximum of $\mathrm{SNR}_{\mathrm{tot}}$ taken over all Γ.

6.1.1 Parameterizations

In any seedless clustering algorithm, Γ is chosen such that it is sensitive to the morphology of the gravitational waves being searched for. There are two types we will

consider in this paper, although the method is generic enough to work for any parameterization.

Bézier curves. For generic narrow-band long transient gravitational waves[299,300], Γ is chosen randomly from the set of quadratic Bézier curves[139] subject to the constraint that the curve persists for a duration $t_{\rm min}$. Three time-frequency control points determine the template: P_0 $(t_{\rm start}, f_{\rm start})$, P_1 $(t_{\rm mid}, f_{\rm mid})$, and P_2 $(t_{\rm end}, f_{\rm end})$, and the curve is parameterized by $\xi = [0, 1]$:

$$\begin{pmatrix} t(\xi) \\ f(\xi) \end{pmatrix} = (1-\xi)^2 P_0 + 2(1-\xi)\xi P_1 + \xi^2 P_2. \tag{6.5}$$

These arrays allow the sum in Eq. 6.2 to be computed for a large number of templates in parallel. For practical applications, the number of templates T is typically chosen to be $T = \mathcal{O}(10^4 - 10^8)$. To perform a computationally feasible all-sky analysis, $T = 2 \times 10^4$ templates are feasible, and we use this number in the analysis that follows.

Post-Newtonian templates for compact binary coalescences. Another parameterization for Γ currently in the literature creates templates based on a post-Newtonian model for chirp-like signals created by circular compact binary coalescences[96]. For searches for compact binary coalescences with seedless clustering, we can use a more specialized template bank consisting of parametrized chirps:

$$f(t) = \frac{1}{2\pi} \frac{c^3}{4GM_{\rm total}} \sum_{k=0}^{7} p_k \tau^{-(3+k)/8}, \tag{6.6}$$

where

$$\tau = \frac{\eta c^3 (t_c - t)}{5GM_{\rm total}}, \tag{6.7}$$

where the expansion coefficients p_k can be found in[57], G is the gravitational constant and M_{total} is the total mass of the binary. These templates are parameterized by the coalescence time and the chirp mass. It was shown in[96] that while the waveform depends on the individual component masses, the main features of the signal can be well-approximated by only the chirp mass, and we can approximate that the individual component masses are equal. This has similarities to the matched-filtering template banks used in compact binary searches[125,126]. The key difference is that to first-order, chirp mass is the only term that contributes to the time-frequency evolution, and therefore the template bank is only one-dimensional. Combined with the fact that this method is only sensitive to the pixelated frequency evolution of the gravitational wave (instead of the phase), the templates used in this analysis are significantly coarser than that in traditional searches.

6.1.2 Semi-analytical approximation

We now describe a semi-analytical approximation to the background of our seedless clustering algorithms. Seedless clustering, which computes the sum of pixels in a track, divided by the square root of the number of pixels in the track, lends itself to modeling due to its simplicity. By the central limit theorem, the sum of a sufficiently large number of independent random variables, each with a well-defined expected value and well-defined variance, will be approximately normally distributed. Therefore, we expect that the sum of many pixels will approach a normal distribution, given by

$$P(z)dz = \frac{1}{\sigma\sqrt{2\pi}} e^{-(z-\mu)^2/2\sigma^2} dz \tag{6.8}$$

Because seedless clustering measures the maximum SNR_{tot} of many tracks, here

we seek the extreme value distribution for $\mathrm{SNR}_{\mathrm{tot}}$. This is motivated by the desire for a distribution with which to compare those measured from an analysis using the algorithm. We can analytically compute a probability distribution for this maximum value as follows. Given a random sample of $\mathrm{SNR}_{\mathrm{tot}}$ drawn from many maps, $(X_1, ..., X_N)$, from a continuous distribution with a probability density function $f(x)$ and cumulative density function $F(x)$, the cumulative density function of the maximum of $\mathrm{SNR}_{\mathrm{tot}}$ is then given by

$$\begin{aligned} \mathrm{CDF}_{\mathrm{Max[SNR_{tot}]}}(z) &= P(\max(X_i) < z) \\ = P(X_1 < z, ..., X_N < z) &= P(X_1 < z)...P(X_N < z) \end{aligned} \tag{6.9}$$

where the third equality assumes that the random samples are independent. In some cases where the random samples are not independent but the correlated distributions are conservative, as in some of our analyses below, an upper-bound can instead be derived

$$\begin{aligned} \mathrm{CDF}_{\mathrm{Max[SNR_{tot}]}}(z) &= P(X_1 < z, ..., X_N < z) \\ &\leq P(X_1 < z)...P(X_N < z). \end{aligned} \tag{6.10}$$

We will discuss the effect of this assumption in section 6.3. In the case where the probability density functions are identical, the equation becomes

$$\mathrm{CDF}_{\mathrm{Max[SNR_{tot}]}}(z) = [P(X < z)]^N = [F_X(z)]^N. \tag{6.11}$$

We show below that we can use this equation, where the CDFs are given by Gaussian CDFs, to approximate the seedless clustering distributions. Even though in our case

$F_X(z)$ is derived from a Gaussian distribution, equation 6.9 is true for any general distribution represented by $F_X(z)$. Hence in cases where the analytic expression for $F_X(z)$ is difficult to derive or approximate, one can use the observed distribution.

6.2 Background Study

We can test the approximations by performing the analysis on Monte Carlo Gaussian noise and initial LIGO noise from the Hanford, WA (H1) and Livingston, LA (L1) detectors. We create complex signal-to-noise ratio spectrograms $\mathfrak{p}(t; f)$ using Eq. 6.3 and analyze each with the various seedless clustering algorithms. Following[299,300], we create 250 s maps in a band between 100–250 Hz with spectrogram resolution of $1\,\mathrm{s} \times 1\,\mathrm{Hz}$ using 50%-overlapping Hann windows. The results for each are as follows.

6.2.1 Bézier parameterization

We begin by analyzing the performance of the analytic model on the Bézier parameterization.

We run the seedless clustering algorithm over hundreds of these maps and save $\mathrm{SNR}_{\mathrm{tot}}$ for each of the tracks in the map. The left of Figure 6.1 shows a histogram of the resulting $\mathrm{SNR}_{\mathrm{tot}}$ distribution for both the Monte Carlo and initial LIGO data. We fit Eq. 6.8 to the resulting distributions. We find best fits of $\mu = 0.0007$ and $\sigma = 0.99$. The fact that the distribution has approximately a mean of zero and a standard deviation of one is expected based on the fact that ρ has a mean of 0 and we use the $\sqrt{N}$ normalization in the $\mathrm{SNR}_{\mathrm{tot}}$ calculation. We find that the agreement is reasonable out to the tails of the distribution. The right of Figure 6.1 shows the standard deviation of the distribution as a function of track length. The standard deviation differs on the

order of a few percent across the track lengths considered. For the sake of simplicity, we assume that the distribution is approximately independent of track length.

We now simulate an all-sky search by performing 100 time-slides in a week of data. The data are processed with a glitch identification cut[246] as if it were a real analysis. In order to apply the algorithm from[246], we assume that the source is optimally oriented with an optimal sky position. To compare this to the analytic approximation in equation 6.11, we use the Gaussian fit shown in Figure 6.1 to approximate the $\mathrm{SNR}_{\mathrm{tot}}$ distribution. The steps required to turn the $\mathrm{SNR}_{\mathrm{tot}}$ distribution into a p-value vs. SNR distribution are as follows. To generate a $\mathrm{SNR}_{\mathrm{tot}}$ value for a single simulated *map*, we generate N random numbers consistent with the Gaussian distribution of mean and variance as estimated above. We then take the maximum value of these values to compute the $\mathrm{Max}[\mathrm{SNR}_{\mathrm{tot}}]$. To generate a p-value vs. SNR distribution, $\mathrm{Max}[\mathrm{SNR}_{\mathrm{tot}}]$ is generated for M instances of spectrograms, where 1/M is the smallest p-value required. $\mathrm{Max}[\mathrm{SNR}_{\mathrm{tot}}]$ is placed in ascending order. The p-value is calculated as an array between 1/M and 1 with spacing given by 1/M. For a Gaussian distribution where the mean and standard deviation are the same across all trials, this process can also be performed analytically by simply computing equation 6.11 for the measured distribution.

We perform two search simulations using the Bézier parameterization. The first uses Bézier templates computed for a specific search direction. The second loops over time-delays for each template. By searching over 40 different time-delays, corresponding to 40 different sky rings, a computationally efficient all-sky search can be performed. This was demonstrated in[96] to be sufficient to recover signals in arbitrary directions. The top left of Figure 6.2 demonstrates the analysis for the first simulation using 20,000 tracks, showing both empirical time-slides as well as the theoretical ap-

proximation method explained as before (both the 10th, 50th, and 90th percentiles). We find excellent agreement between the analytic model and empirical time-slides for the directed search. The distributions for the all-sky search, on the top right of Figure 6.2, however, are not generally within $1\,\sigma$. We explore systematic errors related to this in the next section. Finally, we show the Max[$\mathrm{SNR_{tot}}$] required for a 5-sigma gravitational-wave detection using the Bézier parameterization in Figure 6.3.

6.2.2 Compact binary coalescence parameterization

We now analyze the performance of the analytical model on the chirp templates. We create maps assuming Gaussian noise consistent with the design sensitivity of Advanced LIGO. Following[96], we create 660 s maps in a band between 10–150 Hz with a spectrogram resolution of $1\,\mathrm{s} \times 1\,\mathrm{Hz}$.

We perform a similar analysis to the above. We find best fits for the Gaussian distribution of $\mu = -0.004$ and $\sigma = 1.06$. The major difference between the Bézier and chirp-like template analysis is the degree of correlations between the drawn tracks. In the Bézier case, the tracks are drawn randomly and the degree of correlation is simply determined by the overlap between the tracks. In the chirp-like template case, the degree of correlation is much higher, despite the significantly fewer templates used in the analysis. This correlation arises from the step in time and overlap in parameter space between chirp-like templates of similar chirp mass. This correlation is important because it changes the standard deviation of the $\mathrm{SNR_{tot}}$ of the tracks in individual maps and therefore the final distribution of Max[$\mathrm{SNR_{tot}}$]. Figure 6.3 demonstrates the cumulative density function of the standard deviation of the $\mathrm{SNR_{tot}}$ for the two parameterizations. In the Bézier case, the standard deviation of $\mathrm{SNR_{tot}}$ is approximately a step function, which allows for the use of a single standard deviation to

cover all cases. The distribution is significantly broader for chirp-like templates due to track correlations. It is for this reason that we modify the Bézier p-value algorithm by drawing from the measured distribution of standard deviations of the maps when drawing from the Gaussian distribution. The bottom of Figure 6.2 demonstrates the algorithm using both empirical Monte carlo noise as well as the theoretical approximation method explained as before (both the 10th, 50th, and 90th percentiles) for both a directed and all-sky search. Similar to the Bézier case, we find excellent agreement between the analytic model and empirical time-slides for the directed search, while the distributions for the all-sky searches, however, are not generally within $1\,\sigma$. We explore systematic errors related to this in the next section. We show the $\mathrm{Max}[\mathrm{SNR}_{\mathrm{tot}}]$ required for a 5-sigma gravitational-wave detection using the chirp-like parameterization in Figure 6.3.

6.3 Uncertainties: Statistical and systematic

We now explore the systematic and statistical errors in our measurement. The measurement of the statistical errors in this analysis is straight-forward. Each simulation is computationally cheap, as it involves generation and manipulation of matrices of random numbers, and therefore can be performed over and over again to generate distributions. This was done in order to generate the 1σ distributions in Figure 6.2, for example.

Of more interest, perhaps, is consideration of the systematic errors in the method. There are a number of reasons we might expect small disagreements between the theoretical model and the empirical results. A major source of systematic error is in the rotation of pixels in the all-sky searches, where time-delays are looped over. This

involves a rotation in the complex plane of the individual pixels that make up the tracks. This creates difficulty for the analytic analysis. Because the analysis amounts to a rotation, the 40 time-delays do not correspond to 40 independent trials (which would simply multiply the number of tracks by 40). In the analysis above, we simply multiplied the number of tracks by 40, corresponding to the 40 time-delays in the analysis. In the left of Figure 6.4, we explore this effect by simulating tracks without any rotation (the directional case) and with 40 rotations (the all-sky case), and compare this to the distribution of 40 random tracks. We show that using 40 random tracks is conservative relative to using the 40 time-delays case. This indicates that multiplying the number of trials by 40, as is done in the analysis, is conservative. In this case, using equation 6.10, which places an upper-bound on the distribution is more accurate than equation 6.9, which assumes that the trials are independent.

One possibility to do even better is to actually measure the covariances between the rotated pixels. This situation is similar to[11]. In this work, the authors place limits on gravitational-wave strain from different portions of the sky. This was difficult because the distribution of maximum SNR for a sky map contains non-zero covariances that exist between different pixels (or patches) on the sky. They simulate the covariance between pixels numerically, by simulating many realizations that have expected covariances described by the Fisher matrix. In this case, we could numerically compute a covariance matrix, which we can diagonalize to create a basis of non-covariant variables. Then, one would generate random realizations of these non-covariant variables and use the covariance matrix to convert them into a set of randomly generated covariant variables. One difficulty is that the distribution of the non-covariant variables might not be the same as the covariant variables. With this method, we could determine the set of covariant variables which describe the distribu-

tion of $\mathrm{SNR}_{\mathrm{tot}}$.

Another potential systematic error arises from the use of equation 6.9, in particular the assumption that the trials are independent. One way in which this manifests is that real detectors have noise transients and non-stationary noise, which violate some of the approximations used here. Severe non-Gaussianity which eludes both the pixel thresholds and the Gaussianity cuts applied in the analysis would show up not only potentially as a loud background trigger, but would increase the correlation between tracks (as any track that passes through those pixels would have an increased $\mathrm{SNR}_{\mathrm{tot}}$). Generating purely random numbers to approximate $\mathrm{SNR}_{\mathrm{tot}}$ is an approximation. This is because the tracks are analyzed on the same map, and therefore overlapping tracks will have correlated $\mathrm{SNR}_{\mathrm{tot}}$ values. This has the effect in the analysis of changing the effective σ from map to map. One potential conservative solution would be to measure the σ in each map and then generate $\mathrm{Max}[\mathrm{SNR}_{\mathrm{tot}}]$ distributions using that value. Another implicit assumption is that the pixels in the tracks are uncorrelated. This assumes that the noise is Gaussian and stationary and ignores the correlation between pixels in the maps. However, the cross-power statistic uses PSD's from adjacent pixels (in the time direction) to estimate σ (from Eq. (6.2)). This is to avoid a bias in pixel SNR for an isolated loud pixel. This means there is a correlation between adjacent pixels. In the right of Figure 6.4, we explore this effect by computing the overlaps between the templates used in the compact binary search. Due to the need for maximal coverage of the parameter space, there is significant overlap between templates. The use of equation 6.9 biases the analysis in this case. Computations such as this could be used to modify equation 6.9 to account for the lack of independence between templates by determining the number of *effective trials* from the data.

6.4 Conclusions and Future Work

In previous work, we showed how a seedless clustering algorithm could significantly improve the sensitivity of searches for long-lived, unmodeled gravitational-wave transients[299,300,96,92]. Here, we show how the simplicity of the search statistic allows for the development of a semi-analytic approximation to the background generated by the algorithm and compared the performance using a week of LIGO S5 time-shifted data. We described algorithmic subtleties not addressed by this model and quantify the errors between the model and the measured distribution. We argued that it will be useful for pipeline characterization, as well as potentially for low-latency FAP reporting for gravitational-wave searches.

In the future, we will move beyond the simple models presented here to more complicated models. Some examples could be using non-Gaussian distributions, such as the Student-t distribution, to better approximate the tails of the distribution, which is where we expect the strongest disagreement[257]. Other ideas include using the Edgeworth expansion to put bounds on the deviation from Gaussianity. As the tracks in individual maps are correlated (due to the fact that some will overlap and use the same pixels), we could also consider generating correlated random values when generating our distributions for $\mathrm{SNR}_{\mathrm{tot}}$.

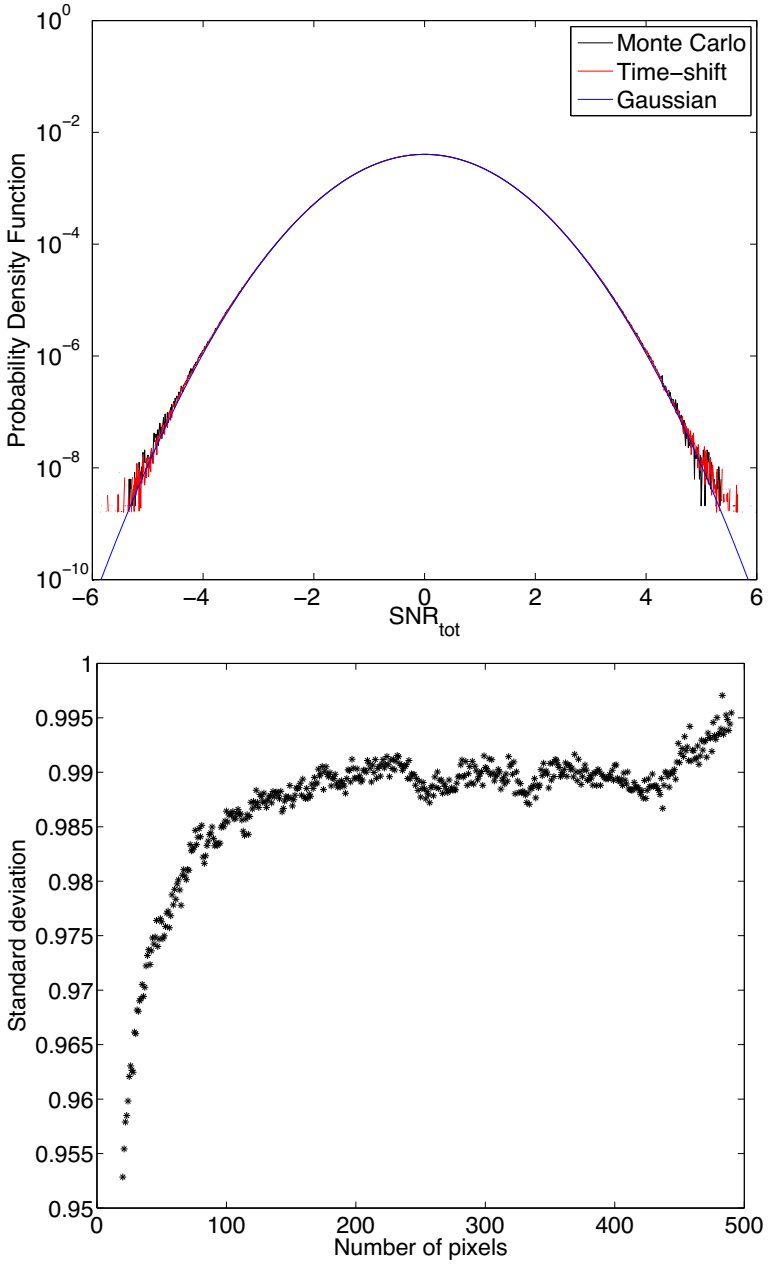


Figure 6.1: The plot on the left is the background distribution for the seedless clustering algorithm cluster SNR defined in equation 6.4. Monte Carlo denotes Gaussian colored noise. Time-shift denotes real time-shifted data with vetoes to limit the effects of instrumental artifacts. The theoretical line corresponds to the Gaussian approximation to the distribution given by Eq. 6.8. The plot on the right is the standard deviation of $\mathrm{SNR}_{\mathrm{tot}}$ as a function of track length. The standard deviation differs on the order of a few percent across the track lengths considered. In our analysis, we approximate the standard deviation of $\mathrm{SNR}_{\mathrm{tot}}$ across track length as constant.

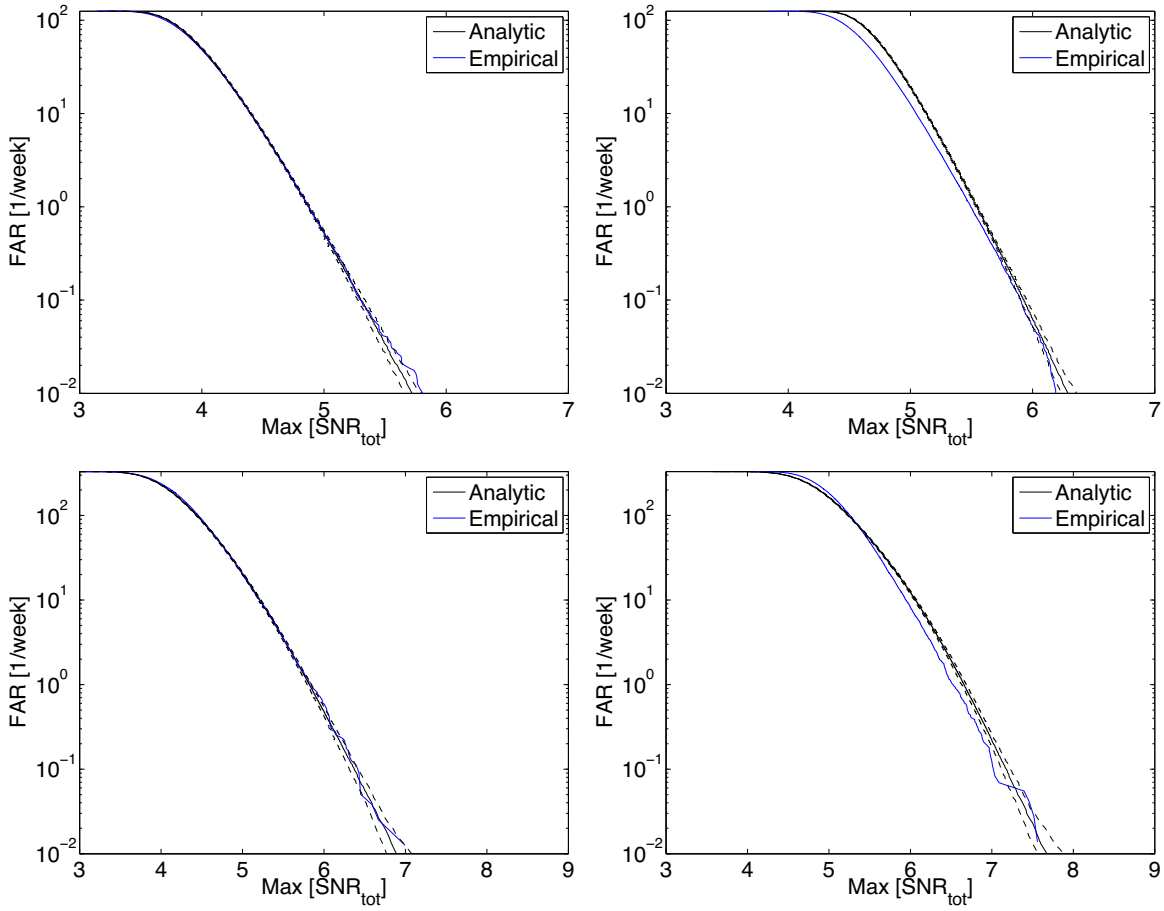


Figure 6.2: Background distributions computed for the seedless clustering algorithm using both Bézier and chirp-like templates. The distributions are generated from time-shifted initial LIGO data. The top row corresponds to the Bézier templates and the bottom row chirp-like templates. The left column corresponds to a directed search (in a specific sky direction) and the right to an all-sky search performed looping over 40 time-delays for each template. The theoretical line corresponds to using Gaussian distributions with standard deviations presented in Figure 6.3. The dotted lines correspond to $1\,\sigma$ error bars on the analytic approximation. These are derived from simulating the p-value vs. SNR distribution using many random seeds, in essence creating thousands of p-value vs. SNR distributions consistent with the measured distributions, and computing the median and $1\,\sigma$ error bar for each p-value. The analytical background distributions for the directed searches are consistent with the measured background (within $1\,\sigma$). The distributions for the all-sky searches, however, are not generally within $1\,\sigma$. This is due to the assumption in the analytic-model that the loop over time-delays creates more independent trials, which is not the case and biases the result (please see the text for more details).

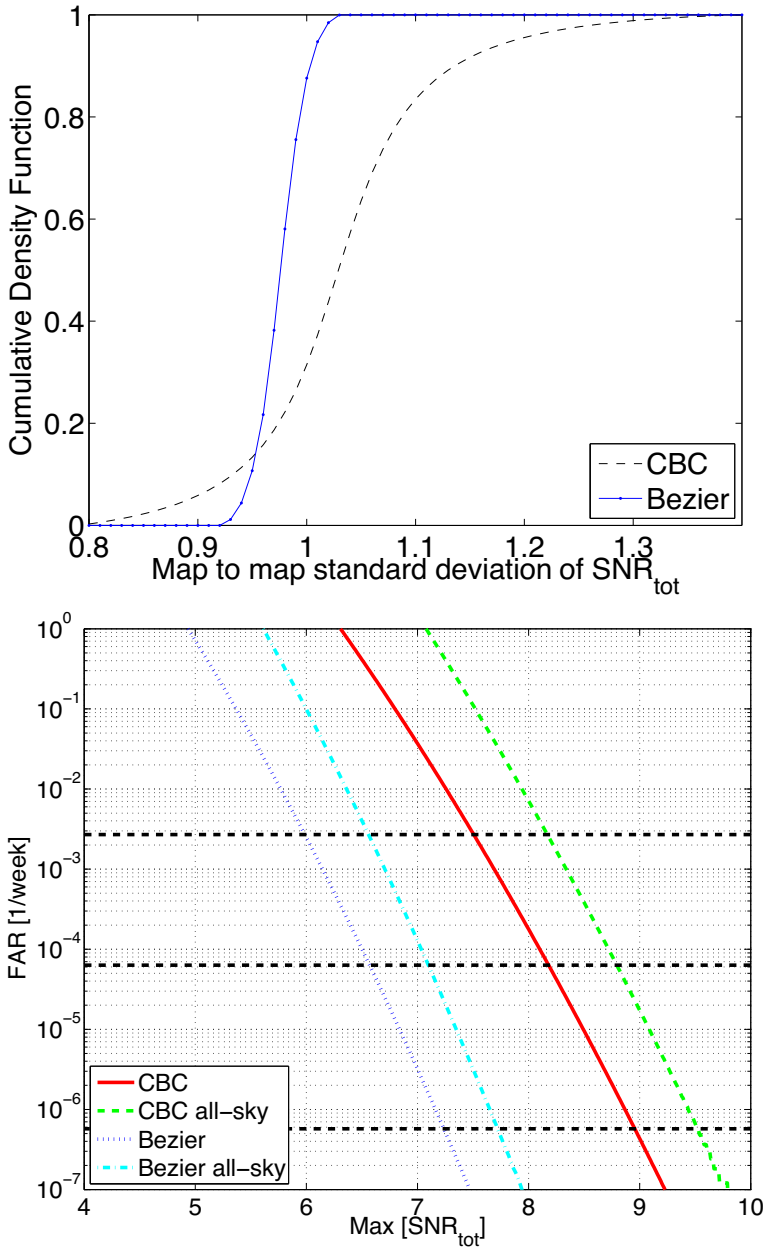


Figure 6.3: The plot on the left is the cumulative density function of the standard deviation of the $\mathrm{SNR_{tot}}$ for the two parameterizations. Distribution is significantly broader for chirp-like templates due to track correlations. The plot on the right is the background distribution using the analytic approximation for the cases considered here. It shows the $\mathrm{Max[SNR_{tot}]}$ required for a 3σ, 4σ, and 5σ gravitational-wave detection using seedless clustering in dotted horizontal lines. The four different lines corresponds to the four-different seedless analysis types considered in this paper (a directed and all-sky Bézier template search and a directed and all-sky compact binary search), which each have significantly different distributions of $\mathrm{Max[SNR_{tot}]}$.

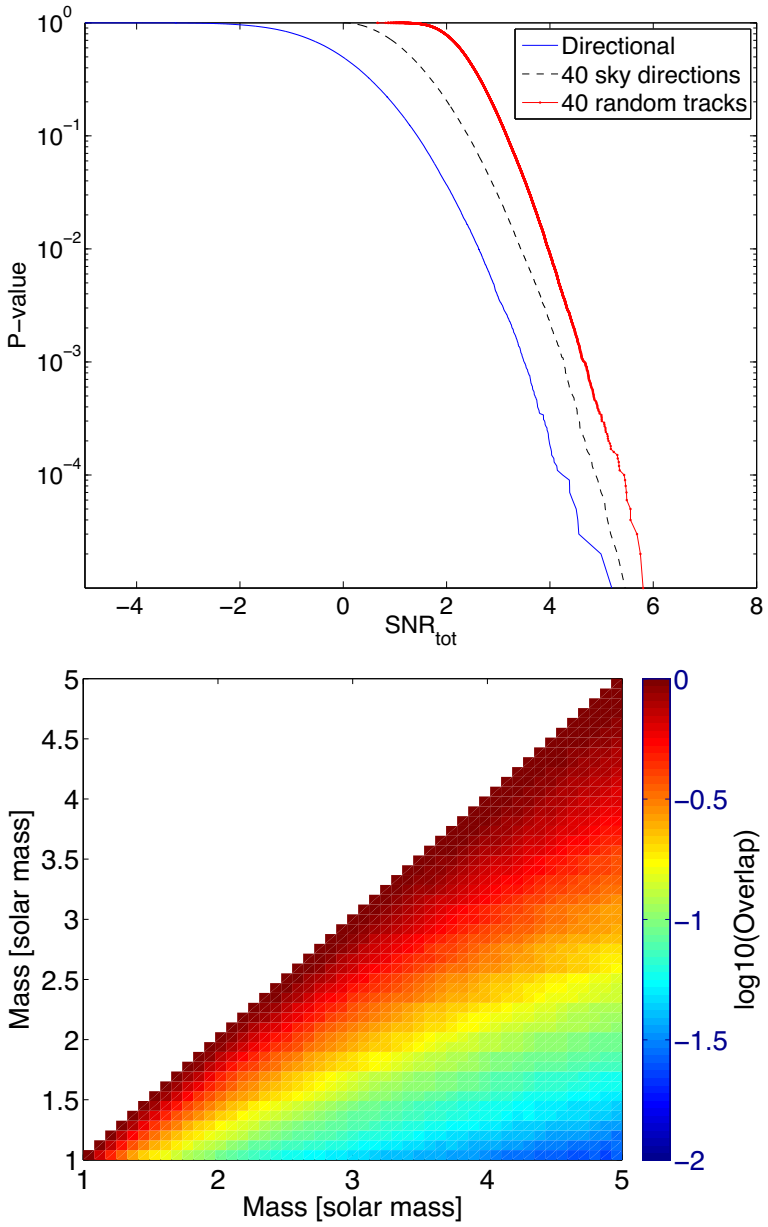


Figure 6.4: The plot on the left is the p-value vs. $\mathrm{SNR}_{\mathrm{tot}}$ distribution for three different cases (for a single map): a directional search, a search looping over 40 sky-directions, and a search using 40 different tracks. As is expected, a search searching over 40 sky-directions results in higher background values for $\mathrm{SNR}_{\mathrm{tot}}$ than the directional case. Similarly, a search using 40 different tracks is conservative relative to the 40 sky-direction case, indicating that it is appropriate to consider such a method conservative. The plot on the right is the overlap between the templates used in the compact binary search algorithm. In general, there is significant overlap between templates, which biases the computation of the theoretical $\mathrm{SNR}_{\mathrm{tot}}$ distribution.

It's a very strange silence that I'm living in right now. It's a silence that has a lot of activity and noise in it from a zone that I don't live in on this earth.

Gary Busey

7

Wiener filtering with a seismic underground array at the Sanford Underground Research Facility

In the next few years, a second generation of laser-interferometric gravitational-wave (GW) detectors will start operating with the goal to directly observe GWs. At high frequencies, sources of GWs include core collapse supernovae[233,211] or the merger of neutron stars and black holes[8]. At low frequencies, a stochastic background of GWs, most likely from cosmological origin, is possible[17]. The global network of detectors

will consist of the two Advanced LIGO[161] interferometers in Louisiana and Washington state, US, the Advanced Virgo[25] interferometer near Pisa, Italy, GEO-HF in Hannover, Germany[213], the KAGRA interferometer at the Kamioka mine in Japan[42], and the IndIGO detector in India[305]. Gravitational waves, which will hopefully be observed by these detectors, produce changes in distance between test masses smaller than 10^{-20} m over kilometer distance scales. Isolating test masses in gravitational-wave detectors from seismic disturbances is one of the foremost challenges of the instrumental design of the detectors. Second-generation detectors will use sophisticated seismic-isolation systems to make possible the detection of GWs above 10 Hz. For this purpose, the isolation systems consist of chains of coupled springs and pendulums with lowest resonance frequencies around 1 Hz so that seismic noise well above these frequencies is suppressed by many orders of magnitude in all rotational and translational degrees of freedom. The goal of third-generation detectors, such as the Einstein Telescope[249], will be to extend the detection band to even lower frequencies. This poses an even greater challenge to the design of the isolation system.

The mechanical, or passive, component of the isolation system is assisted by a complex network of sensors and actuators forming the so-called active seismic isolation[21]. Sensor data recorded on some of the mechanical stages of the passive system are used to calculate a feedback force acting on the mechanical stage to suppress seismic disturbances. Another variant of the active isolation scheme is the feed-forward noise cancellation[147,114,112]. For example, data from a seismic sensor deployed directly on the ground close to a test mass can be used to cancel seismic noise further down the isolation chain, provided that there is correlation between motion of the ground and of some part of the isolation system. Feed-forward noise cancellation has also been implemented as part of the interferometer control using light sensors[195].

Seismic disturbances can also affect GW detector test-mass motion via gravitational coupling circumventing the entire seismic isolation system[262,172,99]. The change in mass density in the rock nearby the detector leads to changes in the local gravitational field, which introduces a force on the test-masses. This so-called Newtonian noise (NN) has never been observed, but it is predicted to be one of the limiting noise sources in second-generation detectors at frequencies between 10 Hz and 20 Hz, and for third-generation detectors, such as the Einstein Telescope, down to their lowest frequencies at 2 Hz. As it is impossible to shield a test mass from NN, another method needs to be found to suppress it. One possibility, at least for future detectors, is to select a site characterized by very low levels of seismic noise[52,157]. The construction of underground detectors has been proposed for this purpose[249]. However, this option is costly, and does not apply to any of the existing surface sites of the LIGO and Virgo detectors. Another idea is to attempt a feed-forward noise cancellation using auxiliary sensors[67]. For example, gravity perturbations caused by seismic fields can be estimated in real time using data from an array of seismic sensors[115].

There are also concepts for a number of future low-frequency GW detectors, called MANGO[160], with sensitivity goals better than $10^{-19}/\sqrt{\text{Hz}}$ in the 0.1 Hz to 10 Hz band. One class of possible detectors includes atom interferometers, which contain a source of ultracold atoms in free fall that interact multiple times with a laser. Another example is a torsion-bar antenna, which uses tidal-force fluctuations caused by GWs which are observed as differential rotations between two orthogonal bars, independently suspended as torsion pendulums[36,273]. A final possibility is using the existing Michelson interferometer detector design optimized to low frequencies. One of the main noise sources in this frequency band will be the NN from seismic surface fields. The study presented in this paper of coherent seismic-noise cancellation in the

frequency range 0.05 – 1 Hz is a first step to investigate the feasibility of a seismic NN cancellation in the same band. It is therefore directly relevant to maximizing the sensitivity of MANGO detectors.

There are a number of important GW signal sources in the MANGO GW detector band. Compact binaries in their inspiral and merger phase are strong possibilities[160]. Intermediate mass black hole binaries can merge in this band[7]. Galactic white dwarf binaries would likely be detectable[160]. Other sources include helioseismic and other pulsation modes[104]. Although interesting in their own right, these would be a foreground for the potential detection of primordial GWs. GWs were recently possibly detected in the B-mode polarization of the CMB background, which would provide confirmation of the theory of inflation[27]. Assuming a slow roll inflationary model, this signal would correspond to a GW energy density spectrum $\Omega_{\rm GW} \approx 10^{-15}$ in the 0.1 Hz to 1 Hz band. Because $\Omega_{\rm GW}(f) \sim S_{\rm GW}(f) f^3$, where $S_{\rm GW}(f)$ is the detector power spectral density, a detector with strain sensitivity of $\sqrt{S_{\rm GW}} \approx 10^{-23}/\sqrt{\rm Hz}$ in this band might have sufficient sensitivity to detect the inflationary signal. Furthermore, due to the relatively limited astrophysically produced foregrounds, this band appears the most promising for a direct detection of the inflationary signal.

Newtonian noise directly contributes to the noise of a gravitational-wave interferometer by introducing gravitational forces on the test masses. One of the dominant contributions to Newtonian noise is seismic Newtonian noise. In the following, we will generically refer to seismic Newtonian noise as Newtonian noise. There are two dominant contributions to Newtonian noise: the change in the surface-air boundary caused by seismic waves, and change in the rock densities also caused by seismic waves. There is a linear relationship between the amplitude of seismic waves and Newtonian noise, and thus identification and subtraction of seismic noise in an array

of seismometers is useful for potential Newtonian noise subtraction in gravitational-wave interferometers. In the study that follows, we will use an array of seismic sensors to subtract seismic noise from a target seismic sensor, which imitates the time-series of a test mass in a gravitational-wave interferometer.

Therefore, there is significant motivation for exploring techniques which would maximize the sensitivity of detectors in this low-frequency band, and this is the major focus of this paper. For stationary, linear systems, the optimal filter used for a feed-forward noise cancellation is the Wiener filter[309]. It is calculated from correlations between data of the auxiliary sensors and data observed at the target point where noise is to be suppressed. The parameters of the optimal linear filter under ideal conditions are fully determined by the data correlations and the frequency range over which noise cancellation is to be achieved. In reality though, as will be shown in the following, filter parameters can be further optimized to account for non-stationary properties of the data and variations of the dynamics of the system; one possible example is temperature drift. With respect to slow changes in noise variance or system dynamics, one can simply update the Wiener filter regularly using the latest observed data or implement an adaptive filter technology[263]. However, as will be shown in this paper, in the presence of non-stationary seismic noise, improvement can also be achieved by optimizing the number of filter coefficients.

Wiener filtering with seismic arrays has been performed in the past to improve signal-to-noise ratios towards weak seismic signals[312]. In this paper, we present results from a study of feed-forward noise cancellation by means of Wiener filters calculated from correlations between seismometers of an underground array. The sensors are broadband instruments sensitive to seismic noise between about 10 mHz and 50 Hz. The array is located at the Sanford Underground Research Facility in the

Black Hills of South Dakota[157]. The facility has 8 environmentally shielded and isolated stations at 4 different depths. The seismometers are installed on granite tiles placed on concrete platforms connected to the bedrock. They are surrounded by a multi-layer isolation frame of rigid thermal and acoustic insulation panels to further stabilize the thermal environment and to achieve suppression of acoustical signals and air currents. These seismometers have been characterized using huddle tests, and they have been shown to have the same noise floor. Three stations with good data quality were active during this study using data from February and March 2012: one at 800 ft depth, one at 2000 ft, and one at 4100 ft. Whereas the challenge of seismic Newtonian-noise subtraction cannot be fully represented by our study, it is explained that some key aspects such as stationarity of the noise, and scattering of seismic waves should affect both, Newtonian and seismic-noise subtraction, in similar ways. Therefore, the results of our study allow us to draw certain conclusions for Newtonian-noise subtraction.

In our analysis, the Wiener filters are realized as finite-impulse response (FIR) filters. The two main parameters investigated here are the rate at which the filters are updated, and the number of filter coefficients. A brief summary on data quality issues in GW detectors in general, and specifically of the seismic data used in this study is given in section 7.1. In section 7.2, the Wiener filtering method used in this work is described. The results are given in section 7.3, and our conclusions are summarized in section 7.4.

7.1 Data Quality

Despite the fact that the optical system is constructed in vacuum, and the test masses are suspended from seismically isolated platforms, detectors are susceptible to a variety of instrumental and environmental noise sources that decrease their detection sensitivity[70,176]. Short in duration, non-astrophysical transient events or *glitches* can mask or mimic real signals. Environmental noise can couple into the interferometer through mechanical vibration or because of magnetic fields which can produce forces on magnets in the suspension systems. Seismic motion from wind, ocean waves, or human activity near the sites are among the most common sources of these disturbances. It is important for filtering methods to be robust against such artifacts, as blindly applying a filter with inputs affected by transients could introduce noise into the target channel. Meadors et al.[218] successfully applied a subtraction algorithm, based on Allen, Hua, and Ottewill's frequency domain transfer function fitting[32] to data from LIGO's S6 science run to increase strain sensitivity. To overcome the transients issue, they only applied the algorithm when the subtraction improved the sensitivity.

In this paper, the reference and target data will come from seismometers of an underground array. Below 1 Hz, the seismic spectrum is dominated by the primary and secondary microseismic peaks. Far from the ocean, microseisms appear with approximately the same amplitude both at the surface and below ground. These occur between 30 – 100 mHz, and 0.1 – 0.5 Hz respectively. This is the main source of coherent noise we seek to subtract. A potential local source of low-frequency seismic disturbances is wind. However, a previous study indicated that at stations at depths of 800 ft or more, correlation between seismicity and wind speeds is insignificant (while

the effect was found to be significant at 300 ft)[157], implying a relatively short correlation length of the respective seismic disturbance. The strongest sources of low-frequency noise are earthquakes. The closest or highest magnitude events can also significantly contribute to seismic motion above 1 Hz. Above 1 Hz, previous work identified the Homestake mine as a world-class low-noise environment[157].

Table 7.1 shows the locations of the seismometers used for our study at the 800 ft, 2000 ft-B, and 4100 ft-A stations. The horizontal distances between them are 800 ft/2000 ft-B = 295 m, 800 ft/4100 ft-A = 517 m, and 2000 ft-B/4100 ft-A = 790 m, and the total distances are 800 ft/2000 ft-B = 503 m, 800 ft/4100 ft-A = 1236 m, and 2000 ft-B/4100 ft-A = 1065 m. The horizontal distances are relevant to estimate coherence from seismic surface fields between stations, whereas the total distances are relevant to estimate coherence from body-wave fields. Whereas the 800 ft and 2000 ft-B seismometers provided high-quality data with coherence consistent with the specified instrumental-noise floor of the instruments, 4100 ft-A showed problems with the data-acquisition system. A frequency comb with 0.5 Hz spacing was visible in the spectra pointing to a coupling between the timing and readout electronics. Nevertheless, the 4100 ft-A data were used for this study since the effect on the sub 0.5 Hz spectrum was a modest increase in the noise floor. It should be emphasized that this excess

Station	Seismometer	Position (E,N) (m)
800 ft	T240	(-88,124)
2000 ft-B	T240	(-234,380)
4100 ft-A	STS-2	(347,-155)

Table 7.1: Table detailing station information, including station names, type of seismometer, and position relative to Yates shaft of the former Homestake mine. For more details on the mine and available stations, please see[157]. T240 stands for Nanometrics Trillium 240 Broadband Sensor, and STS-2 stands for Streckeisen STS-2 Broadband Sensor.

noise cannot be attributed to the seismometer itself since previous self-noise measurements yielded similar noise levels for all instruments.

Horizontal and vertical channels have very similar spectra at underground sites of the Sanford Underground Laboratory[157]. Nevertheless, in the following, the study of Wiener filters and feed-forward noise cancellation will only make use of the vertical seismic channels. Vertical seismic displacement is what produces the by far strongest contribution to NN in MANGO type detectors[160]. Horizontal channels are more relevant to seismic isolation in this frequency band, and the additional challenge of using horizontal channels would be to disentangle tilt motion from true horizontal motion, which makes it difficult to compare measured coherence and Wiener-filter performance with theoretical models. In the future, use of a tiltmeter along with the seismometers could be used to disentangle the effect[111].

7.2 Wiener Filtering

When creating a feed-forward filter to subtract seismically induced noise in GW detectors, the target point can either be located within the seismic isolation chain monitored by a seismic sensor, or perhaps more importantly, it can be the test mass or other optics whose positions are read out interferometrically. The reference sensors used as filter inputs typically include seismometers surrounding the respective optics[114,115]. Therefore, while the first use of these filters has been to supplement the performance of active seismic attenuation, in the more important application of Wiener filtering to GW detectors, the seismometers on site can be used to subtract noise from the detector output. Since there are in general several input sensors and one target point, which is the differential motion between two mirrors, the filter configuration is

also known as multiple-input, single output (MISO). The goal is to design a MISO filter that combines the data from all seismometers to produce an optimal estimate of the motion of the target point. This allows removal of seismic noise coupled to the detector data, including NN, without a priori assumptions about the modal content and directionality of the seismic waves. Instead, the filter is derived solely from the input and output data via the filter optimization process.

The type of MISO filter produced depends on the type of noise. If the noise is modelled as a statistically stationary process (one whose parameters are constant in time), the optimal filter is constant in time. Then, the filter is only created once and thereafter can be applied to the data continuously. These types of filters satisfy the Wiener-Hopf equations and are known as *Wiener filters*[309]. The simplest kind of Wiener filter to implement is a causal FIR Wiener filter, which is characterized by a vector of real numbers that represent an impulse response. This vector is convolved with the input signal in the time domain to obtain the optimal estimate of the noise.

The basic principle of Wiener filters is to use the output of a number of reference traces to predict the noise of a target channel. This prediction is then subtracted from the target channel, leaving the non-correlated residual. While using Wiener filters to supplement seismic attenuation must be done in real time, NN noise removal from the detector output can be done later, which potentially allows for filter optimization. Given the input time series $\vec{x}(k) = (x_m(k))$ with $m = 1, \ldots, M$ from M reference channels, and output time series $y(k)$ from a single target channel, we desire to create an FIR filter with $L + 1$ coefficients $\vec{f}(l) = (f_m(l))$, $l = 0, \ldots, L$ that minimizes the residual error:

$$E = \sum_{k=1}^{N} \left(y(k) - \sum_{l=0}^{L} \vec{f}(l) \cdot \vec{x}(k-l) \right)^2 \tag{7.1}$$

where N is the number of samples. Each coefficient of the optimal filter must obey

$$\frac{\delta E}{\delta f_m(l)} = 0 \tag{7.2}$$

This constraint results in

$$\sum_{l=0}^{L} R_{xx}(k-l) \cdot \vec{f}(l) = \vec{c}_{yx}(k) \tag{7.3}$$

where R_{xx} is the autocorrelation of $\vec{x}$, $\vec{c}_{yx}$ is the cross-correlation between y and $\vec{x}$, and $k \in 0, \ldots, L$. Equation (7.3) is known as the Wiener-Hopf equation, which represents a series of $(L+1)M$ equations for the same number of optimal filter coefficients $f_m(l)$ that must be solved simultaneously. Because the signals are real, their autocorrelation is symmetric, $R_{xx}(k) = R_{xx}(-k)$, resulting in a Toeplitz structure for the system of equations, which makes it possible to apply more efficient algorithms when solving for the filter coefficients. This solution returns the f_m terms. The noise cancellation algorithm can then be written symbolically as a convolution (symbol $*$)[309]:

$$r(k) = y(k) - \sum_{m=1}^{M} (f_m * x_m)(k) \tag{7.4}$$

Because the noise-cancellation filter performs best during times without major seismic disturbances such as earthquakes, one needs to make sure that the data used to calculate the filter coefficients are representative of quiet times. Equation (7.3) shows that the optimal filter coefficient depends on the average correlation between channels, but also on the spectra of all channels (otherwise optimal subtraction could be achieved with a single FIR filter coefficient per input channel). Filter properties can be related to specific properties of the seismic wave during strong ground motion, such as prop-

agation direction, or wave content (surface waves, body waves, polarization, etc). The spectrum of a seismic disturbance is typically determined by its source. The typical situation, however, will be that the seismic field recorded over some time is composed of many seismic waves from different sources, and the Wiener filter calculated from it will be determined by the average correlations between channels and their average spectra.

It should be noted that coherence between channels needs to be very high even for "modest" noise cancellation. The ideal suppression factor $r(f)$ as a function of frequency f in the case of a single reference channel is related to the reference-target coherence $c(f)$ via

$$r(f) = \frac{1}{\sqrt{1 - c(f)^2}} \tag{7.5}$$

where

$$c(f) = \frac{\overline{\tilde{s_1}(f)\tilde{s_2}(f)^*}}{\overline{|\tilde{s_1}(f)||\tilde{s_2}(f)|}} \tag{7.6}$$

and $\tilde{s_1}(f)$ and $\tilde{s_2}(f)$ are the Fourier transforms of the two channels. For example, if coherence between reference and target channels at some frequency is (0.9, 0.99, 0.999), then the residual amplitude spectrum at that frequency will ideally be reduced by factors (2.3, 7.1, 22) respectively. Therefore, a seismic noise reduction by a factor 50 (as achieved here with two reference channels; see section 7.3.2) is very high corresponding to a channel coherence of about 0.9998. We can compare this result with a theoretical prediction from a Rayleigh-wave model. If only one reference channel were used, i. e. taking the 800 ft seismometer as target and the 2000 ft-B as reference, and the Rayleigh-wave field were isotropic, then the channel coherence would be about 0.999 assuming a Rayleigh-wave speed of 3 km/s and using equation (7) in [115]. This means that a factor 50 subtraction is better than what can ideally be achieved with

two channels (under the assumption that the Rayleigh field is isotropic). It can be concluded that the array of two reference channels already provides some ability to measure propagation directions of Rayleigh waves, or to disentangle different wave types and thereby significantly improving the subtraction performance (again, assuming an isotropic Rayleigh field).

7.3 Filter Results

Coherence between channels is what fully determines the Wiener filter coefficients. Coherence is a consequence of the seismometer self noise and the quality of its connection with the ground, but also of the local geophysical settings and properties of the seismic field. Whereas the hard rock of the Black Hills should be beneficial to seismic coherence between stations as seismic waves are relatively long, topographic scattering, especially in mountainous regions, may pose an ultimate limit to what can be achieved with Wiener filtering irrespective of the sensor self noise[85]. Another limit of subtraction performance could be related to a complex composition of the seismic field. With the few seismometers that were used in this study, the Wiener filter is likely not able to subtract ambient noise from body waves to the same degree as the noise from the dominant Rayleigh waves. The latter is not obvious though, and needs to be investigated in the future using extended underground arrays. The basic idea is that a Wiener filter can only train on an average correlation pattern of a seismic array. The sign of average seismic correlation between two seismometers can be different for body and surface waves depending on the distance between them. This leads to partial cancellation of their contributions, which affects subtraction performance. However, if a seismic array is designed to have the ability to distinguish between body

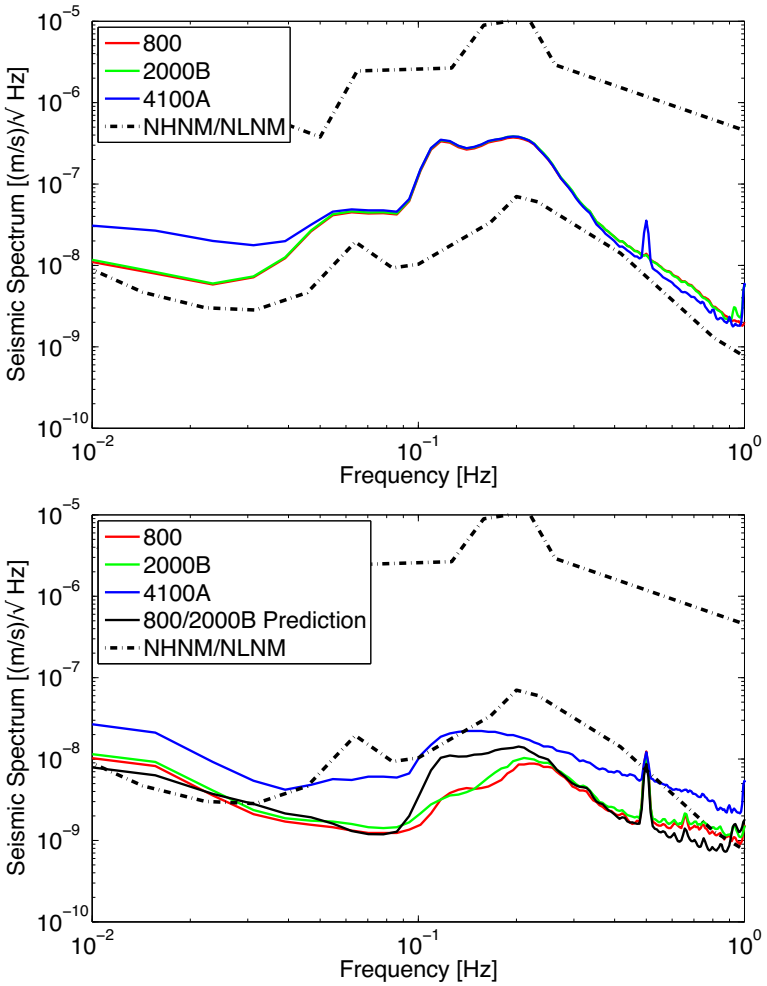


Figure 7.1: The plot to the left shows the medians of seismic spectra for the three seismometers. The dash-dotted lines in black represent the global new low- and high-noise models (NLNM/NHNM)[240]. The primary and secondary microseismic peaks are visible between 30 and 100 mHz and 0.1-0.5 Hz respectively. A line at 0.5 Hz from the data-acquisition is also visible. On the right is the median of the residuals for the three seismometers. The vertical channel of the respective seismometer was the target channel, and channels from the other two sensors were used as reference channels. The expected subtraction for the 800 ft channel based on coherence between the 800 ft and 2000 ft-B stations is plotted in solid black.

and surface fields, then also the Wiener filter will be able to subtract contributions from both.

Figure 7.1 demonstrates the performance of the filter on the seismic array data.

A Wiener filter with 1000 coefficients was calculated from 3 hours of data, and then subsequently applied to subtract ambient seismic noise from target channels over a period of 2 weeks. In all cases, only the vertical channels were used as target and reference. Adding horizontal channels to the reference channels does not lead to significant changes of the subtraction residuals since coherence between horizontal and vertical directions is small. Due to similar coherence between horizontal channels, we expect the subtraction results for vertical channels to hold for horizontal channels as well. For target seismometers 800 ft and 2000 ft-B, subtraction residuals are more than a factor 10 weaker than the original spectra over a wide range of frequencies. Subtraction performance is significantly worse at 4100 ft-A. The reason for this is the elevated noise floor of the 4100 ft-A seismometer, because of problems with the data-acquisition system as explained in Section 7.1. Nevertheless, it is interesting that in all cases a residual microseismic peak (probably two peaks generated by two different ocean-wave fields) remains in the residual spectrum, and that this peak is larger than what is expected from an estimate of the Rayleigh wavelength (more than 10 km) in comparison to the horizontal station distance. This can be due to a geophysical effect, but potentially also because of a weakly non-linear response of the seismometer.

As shown in Figure 7.1, the subtraction residuals are greater than the coherence limit above 0.5 Hz, which means that the Wiener filter injects uncorrelated noise into the target channel. Ideally, this should be impossible, since injection of noise by Wiener filters is suppressed consistent with the loss of coherence due to this noise (e. g. if reference and target channels are uncorrelated, then the Wiener filter function is equal to 0). Therefore, the fact that noise is increased can either be explained by numerical problems in the calculation of the Wiener filter (which involves the inversion of a large matrix), or potentially with non-stationarity of the noise (which can

make the Wiener filter sub-optimal). Additional filters such as low-pass filters can be applied in sequence with the Wiener filter to suppress excess noise at certain frequencies.

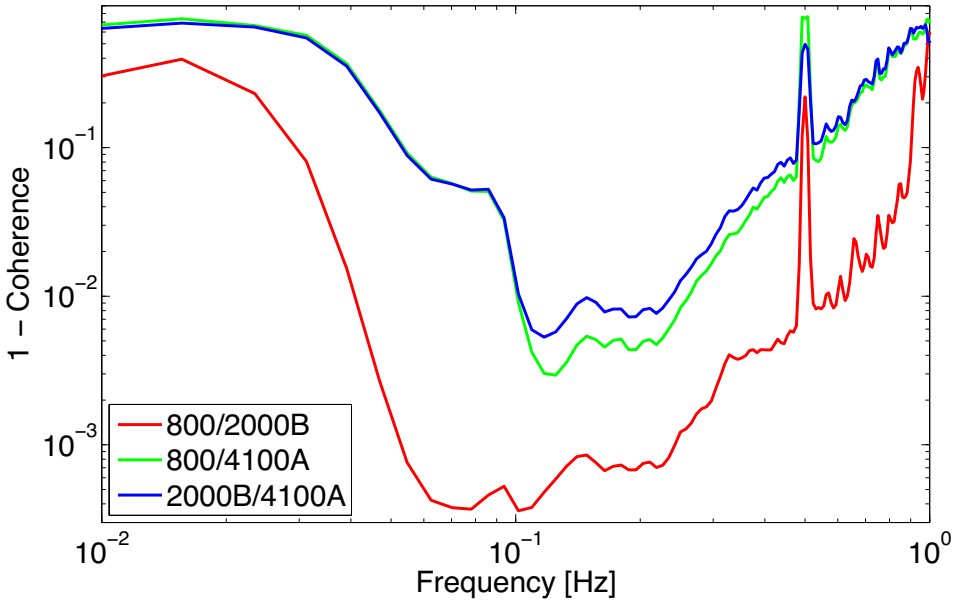


Figure 7.2: Plot of of the measured coherence between the three station pairs. Coherence between the 800 ft and 2000 ft-B stations exceeds 0.9995 at the microseism. Coherence between the other pairs is approximately an order of magnitude lower, which results in the relatively worse subtraction results presented in the paper.

Figure 7.2 presents the coherence between the stations. The measured coherence between two stations can be used to calculate the spectrum of the uncorrelated seismic noise. The result is shown as black solid line on the right of Figure 7.1 for the 800 ft – 2000 ft-B seismometer pair. As can be seen, the residual spectrum of the Wiener filter lies below the coherence limit, which means that with one additional reference seismometer, significant extra information about the seismic field can be obtained to improve noise cancellation.

7.3.1 Filter evolution with time

Slow changes of average properties of the seismic field (e. g. diurnal or seasonal cycles), of instrumental noise, or of the system dynamics may require filter adaptation. When implementing a Wiener filter, it is important to know how often such a filter should be updated, or in case that the required update rate is high, if a genuine adaptive filter technology needs to be implemented. We now study how the filter coefficients evolve over time by recalculating the Wiener filter regularly.

We begin by examining filter evolution on day-long timescales by computing a filter every 128 s. An update scheme this fast is certainly not meant to be used in real applications and only serves to illustrate filter variations. The target seismometer is at the 800 ft station. Figure 7.3 shows the evolution of the Wiener filter over the course of a day. Results are given only for the part of the filter mapping the 2000 ft-B reference channel. Instead of directly showing the FIR coefficients, the filter is represented in the frequency domain to make it easier to connect its variation with properties of the seismic field.

The fluctuations in the seismic spectra predominantly result in changes in the high frequency portion of the filter. The major variations coincide with high amplitude events in the seismic spectra. Due to its high frequency, this noise is likely local and therefore anthropogenic in origin. The histogram of filter magnitude variations is shown in the top right plot. The distribution widens at high frequency, while it is narrowest around the oceanic microseisms. This is consistent with the fact that oceanic microseisms are stationary over the course of a day, whereas local noise below and above the microseismic peak is strongly non-stationary. It is maybe surprising that the filter below 0.4 Hz does not vary as much as the seismic field itself, but the

variation in the filter is determined by variations of correlation between all channels. In the case of high correlation between channels during quiet times, as is the case at lower frequencies, the effect of strong ground motion on correlation would simply be to increase correlation from say 0.9 to 0.95, which means that also the filter response should be expected to vary accordingly. Its efficacy would also increase. Correlation is, however, small at higher frequencies during quiet times, and is increased significantly by strong ground motion, which would lead to large changes in the Wiener filter.

Because the spectral densities of all three channels involved in the noise subtraction are almost identical in the frequency range 0.1 Hz – 0.5 Hz, the fact that filter magnitudes for the 2000 ft-B are smaller than 1 in this frequency range means that the 4100 ft-A reference channel provides the missing part required for subtraction. The 4100 ft-A contribution is smaller due to the elevated noise floor of the seismometer because of data-acquisition problems. The filter magnitudes greater than 1 around 0.8 Hz are also expected because the target channel is closer to the surface and therefore has a significantly greater Rayleigh-wave amplitude at sufficiently high frequencies. The filter magnitude goes to zero at frequencies where coherence is weak, and the optimal filter suppresses the incoherent noise contribution of the reference channel to the target channel.

Next we study how the filter evolves on month-long timescales. Figure 7.4 shows the 10th, 50th, and 90th percentiles of residual noise of the 4100 ft-A station accumulated over the course of two months. The filter is either updated once a day, leading to the dashed-line percentiles, or once per week leading to the solid-line percentiles. The filter order was 1000 calculated from 2 hours of data. The subtraction performance is almost identical in the two cases, which means that seismic correlations av-

eraged over one day do not change significantly within one week. It is in fact remarkable that the residual spectra are so similar over a wide range of frequencies.

7.3.2 Optimal filter order

When designing and optimizing a Wiener filter, there are only a few tunable parameters. This includes the number of reference channels that one uses to create the filter, as well as what kind of additional filtering (if any) to apply to the input data. Another is the order of the Wiener FIR filter. Implementations in GW interferometers[147,114,112] have typically used thousands of filter coefficients at 64 Hz sampling rate. These filters were calculated using 1 hour of data.

One may wonder whether the order of the most efficient Wiener filter, i. e. the filter with minimal order achieving the subtraction goal, only depends on the bandwidth of the noise that one wants to subtract. This assumption seems reasonable, because the filter order and time interval between two filter coefficients determines the minimum and maximum frequency of the filter response. It will be shown in this section that the dependence of subtraction residuals on filter order is not so simple.

We examine the effect of filter order using three separate days of data. For each day, filters are calculated with varying filter order. In Figure 7.5, the performances of the filters are compared. The plot on the left shows the noise reduction at 0.2 Hz (arbitrarily chosen) for the three days and filter orders 1 to 1000, while the plot on the right is the same for 0.4 Hz. Filter order 1 means simple subtraction of data with optimal scaling factor of the input data. Subtraction performance shows less variation from one day to the next for high filter orders, but the price paid for this stability is that the residuals could be much less at certain days using a smaller filter order. In general, the best subtraction performance is only achieved for specific filter orders, of-

ten degraded substantially when changing from optimal filter order to slightly higher or smaller orders. In addition, the optimal filter order is not the same every day, although it could be optimized for each individual day. However, the plots also show that even though choosing the optimal filter order depends on target frequency and varies between days, it is still possible to identify ranges of filter order that work better than others. For example, for the two frequencies 0.2 Hz and 0.4 Hz, Figure 7.5 shows that a filter order slightly below 100 would be a better choice instead of a very high filter order around 1000. A full histogram of residuals achieved for the day represented by the blue markers in Figure 7.5 accumulated from all filter orders between 1 and 1000 is shown in Figure 7.6. Even though dependence of the residuals on filter order seems modest at most frequencies, it should be emphasized that even a factor 1.5 in residual noise can be significant especially with respect to NN, which directly contributes to the detection band. These results suggest that an adaptive filter technology that includes modifications of the filter order could lead to significantly decreased residuals.

Next, we will outline the connection of our results to seismic NN subtraction. The subtraction of seismic NN will be more challenging than the demonstrated seismic-noise subtraction. Most importantly, it has been shown in previous simulations and theoretical work that reduction of NN from Rayleigh waves by a factor 50 or more would require a large number of seismometers[52,115,160], which follows from properties of the Rayleigh-wave field and the way it produces NN. The optimal design of the seismometer array will be a major challenge. There are also similarities between Newtonian and seismic-noise subtraction. Their performance can be limited by weaker contributions from other wave types such as compressional and shear waves generated directly by seismic sources, or by seismic scattering. The effect is similar for

seismic and Newtonian-noise subtraction, since it is the spatial two-point correlation of the seismic field that determines the impact of diverse wave-type composition on NN (see[52] for details), which is the same function that determines the performance of the Wiener filter used for seismic-noise subtraction. Therefore, in this respect, our subtraction results are representative not only for seismic-noise cancellation, but also for NN cancellation. One can conclude that, if technical issues as described below are neglected, a factor 50 NN reduction can be achieved if the maximal spacing between seismometers in horizontal direction is 300 m and 500 m in vertical direction. In other words, at the level of achieved subtraction residuals, contributions from other wave types should not impede NN subtraction performance for the given seismometer spacing. The only way that this conclusion could turn out to be wrong due to properties of the seismic field is that the geologic conditions local to the Homestake mine are significantly more favorable in terms of seismic scattering than at areas at some distance to the mine, which are however still close enough to contribute to seismic NN at a significant level. One should keep in mind though that a seismometer spacing of a few hundred meters is very small for these frequencies, and that this could easily amount to a total of a few thousand seismometers required for a factor 50 NN subtraction. Now, based on this discussion, it may well be possible that the achieved seismic-noise subtraction is already limited by the presence of other wave types, especially since only 2 reference channels were used. This needs to be tested in the future using a larger seismic array that would be able to disentangle contributions from different wave types and possibly lead to better subtraction performance. These experiments will also show if a factor 50 suppression or higher can be achieved with rarer seismometer spacing. Nonetheless, we venture to present our subtraction results as an equivalent reduction of NN produced by Rayleigh waves.

Figure 7.7 shows the MANGO GW detector target spectrum, as well as the NN estimate based on the model presented in[160] and its residual after coherent cancellation using the achieved seismic-noise reduction. Another factor 20 reduction would be missing for the MANGO noise target. Other technical differences between seismic and Newtonian-noise subtraction should be mentioned. For example, a large number of reference channels used to calculate a NN Wiener filter may well come with additional numerical challenges, since the dimension of the correlation matrix that needs to be inverted for the Wiener filter would be much larger. In addition, the design of a seismic array that can provide a factor 50 NN reduction at low frequencies needs to address the additional problem that the seismic noise monitored by each seismometer will produce gravity perturbations that are strongly correlated between different test masses, which are therefore partially rejected by the differential readout of the detector (note that this common-mode rejection is included in the NN model of Figure 7.7). This further increases potential numerical problems of the NN subtraction scheme, since the Wiener filter needs to incorporate the same effect by combining reference channels in a way that common-mode signals are cancelled at its output, and still be able to measure the underlying correlation of its output with the GW channel of the detector. Therefore, it should be clear that our results, though directly relevant to NN subtraction, demonstrate an advance concerning only one of many problems.

Before concluding this section, we want to discuss further details of the seismic NN model used here. First, building a 0.1 Hz detector underground has no significant influence on seismic NN. Seismic waves have lengths of a few tens of kilometers at these frequencies, and therefore relevant properties of seismic fields and seismic NN do not change with detector depths (for feasible depths). Second, the seismic NN model makes simplifications as outlined in detail in[160]. The most important conse-

quence of these simplifications such as flat surface and homogeneous ground is that seismic scattering is not included in the NN model. Whereas this is certainly not an accurate representation of reality, our results show that these effects do not matter at frequencies around 0.1 Hz at a level that is a factor 50 below the observed seismic-noise (assuming that seismic scattering at the Homestake mine is representative for the entire region). Therefore, at this level of accuracy, our results can be taken as a validation of these approximations. We want to emphasize though that our findings here cannot be used to draw similar conclusions concerning NN subtraction at much higher or lower frequencies, and it is possible that the situation changes drastically when noise suppression at 0.1 Hz beyond a factor 50 is tried with larger arrays.

7.4 Conclusion

In this paper, we have investigated limits of coherent seismic-noise subtraction, which serves as a first test bed for the more challenging problem of seismic NN subtraction. The main difference between the two problems is that a much larger number of seismometers will be required for seismic NN subtraction. The question of optimal array design and many technical issues to calculate Wiener filters based on a large number of reference channels are not addressed by our study. However, our results allow us to put constraints on the effect from seismic scattering on coherent NN subtraction with the conclusion that at least a factor 50 NN reduction should in principle be feasible at the Homestake site around 0.1 Hz, provided that seismic scattering at the Homestake site is representative for seismic scattering of the entire region that needs to be included for NN estimates.

We have demonstrated that we can achieve more than an order of magnitude seismic-

noise cancellation between about 0.05-0.5 Hz using Wiener filters with only a few seismometers separated by a distance of order 500 m. We have also shown that this subtraction performance can be achieved without regularly updating the filter, indicating that the average properties of seismic fields at Homestake do not change significantly over timescales of weeks in this frequency band. This is beneficial for realizations in future GW detectors as it simplifies the application of the method to their output. However, in the attempt to optimize noise cancellation, it was found that filter order plays an important role. At frequencies below 0.1 Hz, subtraction residuals varied almost by an order of magnitude for filter orders between 1 – 1000. Whereas continuous optimization of filter order may not be feasible in many applications, especially in system control, the results also show that there are ranges of filter order with near-optimal subtraction performance over a broader range of frequencies. These filter orders maintain near-optimal performance over days.

As shown in various publications in the past [147,114,112], Wiener filters can be used to efficiently subtract noise from data off-line, or in real time by means of feed-forward noise cancellation. In this paper, we focused on subtraction of coherent seismic noise, but many other applications are conceivable and have already been applied in previous generations of GW detectors, often forming an important part of the detector design. Wiener filters can subtract broadband noise as well as narrow-band features such as noise lines, and they will therefore play an important role in future detectors, and also serve as a starting point for the development of more advanced filter technologies.

These results are important as we have achieved factor of 50 subtraction in the low-frequency GW detectors band. For seismic NN, you would need another factor of 20 reduction to achieve 10^{-20} in strain sensitivity. Our work corresponds to the first test

bed of noise subtraction in this band for these detectors. Although there is no direct connection to LIGO-like interferometers due to the low-frequency band, we are exploring pushing Wiener-filter subtraction to its limits and how to maximize its efficacy. With the installation of a larger seismic array, hopefully with good data quality above 1 Hz, subtraction above 1 Hz can be explored. As of now, it is not possible to say whether we can expect NN subtraction at the same levels as achieved in our analysis. This will require a test of the ability to monitor the seismic wavefield with an expanded seismic array.

Because the residual spectra also contain a microseismic peak, it is evident that noise cancellation is not only limited by instrumental noise. A theory that should be tested in the future is whether the residual peak is produced by body waves instead of surface waves. It is known that both wave types contribute to the microseisms, but it is not clear how this affects noise cancellation. Alternatively, it is possible that topographic scattering of seismic waves play a role. The Homestake seismic underground array will be expanded in the future to more seismometers. This will make it possible to carry out a number of important studies relevant to seismic-noise cancellation, which were impossible with the more limited array used here. The extended array will have the capabilities to distinguish between body and surface waves, which, as explained, will be important to explore and possibly understand seismic-noise cancellation limits. It remains to be tested whether a larger array with greater variation in station distances would yield even better subtraction over a broader range of frequencies, potentially down to the instrumental noise limit. This possibility also motivates the development of improved seismometers with reduced self noise performance.

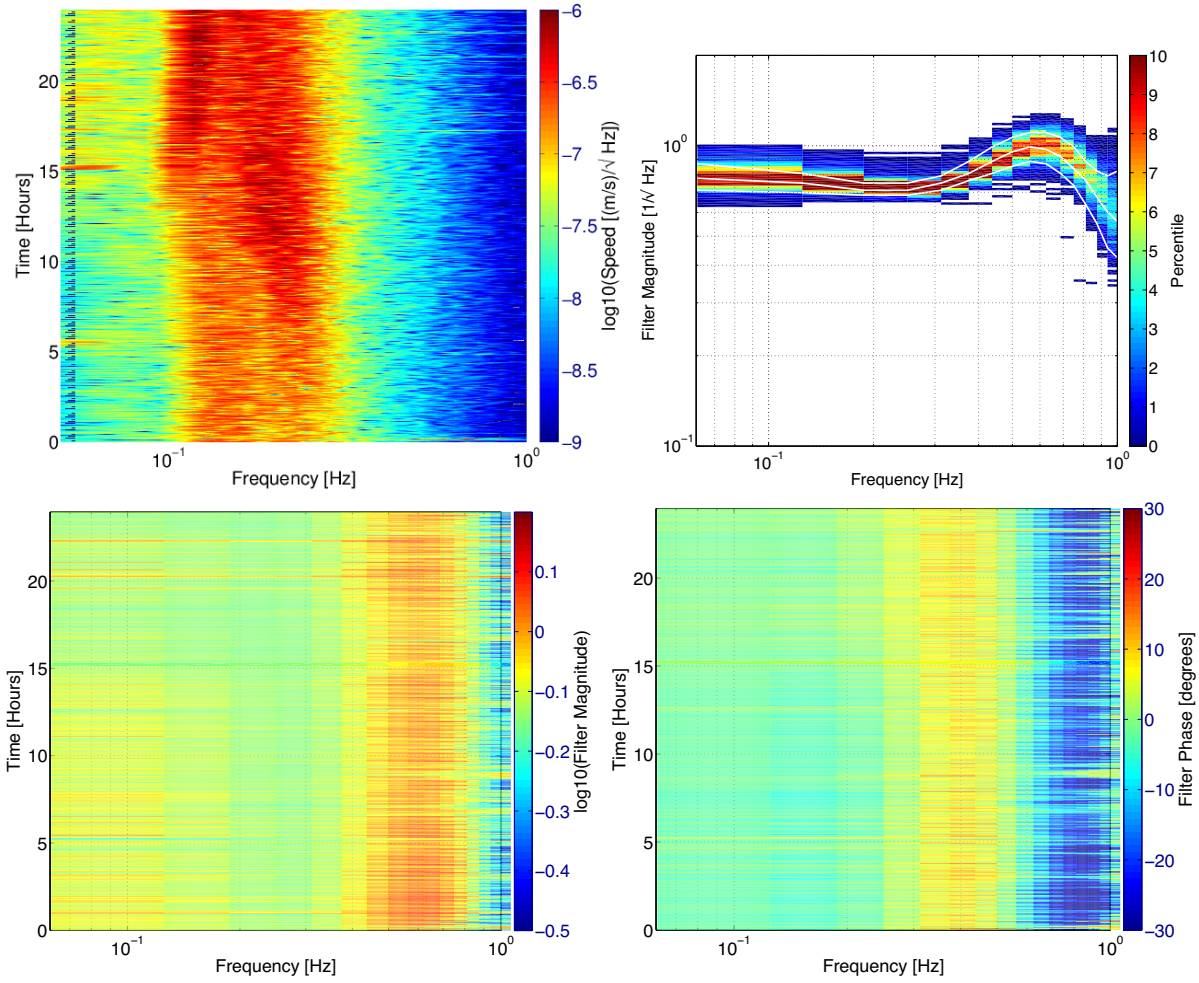


Figure 7.3: Filter variation over the course of a day. The filter is represented in the frequency domain by its magnitude and phase, as in a Bode plot. Top left: Time-frequency plot of the spectra of the 800 ft seismometer. Top right: Filter magnitude histogram for the 2000 ft-B reference channel. The bottom, middle, and top white lines correspond to the 10th, 50th, and 90th percentiles respectively. Bottom left: Time-frequency plot of the filter magnitude for the 2000 ft-B reference channel. Bottom right: Time-frequency plot of the filter phase for the 2000 ft-B reference channel.

.

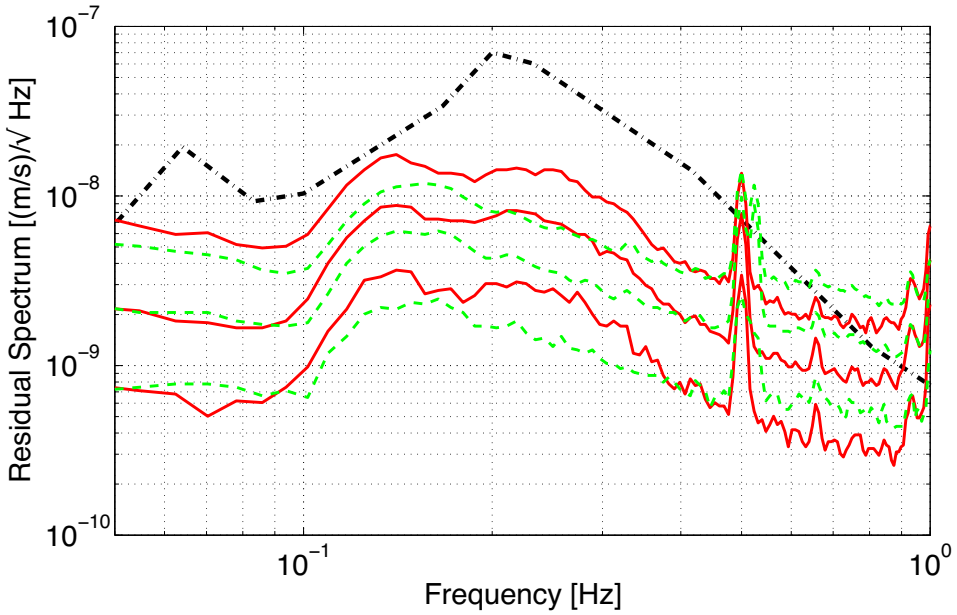


Figure 7.4: Subtraction residuals for the 800 ft channel using 2000 ft-B and 4100 ft-A as reference channels over a month of data. The dashed curves are its 10th, 50th, and 90th percentiles using a filter that is updated once every day. The solid lines are the percentiles of residual noise using a filter updated once every week. The dash-dotted line in black represents the global new low-noise model[240].

.

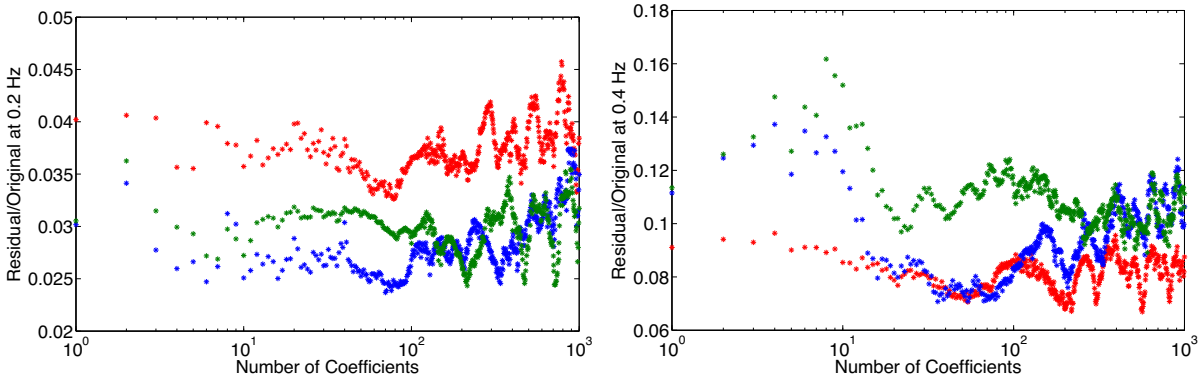


Figure 7.5: Residual noise evaluated over the three separate days as a function of filter order for the 800 ft target channel. The residuals shown in the plot on the left are evaluated at 0.2 Hz, whereas the residuals on the right are evaluated at 0.4 Hz. Each color corresponds to a different day.

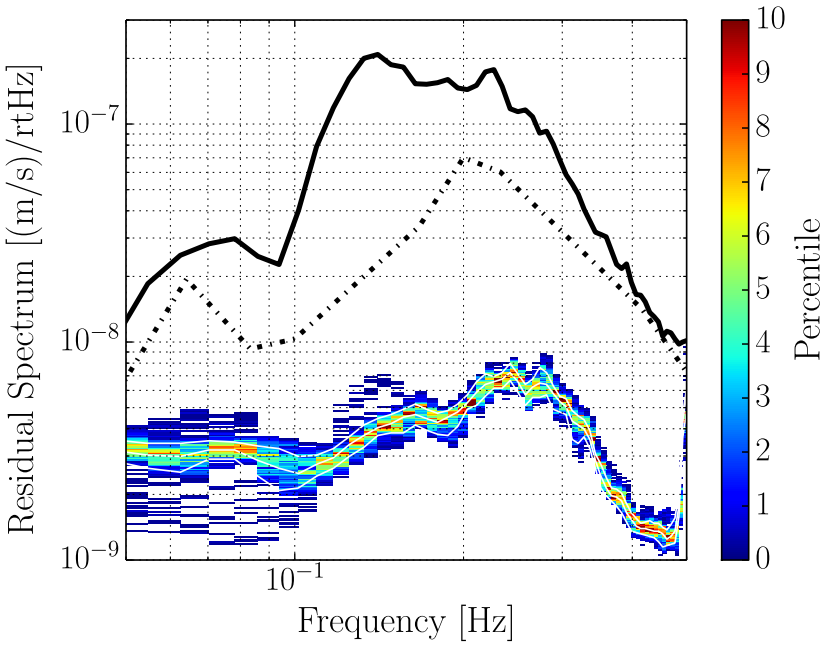


Figure 7.6: The plot shows the histogram of residual spectra for the 800 ft target channel achieved by each of the 1000 filter orders for the day represented by the blue markers in Figure 7.5. The bottom, middle, and top white lines correspond to the 10th, 50th, and 90th percentiles respectively. The dash-dotted line in black shows the global new low-noise model[240]. The original spectra of the 800 ft channel is plotted in solid black.

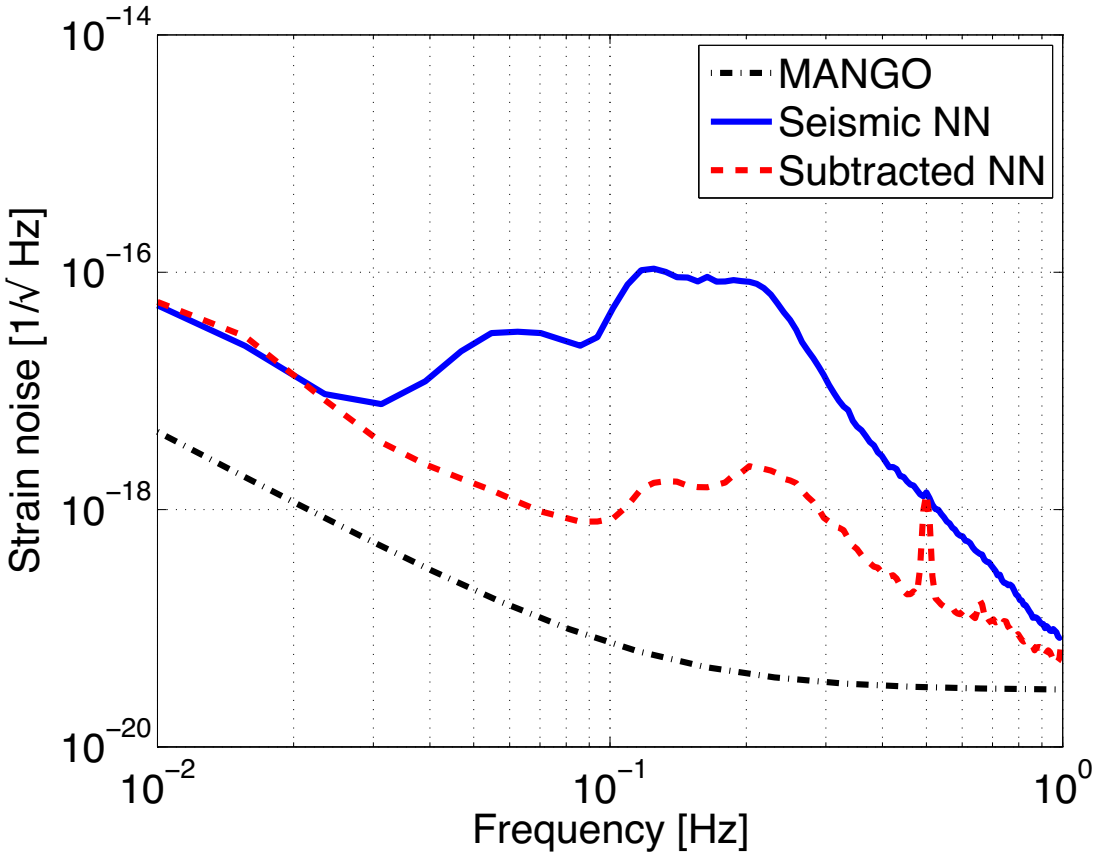


Figure 7.7: The MANGO GW detector target spectrum, as well as the NN estimate and its residual after suppression by the factor that was achieved with seismic data. There is about a factor of 50 subtraction across the microseism. A further order of magnitude subtraction would be required to achieve MANGO GW detector target sensitivity.

8

Towards a first design of a Newtonian-noise cancellation system for Advanced LIGO

With the recent detection of gravitational waves produced by a binary black-hole system[24], efforts to develop novel technology to maximize the sensitivity of the existing gravitational-wave detectors such as Advanced LIGO[180] and Advanced Virgo[295] are being reinforced. A possible upgrade of the advanced detectors with minimal impact on the detector infrastructures is the cancellation of so-called Newtonian noise (NN)

produced by terrestrial gravity fluctuations[67,52,156].

The idea of NN cancellation is to monitor the sources of gravity perturbations, which are generally associated with fluctuating mass density in the vicinity of the test masses. For example, microphones can be used to retrieve information about certain density perturbations in the atmosphere, and seismometers provide information about density perturbations of the ground. Predictions based on a detailed characterization of the LIGO sites show that seismic surface fields give the dominant contribution to NN[115]. In this case, a NN cancellation scheme can be realized using an array of seismometers deployed at the surface near the test masses[156].

In the absence of NN observations, studies of NN cancellation schemes rely on precise modelling. Models of seismic NN have been gradually refined over the past decades[262,172,51,156]. Atmospheric NN was identified as a limiting noise source in superconducting gravimeters at mHz frequencies, and noise cancellation successfully implemented using pressure sensors[228]. However, it is to be expected that atmospheric NN cancellation in future large-scale GW detectors will be significantly more complicated due to a greater variety of atmospheric phenomena that can cause NN[99].

The design of a seismic NN cancellation scheme for the advanced detectors needs to address the optimization of the filter used to calculate a NN estimate from seismic data, and also the optimal placement of seismometers around test masses[115]. The traditional cancellation scheme is based on Wiener filters as was already implemented in feed-forward configuration with respect to other GW detector noise[147,114,112]. Wiener filters are typically calculated from observed correlations between sensors and target channels, but it is also possible to employ models of correlations informed by observations. The latter is advantageous if prior knowledge of the seismic field can be used to constrain the correlation models (such as seismic speeds, or the location of known

seismic sources).

Optimizing the shape of seismic arrays is important for maximizing the efficacy of the noise cancellation. Driggers et al.[115] first explored schemes to mitigate NN by estimating and subtracting it from the interferometer data stream. They simulated seismic fields with local and non-stationary components, achieving subtraction levels of about a factor of 10 with a finite-impulse response implementation of the Wiener filters. In this paper, we explore using measured seismic fields from an array previously stationed at LIGO Hanford to inform the models for the seismic fields we use to perform array optimization. We include four correlation models fit to the observed data. For all of the models, we use the LHO array data to inform parameters in these models, including seismic speeds. At that point, we use high-dimensional samplers computing optimal arrays for these models by minimizing the expected noise residuals.

The structure of the paper is as follows. We review the formalism of NN and the models used in this analysis in section 8.1. In section 8.3, we describe how we perform the array optimization. We discuss how previous measurements from an array of accelerometers at the LHO site inform our seismic field models in section 8.2. In section 8.4, we provide the results of analytic and sampler optimizations for reference seismic fields. Our conclusions are summarized in section 8.5.

8.1 Newtonian Noise Cancellation

8.1.1 Plane-wave Rayleigh Newtonian noise

We briefly review Rayleigh-wave NN (see section 3.4.2 in[156] for details). Rayleigh waves are characterized by an evanescent displacement field, which means that dis-

placement amplitude decreases exponentially with distance to the surface. Density perturbations caused by Rayleigh waves can be produced in two ways. First, one needs to consider density changes due to normal surface displacement $\xi_z(\vec{\varrho}, \omega)$ at frequency ω, where $\vec{\varrho} = (x, y)$ is the horizontal coordinate vector. Second, Rayleigh waves produce density changes inside the medium. We start with gravity perturbations from pure surface displacement, and focus on homogeneous media in a half-space for simplicity.

If surface displacement is associated with a single Rayleigh wave, then the corresponding gravity acceleration along the horizontal direction x of a test mass at location $\vec{\varrho}_0$ can be written

$$\delta a_x(\vec{\varrho}_0, \omega) = -2\pi \mathrm{i} G \rho_0 \xi_z(\vec{\varrho}_0, \omega) \exp(-kh) k_x/k, \tag{8.1}$$

where G is the gravitational constant, ρ_0 the density of the homogeneous medium, k the wavenumber, h the height of the test mass above ground, and the wave vector is $\vec{k} = (k_x, k_y)$ with $|\vec{k}| = k$. Displacement has the same phase at points inside the medium sharing the same horizontal coordinates. This means that additional contributions to the gravity perturbation from density changes inside the medium can be accounted for by multiplying the last equation with a number $\gamma(\nu)$. It depends on the Poisson's ratio ν of the medium. For Rayleigh waves, the value of this factor is about $\gamma \approx 0.8$. This means that NN from density perturbations of the medium partially cancel NN from surface displacement.

8.1.2 Wiener filtering

Noise cancellation using Wiener filters exploits correlations between reference sensors and a target channel to provide a coherent estimate of certain noise contributions to the target channel[54]. Wiener filters are the optimal, linear noise-cancellation filters provided that data from all channels are described by stationary, random processes. In the following, we assume this to be the case.

For seismic NN cancellation, the reference sensors are the N seismometers, and their mutual correlations will be denoted C_{SS} in this paper, which is understood to be a $N \times N$ matrix containing the cross spectral densities of normal surface displacement $C(\xi_z; \vec{\varrho}_1, \vec{\varrho}_2, \omega)$ between two seismometers located at $\vec{\varrho}_1$, $\vec{\varrho}_2$. The matrix contains seismometer instrumental noise on its diagonal. The target channel is the output data of the GW detector, but for simplicity, we only consider NN from a specific test mass. In this case, the N seismometers are located in the vicinity of this test mass. The NN spectral density of a test-mass located at $\vec{\varrho}_0$ is denoted by $C_{\mathrm{TT}} \equiv C(\delta a_x; \vec{\rho}_0, \omega)$. It is straight-forward to extend the analysis to a cancellation of the total NN from all four test masses.

The correlation between NN and seismometers is denoted by $\vec{C}_{\mathrm{ST}}$, which is a N-component vector containing the cross spectral densities $C(\xi_z, \delta a_x; \vec{\varrho}, \vec{\varrho}_0, \omega)$ between normal surface displacement observed at $\vec{\varrho}$ and NN of a test mass at $\vec{\varrho}_0$. The Wiener filter in frequency space can be written $\vec{w} = \vec{C}_{\mathrm{ST}}^{\top} \cdot C_{\mathrm{SS}}^{-1}$, where C_{SS}^{-1} is the inverse matrix of C_{SS}. The coherent NN estimate is now obtained by multiplying the Wiener filter with the amplitudes of seismic displacement observed by the N seismometers. The matrix C_{SS} and the vector $\vec{C}_{\mathrm{ST}}$ depend on seismometer locations.

Subtracting the coherent NN estimate from the actual test-mass NN, an average

relative noise residual R is achieved, which is determined by

$$R = 1 - \frac{\vec{C}_{\mathrm{ST}}^{\top} \cdot C_{\mathrm{SS}}^{-1} \cdot \vec{C}_{\mathrm{ST}}}{C_{\mathrm{TT}}}. \tag{8.2}$$

The cancellation performance can be limited by seismometer instrumental noise, or by the amount of information extracted from the seismic field. We call the first limitation *instrumental*, and the second *geometrical*. For example, a seismometer array with seismometers having distances of order kilometer to each other cannot be used to cancel NN if the seismic wavelength is of order 100 m independent of the seismometer instrumental noise (unless the seismic field is extremely simple, e. g. associated with a single plane Rayleigh wave).

8.1.3 Array optimization

Given a fixed number of seismometers, the optimal array is found by changing seismometer locations and minimizing the noise residual R. From eq. (8.2), one finds that the lowest possible residual with N seismometers is $R_{\mathrm{min}}(\omega) = 1/(N\sigma(\omega)^2)$ with $\sigma(\omega)$ being the signal-to-noise ratio of the seismometers assumed to be equal for all sensors. This residual can only be achieved when geometrical limitations are overcome, which is not always possible even for an infinite number of seismometers (see Figure 8.6).

We could now construct specific plane-wave compositions of the seismic field and use eq. (8.1) to evaluate and minimize the noise residual in eq. (8.2). While this has some merit for analytical understanding of the optimization, the goal of this paper is to present a method to use observable quantities of the seismic field to model NN and its cancellation. Seismic fields can show great complexity for example due to seismic scattering, or presence of local sources, in which case the plane-wave model is imprac-

tical. The key here is to realize that all correlation functions required for calculating the noise residual can be expressed in terms of the two-point spatial correlations $C(\xi_z;\vec{\varrho}_1,\vec{\varrho}_2,\omega)$ of the Rayleigh field:

$$
\begin{aligned}
C(\delta a_x;\vec{\rho}_0,\omega) &= (2\pi G\rho_0\gamma(\nu))^2 \int\int \frac{\mathrm{d}^2k}{(2\pi)^2}\frac{\mathrm{d}^2k'}{(2\pi)^2} S(\xi_z;\vec{k},\vec{k}',\omega)\frac{k_x}{k}\frac{k'_x}{k'}\mathrm{e}^{-hk}\mathrm{e}^{-hk'}\mathrm{e}^{\mathrm{i}\vec{\varrho}_0\cdot(\vec{k}-\vec{k}')},\\
C(\delta a_x;\vec{\varrho}_0,\omega) &= (G\rho_0\gamma(\nu))^2 \int\int \mathrm{d}^2\varrho\,\mathrm{d}^2\varrho' C(\xi_z;\vec{\varrho},\vec{\varrho}',\omega)\mathcal{K}(\vec{\varrho},\vec{\varrho}_0)\mathcal{K}(\vec{\varrho}',\vec{\varrho}_0),\\
C(\xi_z,\delta a_x;\vec{\varrho}_0,\vec{\varrho},\omega) &= -2\pi\mathrm{i}G\rho_0\gamma(\nu)\int\int \frac{\mathrm{d}^2k}{(2\pi)^2}\frac{\mathrm{d}^2k'}{(2\pi)^2} S(\xi_z;\vec{k},\vec{k}',\omega)\frac{k_x}{k}\mathrm{e}^{-hk}\mathrm{e}^{\mathrm{i}(\vec{\varrho}_0\cdot\vec{k}-\vec{\varrho}\cdot\vec{k}')},\\
C(\xi_z,\delta a_x;\vec{\varrho}_0,\vec{\varrho},\omega) &= G\rho_0\gamma(\nu)\int \mathrm{d}^2\varrho' C(\xi_z;\vec{\varrho},\vec{\varrho}',\omega)\mathcal{K}(\vec{\varrho}',\vec{\varrho}_0).
\end{aligned}
\tag{8.3}
$$

with

$$
\begin{aligned}
S(\xi_z;\vec{k},\vec{k}',\omega) &\equiv \int\int \mathrm{d}^2\varrho\,\mathrm{d}^2\varrho' C(\xi_z;\vec{\varrho},\vec{\varrho}',\omega)\mathrm{e}^{-\mathrm{i}(\vec{\varrho}\cdot\vec{k}-\vec{\varrho}'\cdot\vec{k}')}\\
\mathcal{K}(\vec{\varrho}_1,\vec{\varrho}_2) &\equiv \frac{x_1-x_2}{(h^2+|\vec{\varrho}_1-\vec{\varrho}_2|^2)^{3/2}}.
\end{aligned}
\tag{8.4}
$$

Simplified versions of these equations for a homogeneous field, $C(\xi_z;\vec{\varrho},\vec{\varrho}',\omega) = C(\xi_z;\vec{\varrho}-\vec{\varrho}',\omega)$, or a homogeneous and isotropic field, $C(\xi_z;\vec{\varrho},\vec{\varrho}',\omega) = C(\xi_z;|\vec{\varrho}-\vec{\varrho}'|,\omega)$, are presented in[156].

The first and third line in eq. (8.3) follow from eq. (8.1) by calculating expectation values of products of displacement amplitudes at different wavenumbers (note that we do not impose the condition $k = \omega/c$, which holds for waves propagating at speed c). The second and fourth line provide the desired link between seismic observation and NN modelling. It is important that these equations only require seismic correlations and no other prior knowledge of the seismic field such as seismic speeds. Of course,

the simplest analytical models of $C(\xi_z; \vec{\varrho}, \vec{\varrho}', \omega)$ that we can construct will have additional parameters, and seismic wavelength or equivalently seismic speed may be one of them. We are now prepared to either directly use measured correlations between seismometers, or models fit to observed correlations, to optimize seismometer arrays for NN cancellation. Consequently, the path towards a NN cancellation scheme includes a detailed site characterization to measure two-point spatial correlations of the seismic field near all test masses.

8.2 LIGO Hanford Array

In 2012, from April through November, an array of 44 Wilcoxon Research 731-207 accelerometers[Wilcoxon Research] was deployed at an end station building at LIGO Hanford. Figure 8.1 shows the locations of accelerometers in the vicinity of the vacuum enclosure. Each accelerometer's signal was conditioned, including amplification of a factor of 100, before being acquired digitally and saved at 1024 Hz sampling rate. The array configuration followed as closely as possible the shape of a spiral since it has favorable properties for analyzing seismic fields[315].

Two analyses of the array data are presented in the following, which are directly relevant to NN modelling. The first analysis is a measurement of Rayleigh-wave speed in the frequency range 10 – 20 Hz. The method used here is to decompose the seismic field into plane harmonics (see section 3.6.3 of[156]), and collect the phase speeds associated with the maximum-amplitude component over a period of a week. Figure 8.2 shows that mean seismic speed at 10 Hz and 15 Hz is around 300 m/s consistent with previous site-characterization measurements[266], while at 20 Hz measured speeds around 380 m/s are higher than observed previously. This anomalous dispersion can

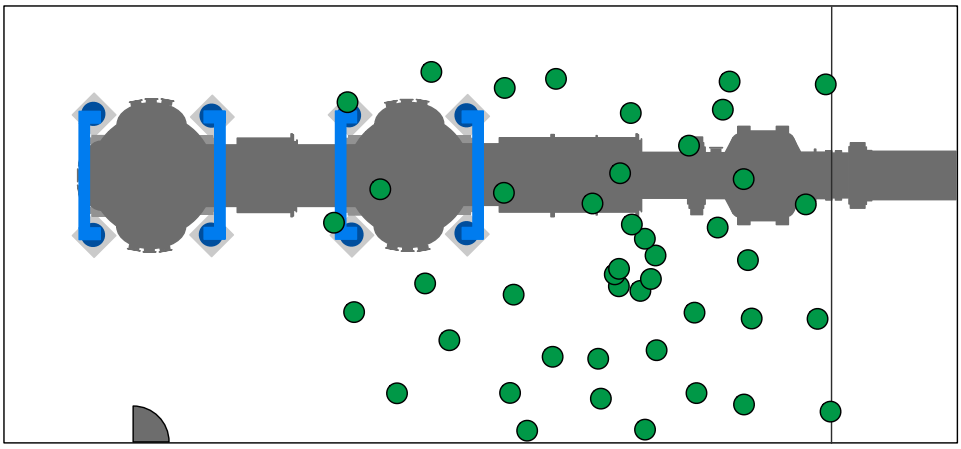


Figure 8.1: Layout of the instrument floor at the Y-end station of the LIGO Hanford Observatory. Green circles indicate placement of accelerometers in the vicinity of the vacuum enclosure. Due to ongoing work at the time, the array is not centered around the vacuum chamber that holds the test mass mirror.

be explained by the concrete slab of the laboratory building, which has greater effect at short seismic wavelengths. A similar result can be expected for the LIGO Livingston site, where Rayleigh-wave speeds in this frequency range estimated from field measurements are around 200 m/s[159]. While the Rayleigh-wave speed is not required to evaluate the integrals in eq. (8.3), it can be used to define simple correlation models as shown in section 8.4.1.

The speed histograms also indicate that seismic noise is dominated by Rayleigh waves. The high-speed tail of the distribution, which is potentially associated with seismic body waves, has very small values. This is a very important conclusion for NN modelling and greatly impact plans for NN cancellation. It remains to be seen of course, if the situation is similar at Livingston and other stations of the Hanford detector.

The second analysis is a measurement of seismic correlations $C(\xi_z; \vec{\varrho}_1, \vec{\varrho}_2, \omega)$ be-

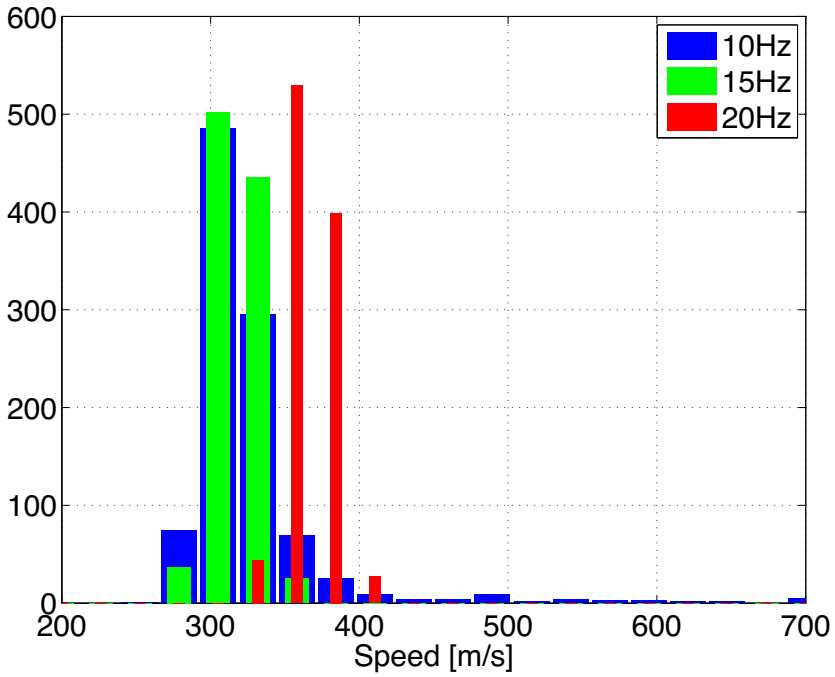


Figure 8.2: Histograms of seismic speed measurements using LHO array data at 10, 15, and 20 Hz.

tween all 29 seismometers used for this study. Figure 8.3 shows values of $C(\xi_z; \vec{\varrho}, \omega)$ at 15 Hz with $\vec{\varrho} = \vec{\varrho}_2 - \vec{\varrho}_1$ and $\vec{\varrho} = \vec{\varrho}_1 - \vec{\varrho}_2$. If the seismic field were homogeneous, then $C(\xi_z; \vec{\varrho}_1, \vec{\varrho}_2, \omega) = C(\xi_z; \vec{\varrho}_2 - \vec{\varrho}_1, \omega)$, and the function outlined by the scatter plot would be smooth. However, there are parts in this plot where high correlation values exist very close to low correlation values. So the observed $C(\xi_z; \vec{\varrho}_2 - \vec{\varrho}_1, \omega)$ is not smooth, and therefore the seismic field is inhomogeneous. The most likely cause of inhomogeneities are local sources, which affect some seismometers of the array more strongly than others altering correlations throughout the array. Nonetheless, in this paper, we will only fit homogeneous models to the scatter plot, assuming that we can understand the result as a smoothly changing correlation function $C(\xi_z; \vec{\varrho}_2 - \vec{\varrho}_1, \omega)$

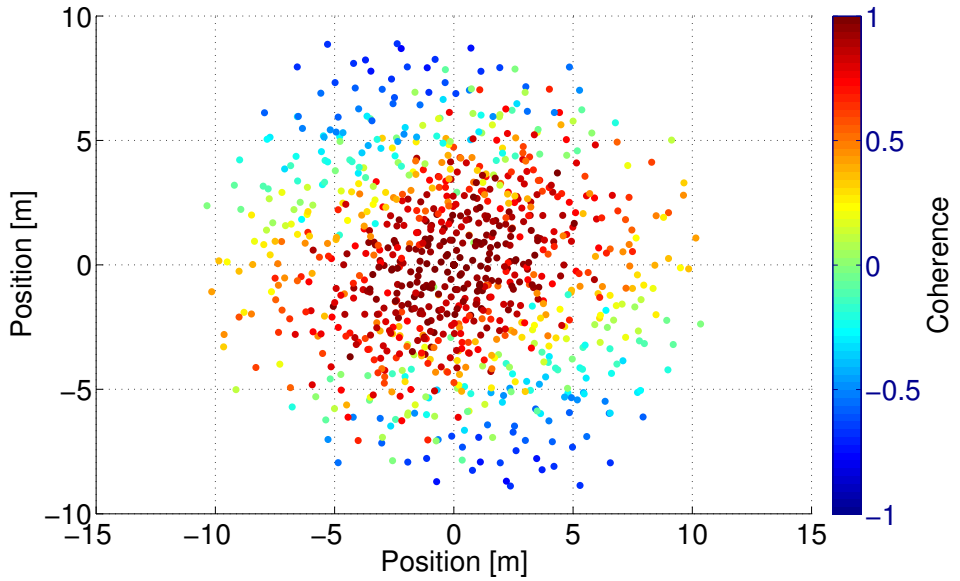


Figure 8.3: Measured correlation function $C(\xi_z; \vec{\varrho}, \omega)$ for the LIGO Hanford site at 15 Hz.

perturbed by a sufficiently small number of outliers.

If inhomogeneities were more pronounced, then NN modelling and array optimization must be directly based on eq. (8.3) valid for inhomogeneous fields. Since it is very hard to conceive a model of $C(\xi_z; \vec{\varrho}_1, \vec{\varrho}_2, \omega)$ that could be fit to observed inhomogeneous correlations, the better strategy may be to calculate the integrals numerically over observed values, possibly using interpolation techniques. These schemes were tested in preparation of this article, but it was found that array optimization based on numerical integration requires a larger number of seismometers. The crucial difference to optimization in homogeneous fields is that with N seismometers, for each seismometer, the function $C(\xi_z; \vec{\varrho}_1, \vec{\varrho}_k, \omega)$ with $k = 1, \ldots, N$ is only sampled N times, while an estimate of the homogeneous correlation $C(\xi_z; \vec{\varrho}_2 - \vec{\varrho}_1, \omega)$ is calculated from $N \times N$ samples. So given a certain precision goal, which is determined by the targeted noise-suppression factor, a much larger number of seismometers is required in the case

of inhomogeneous fields compared to homogeneous fields. Consequently, the level of homogeneity of the seismic field is one of the most important properties concerning NN cancellation.

8.3 Array Optimization

There are different methods to find the optimal array, which are all based on minimizing eq. (8.2). The method used in[156] first applies analytic transformations of the equation to determine the optimal array as zeros of a new set of equations. Alternatively, one can directly find the minimal residual by applying generic high-dimensional sampling algorithms such as nested sampling, Metropolis Hastings MCMC, or particle swarm optimization (the last was used in[115]).

The results in this paper were calculated with a Metropolis Hastings MCMC algorithm implementing adaptive simulated annealing (SA), which statistically guarantees obtaining solutions close to global minima[190,173]. The cost function involves a parameter space with dimensionality $2N$ (for N sensors) with numerous local minima. The algorithm should optimize all seismometer locations simultaneously to obtain near to global solutions within a reasonable execution time. SA is a probabilistic method whose name draws inspiration from a metallurgic annealing process where heating followed by slow cooling results in achieving minimum energy configuration in a crystal lattice . The success of the optimization depends on careful selection of the probability distribution $g_T(x)$ used to span the multi-dimensional parameter space, acceptance criteria $h(\Delta E)$ are used to select the newer points and the temperature or the annealing schedule, which determine the level of vigorousness associated with the search. Algorithm is constructed to begin as a random exploration of the parameter space

and then progress with time towards a greedy search.

Usually the acceptance function is given by $h(\Delta E) = 1/(1 + \Delta E/T)$ where ΔE is the difference in cost function between the new and the previous state. The state space probability distribution is given by a Cauchy distribution $g(\Delta x) = T/(\Delta x^2 + T^2)^{(D+1)/2}$. The exponential annealing schedule is used to calculate temperature at future time steps $T_i(k) = T_{0i}\ \exp(c_i k^{1/D})$ with $c_i = m_i\ \exp(-n_i/D)$. Here m_i and n_i act as free parameters that are used to fine tune the optimization process.

The variation in sensitivities of different parameters during the course of the search is addressed by reannealing or rescaling the time-steps after every user-defined number of accepted states. This essentially decreases or increases the range for those parameters, which show more or less sensitivity at the current annealing schedule. Accuracy of the search after each SA iteration is further enhanced by performing a polling based pattern search, which is well suited for carrying out local minimization when the problem at hand is ill-defined and non-differentiable. In our implementation, we perform parallel analysis at each iteration by executing a MATLAB implementation of adaptive SA on different computing cores and selecting the best configuration for use in further iterations. Here the annealing schedule and the process of newer samples generation get adaptively modified so as to achieve accelerated convergence.

For optimizing the array locations, the algorithm is as follows. We will use either the analytic or measured seismometer correlations, denoted C_{SS}. Arrays with N seismometers are then generated by the algorithms. The C_{SS}, and thereby the C_{SN} using eq. (8.3), is then computed for the various cases of seismic correlations. This process is repeated until the algorithm's stopping criterion is reached, and thereafter the array with the smallest residual is taken to be the optimal array.

We make a number of assumptions in the following analysis. We assume that the

seismic field is stationary, or in other words, the calculated arrays ensure best possible cancellation of the stationary background of the NN, while there may exist better arrays when only higher percentiles of the NN are to be cancelled. We also assume a signal-to-noise ratio (SNR) of 100 for the seismic sensors. This may be a challenge in low-noise environments, but at the existing sites of the LIGO and Virgo detectors, the most sensitive instruments in the NN band such as GS-13, STS-2, or T240 have SNRs of a few 1000. We choose for the test mass to be suspended 1.5 m above ground, which is approximately the height of the LIGO test masses. It should be noted though that the test-mass height has no effect on optimal arrays for plane-wave Rayleigh fields. In our simulation, we search for optimal sensor locations within a 100 m $\times$ 100 m surface area with a test mass at its center. This is conservative, as this is larger than the area from which interesting NN contributions are expected[158].

8.4 Results

The structure of this section is as follows. We present the models we use to fit to the measured LHO array seismic field from section 8.2 in subsection 8.4.1. We then use those models in subsection 8.4.2 to find optimal seismic arrays for each of the models presented.

8.4.1 Models

We solve the integrals of eq. (8.3) for various models of the seismic correlation C_{SS}, including an isotropic plane-wave (IPW) model, which takes the form of a Bessel function[115], an isotropic Gaussian model, an anisotropic plane-wave (APW) model, and the case of a single plane wave (SPW).

Explicit expressions for C_{SS} exist for the IPW model, $C_{\mathrm{SS}} = J_0(k|\vec{r}_i - \vec{r}_j|)$, the Gaussian model, $C_{\mathrm{SS}} = \exp(-|\vec{r}_i - \vec{r}_j|^2/\sigma^2)$, and the SPW model, $C_{\mathrm{SS}} = \cos(\vec{k} \cdot (\vec{r}_i - \vec{r}_j))$. In the APW case, the seismic correlations are calculated numerically by averaging plane-wave contributions over propagation directions with a direction dependent Gaussian weight $A(\phi) = \exp(-(\phi - \phi_0)^2/\delta^2)$, where ϕ is the polar angle quantifying the direction of a Rayleigh wave.

Using the LHO array data presented in section 8.2, we perform fits of the above models to the measured C_{SS}. Taking 300 m/s as the seismic speed, we find that at 15 Hz then, the length of seismic waves is $\lambda = 20\,\mathrm{m}$, which directly determines the wavenumbers of the IPW, SPW, and APW models. For the anisotropic model, we find best fit parameters of $\phi_0 = 110^\circ$ and $\delta = 52^\circ$.

The SPW and Gaussian models are not based on independent fits to observed correlations, but are based on the above best-fit parameter values. The reason for this is that both models are poor representations of observed correlations, but serve as lower (SPW) and upper (Gaussian) bound of achievable noise residuals.

The APW value of ϕ_0 is also used for the propagation direction of the SPW model, which, together with the wavelength parameter from above, determines the wave vector $\vec{k}$. The Gaussian model parameter is defined as $\sigma = \lambda/\pi$, which yields $\sigma = 6.5\,\mathrm{m}$. In this way, the Gaussian model is at least a good fit to observed short-range correlations, while neglecting deviations at larger sensor separations. The Gaussian model is an isotropic, homogeneous correlation model, but it implies a significant impact from local seismic sources, which can also include scattering. There is no underlying plane-wave representation of the seismic field since this would necessarily give rise to a IPW or APW type model. The IPW, APW, and Gaussian models evaluated for the sensor pairs of the LHO array are shown in Figure 8.4.

8.4.2 Optimal Arrays

The structure of the optimal array analysis is as follows. For each of the models presented in section 8.4.1, we use the optimization scheme presented in section 8.3 to minimize the NN residuals, given by eq. (8.2), at 15 Hz. We perform the optimization for each of these cases for arrays containing from 1 to 20 sensors, which allows for the exploration of how many sensors are necessary to achieve a required subtraction.

As discussed above, the optimization analysis is performed minimizing residuals at 15 Hz, corresponding to a wavelength of $\lambda = 20\,\mathrm{m}$ assuming a seismic speed of 300 m/s, and a seismometer SNR of 100. On the left of Figure 8.5, we show optimized seismometer arrays with six sensors for all correlation models. The key features of all arrays optimized for a single test mass are that they are symmetric with respect to the x-axis pointing in the direction of the interferometer arm, with their distance to the test mass located at the center of the plot proportional to the wavelength of interest. This optimal distance depends also on the sensor SNR.

The IPW and APW models yield similar optimal arrays with distances between seismometers and the test mass being slightly shorter for the APW model. This greatly facilitates the design of NN cancellation systems, since anisotropies of the field play a minor role. For the SPW model, there are no distinct solutions for optimal seismometer locations. Instead, seismometers can be deployed anywhere on the two dashed lines and lines parallel to this at larger distances separated by half a wavelength. Also the Gaussian model produces a qualitatively different optimal array, which is further evidence of the fact that there is no underlying plane-wave representation of the seismic field.

For all correlation models, seismometer are placed away from the test mass by a

significant fraction of the seismic wavelength. This is because a sensor located directly under the test mass has vanishing correlation with NN, which means that a sensor not directly under but very close to the test mass must have extremely high SNR to show significant correlation with NN. Therefore, given a finite SNR, optimal array configurations with any number of sensors place seismometers sufficiently far away from the test mass according to their SNR, but not so far that correlation with test-mass NN becomes too small for effective cancellation.

Interestingly, in the case of the IPW and APW models, the 6-sensor optimal arrays also represent the optimal locations of arrays with a higher number of sensors. In other words, the optimization algorithm yields solutions where seismometers are placed on top of each other. In practice, this can be realized by placing seismometers as close to each other as possible, or to conclude that instead of adding new seismometers to a 6-sensor array, seismometers with higher SNR should be used. For the same reason, the 6-sensor configuration is independent of the seismometer SNR, which is not true for optimal arrays with less than 6 sensors where seismometers with higher SNR are positioned closer to the test mass.

In the right plot of Figure 8.5, optimized arrays are again shown for the IPW model. The optimal array at the corner station has a different configuration since seismometers are used to cancel NN from both test masses simultaneously. The effect is greatest on placement of seismometers that are close to both test masses. According to these results, seismic arrays for NN cancellation are located completely inside the buildings.

Figure 8.6 shows subtraction residuals. It is assumed that seismometers have a frequency-independent SNR of 100. In the left plot, residual noise spectra relative to the unsuppressed NN spectra are shown using 6-sensor arrays in the case of the sin-

gle test-mass cancellation, and 10 sensors for the 2-mass cancellation. The Gaussian residuals are consistently high over the entire frequency range supporting its role as worst-case scenario. In all spectra, residuals increase towards lower frequencies. It is a consequence of the fact that the ability of an array to extract information from the seismic field as relevant to NN cancellation decreases if the separation between sensors becomes significantly smaller than the seismic wavelength. At high frequencies, wavelengths become smaller than distances between sensors decreasing correlations between seismometers and NN, again degrading the cancellation performance.

Scaling the seismometer locations relative to the test mass by a constant factor, the residual noise spectra of the plane-wave models with a single test mass are simply shifted towards higher or lower frequencies otherwise maintaining absolute values and shapes. This is not the case for the Gaussian model where NN residuals depend on the test-mass height (this dependence cancels out in all plane-wave models), and for the 2-mass IPW model where the distance between test masses introduces another reference length.

The right plot in Figure 8.6 shows noise residuals at 15 Hz as a function of number of sensors. The residuals can be compared with the absolute sensor-noise limit $1/(\mathrm{SNR}\sqrt{N})$ shown as dashed line, which marks the minimal residuals that can possibly be achieved with N sensors independent of the seismic correlation model. Already with 2 or 3 seismometers, residuals are strongly reduced for all plane-wave models. Beyond $N = 4$ sensors, the IPW, APW, and SPW curves approximately follow an asymptote proportional to $1/\sqrt{N}$. In other words, 4 sensors are already able to overcome all geometric limitations so that residuals are purely sensor-noise limited. Nonetheless, the absolute sensor noise limit of $1/(\mathrm{SNR}\sqrt{N})$ is not reached by the IPW and APW models independent of the number of sensors. In the case of the

IPW, residuals for large numbers of sensors lie about a factor $\sqrt{2}$ above the absolute sensor-noise limit.

In summary, depending on the properties of the seismic field, potential subtraction factors using 6-sensor arrays span 3.5 – 250, with the APW model representing the best fit to the observed data and corresponding to a suppression by 140. Since inhomogeneities of the seismic field have not been accounted for, it is to be expected that NN residuals achieved in the future, and optimal array designs differ from these predictions. However, the APW model captures the dominant features of the observed correlations, and therefore the methods and results presented here serve at least as first, albeit simplified design of a cancellation system for LIGO (assuming that the seismic fields at the other LIGO stations are not significantly more complex).

8.5 Conclusion

In this work, we have presented new methods to calculate optimal seismometer-array configurations for Newtonian-noise (NN) cancellation. The results are used to define a first, simplified design of cancellation system applicable to the LIGO detectors.

We first presented analytical expressions that can be used to calculate optimal arrays in seismic Rayleigh fields based solely on models or observations of seismic correlations. The equations are valid even if Rayleigh waves are subject to seismic scattering or produced by local sources. An important assumption though is that fundamental Rayleigh waves dominate the seismic displacement field in the NN band.

The analysis was based on a variety of models of seismic correlation. One of the models is calculated as a fit to seismic correlations observed at the LIGO Hanford site in 2012. It shows that the dominant component of seismic correlations is consistent

with an anisotropic, fundamental, plane-wave Rayleigh field. Inhomogeneities of the seismic field are also revealed, but the effect on seismic correlations is minor. Therefore, the optimized arrays derived from the anisotropic, plane-wave model serve at least as first, simplified design of a NN cancellation system, and it is to be expected that the efficiency of this simplified system can be improved by gradual modifications.

Array data were also used to measure seismic speeds. A histogram of observed seismic speeds presented in this paper shows that fundamental Rayleigh waves are indeed the dominant component of the seismic field at the LIGO Hanford station where the array was deployed.

We showed that cancellation of NN from any type of plane-wave Rayleigh field, i. e. with any degree of anisotropy, is very efficient approaching the sensor-noise limit with only a few seismometers. Cancellation performance was investigated in detail for 6-sensor arrays. Only a Gaussian correlation model, which represents a worst-case scenario with respect to NN cancellation, yields insufficient noise cancellation. However, this model is clearly inconsistent with the LIGO Hanford observation, and therefore the upper limit of noise residuals set by this model only serves as worst-case scenario for sites that have not been characterized yet.

Another requisite for this analysis is that the surface within about a wavelength distance to the test masses is flat. This means specifically that the array designs cannot be readily applied to the Virgo detector where laboratory space below test masses may significantly modify the generation of NN, and of optimal array configurations. In this case, the design of a NN cancellation system must be partially based on numerical simulations to accurately model the effect of seismic scattering and displacement of uneven surfaces.

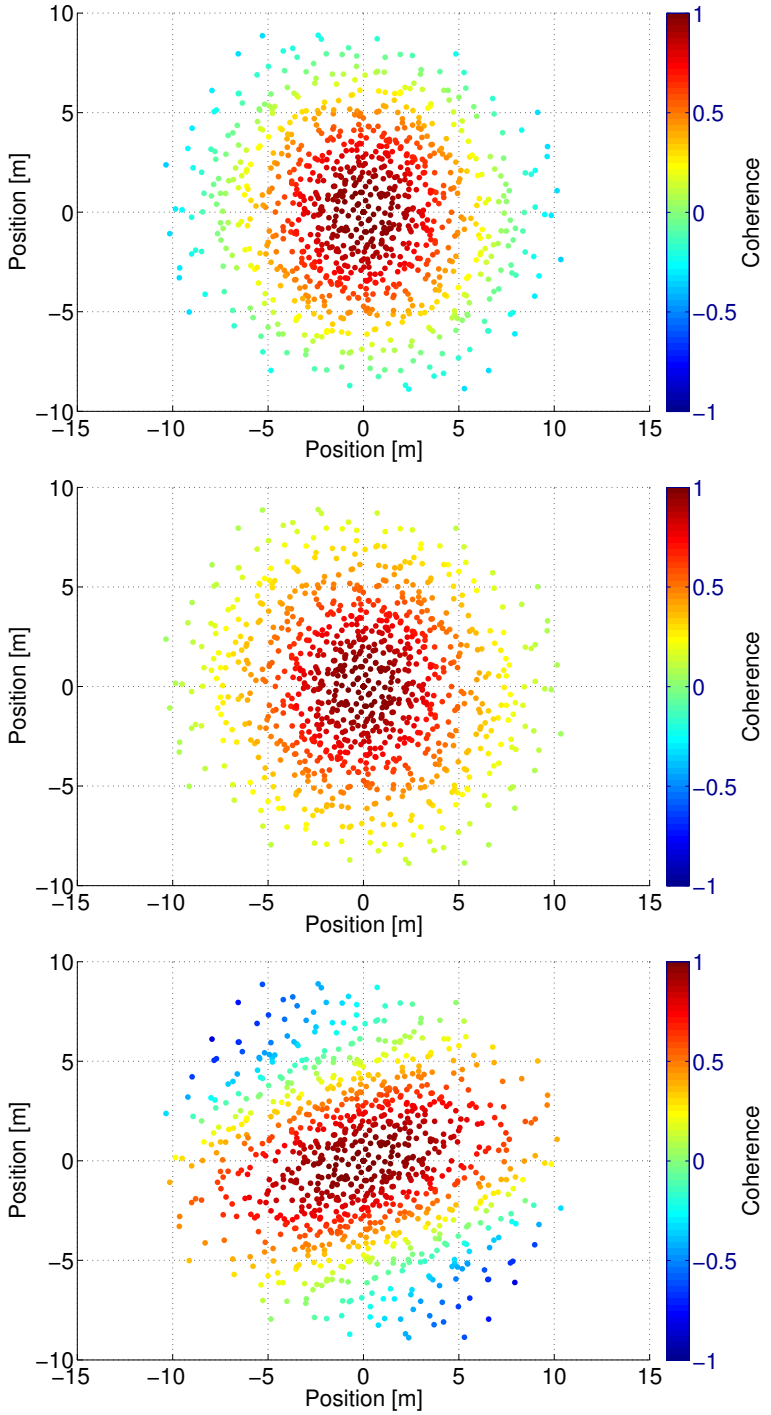


Figure 8.4: From the left to right are the IPW, Gaussian, and APW models for the seismic fields.

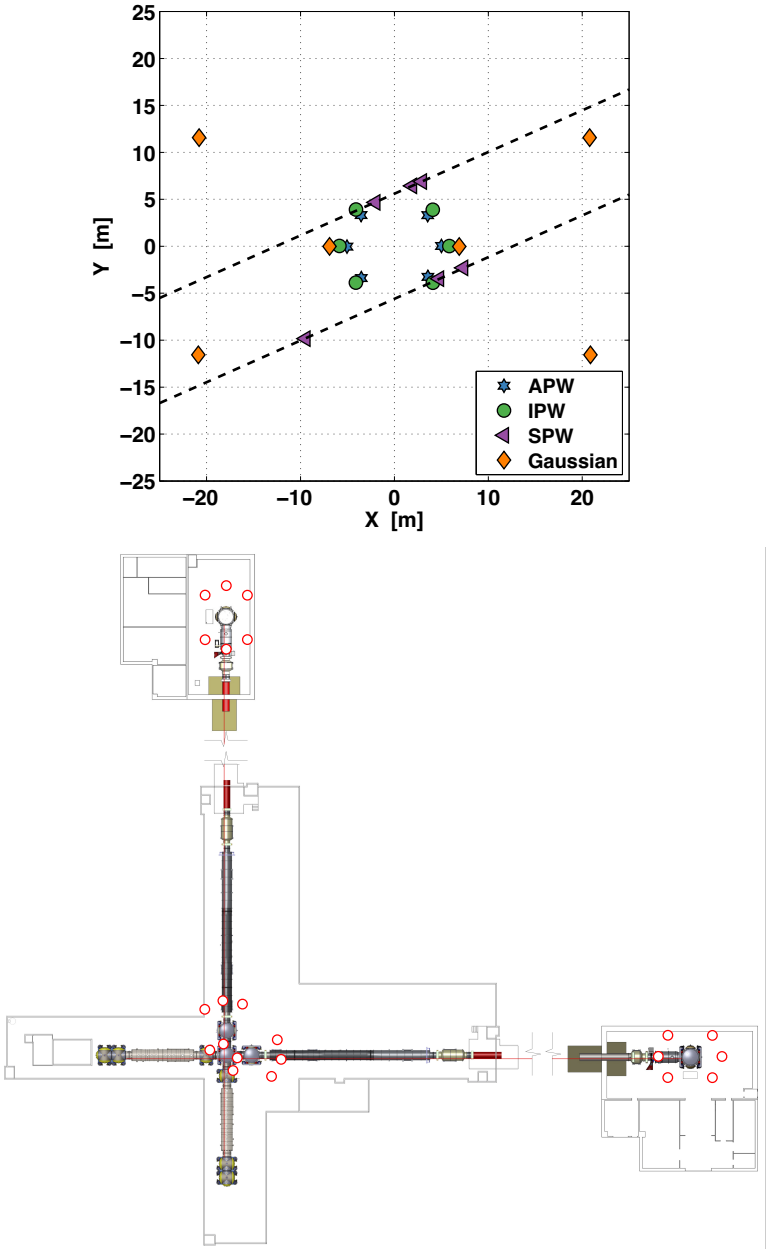


Figure 8.5: On the left are the locations of sensors resulting from numerically minimizing the subtraction residual for the IPW, APW, SPW, and Gaussian correlation functions. The dashed lines indicate that optimal locations of seismometers for the SPW can lie anywhere on these lines. On the right is an example arrangement of seismometers at both end stations and the corner stations, optimized for cancellation at 15 Hz. The end station placement is based on the IPW model discussed in the text. The corner station arrangement is also based on the IPW model, but this time simultaneously minimizing noise residuals from both test masses.

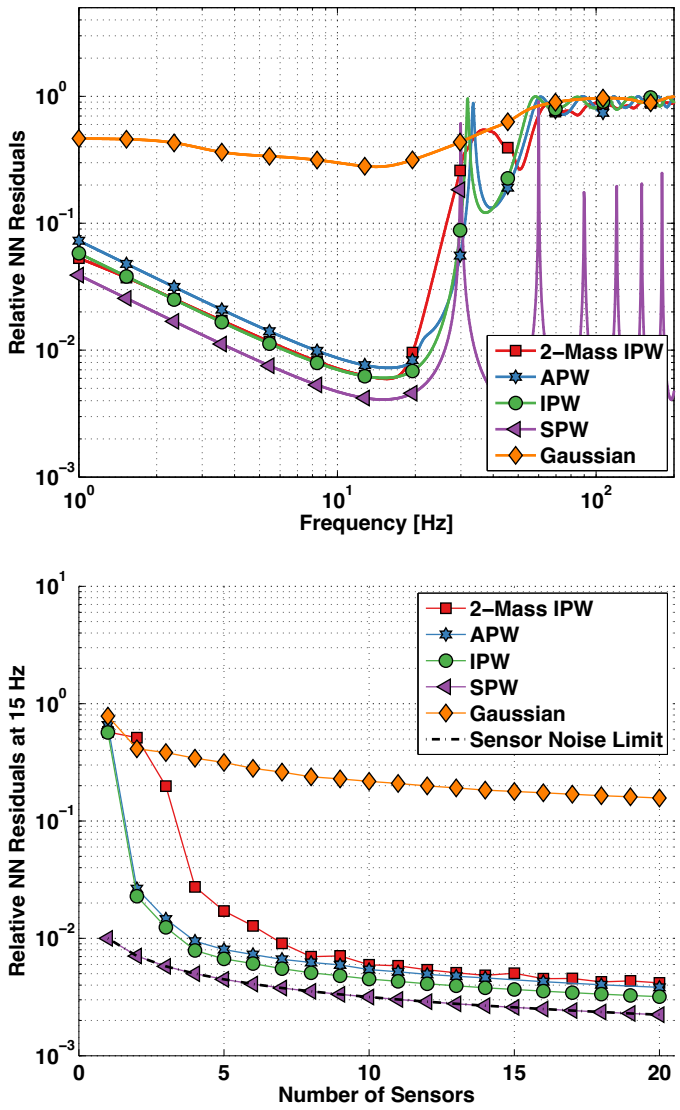


Figure 8.6: The left plot shows the subtraction residual vs. frequency for the optimal arrays based on the various correlation models. The "2-mass" IPW model is for simultaneous minimization of residuals from both test masses at the corner station with a 10 seismometer array. All other curves are for the 6 seismometer arrays shown in Figure 8.5. On the right is the noise reduction at 15 Hz as a function of the number of sensors. For the 6 seismometer arrays, a reduction by approximately a factor of 3.5 is achieved for Gaussian, 150 for IPW, 140 for APW, and 250 for SPW. The last is equal to the theoretical maximum of noise suppression given by SNR $\times\sqrt{N}$.

9

Subtraction of correlated noise in global networks of gravitational-wave interferometers

A stochastic gravitational-wave background (SGWB) is a potential signal source for ground-based, second-generation interferometric gravitational-wave detectors such as Advanced LIGO[180] and Advanced Virgo[295]. An astrophysical SGWB could be produced by objects such as compact binary coalescences, pulsars, magnetars, or core-collapse supernovae. A cosmological background could be generated by various

physical processes in the early universe[17,10]. Previous analyses have achieved interesting constraints on these processes[17,10,3]. In particular, with the recent discovery of a binary black-hole merger[24], there is a chance of observing a SGWB from these systems[20].

Typical searches for a SGWB cross-correlate data from two spatially-separated interferometers, where the detector noise is assumed to be Gaussian, stationary, and uncorrelated between the two interferometers and much larger than the signal. In the case where the noise is uncorrelated, the sensitivity of the search for the SGWB increases with time, $t_{\rm obs}$, and with signal-to-noise ratio (SNR) proportional to $t_{\rm obs}^{1/2}$. Even though the interferometers are spatially separated, with Advanced LIGO consisting of detectors in Livingston, Louisiana and Hanford, Washington, and Advanced Virgo in Cascina, Italy, correlated noise between the detectors has been identified[296,297]. Stationary noise lines, such as those from the 60 Hz power line and 1 Hz timing GPS noise, present at both LIGO sites, were notched in previous data analyzed[209,208,10,3]. Due to the increased sensitivity of second generation detectors, additional magnetic environmental correlations have also been identified[296,297]. These correlations would contaminate the gravitational-wave data streams and thus inhibit the detection of the SGWB. Correlated noise produces a systematic error that cannot be reduced by integration over time and therefore is a fundamental limit for SGWB searches.

Global electromagnetic fields such as the Schumann resonances are an example of environmental correlations between interferometers. By inducing forces on magnets or magnetically susceptible materials in the test-mass suspension system, these fields are predicted to induce correlated noise in the spatially separated gravitational-wave detectors.

Schumann resonances are due to the very small attenuation of extremely low fre-

quency (ELF) electromagnetic waves in the Earth-ionosphere waveguide, which is formed by the highly conducting Earth and the lower ionosphere. The ELF waves are reflected by the lower ionospheric layers at altitudes smaller than the half wavelength, enabling propagation of transverse electromagnetic waves similar to a low-loss transmission line. The attenuation increases with frequency reaching the maximum at the waveguide cut-off frequency of about 1500 Hz. In the lower part of the ELF range, the attenuation rate is particularly small: at 10 Hz it is roughly 0.25 dB/1000 km[199] . This enables observation of strong ELF electromagnetic field pulses (ELF transients) propagating around the world several times.

The main source of ELF waves in the Earth-ionosphere waveguide are negative cloud-to-ground (-CG) atmospheric discharges, in which the vertical component of the dipole moment dominates and effectively generates the electromagnetic waves. An individual -CG discharge is an impulse of current associated with the charge transfer of about 2.5 C in the plasma channel that has a length of 2 to 3 km and lasts for about $75\mu s$. A typical dipole moment (charge moment) of a discharge is about 6 C km[1]. The spectrum of an impulse generated by -CG is practically flat up to the cut-off frequency of the waveguide. On Earth, mainly in the tropics, many thunderstorm cells are always active and produce about 50 -CG discharges per second. Since the vertical atmospheric discharges radiate electromagnetic waves in all directions, it leads to interference of waves propagating around the world. As a consequence, the spectrum of atmospheric noise exhibit resonances. The solutions to the resonance field in a lossless spherical cavity were obtained for the first time by W.O. Schumann[267]. The predicted eigenfrequencies (10.6, 18.4, 26, 33.5 Hz) turned out to be much higher than the observed frequencies, which are close to 8, 14, 20, 26 Hz[46], because of the dispersive character of the attenuation introduced by the ionosphere, which detunes

the Earth-ionosphere cavity[270]. The peaks of the Schumann resonances are relatively wide. Their quality factors for the first three Schumann resonance modes are about 4, 5, and 6, respectively. Due to the attenuation the coherence time of the field in the Earth-ionosphere cavity does not exceed 1 second.

The Schumann resonance background is a global field. The amplitude distribution of the following resonance modes depends on the time of day and year[200]. The spectral density of the first resonance mode is about $1.0\,\mathrm{pT/Hz^{1/2}}$ and is different for different observers because of their location relative to the world thunderstorm centers. The daily and yearly changes in the amplitude are of several tens of percent and are related to the changes of the distance from the active thunderstorm centers (source-observer effect) and the intensity of discharges. These factors have influence on the correlation factor between fields measured in different locations on Earth and at different moments in time.

Strong atmospheric discharges, which are much less frequent, such as positive cloud-to-ground (+CG) discharges and cloud-to-ionosphere discharges associated with Sprites and Gigantic Jets, have a smaller contribution to the Schumann resonance background. Their influence on the fundamental limit for SGWB searches is negligible. However, these discharges generate ELF impulses that have very high amplitudes, so a different approach is required to analyze their influence on detection of gravitational waves.

The Schumann resonances are detected at high SNR with a worldwide array of extremely low frequency (ELF) magnetometers, which generally have the frequency bandwidth of 3-300 Hz, with a sensitivity of $\approx$ $0.015\mathrm{pT/Hz^{1/2}}$ at 14 Hz[146]. These magnetometers can potentially be used to subtract correlated magnetic noise in gravitational-wave detectors. In previous work[296,297], Thrane et al. estimated the effect of the

correlated strain the Schumann resonances would generate for second-generation gravitational-wave detectors and in particular their effect on SGWB searches. In addition to exploring simple Wiener filter schemes using toy models for the gravitational-wave detector strain and magnetometer signals, they show how to optimally detect a SGWB in the presence of unmitigated correlated noise. In this paper, we carry out a demonstration of Wiener filtering with a goal of reducing the coherence between widely separated magnetometers (serving as proxies for gravitational-wave detectors). For our study, we use data from ultra-high-sensitivity magnetometers, which have been deployed for geophysical analyses. Using these previously deployed magnetometers, allows us access to instruments with superb sensitivity, located in very magnetically quiet locations. As shown in[297], this is a requirement for successful subtraction. Unfortunately, the available magnetometers are not situated optimally to reproduce the subtraction scheme we envision for LIGO/Virgo. Ideally, one would want at least one pair of perpendicular magnetometers for each gravitational-wave detector. This witness pair should be far enough from the detector to avoid the local magnetic noise, but close enough that it measures a similar Schumann field as would be present at the detector. For this study, the witness sensors are very far away from the proxy gravitational-wave sensors. Despite these limitations, the work that follows is an important first step to realistic subtraction of correlated magnetic noise in gravitational-wave detectors.

In the most-ideal scenario, magnetometers would be stationed near the gravitational-wave detectors, not directly on-site so as to be directly affected by the local varying magnetic fields, but not so far away as to reduce the coherence of the magnetometers. This is likely to be within a few hundreds of meters of the gravitational-wave detectors. We can test aspects of this by using existing magnetometer infrastructure,

although the distances between these sites are significantly larger. Another caveat is that among the existing magnetometers, the ones near to one another are orthogonal to one another, and so the efficacy of noise subtraction is limited. For these reasons, the work that follows functions as a first step to realistic subtraction of correlated magnetic noise in gravitational-wave detectors.

In this work, we will use ELF magnetometers from two stations of the WERA project *. The Hylaty ELF station is located in the Bieszczady Mountains in Poland, at coordinates 49.2° N, 22.5° E, in an electromagnetic environment with a very low level of anthropogenic magnetic field activity[198]. The Hugo Station is located in the Hugo Wildlife Area in Colorado (USA) at 38.9° N, 103.4° W. Both stations include two ferrite core active magnetic field antennas, one oriented to observe magnetic fields along the North-South direction, the other oriented to observe magnetic fields along the East-West direction. These instruments are sensitive to the Schumann resonances as well as transient signals from individual high peak current lightning discharges. Such large discharges are often associated with so called transient luminous events that occur at stratospheric and mesospheric altitudes[236]. The magnetometers are also sensitive to atmospheric discharges, even when they have a very long continuing current phase. They have a lower cut-off frequency of 0.03 Hz with the overall shape of the spectrum dominated by $1/f$ noise.

In addition to the ELF stations, we will also use magnetic antennas at and nearby to the Virgo site. A temporary station was created at Villa Cristina between June 22-25, 2015 and June 29 - July 3rd, 2015. This location is 12.72 km southwest from Virgo, and the magnetometer was placed on the ground floor of an uninhabited house and oriented North-South. The house was not running electricity, and the nearest

*http://www.oa.uj.edu.pl/elf/index/projects3.htm

location served by electricity is a small service building 500 m away. The house is surrounded by about a 2 km radius of woods, and there was some excess magnetic noise induced by nearby truck transits working on logging. In addition, there are 6 sensitive magnetic antennas located inside of Virgo experimental halls, which are "Broadband Induction Coil Magnetometers", model MFS-06 by Metronix. In the following analysis, we will take a single magnetic antenna from on-site to represent Virgo's magnetic environment, located in the North End Building along the West detector arm. The Virgo detector North arm is rotated about 20 degrees clockwise from geographic North. The Hylaty and Hugo stations are 8900 km away from one another. Hylaty and Villa Cristina and Hugo and Villa Cristina are 1200 km and 8700 km away respectively. This can be compared to the 3000 km separation between the two LIGO sites.

Formalism. Typical searches for a SGWB use a cross-correlation method optimized for detecting an isotropic SGWB using pairs of detectors[33]. This method defines a cross-correlation estimator:

$$\hat{Y} = \int_{-\infty}^{\infty} df \int_{-\infty}^{\infty} df' \delta_T(f - f') \tilde{s}_1^*(f) \tilde{s}_2(f') \tilde{Q}(f') \tag{9.1}$$

and its variance:

$$\sigma_Y^2 \approx \frac{T}{2} \int_0^{\infty} df P_1(f) P_2(f) |\tilde{Q}(f)|^2, \tag{9.2}$$

where $\delta_T(f - f')$ is the finite-time approximation to the Dirac delta function, $\tilde{s}_1$ and $\tilde{s}_2$ are Fourier transforms of time-series strain data from two interferometers, T is the coincident observation time, and P_1 and P_2 are one-sided strain power spectral densities from the two interferometers. The SNR can be enhanced by filtering the data with an optimal filter spectrum $\tilde{Q}(f)$[69,33]. Any correlated noise sources will appear in

the inner product of the two strain channels, $\tilde{s}_1^*(f)\tilde{s}_2(f')$. We can see this by writing

$$\begin{aligned}\tilde{s}_1(f) &= \tilde{h}_1(f) + \tilde{n}_1(f) + k_1(f)\tilde{m}(f) \\ \tilde{s}_2(f) &= \tilde{h}_2(f) + \tilde{n}_2(f) + k_2(f)\tilde{m}(f)\end{aligned} \tag{9.3}$$

where $\tilde{h}_i(f)$, $\tilde{n}_i(f)$, and $k_i(f)$ are the gravitational-wave strain, the independent instrumental noise, and the magnetic coupling transfer function respectively. $\tilde{m}(f)$ is the correlated magnetic spectrum, which is the same at both detectors. The effect of the local varying magnetic field on the interferometers is contained within the $\tilde{n}_i(f)$ terms, and in principle, on-site magnetometers can be used to monitor and subtract their effect from the data. One metric for measuring this correlation is the coherence $c(f)$

$$c(f) = \frac{\overline{\tilde{s_1}(f)\tilde{s_2}(f)^*}}{\overline{|\tilde{s_1}(f)||\tilde{s_2}(f)|}} \tag{9.4}$$

where $\tilde{s_1}(f)$ and $\tilde{s_2}(f)$ are the Fourier transforms of the two channels.

A proposed method for mitigating magnetic noise in gravitational-wave detectors is to coherently cancel the noise by monitoring the magnetic environment. There are two potential ways this could be done. First, one could directly correlate magnetometer and gravitational-wave strain data to calculate a *Wiener filter*. This has the benefit of not relying on any magnetic coupling models, but the downside is that the Wiener filter will require very long correlation times to potentially disentangle local magnetic foreground from Schumann resonances and due to the small coherence between magnetometers and strain data.

The other option is to use magnetometers as witness sensors for magnetic noise produced at each test mass, apply measured magnetic coupling functions to strain data, and subtract these channels from the strain data. This has the benefit of not

relying on weakly correlated measurements as in the case of the Wiener filter, but the downside is that there is no direct feedback on errors in the coupling model and cancellation performance. This transfer function model, which will depend on the propagation direction of the electromagnetic waves, will be difficult to compute precisely in practice also because of the correlation of the Schumann resonances between test masses, and magnetic coupling can potentially also vary with time. If, for example, the Schumann resonances produce very similar noise at two test masses, very precise estimates of the coupling are required to perform accurate subtraction (although this also implies that the Schumann resonances will produce smaller strain noise). Otherwise, measurement errors in the coupling function could dominate the error of the Schumann noise estimate in the gravitational-wave strain channel. Both options are similar in the sense that they both rely on the use of witness sensors, with transfer functions either provided by a Wiener filter in the first case or a magnetic coupling model in the second case.

In this paper, we test noise subtraction between magnetometers as a first step towards subtraction of correlated noise from interferometer strain channels. Cancellation filters applied to magnetometers can be implemented in the time-domain as vectors of real numbers representing impulse responses and convolved with the input signal to obtain the vector to subtract from the gravitational-wave channel[88]. The idea is to predict the correlated noise seen in the target channel, which could be either a gravitational-wave strain channel, or, as in the case presented in this study, a magnetometer, using witness sensors, which are magnetometers. We are only able to test certain aspects of this calculation, as a gravitational-wave interferometer has more than one test-mass with non-trivial couplings between them. The witness sensors are used to predict and subtract the noise in the target channel. In the case where the

witness sensors have infinite SNR, only the non-correlated residual remains.

To maximize the efficacy of the filter, it is necessary to compute the filter during times of minimal local varying magnetic field activity, or equivalently, during times when the witness sensors are mostly detecting global electromagnetic noise. The calculation of the filter coefficients depends on the autopower spectra of the input channels as well as the average correlation between channels. The noise cancellation algorithm can then be written symbolically as a convolution (symbol $*$)[309,88]:

$$r(f) = y(f) - \sum_{m=1}^{M} (a_i * x_i)(f) \tag{9.5}$$

where f is the frequency, $r(f)$ is the residual (or the cleaned data channel), a_i is the correlation coefficient, $y(f)$ is the target channel, and x_i are the witness channels. The convolution is defined as

$$a_i * x_i = \sum_{i=-N}^{N} a[n]x[i-n], \tag{9.6}$$

where N is the number of filter coefficients. In this analysis, $y(f)$ corresponds to $\tilde{s}_i(f)$ from equation 9.3. One can predict the residual for a single witness sensor using the equation[88]

$$r(f) = \frac{1}{\sqrt{1 - c(f)^2}}. \tag{9.7}$$

where $c(f)$ is the coherence calculated in equation 9.4.

Data analysis. Figure 9.1 shows the power spectral density (PSD) of magnetic antenna data for the sites of interest in this analysis. The broad peaks at 8, 14, 21, 27, and 32 Hz in the spectra correspond to the Schumann resonances, while there are many sharp instrumental line features in the Virgo spectra and two in the Villa

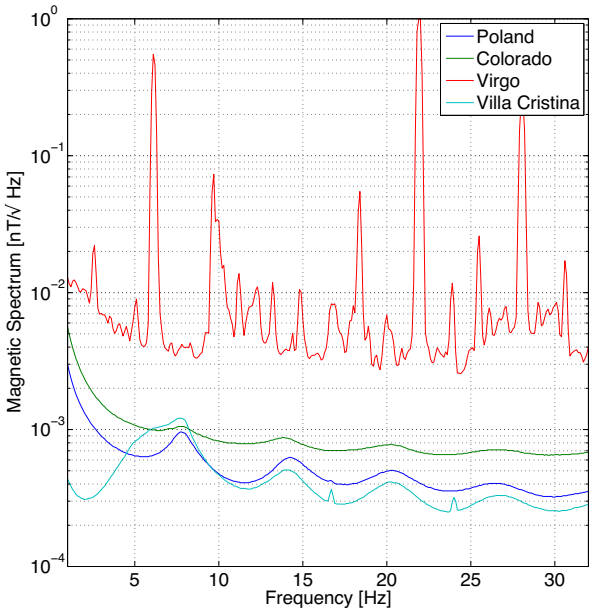


Figure 9.1: The median power spectral density of the North-South Poland, North-South Colorado, Virgo, and Villa Cristina magnetic antennas. These are computed using 128 s segments. The Hylaty station in Poland, Hugo station in Colorado, and Villa Cristina antennas all achieve peak sensitivities of less than $1\,\mathrm{pT}/\sqrt{\mathrm{Hz}}$, while the local varying magnetic field at Virgo prevents those magnetic antennas from reaching that sensitivity.

Cristina magnetic antenna as well. It is clear that the ELF stations contain sufficient sensitivity to detect the Schumann resonances at high SNR. On the other hand, the magnetic antenna stationed inside of Virgo is dominated by local varying magnetic fields as well as the 50 Hz power-line and associated sidebands. For these local magnetic antennas, suppression of the power-line noise will be important to maximize the potential subtraction of the underlying Schumann resonances. We can use this power-spectrum, in addition to the most recent magnetic coupling function published in[19], to determine the effect the global electromagnetic noise has on SGWB searches. We note here that the calculation of common and differential mode coupling performed

are conservative and in the future, separate coupling functions for each test mess would be ideal[297].

We can relate the strain noise induced by the magnetic fields, $S_{\rm MAG}(f)$, which is the magnetic power spectrum multiplied by the magnetic coupling function, to $\Omega_{\rm MAG}$ by[10]

$$\Omega_{\rm MAG} = \frac{10\pi^2}{3H_0^2} S_{\rm MAG}(f) f^3 \tag{9.8}$$

where we assumed a value $H_0 = 67.8\,\mathrm{km/s/Mpc}$ for the Hubble constant[77]. The Schumann resonances induce correlated noise such that $\Omega_{\rm MAG} = 1 \times 10^{-9}$, which is a potential limit for Advanced LIGO. Here we have integrated over a year at design sensitivity and included the Schumann frequency band. We note here that the Schumann resonances are strongest in the fundamental and first few harmonics and as well as the fact that the magnetic coupling is the strongest at the lowest frequencies[19]. For these reasons, if instead of performing a SGWB search from 10 Hz, one integrates from 25 Hz, the effect from the Schumann resonances on SGWB searches decreases by about an order of magnitude.

The left of Figure 9.2 shows the coherence between the North-South Poland and North-South Colorado, Virgo, and Villa Cristina magnetic antennas. The coherence between Poland and Colorado and Villa Cristina show clear peaks in the coherence spectrum, while the coherence between the Virgo and Poland stations are less pronounced due to very high local magnetic noise level at the Virgo site. The right of Figure 9.2 shows the variation in the coherence between the Hylaty station in Poland and Villa Cristina stations. These coherent peaks are potentially problematic for the SGWB searches. The most important peaks for the gravitational-wave detectors are the secondary and tertiary harmonics at 14 Hz and 20 Hz respectively, as the primary

is below the seismic wall of the gravitational-wave detectors at 10 Hz. In the future, it will be beneficial to measure the coherence between quiet magnetometers stationed near LIGO and Virgo. As we show below, high coherence indicates the potential for significant signal subtraction.

Figure 9.3 shows the time-frequency coherence between the North-South Poland and North-South Colorado stations on the left and the coherence time-frequency map between two co-located but orthogonal Hylaty station in Poland magnetic antennas on the right. These plots indicate that the Schumann resonances are only present, at least at detectable levels, at certain times and not others. The coherence between the two perpendicular Hylaty station in Poland magnetic antennas show relatively weak coherence due to the fact that they overlook different regions of the thunderstorm activity on Earth. In addition, their correlation is dominated by collocated magnetic fields, predominantly due to nearby thunderstorms, which can lead to ADC saturations.

Typically, Wiener filters are used to make a channel less noisy, e.g.,[88]. The success of the filtering procedure is determined based on the observed reduction of the channel's auto power spectral density. However, when the goal is to minimize correlated noise in two channels, we must use a different metric to determine the efficacy. In the case of Schumann resonances, the noise in question contributes a very small amount to the auto power spectral density in each gravitational-wave strain channel, perhaps 0.1%. The key metric for our study is the reduction in coherence between the two channels.

As described above, Wiener filtering allows for the subtraction of noise from a particular target channel using a set of witness channels. It is instructive to think of the target magnetometer as a proxy for a gravitational-wave interferometer strain

channel. The above analysis is similar to the potential scenario in subtraction of the Schumann resonances from gravitational-wave interferometer strain channel data. In this case, both on-site and off-site magnetometers will be used in coordination to subtract the effects of both local and global electromagnetic fields from the strain data. If the local varying magnetic fields have a difference in phase and/or direction with the global magnetic fields, their use will likely inject extra noise from the Schumann resonances when subtraction is performed. In our particular example, we take the North-South Poland magnetic antenna as our target channel and the East-West Poland magnetic antenna, the two Colorado magnetic antennas, and the Villa Cristina magnetic antenna as the witness channels. Using both of the magnetometers allows for coverage of both the North-South and East-West magnetic fields. The idea is that using closely spaced, orthogonal magnetometers are likely to contain complementary information, even if local varying magnetic field disturbances will be correlated between them. On the other hand, using co-located magnetometers measuring magnetic fields in the same direction, assuming the local varying magnetic fields dominate, provides higher SNR for the Wiener filter if and only if the intrinsic noise (not due to the global electromagnetic noise) in each magnetometer is independent. This example shows the subtraction that can maximally be expected given the currently deployed sensors in this study and properties of the local varying magnetic fields. It is also similar to the gravitational-wave detector case in that the magnetometers used to perform coherent subtraction will be a combination of local magnetometers to subtract the local varying magnetic fields and magnetometers installed outside of the gravitational-wave detector beam arms to maximize coherence with the Schumann resonances; this has the benefit of limiting the effects from the local varying magnetic fields on site, which can be quite strong[179]. In this case, using two witness sensors

subject to the same local varying magnetic fields is suboptimal, as any noise in the witness sensors limits the efficacy of the subtraction. In the case where the witness sensors have the same limiting noise source, which is generally a sum of instrumental and environmental/local noise sources, the effective coherence will be dominated by the local varying magnetic fields. This is true regardless of the target sensor, be it another magnetometer or a gravitational-wave detector strain channel. This noise floor will set the possible SNR for Wiener filtered subtraction, which must be high enough to provide the required subtraction.

On the left of Figure 9.4, we show the subtraction using a frequency domain Wiener filter between 1-32 Hz where we use 30 minutes of data to generate the filter. In this analysis, we use a time with minimal local disturbances to estimate the Wiener filter and apply it across the entire run. This makes an implicit assumption that the correlation between the target and witness sensors is not changing significantly with time. We have checked that updating the Wiener filter every five minutes gives similar results, indicating that the time-scale does not make a significant difference in this case for the magnetic field subtraction. Magnetometers dominated by local varying magnetic fields may require regular updates if the local varying magnetic field is changing often such that the sensitivity between the gravitational-wave detectors and magnetometers to the Schumann resonances changes. In the case where the target sensor is a gravitational-wave strain channel, it will likely be useful to regularly update the filter due to possible changes in the magnetic coupling function of the detector with time. The time between updates will be affected by interferometer commissioning activities interspersed with data acquisition. The coherence results discussed above give us an expectation of the amount of subtraction we can expect between magnetometers using equation 9.7. This is consistent with the result of the Wiener filter implementa-

tion.

We now turn our attention to the metric most appropriate for searches for stochastic gravitational-wave backgrounds. We can use the available magnetic antennas as a proxy for a 2-detector for a gravitational-wave interferometer network. We assign the North-South Colorado and Villa Cristina magnetic antennas to be gravitational-wave strain channels and use the North-South Poland magnetic antenna to subtract the coherent Schumann resonances. On the right of Figure 9.4, we measure the coherence between the North-South Colorado and Villa Cristina magnetic antennas before and after the subtraction, to measure the effect that the Wiener filtering has had on the correlations. We find a reduction of approximately a factor of 2 in coherence near the peak of the dominant harmonic.

Using the results of Thrane et al.[297], we can place these results in context for Advanced LIGO. The authors of that work showed that the integrated SNR from correlated magnetic noise in one year of coincident data from the LIGO Hanford and Livingston detectors operating at design sensitivity is between 24-470, depending on magnetic field coupling assumptions, significantly limiting a potential measurement of $\Omega_{\rm GW}$. With the help of recent commissioning activities to improve the magnetic coupling functions, these numbers are likely to be a worst-case-scenario. The idea is that correlated noise can only be safely ignored in SGWB searches if the SNR contribution from correlated noise is much less than 1. As SNR $\propto \tilde{r}_1^* \tilde{r}_2 \tilde{m}_1^* \tilde{m}_2$, any reduction made in the power spectrum of the magnetic noise $\tilde{m}_1^* \tilde{m}_2$ will reduce the SNR by that same factor. One possibility to improve upon this subtraction would be to use multiple sensors to improve the effective SNR of the witness sensors. Another (perhaps more promising) possibility would be to use magnetometers located closer to the gravitational-wave interferometer site.

Conclusion. In summary, the magnetic fields associated with Schumann resonances are a possible source of correlated noise between advanced gravitational-wave detectors. The optimal method for subtracting correlated noise in these detectors is Wiener filtering. In this paper, we have described how the global electromagnetic fields create a potential limit for SGWB searches with advanced gravitational-wave detectors. In particular, without subtraction, the Schumann resonances induce correlated noise such that $\Omega_{\rm MAG} = 1 \times 10^{-9}$, using the most recent magnetic coupling function published in[19] and neglecting common-mode rejection, is a potential limit for Advanced LIGO, where we have integrated over a year at design sensitivity and included the Schumann frequency band. We have also discussed the implications of the coherence achieved between extremely low frequency magnetometers in their use in stochastic searches. This coherence is sensitive to the magnetometer SNR of the Schumann resonances to the fundamental instrument noise as well as the local varying magnetic fields. Both the LIGO and Virgo sites will benefit from sensitive magnetometers at magnetically quiet locations that are outside of the buildings housing the gravitational-wave detectors. We have also shown that careful treatment of the magnetometer data, which include significant sensitivity fluctuations due to local varying magnetic fields, will be required for subtraction of the Schumann resonances. We show that magnetometer pairs thousands of kilometers apart are capable of reducing magnetic correlations by about a factor of 2 at the fundamental peak. This gives hope that magnetometers near to the interferometers can effectively subtract magnetic noise with Wiener filtering.

There is significant work to be done looking forward. It will be a challenge to measure the Schumann resonances at the sites due to the local magnetic foreground. It will be important to perform a similar measurement where the distance between

the magnetometers is similar to the distance between the magnetometer and the gravitational-wave detectors, which will allow for updated coherence calculations. Finally, it will be useful to have coupling measurements at all of the test masses at the gravitational-wave interferometers, which will determine the level of the correlations of the Schumann resonances at multiple test masses.

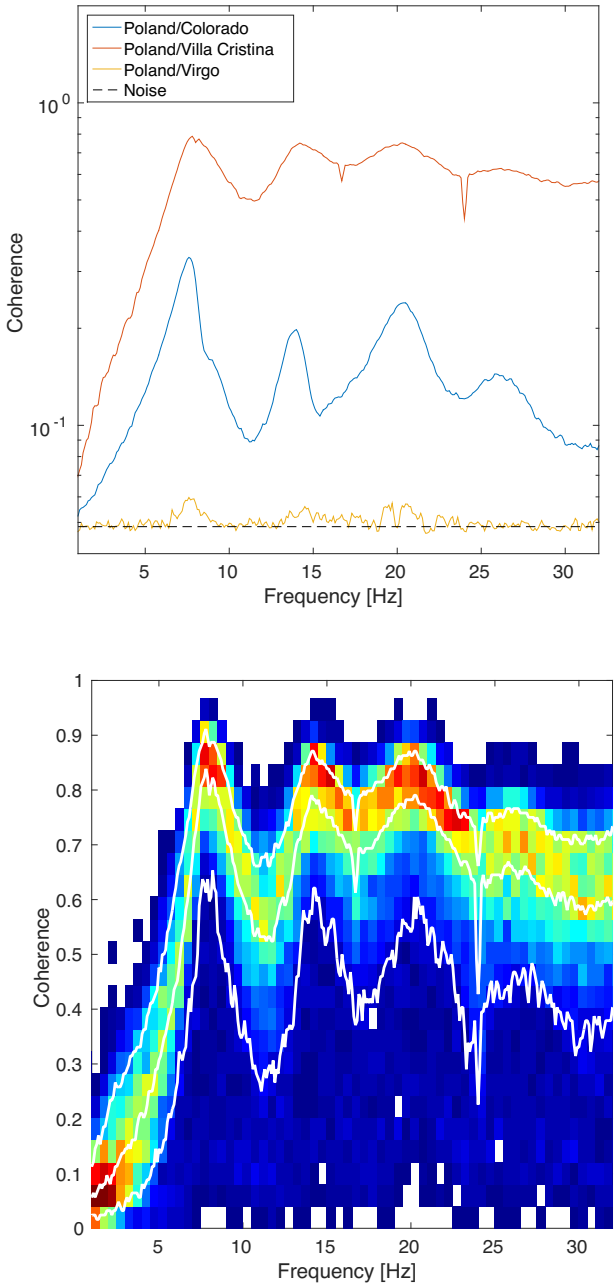


Figure 9.2: The plot on the left is the coherence between the North-South Poland, North-South Colorado, Virgo and Villa Cristina magnetic antennas over 4 days of coincident data divided into 128 s segments. In addition, we plot the expected correlation given Gaussian noise. The coherence between the Virgo and Villa Cristina antennas is similar to that of Virgo and North-South Poland. The plot on the right is the variation in the coherence between the Hylaty station in Poland and Villa Cristina. The colors represent the percentage of the segments which have any given coherence value. The white lines represent the 10th, 50th, and 90th coherence percentiles.

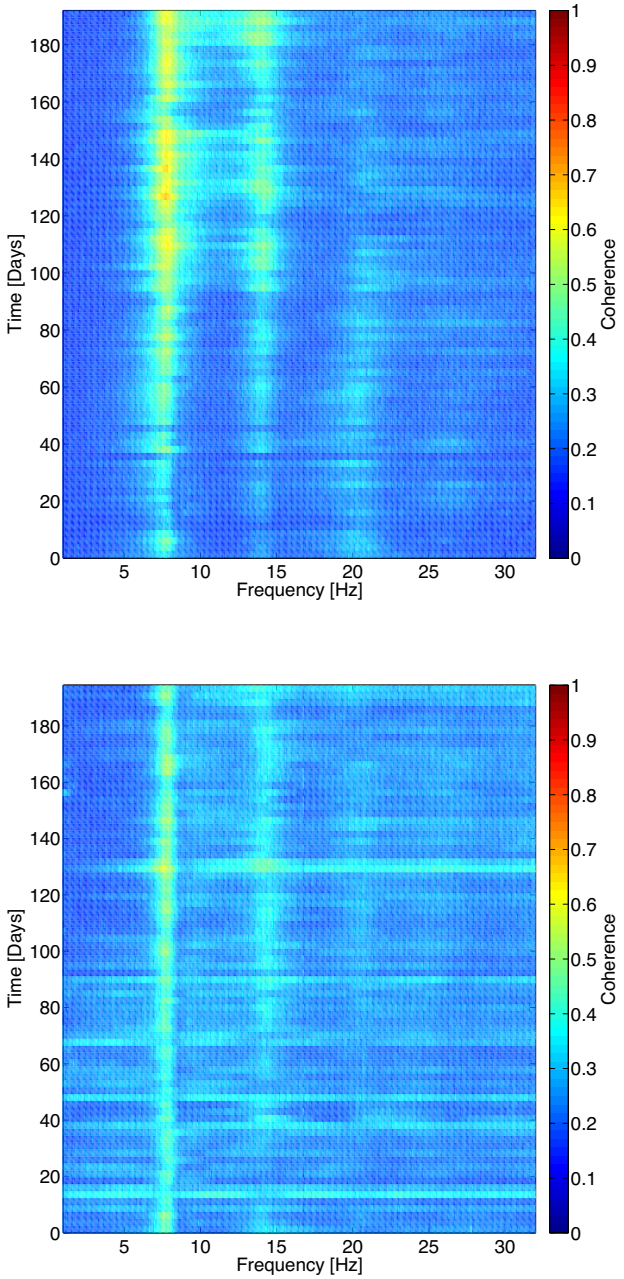


Figure 9.3: The plot on the left is a time-frequency map of the coherence between the North-South Poland and North-South Colorado magnetic antennas. The plot on the right is the same between the North-South and East-West Hylaty station in Poland magnetic antennas.

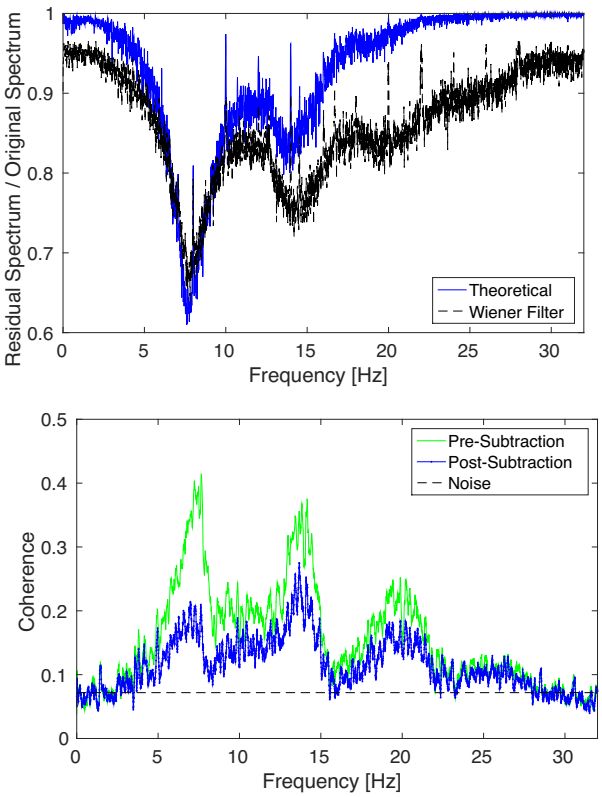


Figure 9.4: Success of the Wiener filtering procedure under two metrics: reduction in auto power spectral density and reduction in coherence. On the left is the ratio of the auto power spectral density before and after Wiener filter subtraction using the North-South Poland antenna as the target sensor and East-West Poland magnetic antennas, the two Colorado magnetic antennas, and the Villa Cristina magnetic antenna as witness sensors. The "theoretical" line corresponds to the expected subtraction from the maximum coherence between the target and witness sensors (in any given frequency bin) given by equation 9.7, while the "subtraction" line corresponds to the subtraction achieved by the Wiener filter. The "subtraction" line exceeds the performance over the "theoretical" over part of the band because it ignores the benefit of having multiple witness sensors. On the right is the coherence between the North-South Colorado and the Villa Cristina magnetic antenna before and after Wiener filter subtraction using the North-South Poland antenna. There is approximately a factor of 2 reduction in coherence at the fundamental Schumann resonance.

10

Real-time earthquake warning for astronomical observatories

Early earthquake warning (EEW) is a rapidly developing field, which includes the efforts of California systems such as Berkeley's ElarmS and Stanford's Quake-Catcher Network, Japan's Earthquake Early Warning System, and systems in other countries, including Taiwan, Mexico, Turkey, and Romania[252,201,202,203,74,75,63,168]. All EEW systems seek to rapidly detect and characterize earthquakes to give warning to people before the most severe shaking occurs. In general, longer warning time allows more protective action to be taken.

Earthquakes are a potental problem for large-scale scientific experiments. They are of course dangerous as well for the personnel inside of the facilities, although in this paper, we will focus on the facilities themselves. There are three potential consequences of seismic events to scientific facilities. The first is physical damage to components and systems. Damage has economic consequences due to the procurement of replacement parts plus the cost of down time. The second is loss of operating time, which has the consequence of not taking data and therefore a loss of efficiency. The third is loss of information due to damaged data storage systems and the cost is replacing the data and information. Our goal is to maximize the protection of these facilities to minimize the losses to instruments and minimize downtime. Examples of recent experiments that have been affected by earthquakes are astronomical observatories, such as meter-class telescopes and gravitational-wave interferometers. In this study, we will explore the potential benefits of EEW for these two types of astronomical observatories. Due to design differences, these two types of facilities represent the opposite ends of the spectrum of sensitivity to earthquakes. Telescopes are primarily susceptible to large, regional earthquakes which can potentially damage the instruments, while gravitational-wave observatories are sensitive to earthquakes that occur around the world, creating ground motion that makes it difficult to take data.

In the case of telescopes, the predominant concern is the potential for large ground motions which might damage the telescope drives, instruments, enclosures or the mirrors. The telescope facilities typically have extensive performance requirements related to their ability to either remain operational during or simply survive the passing of seismic waves. The requirements are broken up into two types. "Operational" earthquakes are relativity small magnitude earthquakes, and modern telescope systems are designed to withstand them with no structural yielding or loss of function,

with expected repair times on the order of days (not including re-verification and testing). "Survival earthquakes" are large earthquakes, and systems must be designed to not fail (exceed ultimate stress), especially if a failure could lead to loss of life, damage exceeding millions of dollars, or repair times on the order of years. Thus, any significant damage to an instrument, filters, or wholesale dropping of jetsam onto the primary, second, or tertiary mirror are to be avoided. The performance requirements are created based on probabilistic ground motion levels for the sites on which the telescopes are situated, depending on the occurrence of regional earthquakes[133]. The Large Synoptic Survey Telescope (LSST), in particular, uses estimated survival levels for earthquakes that have a 10% probability of occurring within a 30 year lifetime[226]. These analyses informed the LSST seismic design requirements[227]. LSST has specifications to remain operational after sustaining accelerations of 3.8 g transverse, 1.21 g along +Z-axis, and 1.86 g along -Z-axis, while survival earthquake levels are 5.7 g transverse, 2.04 g along +Z-axis, 2.45 g along -Z-axis.

A recent example of significant telescope downtime was from the magnitude 6.7 Hawaiian earthquake (with a 6.1 aftershock) on October 16, 2006. The epicenter was 58 km away from the Keck telescopes, at a depth of 29 km. After the earthquake occurred, it took more than a month for Subaru, Keck 1, Keck 2, CFHT, and Gemini to return to full operations[329]. Although the domes and shutters were largely spared from damage, on Keck I the azimuth drive track and encoder surface was damaged by significant translation of the telescope, which was about 12 mm. There was also significant damage to individual instruments. A more recent example is the Arecibo Observatory 305 meter radio telescope in Puerto Rico which has cables that were seriously damaged from a 6.4 magnitude earthquake in January 2014. The earthquake was 78 km from the telescope, at a depth of 20 km. There are also examples of large

earthquakes that did not generate damage. The April 1, 2014, 8.2 magnitude earthquake near Iquique, Chile did not damage the Chilean telescopes. The earthquake was 1047 km from the Magellan telescope, at a depth of 25 km. The Lick observatory was not damaged by the August 2014 Napa Valley Earthquake. The earthquake was 115 km from the telescope, at a depth of 11 km. This earthquake has been thoroughly analyzed in a recent series of articles, which show that another large earthquake is likely to occur in the same region in the near future[64,129,127]. It is clear from recent history that damage to telescopes will depend significantly on the particular situation, specifically distance, magnitude, and the particular telescope in question. Heuristically, these examples suggest that earthquakes closer than 100 km are required to do the most damage, and we show why this is likely to be the case in section 10.2.

The Laser Interferometer Gravitational-wave Observatory (LIGO)[180], Virgo[134], and GEO600[152] detectors are part of a network of gravitational-wave interferometers seeking to make the first direct observations of gravitational waves. These detectors are designed to limit their sensitivity to environmental effects, such as from local magnetic fields or ground motion, but they are still susceptible to a variety of instrumental and environmental noise sources that decrease their detection sensitivity[71]. Environmental noise can couple into the interferometer through mechanical vibration or because of electromagnetic influence. When an interferometer is running with low noise, data are recorded in what it is called "science time" and the interferometer is said to be "locked."

Seismic motion from human activity near the sites, from wind, and from ocean waves are among the most common sources of disturbances that affect the detector. Earthquakes, due to the ground motion they induce, can destabilize the gravitational-wave detectors. The predominant concern is the difficulty of staying locked during the

presence of ground motion from teleseismic signals from around the world[214]. The second-generation gravitational-wave detectors contain upgraded seismic isolation systems (see[22,284] and references therein). The interferometer optics use seven stages of isolation for the core optics, two internal, one external, and four passive (pendulums). Both the first external stage and internal stages use position and inertial sensors along with actuators to limit their platforms' motion. Despite this sophisticated system, the optics are still affected by the ground motion during earthquakes. Another potential concern is simultaneous arrival of transient seismic disturbances that masquerade as false gravitational-wave signals.

During the last LIGO science run, large amplitude earthquakes from around the world would typically cause the detectors to fall out of lock. Not only were the data around the time of the earthquake not useful for gravitational-wave detection, but it would also take hours of dead time for the detectors to return to the locked state. Although there have not yet been detailed studies of this phenomenon (currently underway to characterize the effects on the advanced detectors), we can perform a simple back-of-the-envelope calculation. During the last data collection run, the Hanford and Livingston detectors took 245.6 and 225.2 days of science time respectively[126]. Taking the earthquakes with magnitudes greater than 6.0 that occured during that time, loss of interferometer lock occurred 139 times for Hanford and 127 times for Livingston within an hour of the expected surface wave arrivals. The dropouts incurred caused a total downtime of 12.8 and 17.1 days respectively. Although these estimates are likely conservative (loss of lock occurs for a variety of reasons), they provide an order of magnitude estimate of the potential gains to be made with an early warning system assuming that the incurred downtime could be reduced with sufficient advance notice of the earthquakes' arrivals.

In this paper, we will describe the benefits of a potential early warning system to astronomical observatories. We quantify the ground motion from earthquakes that these detectors are likely to experience and attempt to quantify their effects based on seismic data from near the observatories. In section 10.1, we outline the background of earthquakes and their identification. In section 10.2, we describe seismic hazard formalism and their application to observatories. In section 10.3, we outline the benefits of potential early warning systems to observatories. In section 10.4, we determine the optimal distance at which a circular seismic array could be deployed to maximize the efficacy of an early earthquake warning network for a telescope in Chile. In section 10.5, we offer concluding remarks and suggest directions for future research.

10.1 Earthquake Properties and Identification

We begin by presenting a review of earthquakes and their identification. Seismic waves can be split into two major categories, surface and body waves. Surface waves travel across the surface of the Earth, while body waves travel through the interior. Body waves propagate in three dimensions, radiating away from the epicenter. Surface waves instead propagate in two dimensions, which means they decay more slowly with distance than the body waves. Surface waves also tend to have larger displacement amplitude than body waves, which increases the damage they cause. As body waves travel through the Earth, they are refracted by variations in seismic speed.

There are two predominant types of body waves, both of which will be important for low-latency earthquake identification. The first are primary waves (P-waves), which are compressional longitudinal waves. They are the fastest of the wave types, with typical speeds ranging from 6-13 km/s (although in some soils these velocities

can be much lower), and therefore arrive at seismometers first. Low-latency epicenter location estimates typically rely on the P-wave arrivals at a number of stations. The second category of body waves are secondary waves (S-waves), also known as shear waves, which are transverse waves. Shear waves arrive after the P-waves, with typical speeds ranging from 3-6 km/s (although, again, in some soils these velocities can be much lower). They do not travel through fluids, such as the outer core, as shear stresses are not supported in fluids.

Surface waves come in three different flavors, Rayleigh waves, Love waves, and Stonely waves (Stonely waves are interface waves and are not important for this discussion). Rayleigh waves travel along the surface of the Earth with a velocity lower than those of the body waves. Love waves also travel along the surface of the Earth, but with velocity equal to that of shear waves. They travel more slowly due to lower shear wave velocities near the surface of the Earth. Love waves also experience significant dispersion as they travel along the surface, which stretches out their arrival at a given location in time. They also tend to have larger amplitudes than body waves. Large-amplitude earthquakes are capable of driving up the normal modes of the Earth[178]. Earth's slowest normal-mode oscillation occurs at about 0.3 mHz, and distinct modes can still be identified up to a few millihertz. At higher frequencies, the discrete vibrational spectrum transforms into a quasi-continuous spectrum of seismic vibrations that are increasingly driven by local sources.

We now briefly describe the process by which earthquakes are identified and what the ground motions due to the events look like. Figure 10.1 shows example timeseries at a seismic station at LIGO Hanford for the April 1, 2014, 8.2 magnitude earthquake near Iquique, Chile. After an earthquake occurs, seismometers nearest the epicenter first record the P-wave arrival times. Using a number of arrival times, the time,

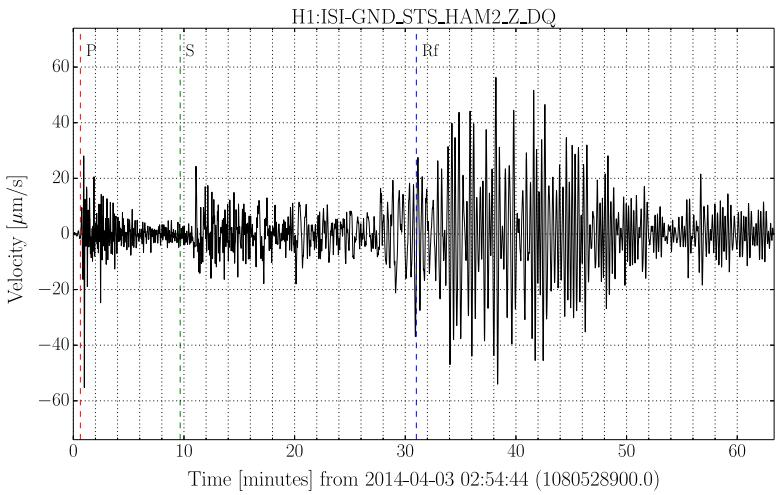


Figure 10.1: Time-series of vertical ground motion from the April 1, 2014, 8.2 magnitude earthquake near Iquique, Chile at the LIGO Hanford site located in Washington, USA. The P, S, and surface waves all have distinctive arrivals and are indicated with P, S, and Rf respectively. The surface waves are shown to last tens of minutes.

latitude, longitude, and depth of the event can be determined. Magnitude estimates come later, which measure the total moment release of the earthquake. This is computed by multiplying the distance a fault moved and the force required to move it. This corresponds to the product of the fault area, the average displacement, and the rigidity modulus. Seismometers read out the ground velocity beneath them. Conventional seismometers are simple to convert from raw data to ground velocity, as their frequency response is flat between 0.008 Hz – 70 Hz and relative calibration errors of broadband seismometers lie well below 0.1[135].

At the point in time when latitude, longitude, and depth information for an earthquake have been determined, predictions of the earthquake's effect on places away from the epicenter can be made. In general, both P- and S-wave arrival times, which depend only on the distance between the epicenter and location in question, can be

accurately determined. Using the iaspei-tau package[279] wrapped by Obspy[223], travel times for the P (pressure) and S (shear) wave components are calculated for known earthquakes. Approximate arrival times for the surface waves are calculated assuming constant 3.5 km/s speed values.

10.2 Hazard Assessment

We have outlined the properties of earthquakes, and we now turn our attention to the effect of earthquakes on the observatories. To do so, we analyze the effect that seismic ground motion has on observatories. We then examine historical earthquake catalogs and predict the likely ground motion. We then use seismic data from on site observations to predict how ground motion will affect the observatories.

We now determine a transfer function which we can be used to scale the seismic ground motion to the effect on the astronomical observatories. Due to the coupling of ground motion to these systems, the transfer function between the ground motion and observatory instruments can be significantly greater than one. While telescopes often contain non-linear structures, including base isolators, viscous dampers, seismic restraints, or seismic releases[133], while gravitational-wave detectors can experience significant upconversion[71], the transfer functions calculated here are approximations in that linear coupling is assumed. One can compute the transfer function by approximating the system as a series of oscillators with varying natural frequency where each oscillator undergoes the same ground motion. This model can be used to model the response of the structure assuming both the spectrum of the ground motion, the natural frequency of the structure, and the seismic speeds of the ground around the telescope is known. Instead, we determine empirical transfer functions using seismic sta-

tions at the observatories during large scale ground motion, one on the ground and another on the instrument platforms. As an example telescope, we use the Southern Astrophysical Research (SOAR) telescope, which is a 4.1 m optical and near-infrared telescope located on Cerro Pachn, Chile. As example gravitational-wave detectors, we use the LIGO gravitational-wave detector located at Hanford, WA (H1) and Livingston, LA (L1). We use seismometers on the secondary mirror cage in the case of SOAR and an optical platform in the case of the gravitational-wave detector. These plots can be seen in Figure 10.2. SOAR has resonances at 7.5, 20, and 29 Hz, resulting in over an order of magnitude amplification of the ground motion at those frequencies. LIGO also has significant amplification at earthquake frequencies below 1 Hz, particularly at 0.06 and 0.15 Hz. The idea is that we can multiply the spectrum of the local ground motion by this function to find the response motion of the observatories. We see that both observatories suffer from order of magnitude amplifications of ground motion. This verifies our assumption from above that even 0.1 g earthquakes can induce significant accelerations for the telescopes, and relatively minor ground motion at gravitational-wave detectors is sufficient to create significant motion at the test masses.

We now turn our attention to predicting seismic ground motion based on earthquake parameters. Probabilistic seismic hazard analysis (PSHA) is a well-developed field[81]. In the following, we will concentrate on the application of telescopes in Chile. To be specific, we take the Magellan telescopes, which are a pair of 6.5 m diameter optical telescopes located at Las Campanas Observatory in Chile. The basic goal is to predict expected ground motions given two components. The first is a distribution of potential earthquake magnitudes and locations. This can be generated from an historical earthquake record. The second is a ground motion prediction model, which

describes the probability distribution of local ground motion intensity as a function of many predictor variables such as magnitude, distance, faulting mechanism, the near-surface site conditions, the potential presence of directivity effects, and others[187]. These models are usually developed using statistical regression on observations from large libraries of observed ground motion intensities and are known to have large variability. The variability is due to prediction of a highly complex phenomenon (ground shaking intensity at a site) using very simplified predictive parameters such as magnitude, distance, and the others described above. We attempt to represent earthquake rupture, which is a complex spatial-temporal process, as a single number such as magnitude, which measures the total seismic energy released in the variable-slip rupture. Additionally, a metric such as distance ignores the complex non-linear wave scattering and propagation through the Earth that seismic waves undergo. And although more detailed models may improve the predictions, more detailed predictions of future earthquakes would also require more knowledge than magnitude and distance probability distributions. Therefore, the significant uncertainties associated with ground motion prediction is an inherent variability in the earthquake hazard environment that must be accounted for when identifying a design ground motion intensity. We note here that a potential third model to include is the frequency-dependent attenuation of seismic waves, which can occur due to friction or from seismic scattering. There are many empirical formulations to model this effect (please see[306] for a review). Below, we do not include this effect in the amplitude predictions, as it depends significantly on the frequency of interest chosen. We leave its inclusion for future study.

We perform a Monte Carlo simulation using information from the historical earthquake record to determine the properties of earthquakes that we expect could harm

them. This simulation requires the expected peak ground acceleration (PGA) given earthquake magnitude and distance, PGA(R,M), the probability of having an earthquake of a certain size, $P(M_i = m_j)$, and the probability of an earthquake occuring a certain distance away, $P(R_i = r_k)$.

The probability distribution of earthquake magnitudes was first studied by Gutenberg and Richter[154], who noted that the distribution of these earthquake sizes in a region generally follows a particular distribution, given as follows

$$\ln(\lambda_M) = a + b \times M \tag{10.1}$$

where λ_M is the rate of earthquakes with magnitudes M, and a and b are constants. This equation is called the Gutenberg-Richter recurrence law. The a and b constants from equation 10.1 are typically estimated using statistical analysis of historical observations, with additional constraining data provided by other types of geological evidence. The a value indicates the overall rate of earthquakes in a region, and the b value indicates the relative ratio of small to large magnitudes (typical b values are approximately equal to -1). From this equation, we can compute the magnitude distribution of earthquakes that are larger than some minimum magnitude $M_{\min}$.

$$f_M(M) = b\ln(10)\frac{10^{-b(M-M_{\min})}}{1 - 10^{-b(M_{\max}-M_{\min})}} \tag{10.2}$$

We can measure this probability density function empirically using data from regional Chilean earthquakes. The plot on the left of Figure 10.3 corresponds to the probability density function of the magnitude distribution of regional Chilean earthquakes from the past forty years, which we approximated as being between latitudes

of $-80 \leq \psi \leq -10$ and longitudes of $-80 \leq \lambda \leq -60$, using a bin size of 0.5 in magnitude. The probability density function is fit to a semi-log scale consistent with Eq. 10.1.

The second factor we must calculate is $P(R_i = r_k)$, which corresponds to the probability density function of the distance of the earthquakes to the site of interest. This can be computed analytically for a number of fault types. This captures the spatial earthquake density about the facility of interest and depends on the local fault and subduction zone structure. In our case, we can use the same set of historical earthquakes in Chile to empirically calculate $P(R_i = r_k)$. On the right is the probability density function of the distance from the Magellan telescope, to which we have fit a Lorentzian distribution. We have taken all earthquakes with magnitude ≥ 5 in this study. We use this cut as earthquakes with magnitudes smaller than this value need to be $\leq 10\,\text{km}$ from the telescope to create significant ground motion.

The PGA(R,M) is a function of both magnitude and distance to the epicenter. There are specific equations used for Chile. Medina[219] gives the horizontal peak accelerations due to shallow interplate earthquakes (plate interface) as

$$\text{PGA} = 733e^{0.7M}(R+60)^{-1.31}, \tag{10.3}$$

while Ruiz and Saragoni[258] give an expression for intermediate depth earthquakes (H $\geq 70\,\text{km}$)

$$\text{PGA} = 565898e^{1.29M}(R+80)^{-3.24}, \tag{10.4}$$

where PGA is in cm/s^2, M is magnitude, and R is the distance to the earthquake epicenter in km.

The left panel of Figure 10.4 shows the model for peak ground acceleration as

a function of magnitude and distance for the Medina[219] model using the historical earthquake record. Based on the above equations, we expect that shallow earthquakes, corresponding to depths $\leq$ 70 km, are predicted to have the greatest effect on the telescopes. The plot shows that 0.1 g peak ground acceleration can occur for earthquakes magnitude 6.5 and 100 km away. As shown below, telescope resonances can amplify this ground motion significantly. Therefore, taking steps to limit their effects on the detectors will be useful. On the right is a Monte Carlo simulation of regional Chilean earthquakes using the Medina model as well (we found that shallow earthquakes are much more common and have larger amplitude, and so this assumption is reasonable). We denote with dotted lines the earthquakes that correspond to 10 s of warning time and 0.1 g of peak ground acceleration. These correspond to a distance of 100 km with depths $\leq$ 70 km. We assume that about 10 s warning time will be required to make a positive impact in terms of telescope safety. We see that a significant number of events with warning time greater than 5 s will create significant ground motion. The time axis on the plot corresponds to warning time at Magellan assuming a seismometer on site (which is the difference in P and surface wave arrivals).

We can also calculate based on these results the annual rate of exceedance of a given ground motion intensity. About 1% of earthquakes with magnitude $\geq$ 6.0 cause ground motions at Magellan exceeding 0.1 g of peak ground acceleration (including magnitudes smaller than this does not change the results sigificantly). There are about 7.8 earthquakes with magnitude $\geq$ 6.0 per year in Chile. Therefore, there is about an 8% chance of exceeding 0.1 g of peak ground acceleration per year.

10.3 Early Earthquake Warning

We now explore the potential increase of warning times (above and beyond using the difference between surface and P-wave arrivals at a seismometer on site) using seismic networks. Astronomical observatories such as LIGO and LSST have or will have seismometers on site, which are capable of exploiting the difference in P to surface wave arrival differences. Below, we explore the benefits of augmenting these seismometers with off-site sensors. As an example application, we take the Magellan telescopes as well as the LIGO gravitational-wave detectors. We used the historical earthquake record and propagation model to compute the time between an event and the arrival of the surface waves at these observatories. In the case of Magellan, we use earthquakes from the Monte Carlo analysis in section 10.2 which exceed $a \geq 0.1\,\mathrm{g}$. We use global earthquakes for the LIGO sites. This difference dramatically affects the timescales.

Figure 10.5 shows the cumulative probability distribution of time delays between the earthquake and approximate arrival of surface waves for Magellan and the LIGO Hanford and Livingston sites. For Magellan, the majority of earthquakes have surface waves which will arrive less than 1 minute after the earthquake occurs. For LIGO, the amount of time between earthquake and surface wave arrival is typically more than 10 minutes.

It is at this point that the setup for EEW systems for telescopes and gravitational-wave detectors diverge. Due to the significant time-delay, gravitational-wave detectors do not require regional seismic networks with low-latency warning. Instead, we can rely on an existing world-wide notification system from the United States Geological Survey (USGS) that uses available seismic networks to create earthquake notices.

Location and magnitude estimates for these events are typically generated within a few minutes by USGS and distributed for observatory use through USGS's Product Distribution Layer (PDL)[290], which has been configured to receive all notifications of earthquakes worldwide. This portal will be sufficient for the purposes of current gravitational-wave detectors, which are typically built far from subduction zones (the future KAGRA interferometer at the Kamioka mine in Japan could be an exception to this rule[42]).

Due to the short time-delays required for optical and radio telescopes, this system will not be sufficient. Earthquake early warning in a regional setting (as is required for major telescopes) is difficult. The first requirement is a robust data acquisition and transmission system for the seismic data with limited reception delays. The second is identification of the P-waves in seismic sensor timeseries. This is a well-studied problem in seismology and not difficult for the large magnitude of the earthquakes problematic for this analysis[336]. There are, however, three potential difficulties to consider. The first is that the magnitude of earthquakes is difficult to determine quickly. Large earthquakes have energy releases which can last tens of seconds, and so often magnitudes can only be determined after the entire rupture has occurred. Global GPS is often used to determine the overall magnitude of the earthquake by measuring the actual displacements of the Earth's surface close to the fault. Conventional seismometers and accelerometers roll-off in sensitivity at low frequencies, and therefore are not able to provide accurate displacements for this purpose. There is a large effort in developing methodologies that allow magnitude estimation with the initial portion of the P-wave arrival[201]. A third issue is that the communication of seismic signals from the seismic sensors to the location where the data is processed must be robust against both power and telecommunication failure. During major earth-

quakes, power often goes out, as well as many telephone services. Therefore, techniques like using solar panels or uninterrupted power supplies should be used for the seismic stations, and communication that is independent of internet services, such as RF communication, should be employed. Satellite communication is a potential alternative but also has potential delays.

Figure 10.6 shows a map of the probability distribution for regional Chilean earthquakes, computed using the historical earthquake record, as well as the locations of current broadband seismometers (black Xs), telescope locations (green crosses), and proposed low-latency alert sensors (purple triangles). Currently, there is up to a 5 s delay in data transmission from the current broadband seismometer stations, which significantly hampers their contribution in a system where every second counts. Therefore, there are three proposed locations for low-latency alert sensors to be placed near the current and future telescope sites. Figure 10.7 shows the potential warning times for a low-latency earthquake network for Chile for earthquakes from the Monte Carlo analysis in section 10.2 which exceed $a \geq 0.1\,\mathrm{g}$. The potential gain in warning time using only the proposed low latency alert network or those sensors in conjunction with the current broadband seismic network is shown. These warning times correspond to improvements to the times given by Figure 10.5. This analysis assumes that the equipment configuration and technology improves such that the 5 s delay from the broadband seismometers can be significantly reduced. Both show that there is a significant advantage to using a network of some kind over a single on-site sensor to perform the measurement (simply measuring the difference in P-wave and

surface-wave arrival at the site). This can be quantified by the expression in Eq. 10.5

$$\Delta t_{\text{warning}} = (t_{\text{TR}} - t_{\text{SP}}) - t_{\text{latency}} = (\frac{\sqrt{r_T^2 + z^2}}{c_R} - \frac{\sqrt{r_S^2 + z^2}}{\alpha}) - t_{\text{latency}} \tag{10.5}$$

where t_{warning} is the warning time for the telescope, t_{TR} is the time-of-arrival for the surface waves at the telescopes, t_{SP} is the time-of-arrival for the P-wave at the nearest alert sensor, and t_{latency} is the latency associated with taking the seismic trace, determining the presence of a P-wave, and informing the telescope, r_T is the horizontal distance between the earthquake and telescope, r_S is the horizontal distance between the earthquake and nearest alert sensor, z is the earthquake depth, c_R is the speed of surface waves, and α is the speed of P-waves. There are two limiting cases when considering potential warning times. The first is the case that the distance is dominated by horizontal distance. In this case, it is likely that an optimally placed seismic network is able to provide substantial improvements over a warning time based solely on on-site P arrival warning. The second case is that the distance is dominated by vertical separation (i.e. that the earthquake is directly beneath facility). In this case, seismometers on site will provide the only possible warning time, which will correspond to the difference between the P-wave and surface wave arrivals. Thus, the amount of warning time provided will then depend only on the depth of the earthquake.

10.4 Seismic network optimization

We now seek to determine the optimal distance at which a circular seismic array could be deployed to maximize the efficacy of an EEW network. We note here that this analysis is for demonstrative purposes only, please see[282,241,232] for applications

of genetic algorithms to the problem of optimal sensor placement in EEW networks. We make a number of simplifying assumptions. The first is that P-waves travel at $\alpha = 8\,\mathrm{km/s}$ and surface waves travel at $c_R = 3.5\,\mathrm{km/s}$. This P-wave speed is appropriate for portions of Northern Chile, which has P-wave speeds between 7-8 km/s[79]. The second is that we are not concerned about false alarms, such that P-wave arrivals at a single sensor can be used to discriminate between events above and below threshold. Because large earthquakes fault over large regions and can take minutes to complete, early and accurate estimation of earthquake magnitudes is nearly impossible. For our purpose, we do not require extreme accuracy, but by placing the seismometers as near to the telescope as possible, we may limit our ability to determine the magnitudes.

We consider two optimization schemes, although more are possible. The first is the case where one desires to catch as many earthquakes as possible (assuming a fixed, minimum warning time of 10 s). Seismometers on site can give warning times corresponding to the difference in the P- and surface wave seismic velocities, as can be seen by equation 10.5. Assuming $\Delta t_{\mathrm{warning}} = 10\,\mathrm{s}$, this gives a minimum earthquake distance of 62 km. Therefore, improvements to the number of caught earthquakes would require a network at a distance closer than this. To determine this distance, we take the distribution of earthquakes that exceeded the threshold of 0.1 g from the right of Figure 10.4 and calculate the warning times for a circular array at fixed distance from the telescope. The dashed line in Figure 10.8 shows that the peak number of earthquakes caught as a function of distance occurs when the sensors are placed between 30-50 km. Therefore, an EEW seismic system consisting of a circle of seismometers surrounding the telescope would be most usefully placed at that distance to catch the most earthquakes. A second possible optimization scheme is to maximize the warning times for as many earthquakes as possible. The solid line in Figure 10.8 shows that

the peak median warning time as a function of distance occurs between 70-100 km. The peak median warning time is about 25 s.

These estimates do not account for potential differences in the seismic hazard as a function of distance from the telescope as well as differences in the hazard in different directions from the telescope. An improvement could account for the fact that the lower the magnitude of the earthquake, the more time is required to determine whether it is a large enough of an event to warrant telescope response. Higher magnitude events can be more clearly defined as such based on the P-wave arrival and thus require less analysis time. For the magnitudes of the earthquakes discussed here, this effect is likely negligible, as all P-wave arrivals should be sufficient. More important may be to account for the spatial distribution of earthquakes as given by Figure 10.6. If a limited number of seismometers are to be used in an EEW network, due to limited equipment, it could be important to place seismometers in directions that will maximize the warning time from potential earthquakes.

10.5 Conclusion

In this paper, we have discussed the problem of earthquakes for large-scale astronomical observatories. We have shown how it is important to develop an EEW network to maximize the warning time for these experiments. We have discussed how a strong motion local seismic network in Chile could provide more than 10 s of warning time for conventional telescopes. We have shown that a circular network should be placed nearer than 100 km away from the telescope. We have also shown that existing worldwide networks of seismometers are adequate for a potential gravitational-wave detector warning system. An earthquake warning system can do two things: predict

likely earthquake arrival times and expected minimum ground velocity amplitudes. The earthquake arrival times are required to provide the amount of delay before surface waves arrive, which can facilitate protective action. Approximate ground velocity amplitudes are necessary to determine the type of protective action to take, if at all. Prediction of the ground velocity amplitude based on earthquake magnitude and distance will be required to limit the false alarms. This prediction should account for physical effects with variable parameters used to fit to the seismic data currently available.

The hope is that with knowledge that seismic waves of significant amplitude were about to arrive, scientists on site could take preventative measures to limit the amount of damage and downtime the detectors experienced. In the case of telescopes, most likely this action will be to close mirror covers, telescope dome, and stop slewing of the telescope. For gravitational-wave detectors, this will most likely be a change in gain control for the seismic isolation system. In the future, we hope to provide more detailed models of the response of current and future telescopes to significant ground motion. We intend to implement a gravitational-wave detector early warning system and study the steps that can be taken to minimize the effect of ground motion on the detectors. We will also study potential locations and methods for sensors for a Chilean telescope EEW system.

We have discussed some of the scientific systems that could benefit from early seismic warning. There are other benefits in personnel safety, as well as public utilities, including reactors, and public transportation systems. There are a number of common sense recommendations to be made going forward:

1. Science facilities: stay abreast of rapidly changing seismic warning systems and make provisions for actions to take in response to seismic warning.

2. Universities: Distribute low-latency alert to subscribing on-campus devices.

3. Manufacturers: Make provisions for safe-mode response to seismic triggers.

4. Data Centers: Store particularly valuable data at redundant (earthquake-uncorrelated) sites and provide means to take data protection steps upon seismic alert.

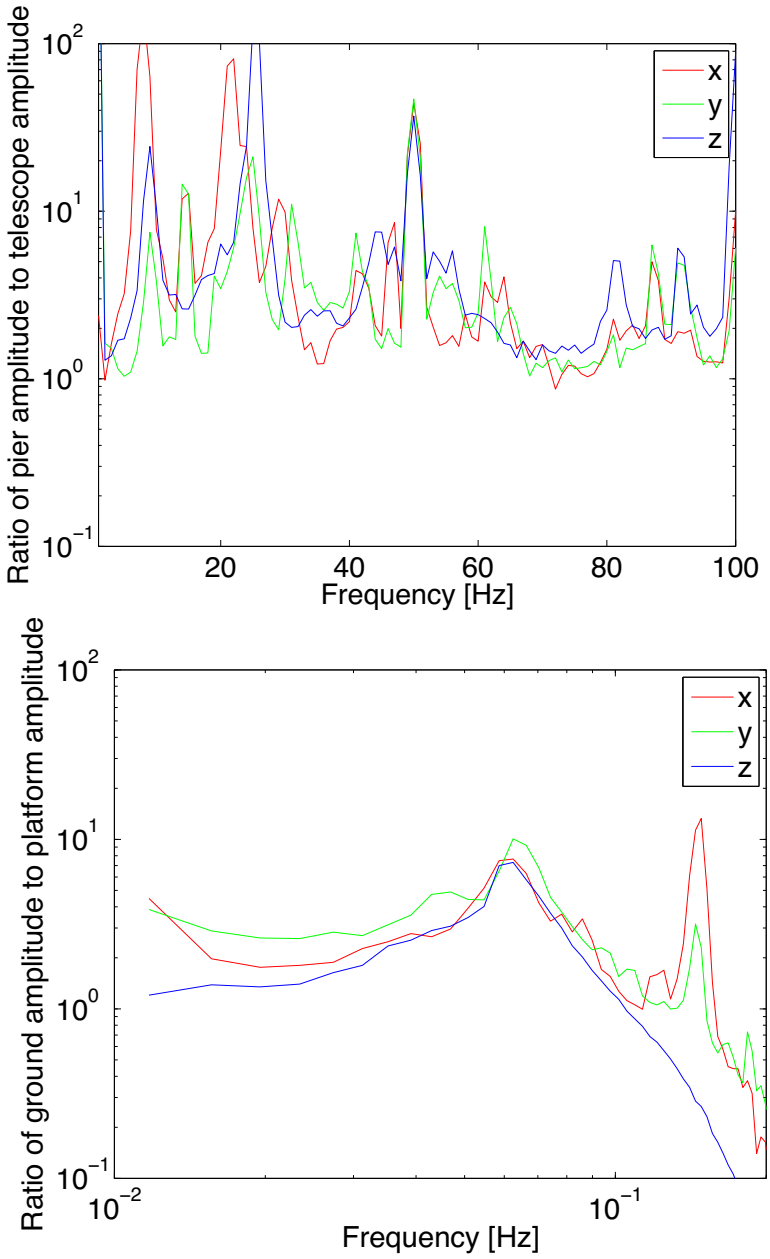


Figure 10.2: Effect of strong ground motion on the observatories. The plots show a simplified ground motion transfer function for both SOAR and LIGO observatories using a single earthquake each. SOAR's transfer function corresponds to the structural resonances, while LIGO's transfer function is due to the LIGO seismic isolation system. For the LIGO transfer function, we used the 6.8 magnitude earthquake in Peru on August 24, 2014. The transfer function presented is consistent with results from other large teleseismic earthquakes. For the SOAR transfer function, we used a local 5.3 magnitude event that occurred on July 13, 2014. The transfer function presented is consistent with results from other regional earthquakes. SOAR has resonances at 7.5, 20, and 29 Hz, resulting in over an order of magnitude amplification of the ground motion at those frequencies. LIGO also has significant amplification at earthquake frequencies below 1 Hz, particularly at 0.06 and 0.15 Hz. These results show that the transfer function resonances lie within the earthquake band.

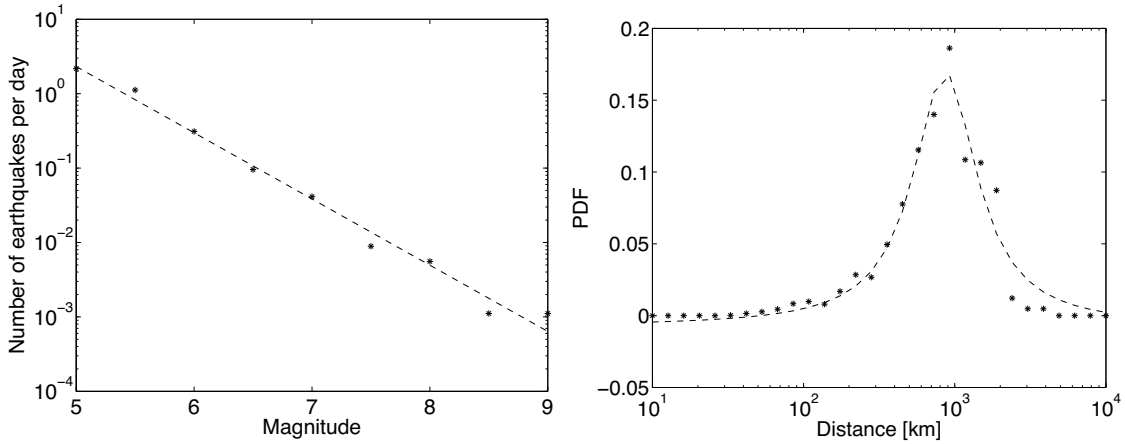


Figure 10.3: The left plot shows the magnitude distribution of regional Chilean earthquakes and a log fit to the distribution. Earthquakes with a source magnitude $m \geq 5$ occur at a rate of about 3.7 per day in the region between latitudes of $-80 \leq \psi \leq -10$ and longitudes of $-80 \leq \lambda \leq -60$. The right plots shows the distribution of distances between the same earthquakes and the Magellan telescope and a Lorentzian fit to the distribution. The cutoff at large distances is due to the requirement that earthquakes are regional. The cutoff at short distances is due to the lack of large earthquakes that have occurred within a few kilometers of Magellan.

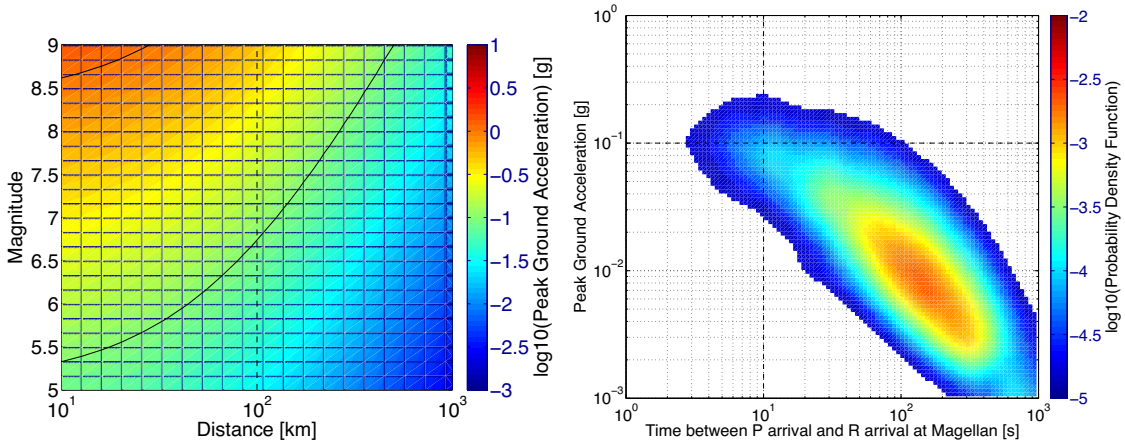


Figure 10.4: On the left is the predicted peak ground acceleration as a function of magnitude and distance. This used the Medina[219] model for the distribution of ground motion intensity. The black solid lines denote the 0.1 g and 1 g of ground motion predictions. The black dotted line corresponds to earthquakes at 100 km, which provide about 10 s of warning time for an on-site seismometer. On the right is a Monte Carlo simulation of regional Chilean earthquakes based on the historical record. We denote with dotted lines the earthquakes that correspond to 10 s of warning time and 0.1 g of peak ground acceleration.

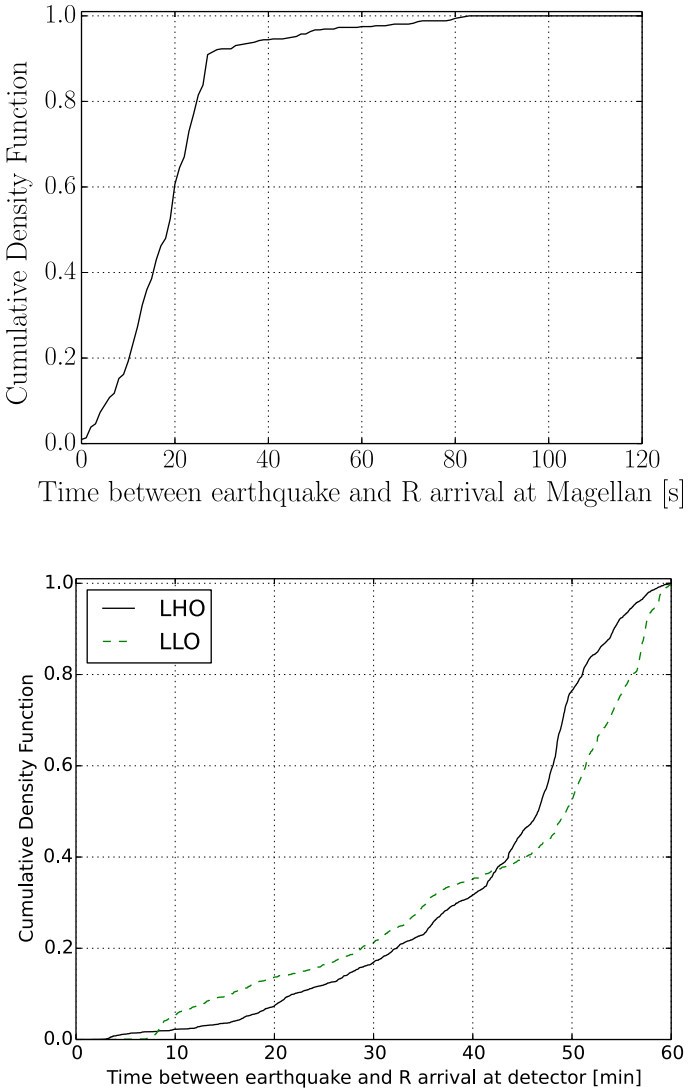


Figure 10.5: The left plot shows the time delay between the earthquake and approximate arrival of surface waves at Magellan from the Monte Carlo analysis in section 10.2 which exceed $g \geq 0.1$. A majority of the earthquakes are at distances such that their surface waves arrive within 1 minute to the site. The right shows the same at the LIGO Hanford and Livingston sites for global earthquakes (as LIGO is susceptible to all earthquakes). A majority of the locations allow for more than 10 minutes of time between earthquake and site arrival. These delays are optimistic in the sense that an earthquake warning requires a P-wave arrival at at least one seismic station.

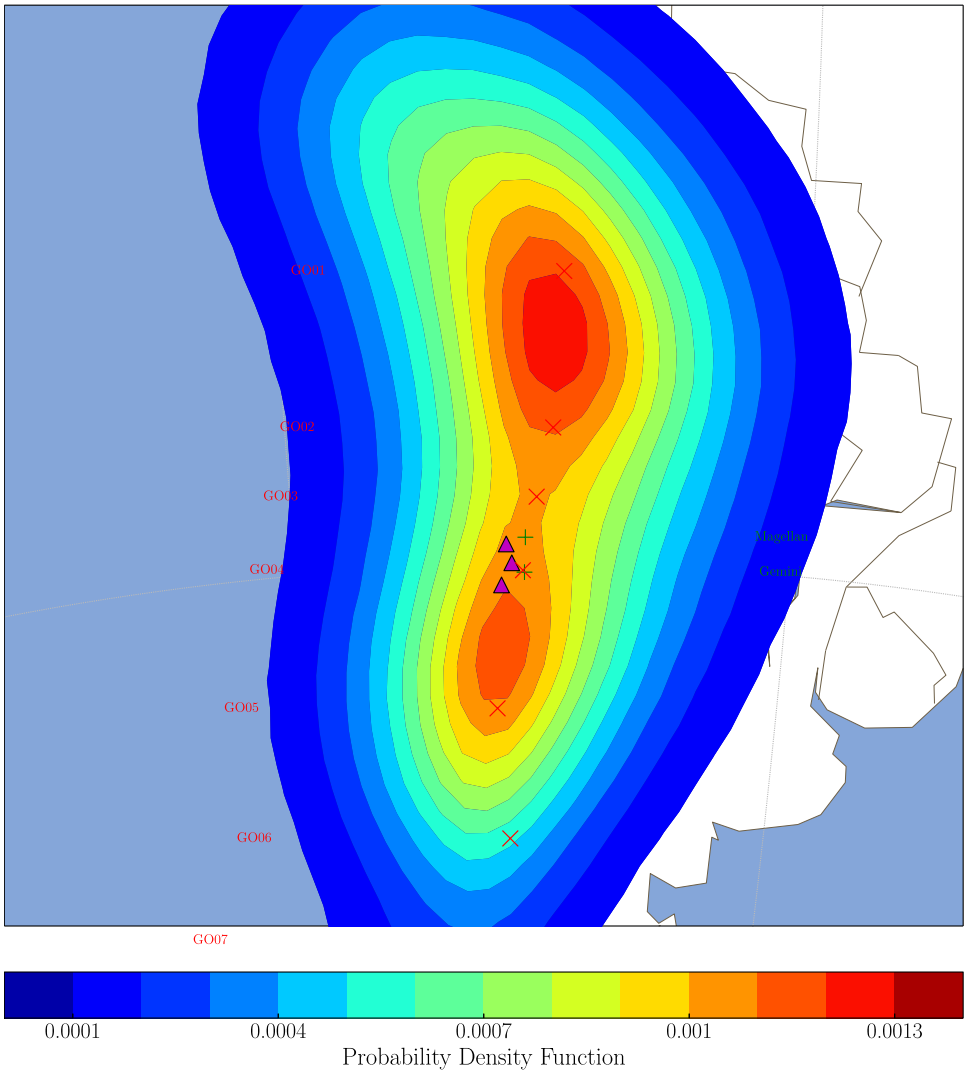


Figure 10.6: Map of the probability distribution for regional Chilean earthquakes, as well as the locations of current broadband seismometers and telescope locations. The broadband seismometers are represented by red Xs, the telescopes by green crosses, and the proposed low latency alert sensors by purple triangles. We have taken all earthquakes with magnitude ≥ 5 for this plot.

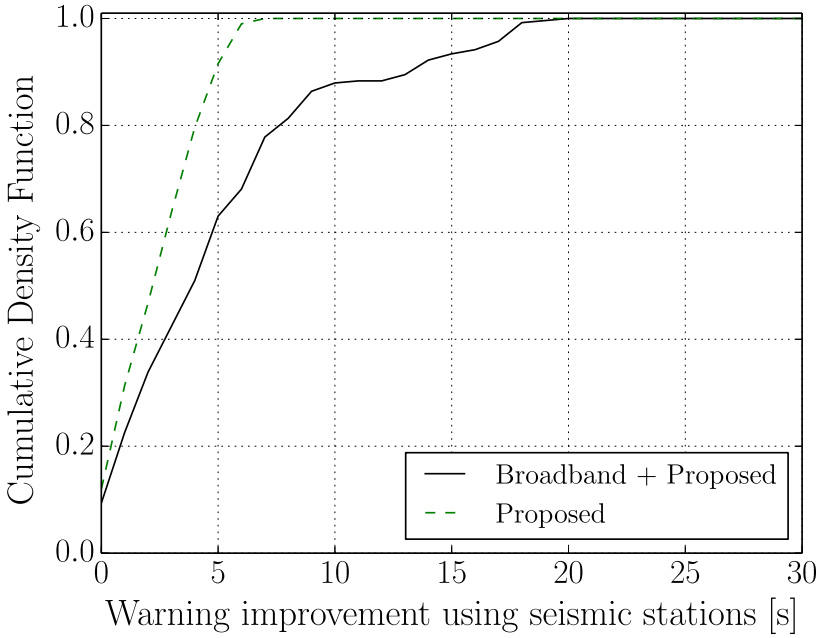


Figure 10.7: Potential gain in warning time, which is determined by the difference between the P-wave arrival at the nearest seismometer and the surface wave arrival at Magellan, using only the proposed low latency alert network or those sensors in conjunction with the current broadband seismic network. This is the gain on top of using a single on-site sensor. We use earthquakes from the Monte Carlo analysis in section 10.2 which exceed $g \geq 0.1$. Both show that there is a significant advantage to using a network of some kind over a single on-site sensor.

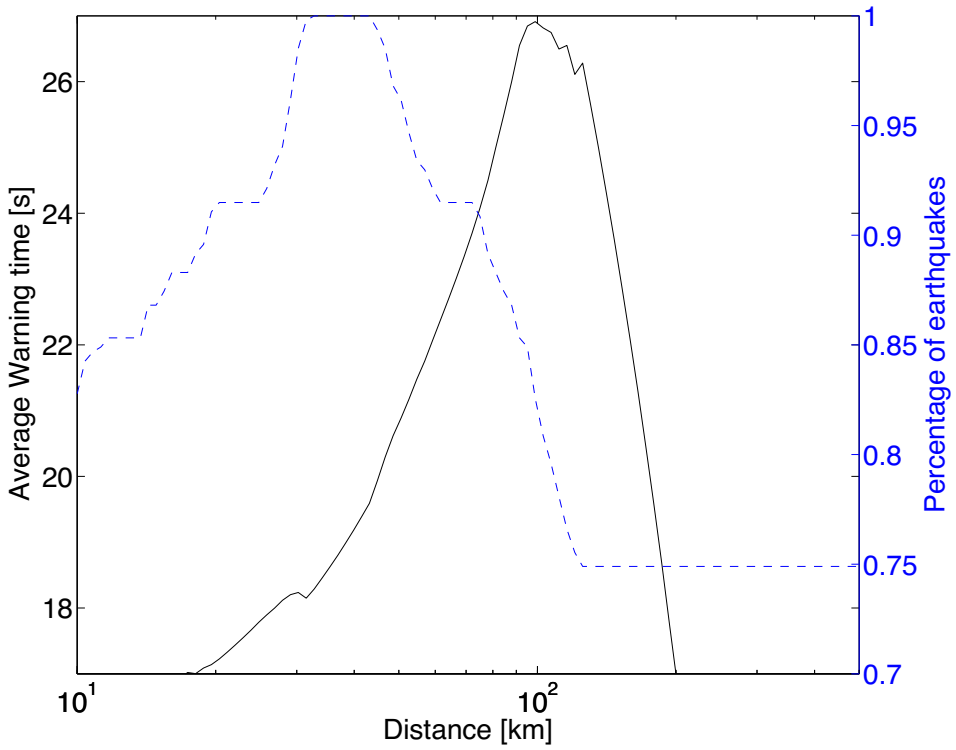


Figure 10.8: Optimal seismometer distances for the EEW seismic network. The solid line shows the median warning time as a function of distance. The dashed line shows the percentage of earthquakes caught with warning times exceeding 10 s as a function of distance. The roll-off for larger distances is due to attentuation that suppresses impact of large and distant earthquakes.

Remember to look up at the stars and not down at your feet.

Stephen Hawking

11

Maximizing the Probability of Detecting an Electromagnetic Counterpart of Gravitational-wave Events

With the recent discovery of a compact binary black hole system[24], there is significant interest in the combined observation of electromagnetic (EM) and gravitational-wave (GW) emission[20]. EM emission likely occurs on a variety of timescales and wavelengths ranging from seconds to months in X-ray to radio, respectively[225,222]. It is suspected that compact binary coalescences (CBCs) are also the progenitors of

some or all short, hard γ-ray bursts[303]. Plausible CBC event rates suggest that Advanced LIGO and Advanced Virgo could detect about 40 binary neutron star and 10 neutron star-black hole events per year of observation time[9]. In addition to CBCs, there are other possible sources of coincident EM and GW emission, including asymmetrical type II supernovae, soft γ repeaters, anomalous X-ray pulsars, neutron stars recovering from pulsar glitches, cosmic string cusps, or radio bursts. Kilonoave are one promising source that can be identified, produced during the merger of binary neutron stars or a neutron star-black hole systems, likely peaking in the near-infrared with luminosities $\approx 10^{40} - 10^{41}$ ergs/s and lasting over a week[221,48].

On the gravitational-wave side, a number of algorithms exist to derive inferences of compact binary source parameters based on gravitational-wave observations, as determined by Bayestar or LALInference[276,128]. Bayestar is an algorithm which takes in information from compact binary search pipelines and returns gravitational-wave skymaps within seconds. LALInference instead provides inferences of intrinsic source parameters such as masses and spins, as well as extrinsic parameters such as sky direction and distance, but takes orders of magnitude longer to run. These algorithms produce GW likelihood sky areas typically spanning $\approx 100\,\mathrm{deg}^2$ [137,138,153,323,274,276,128]. Finally, there are very-low latency algorithms proposed for performing rapid sky localization[142]. There also exist algorithms to characterize generic gravitational-wave transients[122,82].

There has been a significant amount of work in recent years to improve follow-up of gravitational-wave sources with optical telescopes. Galaxy catalogs, such as the Gravitational Wave Galaxy Catalogue (GWGC)[325], the Compact Binary Coalescence Galaxy Catalog[196], and the 2MASS Photometric Redshift catalog[56] have been used to identify individual galaxies within the anticipated GW detection range. Another

option is to rapidly create galaxy catalogs on-the-fly, after a gravitational-wave detection has been made[49]. Techniques for optimizing multiple telescope pointings also exist[277]. Antolini and Keyl[37] showed how to use the 2MASS Photometric Redshift catalog to optimize telescope pointings.

There are many factors that go into the probability of detecting a transient with a telescope. These include internal factors such as the exposure time, filter, field of view, and limiting magnitude, and external factors such as seeing and sky conditions. Fields of view are often approximately rectangular, although dead or defective pixels or vignetting from the optics can make this more complicated. We seek to maximize the likelihood of detecting an electromagnetic counterpart for a fixed allocation of observing time. This is especially important in an era with very different exposure times, limiting magnitudes, and field of views for telescopes. For example, the Dark Energy Camera on the Blanco 4m telescope at CTIO has a 3deg^2 FOV, and 3600 s r-band exposure length to reach 26 mag in 1 arcsecond seeing[108], while LSST will have a 9.6deg^2 FOV, and 810 s r-band exposure length to reach the same[205]. There are few operating or planned deep survey telescopes that have fields of view (FOVs) comparable to error regions of the gravitational-wave skymaps. For example, the James Webb Space Telescope, a highly sensitive infrared space telescope with an expected launch in 2018, will have a 0.0013deg^2 FOV[50]. On the other hand, there are several shallow and wide-field operating telescopes such as Pi of the Sky[215].

In this paper, we explore the benefits of optimizing single telescope pointings given limited time on the telescope. We show how adopting priors on the rate of compact binary detections and the distribution of sky areas produced by gravitational-wave detectors allows for a significantly more efficient follow-up than a naive follow-up strategy. We will explore four particular cases, corresponding to two different mass distri-

bution assumptions and two different prior flux assumptions. The first assumes that in a particular field, there are 0, 1 or a few galaxies. In this regime, the mass distribution will be very field-dependent. In the other regime, there are many galaxies such that the mass distribution is no longer field dependent. We will also explore two different luminosity distribution assumptions. The first is a delta function prior, while the second is a flat prior.

We derive the scaling relations for optimizing telescope followup, in particular that the optimal exposure time allocated to any given field, under certain assumptions, can go as $t_i \propto \left(\frac{L_{\rm GW}(\alpha_i,\delta_i)}{a(\alpha_i,\delta_i)}\right)^{2/3}$, where $L_{\rm GW}(\alpha_i,\delta_i)$ is the gravitational-wave likelihood and $a(\alpha_i,\delta_i)$ is Galactic extinction. This fits into a framework for planning optimal follow-up of gravitational-wave candidates. We show that the required time to achieve a 90% confidence level of detecting a gravitational-wave electromagnetic event is decreased by a factor of 3. In this work, we will ignore a number of complications. One is the "needle in the haystick problem," which involves the difficulty of discriminating the optical transient associated with the gravitational-wave event from other astrophysical transients[222,98]. In particular, Cowperthwaite and Berger[98] recently showed how the existence of pre-existing deep template images in the gravitational-wave sky localization region can greatly improve the detection rate over searches without prior template images. They also showed that kilonovae can be robustly separated from other known and hypothetical types of transients utilizing cuts on color and rise time.

The remainder of this paper is organized as follows. We describe the formalism used in this paper in section 11.1. We discuss the methods used to optimize telescope allocations and demonstrate their application in section 11.2. We conclude with a discussion of topics for further study in section 11.3.

11.1 Formalism

11.1.1 Definition of variables

We seek to derive the optimal observing strategy for a single telescope for LIGO/Virgo follow-up observations. Telescope time is our limiting resource. The goal is to develop an observing program that maximizes the probability of finding an associated optical transient that is expected to have some absolute magnitude M. The apparent magnitude m of the transient is $m = M + \mu + A(\alpha, \delta)$, where μ is the distance modulus and $A(\alpha, \delta)$ is Galactic extinction, which is the absorption and scattering of electromagnetic radiation by dust and gas between an emitting astronomical object and the observer. We denote the "flux attenuation" due to extinction by $a(\alpha, \delta)$, which is proportional to $10^{A(\alpha,\delta)}$ and will enter the merit function we will derive below. In our analysis, we use extinction maps provided by Schlegel et al. [265].

We denote the number of detected photons from the object of interest as $N_{\rm Object} = \phi_{\rm Object} t$, where $\phi_{\rm Object}$ is the detectable flux from the object and t is the observation time. The noise associated with the observation of this object is

$$\text{Noise} = \sqrt{\phi_{\rm Object} t + n_{\rm pix}(\phi_S t + \phi_D t + N_R^2)}, \tag{11.1}$$

where $\phi_{\rm S}$ is the sky luminosity in the direction of the object within the photometric aperture, $\phi_{\rm D}$ is the dark current of the detector, $N_{\rm R}$ is the read-noise of the detector, and $n_{\rm pix}$ is the number of pixels encompassed in the point spread function. The signal-to-noise for detection of the transient is

$$\text{SNR} = \frac{N_{\rm Object}}{\text{Noise}} = \frac{\phi_{\rm Object} t}{\sqrt{\phi_{\rm Object} t + n_{\rm pix}(\phi_S t + \phi_D t + N_R^2)}}. \tag{11.2}$$

In what follows, we will ignore observing overheads due to, for example, image read-out and telescope slews. We expect all sources of interest in the advanced detector era to be in the sky-dominated case, except for perhaps a Galactic supernova or other very nearby event, which is a source-dominated case. In the source-dominated regime, SNR $\propto \sqrt{\phi_{\rm Object} t}$, while in the sky-dominated regime, SNR $\propto \frac{\phi_{\rm Object}}{\sqrt{\phi_{\rm Sky}}}\sqrt{t}$. For fixed $\phi_{\rm Object}$ and $\phi_{\rm Sky}$, the time required to sustain a given SNR scales as $\phi_{\rm Object}^{-2}$. Due to the inverse square law (ignoring additional cosmological dimming for the redshift regime of interest here), $\phi_{\rm Object}$ scales as R^{-2}. This means that the time required to sustain a constant SNR for a target absolute magnitude scales as R^4. Inverting this relation, the distance out to which we can find the desired magnitude scales very slowly with exposure time, as $t^{1/4}$.

We will assume that there is a given maximum counterpart absolute magnitude $M_{\rm max}$. As the initial goal is to detect a transient optical source with some SNR, any exposure time used beyond what is needed to accomplish this is a waste. On the other hand, any exposure that does not go deep enough to acheive this is also a failure. If we point the followup telescope in some direction and integrate for a time $t_{\rm field}$, we accumulate electromagnetic counterpart detection probability over all the galaxies in the field of view for which the integration time exceeds $t_{\rm max}$, i.e. the exposure time needed to detect the brightest plausible counterpart. Each galaxy's counterpart likelihood is presumed to be proportional to its stellar mass or luminosity. The figure of merit for that observation is given by the integrated detection likelihood over all these galaxies. We go deeper in the nearby galaxies, but obviously most of them are out at the edge of the useful detection volume, residing at a distance where we can just barely detect the brightest plausible source. The figure of merit for an observation is then the volume integral of the detection probabilities. In the following, we will

compute the dependence of the time required to achieve a given SNR on a number of quantities. This time depends on the the distance to the transient and the stellar mass in the direction of the field.

Singer et al.[276] and subsequently Berry et al. [128] explored the directional dependence of the gravitational-wave likelihood $L_{\rm GW}(\alpha, \delta)$ in great detail. They showed that when both the Hanford and Livingston interferometers are operating, the sky position reconstructions will look like two antipodal islands on opposite sides of the sky, one over North America and one on the opposite side of the Earth. These occur due to degeneracies from the relative positions of the two interferometers. When more detectors are included, in general the sky positions become more tightly constrained. We now briefly turn our attention to the likely distance posteriors, $L_{\rm GW}(R)$. Due to the antenna pattern of gravitational-wave detectors and the unknown inclination angle of the gravitational-wave source, the possible distances for a given gravitational-wave amplitude cover a very broad range. Singer et al.[130] show how combining the gravitational-wave distance posteriors with a galaxy catalog leads to significant reduction in the total time required to image a counterpart.

We finally explore the assumption about whether a telescope is in the regime where there are many galaxies in a field or few. This will motivate the examples we use below, where we take one regime where the number of galaxies is significantly different across different fields and the other where it is approximately uniform. Figure 11.1 shows the relative variance in the number of galaxies as a function of field of view and reach of the gravitational-wave detectors in redshift. In general, telescopes with a small field of view or when gravitational-wave detectors are sensitive to only nearby transients are likely to have a high variance in the number of galaxies per image. On the other hand, telescopes with a large field of view or when the gravitational-wave

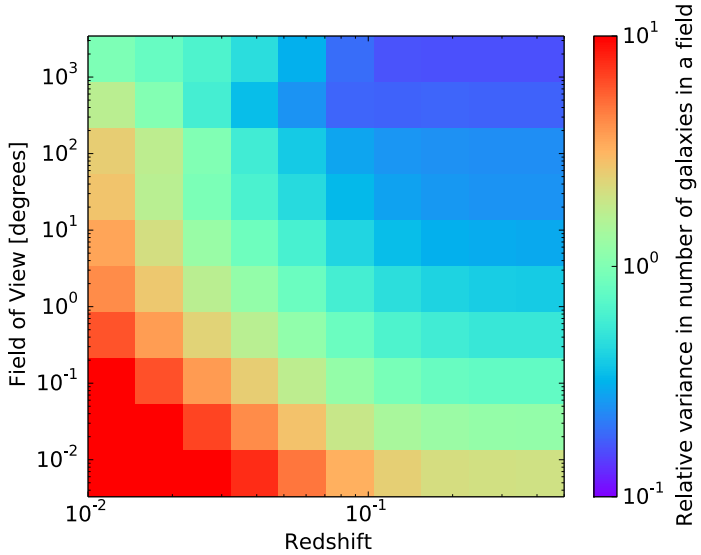


Figure 11.1: Plot of the relative variance, σ_N/N, in the number of galaxies as a function of field of view and reach of the gravitational-wave detectors in redshift. The results are derived from the 2MASS Photometric Redshift catalog[56]. In general, telescopes with a small field of view or when gravitational-wave detectors are sensitive to only nearby transients are likely to have a high variance in the number of galaxies per image. On the other hand, telescopes with a large field of view or when the gravitational-wave detectors are very sensitive have little variance from field to field.

detectors are very sensitive have little variance from field to field. It is clear that the regime of interest is significantly dependent on the sensitivity of the gravitational-wave detectors. As the detectors are commissioned and more detectors enter the network, the sensitivity distance will increase. Therefore, inclusion of the dependence of the number of galaxies as a function of FOV will be important, and we return to how to incorporate this later.

11.1.2 Detection probabilities for fixed telescope time allocations

We now explain how to derive telescope pointing optimizations given a set of assumptions, which we outline below:

1. The observations are sky-noise dominated.

2. We know the gravitational-wave likelihood in right ascension (α), declination (δ), and distance (R). We denote the likelihood as $L_{\rm GW}(\alpha, \delta, R)$.

3. We ignore cosmological subtleties like redshift dependence of volume, which is reasonable out to z=0.1.

4. We assume that the transient arises from an old stellar population (as opposed to young objects) so that the likelihood of a gravitational-wave source in a galaxy is proportional to the galaxy's stellar mass (as opposed to, for example, the star formation rate).

5. We assume that a particular cadence has been adopted for the fields (i.e. one visit per night, two visits 3 hours apart on the first night, followed by a visit every other night, etc.).

We assume that for each galaxy i, there is a probability of detecting a counterpart p_i, which can be computed as follows:

$$p_i(t_i) = \frac{M_i}{M_{\rm tot}} \frac{L_{\rm GW}(\alpha_i, \delta_i, R_i)}{L_{\rm GW\ tot}} \frac{F_i(t_i)}{a(\alpha_i, \delta_i)} \tag{11.3}$$

where M_i is the stellar mass in the galaxy, $a(\alpha_i, \delta_i)$ is the attenuation in the direction, $L_{\rm GW}(\alpha_i, \delta_i, R_i)$ is the gravitational-wave likelihood in the field, F_i is a weight factor that accounts for assumptions about the luminosity of the counterpart, and t_i is the amount of time allocated to that field. For a followup campaign that observes multiple galaxies, the total counterpart detection probability $p_{\rm tot}$ is the sum over galaxies

$$p_{\rm tot} = \sum_{i=1}^{N} p_i(t_i). \tag{11.4}$$

If we have multiple fields, the distribution of the total observing time t across field-dependent exposure times t_i is optimal when the partial derivatives of the individual field p_i's with respect to t_i are all equal, such that $(\partial p_i(t_i)/\partial t_i) = C$. This means that when the exposure times are optimized, moving one second of exposure from one field to another has the probability lost in one equal to the probability gained in the other.

11.1.3 Electromagnetic Luminosity of gravitational-wave counterparts

The amount of electromagnetic energy emitted by a coalescence event is not well-known. Not only is the emission mechanism poorly understood, but host galaxy extinction will attenuate and redden the light that emerges. Cowperthwaite & Berger[98] have summarized both the expected electromagnetic luminoisties and astrophysical contaminants associated with a variety of potential gravitational wave sources. The anticipated peak luminosities for optical counterparts range from 10^{39} to $10^{41.5}$ ergs/s, with a considerable range in expected effective temperatures and evolution of the spectral energy distributions across the diversity of astrophysical cataclysm scenarios. If we take a conservative upper bound of $\Phi_{\rm max} = 10^{41}$ ergs/s luminosity as the brightest plausible source, this corresponds to a peak apparent magnitude of $i_{\rm AB} = 23$ at a distance of 200 Mpc. These numbers determine R_0 and t_0, the time needed to detect the brightest plausible transient at a given distance. The LSST exposure time calculator estimates that a single 15 second exposure is sufficient to attain SNR > 5 at this apparent magnitude, even at 1.5 airmasses in 1" seeing. So we can adopt $t_0 = 15\,s$

and nominal $R_0 = 200\,\mathrm{Mpc}$, for an effective telescope diameter equal to LSST, namely 6.5 meters. Given these uncertainties, in the following, we will explore two regimes of interest: a delta function prior on luminosity and a flat prior on luminosity.

Delta function prior on luminosity

We take the object luminosities to be a delta function, $\delta(\phi - \phi_0)$, such that all of the electromagnetic counterpart objects have the same luminosity ϕ_0. For a fixed exposure time, there is a threshold distance $R_{\rm max}$ out to which we can detect the transient of interest. $F_i(t_i)$ is a Heaviside step function $\Theta(R_{\rm max}(t_i) - R_i)$, where any galaxy within $R_{\rm max}$ is given a weight of 1 and further than $R_{\rm max}$ is given a weight of 0. This implies that

$$p_i = \frac{M_i}{M_{\rm tot}} \frac{L_{\rm GW}(\alpha_i, \delta_i, R_i)}{L_{\rm GW\ tot}} \frac{\Theta(R_{\rm max}(t_i) - R_i)}{a(\alpha_i, \delta_i)} \tag{11.5}$$

The time dependence arises through $t_{max,i}$, the time needed to detect the brightest counterpart at a distance R_i. For a sky-dominated set of observations this time scales as R_i^4. We now express all detection probabilities relative to a fiducial host galaxy at a distance R_0 for which it would take a time t_0 to achieve a 5σ detection of the brightest plausible counterpart. We can now make a change of variables, since there is a direct relationship between $R_{\rm max}$ and t, given by $R_{\rm max}(t_i) = R_0(\frac{t_i}{t_0})^{1/4}$. This means that

$$p_i = \frac{M_i}{M_{\rm tot}} \frac{L_{\rm GW}(\alpha_i, \delta_i, R_i)}{L_{\rm GW\ tot}} \frac{\Theta(R_0(\frac{t_i}{t_0})^{1/4} - R_i)}{a(\alpha_i, \delta_i)} \tag{11.6}$$

Flat prior on luminosity

In this scenario, we adopt a flat prior for the luminosity (in some electromagnetic detection passband) that emerges from the host galaxy, up to an upper limit, so that

$P(\phi)$ =C for $\phi < \phi_{max}$:

$$P(\phi > \phi_0) = \begin{cases} 1 - \frac{\phi_0}{\phi_{\max}}, & \text{if } \phi_0 < \phi_{\max} \\ 0, & \text{otherwise} \end{cases} \tag{11.7}$$

For the sky-noise-dominated case under consideration here, the 5σ point source detectable luminosity (in linear luminosity units rather than magnitudes) scales as $1/\sqrt{t}$, so the exposure time needed to reach sources fainter than ϕ_{max} is $(\phi_{max}/\phi)^2$ longer than needed to detect $\phi_{\max}$. The probability of detecting a source of interest, given the flat prior described above, is then a function of the integration time. If we scale all exposure times by the time t_{max} needed to achieve 5σ sensitivity to ϕ_{max}, we can determine the counterpart detection probability as a function of exposure time. Taken together, this implies that

$$p_i(t) = L_i M_i (1 - \frac{\phi_0 r^2}{\phi_{max}\sqrt{t}}) \tag{11.8}$$

We can draw some initial conclusions at this stage. Obviously, a total integration time that falls short of that needed to detect the brightest possible counterpart is not time well spent. Perhaps most importantly, half the detection probability is for sources brighter than half the maximum. In order to achieve 50% detection probability therefore requires that we integrate for 4 t_{max}, *i.e.* four times as long as is required to detect the brightest plausible counterpart. Attaining 80% or 90% counterpart detection probability, however, requires exposures times of 25 t_{max} and 100 t_{max}, respectively.

11.2 Optimization

We now explore how to optimize time allocations across potential fields. We first explain how to optimize for the 2 pointings case for both the delta and flat luminosity prior. Thereafter, we generalize to N pointings.

11.2.1 2 pointing case

For intuition purposes, we now explore a situation where we have 2 potential galaxies, with different gravitational-wave likelihoods and masses. In this case, we have

$$\begin{aligned} p_1 &= \frac{L_1 M_1 F_1}{a_1} \\ p_2 &= \frac{L_2 M_2 F_2}{a_2}. \end{aligned} \tag{11.9}$$

We now compare the use of the two different luminosity assumptions used in this paper. In the case of a delta function prior on luminosity,

$$\begin{aligned} p_1 &= \frac{L_1 M_1}{a_1} \Theta(R_0 (\frac{t_1}{t_0})^{1/4} - R_1) \\ p_2 &= \frac{L_2 M_2}{a_2} \Theta(R_0 (\frac{t_2}{t_0})^{1/4} - R_2), \end{aligned} \tag{11.10}$$

where we constrain the total time allocated to be $t = t_1 + t_2$. In this case, one simply allocates time t to the field with the larger $\frac{LM}{R^4}$ until $R = R_0(\frac{t}{t_0})^{1/4}$, and then switches over to the other.

In the case of a flat luminosity function,

$$\begin{aligned} p_1 &= L_1 M_1 (1 - \frac{\phi_0 r^2}{\phi_{max}\sqrt{t_1}}) \\ p_2 &= L_2 M_2 (1 - \frac{\phi_0 r^2}{\phi_{max}\sqrt{t_2}}), \end{aligned} \tag{11.11}$$

where we again constrain the total time allocated to be $t = t_1 + t_2$. The total probability of detecting a counterpart is simply given by $p_{\rm tot} = p_1 + p_2$ and $p = L_1 M_1 (1 - \frac{\phi_0 r^2}{\phi_{max}\sqrt{t_1}}) + L_2 M_2 (1 - \frac{\phi_0 r^2}{\phi_{max}\sqrt{t_2}})$. To maximize the probability, we set $\frac{\partial p}{\partial t_1} = 0$, which implies that $\frac{t_1}{t_2} = \left(\frac{M_1 L_1}{M_2 L_2}\right)^{2/3}$.

11.2.2 N POINTING CASE

The extension to an arbitrary number of pointings is straightforward. In the delta function luminosity case,

$$p_{\rm tot} = \sum_{i=1} \frac{M_i}{M_{\rm tot}} \frac{L_{\rm GW}(\alpha_i, \delta_i, R_i)}{L_{\rm GW\ tot}} \frac{\Theta(R_0(\frac{t_i}{t_0})^{1/4} - R_i)}{a(\alpha_i, \delta_i)} \tag{11.12}$$

where $t = \sum_i t_i$. Similar to the above, the pointings are rank-ordered by $\frac{LM}{R^4}$, the time is allocated on the first field until $R = R_0(\frac{t}{t_0})^{1/4}$, and then switches over to the next, and so on.

In the case of a flat luminosity function,

$$p_i = \left\{ \begin{array}{ll} \int_0^\infty L_i \rho \Omega (1 - \frac{\phi_{5,i}^{em}}{\phi_{max}}) r^2 dr & (1 - \frac{\phi_{5,i}^{em}}{\phi_{max}}) \geq 0 \\ 0 & (1 - \frac{\phi_{5,i}^{em}}{\phi_{max}}) < 0 \end{array} \right\}$$

This means that

$$p_i(t) = \rho \Omega \int_0^\infty \frac{L_{\rm GW}(\alpha_i, \delta_i)}{a(\alpha_i, \delta_i)} (1 - \frac{\phi_0 r^2}{\phi_{max}\sqrt{t}}) r^2 dr \tag{11.13}$$

We now assume the telescope has integrated long enough to see the brightest source in some distant galaxy. Due to the finite sensitivity of the gravitational-wave detectors, there is also a $R_{\rm min}$ and $R_{\rm max}$ to which they are sensitive. We make the fur-

ther assumption that the distance dependence of the gravitational-wave likelihood is largely independent of position across the field of view. Due to the antenna factors of the gravitational-wave detectors, this can be a poor assumption and improvements will be explored in the future. We can make this integral more concrete by putting in explicit limits of integration and realizing that the angular portion factors out and we are left with a purely radial integral,

$$p_i(t) = \Omega \frac{L_{\rm GW}(\alpha_i, \delta_i)}{a(\alpha_i, \delta_i)} \rho \int_{R_{\rm min}}^{R_{\rm max}} (1 - \frac{\phi_0 r^2}{\phi_{max}\sqrt{t}}) r^2 dr \tag{11.14}$$

Solving this integral

$$p_i(t) = \rho \Omega L_{\rm GW}(\alpha, \delta, R) \left(R_{\rm max} - R_{\rm min} - \frac{R_{\rm max}^5 \alpha}{5\sqrt{t}} + \frac{R_{\rm min}^5 \alpha}{5\sqrt{t}} \right) \tag{11.15}$$

Taking the partial derivative of p_j with respect to t,

$$\frac{dp_j}{dt} = \frac{\rho \Omega L_{\rm GW}(\alpha, \delta, R) \left(R_{\rm max}^5 - R_{\rm min}^5 \right) \alpha}{10 t^{3/2}} \tag{11.16}$$

This means that $t_i \propto L_i^{2/3}$.

11.2.3 Demonstration

We now provide a demonstration of the technique from the previous sections. We begin with the case where we have a single gravitational-wave event with an associated skymap, such as in Figure 11.2, and desire to know how to pursue optimised follow-up. We assume that we have been allocated a fixed period of time t on a telescope.

The recipe for construction of the pointing directions and time-allocations are as follows. Depending on the source model and mass distribution assumptions, the rele-

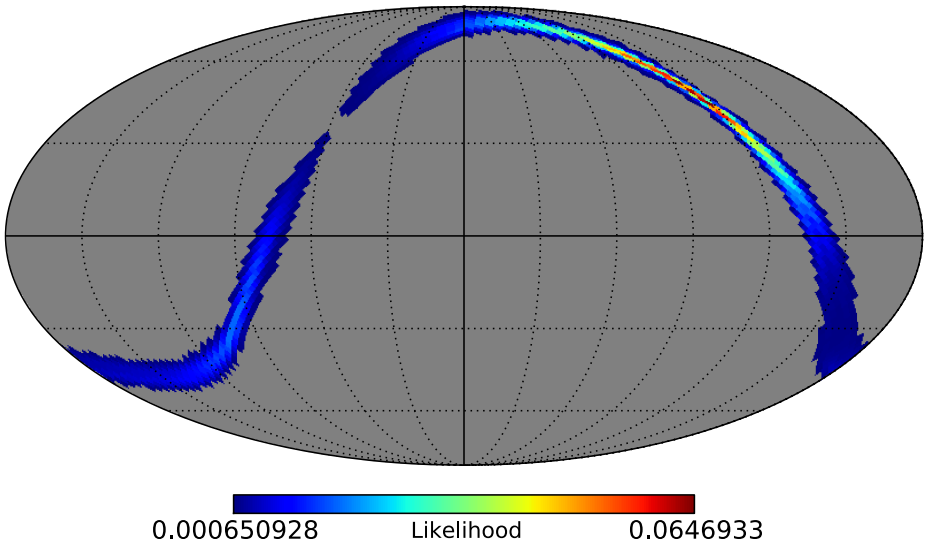


Figure 11.2: The gravitational-wave likelihood $L_{\rm GW}(\alpha, \delta, R)$ for the event of interest. This likelihood is to give the scaled optimal observation time allocation for this same event, assuming a continous mass distribution, such that the probability goes as $\left(\frac{L_{\rm GW}(\alpha,\delta,R)}{a(\alpha,\delta)}\right)^{2/3}$.

vant metric from the previous section is computed. For example, in the uniform mass density case, the metric is $t_i \propto \left(\frac{L_{\rm GW}(\alpha,\delta,R)}{a(\alpha,\delta)}\right)^{2/3}$ for the skymap of interest. The FOVs are rank-ordered by this metric and images taken with time for the allocation appropriate for that field.

We now perform a Monte Carlo simulation where we place sources on the sky consistent with the given skymap and determine the number of images required to successfully recover them. For concreteness, we adopt the parameters for a source with an absolute magnitude of m=-11. We adopt as our current telescope the Panoramic Survey Telescope and Rapid Response System (Pan-STARRS) is a telescope designed to discover new Near Earth Objects (NEOs), as well as provide astrometry and photometry of already detected objects. It has a 3° FOV with a limiting magnitude of

about 24, taking images of the entire sky about 4 times per month. We compare three scenarios. The first is where the event location is previously known. In this particular case, we obtain a 50% detection probability after 540 s of integration. In the case where a naive strategy is employed, where all fields are tiled equally, the event can be imaged with 50% probability in 118 hrs. Finally, in the case where the optimal strategy is employed, the event can be imaged in 36 hrs with 50% probability. This corresponds to approximately a factor 3 typical reduction in the amount of time required to image the event.

11.3 Conclusion

We have described an implementation of an optimization strategy for the detection of gravitational-wave optical counterparts. We showed how an implementation of this kind can improve searches for these transients. We find that by making assumptions about the event rate and sky localization abilities of the gravitational-wave detectors, follow-up imaging can be significantly improved. Therefore, this approach may provide further opportunities for improving electromagnetic follow-ups.

In the future, we can consider the case that we have many events that will be available for follow-up over the science run. If all goes well, gravitational-wave detectors will detect an event rate of $N_{\rm events} = 40$ events per year. It is possible that there are significantly fewer events than this, if pessimistic astrophysical models prove to be the case. Luckily, during any given science run, it will quickly become apparant the number of triggers being generated by the gravitational-wave detectors is not as expected. Therefore, the number of events assumed can be updated based on the number of events seen in the first few months, for example.

Further, we can explore the coordination of multiple telescopes with different fields of view and limiting magnitudes. We expect that a similar formalism can be compiled for this case. This will be important especially for coordinating, for example, Pan-STARRS and ATLAS. Pan-STARRS has a FOV of about 3 square degrees. Coupled with the reduction in FOV due to the fill factor and hexagonal tiling due to using a circular field, it usually takes multiple exposures. ATLAS, on the other hand, is 5.4 x 5.4 square degrees. Due to its larger field of view, no fill factor, and square footprint tiles with very little loss, the difference in the number of images required for an ATLAS and Pan-STARRS field can be about an order of magnitude. Therefore, an optimal observing strategy must account for this difference.

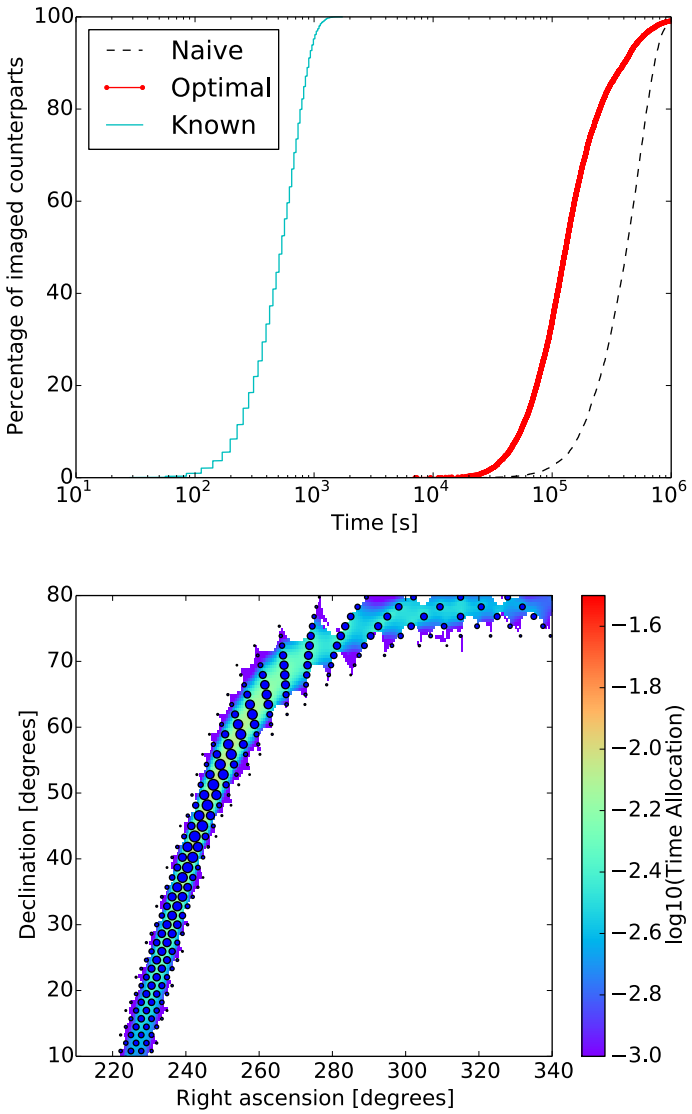


Figure 11.3: On the left is the proportion of imaged counterparts as a function of time allocated to an event. We plot this for three scenarios: where the event location is previously known, where the likelihood is scaled in the optimal way derived in this work, and finally a naive strategy of imaging all fields equally. On the right are the proposed fields for observations by Pan-STARRS using time scalings shown by the size of the dots.

12

A Daytime Measurement of the Lunar Contribution to the Night Sky Brightness in LSST's *ugrizy* Bands– Initial Results

Efficient telescope scheduling is essential to maximize the scientific output of survey telescopes. Optimizing a survey's scientific merit function requires scheduling decisions that consider slew rate, sky brightness, source location, transparency and extinction, and many other factors. For surveys such as LSST that will scan the entire accessible sky[177], a determination of the sky brightness as a function of azimuth, ele-

vation and passband is an important factor in crafting an optimal sequence of observations. Contributions to the night sky include unresolved or diffuse celestial sources, emission from OH molecules in the upper atmosphere, zodiacal light, man-made light pollution, and moonlight that scatters from clouds and from the constituents of the atmosphere. Some of these contributions to the night sky are stable over time and do not impact the order in which we observe fields. Other contributions to the night sky are time-variable but deterministic. The monthly variation due to moonlight falls in this category, for cloud-free conditions. Other contributions to sky brightness, such as variable OH emission[163] and moonlight scattering from clouds, are more stochastic in nature.

Understanding the brightness of the cloudless moonlit sky in the LSST bands is one key component in scheduling decisions. To make predictions of potential future performance, LSST has developed an operations simulator to study different scheduling algorithms[110]. Thus far, the LSST operations simulator has used historical weather records and measures of the atmospheric conditions for the Cerro Pachon site (taken over a 10-year time period). The operations simulator generates a sky model that predicts sky brightness based on the Krisciunas and Schaefer model[197], which is further discussed below. It also simulates atmospheric seeing and cloud coverage as a function of time. This information is used to estimate the efficiency of the survey for different candidate scheduling algorithms. As LSST advances into the construction phase, and eventually into full operation, we need a higher fidelity determination of the brightness of the cloudless night sky. This will be augmented with all-sky-camera data[84] to make real-time, condition-dependent adjustments to the sequencing of LSST observations.

We define the lunar contribution to sky brightness as the difference between the

observed sky brightness (in units of magnitudes per square arc sec) with the Moon above the horizon and the moonless sky brightness, for a given the phase of the lunar cycle. From the standpoint of scheduling decisions, what matters most is the *relative* lunar brightness variation across the accessible sky, and so our primary goal in this paper is to determine this spatial structure, using the sun as a proxy for the moon. This allows us to obtain high signal-to-noise data, without complications from other contributions to sky brightness.

An *ab initio* computation of the lunar sky illumination is complicated due to multiple scattering effects. Sunlight reflects off the moon, and a portion of this light is scattered towards the Earth. This light impinging on the top of the atmosphere is then scattered by molecules and aerosols, and some is absorbed. The moonlight can be scattered multiple times, including off of the ground, before it reaches the telescope pupil. An empirical measurement is arguably more secure than a radiative transfer calculation that must make assumptions about the size, shape, and vertical distribution of aerosols.

Walker developed[2] a scattered moonlight model that included a table of sky brightness in five photometric bands, at five different moon phases. It did not account for the positions of the Moon or observation target, and was measured during solar minimum. Because of these shortcomings, it is not accurate enough for current and future telescope operations. Later, Krisciunas and Schaefer used an empirical fit to 33 observations taken in the V-band taken at the 2800 m level of Mauna Kea, resulting in an accuracy between 8% and 23% if not near full Moon[197]. This model predicted the moonlight as a function of the Moon's phase, the zenith distance of the Moon, the zenith distance of the sky position, the angular separation of the Moon and sky position, and the band's atmospheric extinction coefficient. More recently, a spectroscopic

extension of this model was used to fit sky brightness data from Cerro Paranal[229]. This treatment includes all relevant components, such as scattered moonlight and starlight, zodiacal light, airglow line emission and continuum, scattering and absorption within the Earth's atmosphere, and thermal emission from the atmosphere and telescope. This model was recently updated with an observed solar spectrum, a lunar albedo fit, and scattering and absorption calculations[185,184]. Winkler et al. characterized the nighttime sky brightness profile under a variety of atmospheric conditions using measurements from the South African Astronomical Observatory soon after the Mount Pinatubo volcanic eruption in 1991[155]. Our goals in this paper are more limited, as we are primarily interested in the spatial structure and spectrum of the scattered moonlight component of the night sky.

Based on this discussion, it is clear that models for scattered moonlight are very complicated. This motivates our attempt to empirically determine the relative sky brightness as a function of lunar phase, and its dependence on the positions of the target and the moon. We measured the solar sky brightness as a function of angle between sky location and the sun, as well as zenith angles of the sun and the telescope. We argue that this is useful because up to wavelength-dependent lunar albedo factors as well as an azimuthal dependence around the lunar disk at phases less than Full Moon, the sky illumination pattern that the moon casts has the same functional form as from the sun in the daytime. In this work, we will use a lunar model to correct for the albedo factors, and assume that the effect of the azimuthal dependence from sub-Full moon phases is small as survey observations will be pointing far from the Moon.

We have made measurements of the daytime sky brightness at Cerro Pachon, the LSST site in Chile, with an array of six photodiodes with filters in the *u, g, r, i, z,* and *y* bands. There is an extensive history of daytime sky brightness measurements.

In particular, the angular and wavelength dependence of the observed solar scattering can be used to deduce properties of atmospheric aerosols and precipitable water vapor. We use a similar measurement scheme to the AERONET remote sensing aerosol monitoring network[58]. The AERONET sky brightness data are taken in optical passbands that differ from those that LSST will use. Rather than invoke a set of color transformations to convert from AERONET into LSST bands, here we make a direct measurement of sky brightness in the LSST passbands. This constitutes an initial effort to make this measurement; as the data are taken over four days in Chile, one of which had high cirrus clouds in the sky, the analysis will benefit from further measurement.

We describe the apparatus in section 12.1. Measurements and analysis are presented in section 12.2. We conclude with a discussion of topics for further study in section 12.3.

12.1 Apparatus

Figure 12.1 shows a sketch of the photodiode mount, which is identical for all six channels except for the interference filters that define the passbands. Light enters a 50 mm inner diameter cylinder, 152.4 mm long, that serves to block off-axis stray light. The 50 mm diameter filters are placed at the base of this baffle tube.

We used "Generation 2 Sloan Digital Sky Survey (SDSS)" u,g,r,i,z,y filters from Astrodon[43]. Figure 12.2 shows their transmission spectra as well as the current-design LSST filters[177], for comparison. The Astrodon filters we used are essentially flat-topped, with minimal leakage or in-band ripple. An adjustable iris (Thor Labs SMD12C) sits behind the interference filter. We found we could operate with these irises set

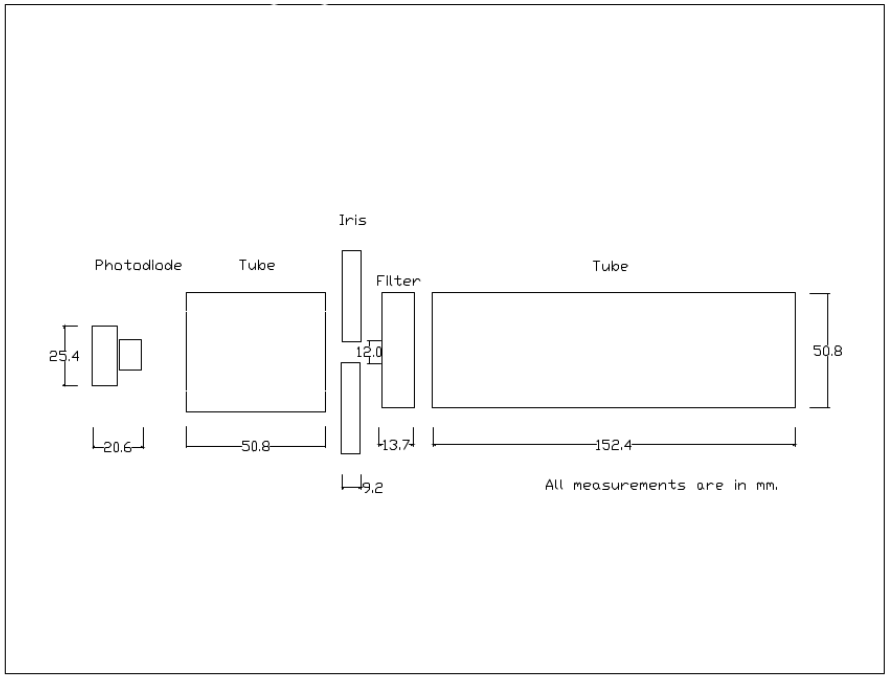


Figure 12.1: Sketch of the photodiode portion of the apparatus. The photodiode mounts include a photodiode, an iris, a filter, and a baffle tube.

to their maximum opening diameter of 12 mm, for all six passbands. The only other transmissive optical element that lies between the Si and the sky is a quartz window in front of the photodiode.

The photodiodes are SM1PD2A cathode-grounded Si UV-enhanced photodiodes, obtained from Thor Labs. The photodiodes have a 10 mm x 10 mm active area behind a 9 mm diameter input aperture. The only other transmissive optical element that lies between the Si and the sky is a quartz window in front of the photodiode. The

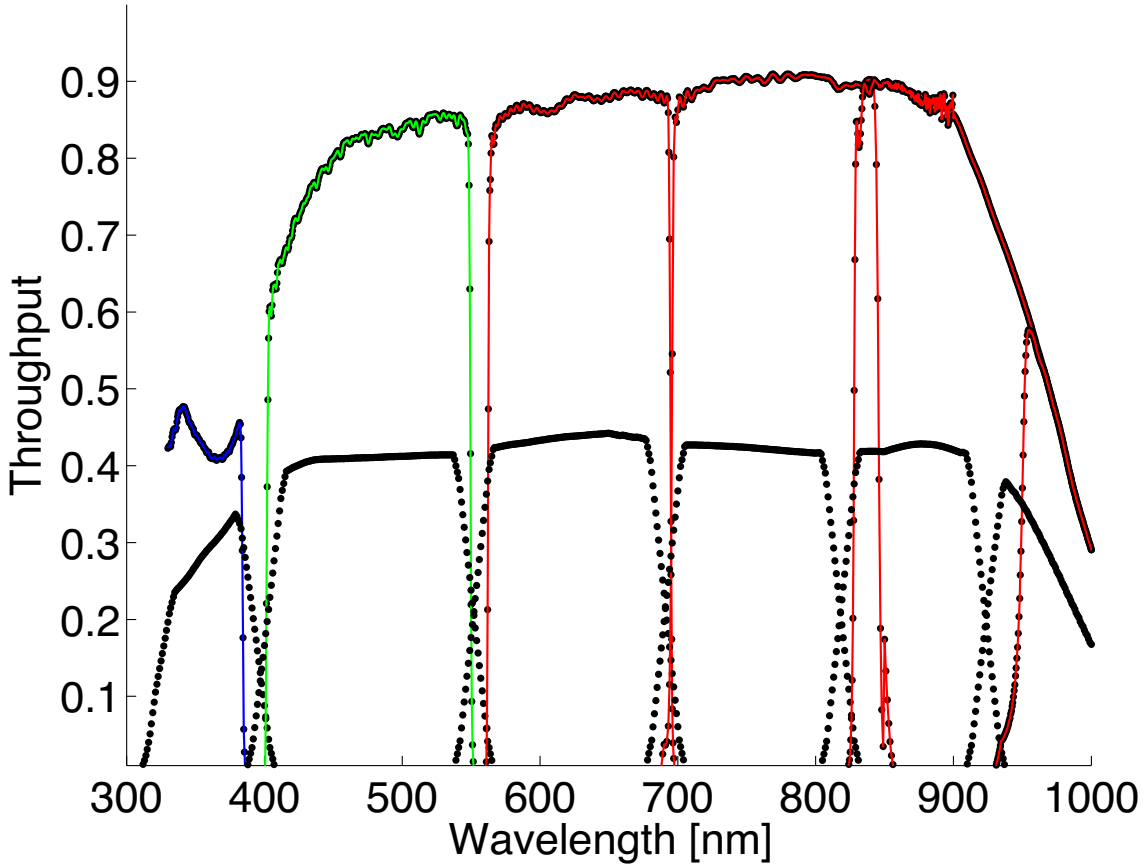


Figure 12.2: Photon sensitivity function curves for the photodiodes (upper) used in this experiment, and the expected photon sensitivity function for LSST (lower curves, due to more complex optical system). From left to right the bands are u, g, r, i, z and y. We use this information to make a throughput correction when predicting scattered moonlight backgrounds for LSST. The Astrodon filters we used for the photodiodes are designed to avoid the water band at 940 nm.

etendue of the system is established by the combination of the 12 mm diameter iris and the 9 mm circular photodiode input aperture. These two circular apertures are separated by a distance of 60 mm.

12.1.1 Etendue of the photodiode plus tube system, in comparison to an LSST pixel

As seen from the plane of the diode aperture, the full-angle subtended by the adjustable iris is then $2\arctan(\frac{6}{60}) = 11.4°$, which subtends a solid angle of $\Omega_{\rm diode} = 2\,\pi\,(1 - \cos(\frac{14}{2})) = 3.11 \times 10^{-2}$ steradians. For comparison, a pixel on LSST subtends 0.2 arcsec on a side, for a solid angle of $\Omega_{\rm LSST} = 4\,\tan^{-1}(\frac{9.7\times10^{-7}}{2})) = 9.4 \times 10^{-13}$ steradians/pixel.

If we consider the iris as establishing the field of view of the photodiode system, then the aperture in front of the diode determines the sensor's unvignetted collecting area, where $A_{\rm photodiode} = \pi\,(4.5 \times 10^{-3}{\rm m})^2 = 6.36 \times 10^{-5}\,{\rm m}^2$. This amounts to computing the effective photodetector area. For comparison, the effective collection area of LSST is equivalent to a diameter of 6.5 m, for a collection area of $A_{\rm LSST} = \pi\,(\frac{6.5{\rm m}}{2})^2 = 33.2\,{\rm m}^2$. The ratio of the etendue of an LSST pixel to the photodiode is then $R = \frac{A_{\rm LSST}\Omega_{\rm LSST\ pixel}}{A_{\rm photodiode}\Omega_{\rm photodiode}} = 1.58 \times 10^{-5}$.

The interpretation of the data will benefit from knowing the ratio between the instrumental response function of the photodiode system and LSST. We are interested in the system "throughput", or relative spectral response. Table 12.1 compares the band-integrated system throughput Figure for the photodiode system (the Thor labs QE times the Astrodon filter response) with two versions of the LSST throughput. LSST is considering using CCDs from two vendors, e2v and ITL, and these have somewhat different quantum efficiency curves. We have, therefore, provided in Ta-

ble 12.1 the results from integrating over the response functions (including in the LSST case the three reflections, the obscuration, the filter and corrector transmissions, and the detector QE) at a spacing of one nm. The units in Table 12.1 are nm, and can be interpreted as the sensitivity-weighted equivalent width of the respective filters. Taking the ratio of these numbers, passband by passband, allows us to scale the photodiode measurements to anticipated values on the LSST focal plane.

band	diodes	LSST with ITL	LSST with e2v	$\left[\frac{T_{ITL}}{T_{diodes}}\right]$	$\left[\frac{T_{e2v}}{T_{diodes}}\right]$
u	33.8	20.6	15.3	0.61	0.45
g	99.0	61.3	65.4	0.62	0.66
r	93.2	60.3	62.9	0.65	0.67
i	106.7	53.7	53.2	0.50	0.50
z	155.2	-	-	-	-
zs	65.8	44.3	43.3	0.67	0.66
y	69.5	27.9	27.2	0.40	0.40

Table 12.1: System throughput values. The first three columns are the integral of the system response function at 1 nm spacings, for each passband in the different systems. The last two columns show ratios of the LSST throughput to that of the diodes. The diode instrument has no reflective optics and a minimum of air-glass interfaces, whereas LSST has three reflections from aluminum as well as a three element corrector. Also, the photodiodes are considerably thicker than the LSST CCDs, and have enhanced UV sensitivity. This accounts for the increased diode throughput compared to the LSST system.

The photodiodes are connected via coaxial cable to a set of manual switches that feed a selected one of the six signals to a Thor Labs model PDA200C photocurrent amplifier, which produces a $\pm$ 10 V signal proportional to the current from the selected photodiode. This signal was connected to an Arduino Uno, which digitizes this signal with a 10 bit A/D converter. The Arduino was connected to a serial port on the data collection computer.

The six photodiode tubes are mounted on a Celestron model CG-5 equatorial telescope mount, which is controlled by external connection to a laptop computer. Stel-

larium ([73]) is used to control the telescope mount pointing. The mount's RA and DEC motors have a precision of 0.05°. The computer registered the right ascension (α) and declination (δ) for each brightness measurement, along with the photocurrent from each of the six photodiodes.

12.1.2 Sky Scanning Strategy and Angular Coordinates

Assuming that the scattering properties of the atmosphere are axisymmetric about local vertical, the normalized sky brightness (scaled to the brightness of the illuminating source) depends on three angles: the zenith angle z_{source} of the source (sun or moon), the zenith angle z_{tel} of the telescope boresight, and the azimuthal angle $\Delta\phi$ between the source and the boresight.

An "almucantar" is the line on the sky at the elevation angle of the Sun, at some given time. An advantage to making sky brightness measurements along an almucantar is that the boresight and source elevation angles are constant, and equal. Only their azimuthal separation is varied. During an almucantar measurement, observations are made at the solar elevation angle through 360° of azimuth. The almucantar sweep is a special case of a constant-zenith-angle scan, which is our favored data collection method. The range of scattering angles along an almucantar decreases as the solar zenith angle decreases; thus almucantar sequences made at airmass of 2 or more achieve maximum scattering angles of 120° or larger.

We elected to obtain our sky brightness data in a succession of constant-zenith angle scans, taking a data point every 45° of azimuth, except near the zenith. This gives us 8 data points in azimuth at each telescope zenith angle. While these are sufficient to perform simple linear fits, which we discuss below, future analyses would benefit from significantly more observations. We obtained data at zenith angles of 0, 30, 45,

60, and 75°, and along the almucantar, over the course of the day, in each passband. The resulting daytime sky brightness (DSB) data by passband, $DSB(z_{\text{source}}, z_{\text{tel}}, \phi, \text{filter})$, comprise our measurement. We generate an all-sky map of sky brightness. The data are processed as follows. For each solar zenith angle, we generate an all-sky map of brightness vs. position. We then repeat for different values of solar zenith angle. We make a polynomial fit of degree 1 to brightness vs. altitude and delta-azimuth. This is a map of relative night sky brightness if the moon were at the location of the sun, up to an overall scale factor per passband. We can use the geometry of the photodiode tube to compute number of photons per square arcsec per square meter and then scale the value by about 14 magnitudes to get the lunar contribution. The scaling factors are computed in the next section. We can then compute an estimate for other lunar phases, based on the lunar phase function. Of course, the actual sky brightness is a combination of the lunar contribution, which we compute, plus other factors such as solar cycle and site characteristics. In addition, what instruments attribute to "signal" and "noise" from the astrophysical light depends on plate scale, integration time, etc.

12.1.3 Scaling from Solar to Lunar Illumination

Keiffer and Stone ([189], hereafter K&S)) describe how to scale between solar illumination and lunar illumination at the top of the atmosphere, depending on both reflection geometry and wavelength. The ratio R of the lunar to solar irradiance at the top of the atmosphere is given by $R(\lambda, g) = A(\lambda, g)\,[\Omega_M/\pi]$, where Ω_M is the solid angle subtended by the moon, and $A(\lambda, g)$ is a wavelength dependent scattering function that depends on the angle, g, between the vectors from the moon to the Earth and the moon to the sun. We have assumed nominal values for the sun-moon (1 AU =

Band	Δmag($g = 2°$)	Δmag($g = 10°$)	Δmag($g = 45°$)	Δmag($g = 90°$)
u	2.7	3.1	4.2	5.7
g	2.4	2.8	3.8	5.2
r	2.1	2.5	3.4	4.9
i	1.9	2.3	3.3	4.7
z	1.9	2.2	3.2	4.6
y	1.8	2.2	3.1	4.5

Table 12.2: Irradiance attenuation due to lunar scattering, in the LSST bands, at various lunar phase angles. The illumination from the moon is slightly redder than sunlight, in general. This reddening effect increases as the phase angle increases.

149,597,870.7 km) and moon-earth distances (384,403 km). The geometrical dilution factor is $6.42/\pi \times 10^{-5} = 2.04 \times 10^{-5}$, or 11.7 magnitudes.

To correct for the wavelength-dependent and phase-angle-dependent lunar scattering function, we took the parametric description of $A(\lambda, g)$ provided in K&S, integrated across our passbands (note: truncated u band at 350, no data bluer), to determine the scattering-dependent magnitude differences between sunlight and moonlight at the top of the atmosphere, for different lunar phases. We limited the range of phase angles to $|g| > 2$ degrees, which is an approximate lower limit of the lunar phase angle observable from the ground.

The additional attenuation from lunar scattering as a function of passband at full moon (taken here to be our minimum scattering angle of 2 degrees) is listed in Table 12.2. We obtained these values by numerically computing

$$\Delta\mathrm{mag}_i(g) = -2.5\log_{10}\left(\frac{\int A(\lambda, g)T_i(\lambda)\mathrm{d}\lambda}{\int T(\lambda)\mathrm{d}\lambda}\right) \tag{12.1}$$

where $T_i(\lambda)$ is a top-hat approximation of filter i.

Based on these values, since the sky brightness scales linearly with the irradiance

Filter	Dark Current [nA]	1σ Uncertainty [nA]
Channel 1	4.3	0.2
Channel 2	2.1	0.3
Channel 3	5.3	0.2
Channel 4	4.2	0.2
Channel 5	4.6	0.2
Channel 6	2.0	0.3

Table 12.3: Dark current measurement for all six filters. Measurements were taken periodically during data taking to check if there was a significant temperature dependence. Dark current values were found to be approximately the same over the run, and these values are about 100 times smaller than the currents in the sky brightness analysis.

provided at the top of the atmosphere, we expect the r band full-moon lunar sky brightness to be a factor of 11.7+2.1=13.8 magnitudes fainter than what we observe in the daytime, if the moon were placed in the same alt-az position as the sun.

This allows us to generate, up to a single passband-dependent overall scale factor that depends on the effective etendue of the photodiode tube, the equivalent full-moon sky brightness map for the case where the moon is in the same location as the sun. We simply take the solar-illuminated sky brightness data, and scale all values to the r band brightness at the zenith. Then we make a passband-dependent adjustment based on the color of the reflected sunlight as shown in Table 12.2.

12.2 Results

We begin by measuring dark current values for each photodiode channel, performed by capping the photodiode tubes and laying a dark blanket over the apparatus, and the results are displayed in Table 12.3. The photodiodes have dark current values ranging from 2.0 to 5.3 nA with statistical uncertainties between 0.2 to 0.3 nA. These dark currents are well under 1% of the signal levels from the sky. Because it is a neg-

ligible contribution, we ignore the dark current contribution in the analysis that follows.

12.2.1 Observations

We obtained sky brightness data from the roof of the ALO building on Cerro Pachon, (located at S 30:15:06, W 70:44:18) during the daytime on 2014 Sept 4, 5, 6 and 7. The conditions on Sept 5 were less favorable, with high cirrus clouds in the sky. Due to the limited data, future analyses will benefit from more data with varied conditions, especially due to the potential significant weather variations during the winter in Chile. We cycled through the sky sampling strategy described above, taking 2000 data points in each passband, running through the 6 bands in succession. Each data collection period at a fixed pointing lasted about two minutes, and a full cycle across the sky lasted about an hour. In all, we collected 10 sequences, spanning a range of solar elevations from 20° to 55°.

12.2.2 Spatial structure of scattered light and Lunar sky brightness

Night sky structure was investigated by[136], in the context of flat-fielding. The authors are unaware of a comprehensive program to map (and visualize) the sky brightness under variable lunar illumination conditions. In the following, we show the sky brightness dependence on the zenith angle $z_{\rm source}$ of the source (sun or moon), the zenith angle $z_{\rm tel}$ of the telescope boresight, and the azimuthal angle ϕ between the source and the boresight. We perform fits of sky brightness to the three independent variables and compute the effect on 5 sigma point source detection magnitude for a sur-

Band	a ($\times 10^{11}$)	b ($\times 10^{11}$)	c ($\times 10^{11}$)	d ($\times 10^{11}$)	Median Residual ($\times 10^{11}$)
u	88.5 (6.2)	-0.5 (0.1)	-0.5 (0.1)	0.4 (0.1)	5
g	386.5 (34.0)	-2.2 (0.2)	-2.4 (0.2)	0.8 (0.5)	13
r	189.0 (32.7)	-1.4 (0.2)	-1.1 (0.2)	0.8 (0.5)	11
i	164.8 (33.1)	-1.5 (0.2)	-0.7 (0.2)	0.6 (0.5)	12
z	231.2 (62.3)	-2.8 (0.3)	-0.7 (0.4)	1.4 (0.9)	21
zs	131.1 (45.6)	-1.4 (0.2)	-0.5 (0.3)	0.2 (0.6)	10
y	92.0 (32.7)	-1.3 (0.2)	-0.2 (0.2)	0.9 (0.5)	20

Table 12.4: Daytime sky brightness values as function of angle between the point on sky and sun, altitude of the point on the sky, and altitude of sun fit to a plane of the form $a+bx+cy+dz$ in electrons/s. The zs band values, which are given to approximate the LSST z filter, are computed using Astrodon z minus y. Here, x corresponds to the angle between the point on the sky and the sun, y corresponds to the altitude of the point on the sky, and z corresponds to the altitude of the sun. The median of the absolute value of the residuals is given by the final column. The statistical errors arising from the $1\,\sigma$ RMS errors from the plane-fitting analysis are given by the numbers in parentheses.

vey such as LSST. The data allows us to study the color across the sky. We also note how to scale overall brightness in each band as a function of lunar phase.

The first result we present is sky brightness as a function of angle between the point on sky and the sun, the altitude of the point on the sky, and the altitude of the sun. The measurements describe a three-dimensional surface corresponding to these parameters. We convert the photodiode output from μA to electrons/s. We fit resulting data to a plane of the form $a + bx + cy + dz$ for each of the six bands. Here, x corresponds to the angle between the point on sky and the sun, y corresponds to the altitude of the point on the sky, and z corresponds to the altitude of the sun. An example of these fits for the u-band are shown in Figure 12.3. The coefficients and the standard errors, as well as the median of the residuals for the fits are shown in Table 12.4. We find the residuals of the fits to be small; these are generally an order of magnitude smaller than the overall scale factor (a). There are a number of notable

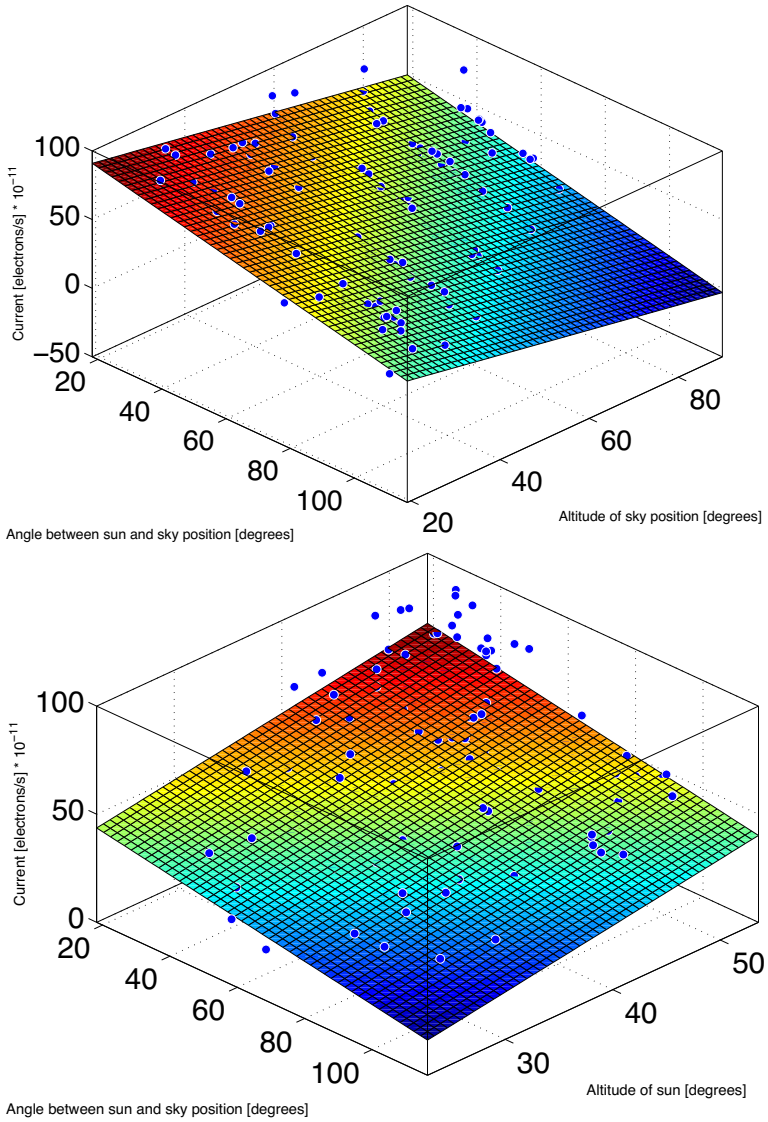


Figure 12.3: Linear fit to the u-band fluxes (and the data points) for both the angle between the point on sky and sun and altitude of the point on the sky (on the left) and the angle between the point on sky and sun and the altitude of the sun (on the right). The coefficients for the fits in all of the bands can be found in Table 12.4.

features. The first is that as ϕ increases, the sky brightness decreases. This in and of itself is not surprising, but the rates of decrease are significant. For example, in the g band, for every 10 degrees that ϕ decreases, the number of photons increases by more than a factor of 2. There is a similar effect for the altitude of the point on the sky. As the point moves to the horizon, the sky brightness increases. This effect is more pronounced for the bands near the blue. Finally, the sky brightness increases as the altitude of the sun increases. Perhaps more interesting is the significant color dependence of the results. Although the trends described above hold true regardless of color, the magnitude of their effect is very different. The difference between the g and y bands is about a factor of 2 difference in the point on the sky dependence and more than a factor of 10 difference in the altitude of the point on the sky. The effect of the altitude of the sun, z_{source}, is more constant across color.

It is straightforward to apply the measured planar fit coefficients to an individual observation. Table 12.2 provides the appropriate scale factor for different moon phases and passbands. If the passband of interest varies significantly from the filters in this study, one can compute the appropriate factor from equation 12.1. After this, one computes the altitude and azimuth at the site of interest at the time of the observation as well as the altitude and azimuth of the target. Three angles are then computed from these quantities: the angle between the point on the sky and the moon, the altitude of the point on the sky, and the altitude of the moon. One then computes $a + bx + cy + dz$ for the appropriate passband, where a, b, c, and d are given in Table 12.4, and x corresponds to the angle between the point on the sky and the moon, y corresponds to the altitude of the point on the sky, and z corresponds to the altitude of the moon. This table allows for a straightforward comparison between the ratio of sky brightnesses for different colors. The ratio of fluxes in u to g,

for example, are about 5 in the angle between the point on the sky and the sun and the altitude of the point on the sky terms, and 2 for the altitude of the sun. On the other hand, the ratio of fluxes in u to i, depends heavily on angle to the source, with virtually no dependence on zenith angle. This indicates that the sky is much redder close to the moon than far away. A code that performs these steps is available at https://github.com/mcoughlin/skybrightness for public download. Hopefully, this will allow other researchers to easily use the data product. Required inputs are the latitude, longitude, and elevation of the site, right ascension and declination of the source, the passband of interest, and the times of observation.

12.2.3 From Relative Sky Brightness to m_5 Variations to Optimal Scheduling

We can use the data we have generated of *relative* daytime sky brightness to generate a sky map of degradation in the point source magnitude that can be detected in the case where scattered moonlight dominates the Poisson noise. We define the *sky brightness factor*, SBF, to be the ratio of the local sky to the darkest attainable sky surface brightness at that moment. In order to achieve the same SNR with varying sky backgrounds, the source must be brighter by a factor of $\Delta m_5 = \frac{1}{2} \times -2.5 \log_{10}(SBF)$. Because the sky brightness structure is linear in the illumination level, the sun-illuminated measurements are perfectly valid for making these Δm_5 maps. If one region of the sky is twice as bright as another in the daytime, then for the moonlight-dominated case, replacing the sun with the moon will not change that fact. An example is shown in Figure 12.4, for the u-band. For the scheduling of LSST observations over the course of a night, a week, or a month, this is the format in which we think the sky brightness data is most useful. We stress that this comes directly from the daytime

measurements of relative brightness, with no conversion needed, as long as scattered moonlight dominates the sky background.

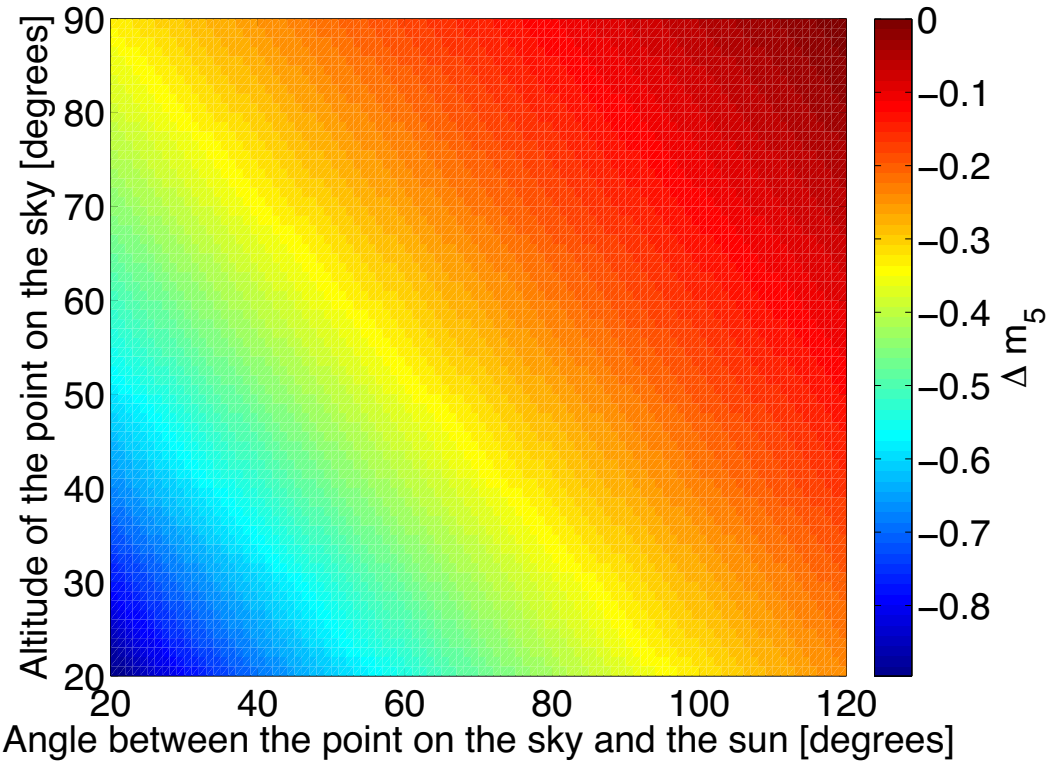


Figure 12.4: Variation Δm_5 in the point source magnitude that can be detected at 5σ in the u-band, against spatially varying sky brightness. This contour plot shows the change in point source detection threshold as a function of altitude and angular separation from the moon. The color bar indicates the change in m_5 for a fixed exposure time, in magnitudes.

12.2.4 Prediction of Scattered Moonlight Contribution to LSST backgrounds

Table 12.5 presents the data analysis sequence, for sky brightness obtained at zenith with a source elevation angle of 45°. The table shows, for each passband, the mea-

sured photocurrent, the dark current value, the number of photoelectrons per second produced in the photodiode, the geometrical factor GF for scaling from solar to lunar irradiance, the attenuation due to the lunar phase function at PF full moon ($g = 2^\circ$), the ratio R of LSST pixel to photodiode etendues, the ratio of throughput times etendue for the two systems, and the number of LSST photoelectrons per pixel per second. We compute

$$\Phi_{\mathrm{LSST}} = \left[\frac{I_{\mathrm{meas}} - I_{\mathrm{dark}}}{1.60 \times 10^{-19} Coul}\right] * GF * PF * \left[\frac{T_{LSST}}{T_{diodes}}\right] * \left[\frac{(A\Omega)_{LSST\ pixel}}{(A\Omega)_{diodes}}\right] \qquad (12.2)$$

to obtain the expected number of photoelectrons per pixel per second we expect on the LSST focal plane, for full moon conditions, with the telescope pointed to the zenith, and a lunar zenith angle of 45°. Note that we do not include any factor for atmospheric attenuation since we wish to use the photon arrival rate on the photodiode to predict the lunar background flux on the LSST focal plane. There is qualitative agreement between the values calculated from the daytime measurement and the LSST exposure time calculator. The exposure time calculator uses the full sky spectrum, not just lunar part, and thus we expect the photodiode measurements to generally underestimate the exposure time calculator numbers. This is shown to generally be true in Table 12.5.

12.2.5 Statistical and Systematic Errors

The systematic and statistical errors in our measurement are now discussed. The statistical errors arising from the $1\,\sigma$ RMS errors from the plane-fitting analysis are shown in Table 12.1. For example, u, g, r, i, z, zs, and y have relative errors of 7%,

Band	I_{meas} μA	Geometry Factor	Phase Factor	$\frac{T(ITL,e2v)\,A\,\Omega(LSST)}{T\,A\,\Omega(Photodiode)}$	Φ_{ITL} e/pix/s	Φ_{e2v} e/pix/s	ETC e/pix/s
u	1.0	2.04×10^{-5}	0.091	(0.61,0.45)*1.58×10^{-5}	110	81	106
g	3.5	2.04×10^{-5}	0.114	(0.62,0.66)*1.58×10^{-5}	494	526	451
r	1.8	2.04×10^{-5}	0.14	(0.65,0.67)*1.58×10^{-5}	332	342	186
i	1.5	2.04×10^{-5}	0.17	(0.50,0.50)*1.58×10^{-5}	255	255	116
z	2.2	2.04×10^{-5}	0.13	(0.67,0.66)*1.58×10^{-5}	386	380	-
zs	0.9	2.04×10^{-5}	0.13	(0.67,0.66)*1.58×10^{-5}	154	151	89
y	1.1	2.04×10^{-5}	0.20	(0.40,0.40)*1.58×10^{-5}	169	169	23

Table 12.5: Zenith daytime sky brightness values, converted to expected LSST lunar sky backgrounds at zenith at full moon. These are all adjusted to a common angle between the point on sky and sun, altitude of the point on the sky, and altitude of sun of 45°. The zs band values, which are given to approximate the LSST z filter, are computed using Astrodon z minus y.

9%, 17%, 20%, 34%, and 35% respectively in the constant part of the fit. In general, the statistical errors increase as the wavelength increases. The systematic errors can also be substantial. First of all, in the analysis, we have assumed that the distance between the Sun-Moon and Earth-Moon is constant. In actuality, the distance between the Sun and Moon can vary from the average by about 3.3% (and therefore in total about 7%), which corresponds to a difference of 0.036 mags (or about 0.072 mags). Similarly, the distance between the Earth and the Moon can vary between 358000 - 406000 km, corresponding to a difference of -0.075 - 0.059 mag relative to the value of the major axis. This corresponds to a total difference of 13.5%. There are other effects present less easily quantified. The model of Krisciunas and Schaefer[197] make a number of assumptions. For example, the model ignores the fact that the Lunar Mare and highlands create irradiance differences across the moon. Also, due to the change in the distance of the moon, the magnitudes can vary by up to 0.12 mags. The model of Kieffer and Stone[189] have statistical errors generally no greater than

5%, although the absolute calibration is more difficult to quantify, as it relies on absolute flux data with an assumed energy distribution for Vega. We will take 10% to be the relative error from the Kieffer and Stone model. Another example is the temporal variation of atmospheric extinction, due to variation in aerosol and water content as well meteorology[288]. Stubbs et al. estimate that atmospheric water content variation creates 1-2% variations in absolute zeropoint. The moon model of Jones et al.[185] find average uncertainties of 0.15 mags. They estimate an uncertainty of less than 5% from the solar spectrum used, as well as another 5% from uncertainty in the scattering model, and the remaining uncertainty is dominated by atmospheric conditions. In our case, we can use the 1-sigma errors from the fit to estimate the associated errors. These errors depend on the particular values for the angle between the point on sky and the Sun, the altitude of the point on the sky, and the altitude of the Sun, but generally vary from 0.3-0.7 mags from the u to the y band respectively.

12.3 Conclusion

Measurements of sky brightness are important for efficient telescope scheduling and predictions for LSST. While daytime measurements are approximations to Lunar measurements, it provides high signal to noise ratio measurements in the LSST bands. We measured the fall-off in sky brightness with angle from the sun and zenith angle.

There are a number of important conclusions to draw from the measurements. The first is that there are substantial gradients in scattered sky brightness, as much as 2 magnitudes. The second is that the scattered sky brightness increases closer to the horizon, perhaps due to more column density winning over extinction. The third is that when observing in bright time, there is significant benefit to point away from the

moon.

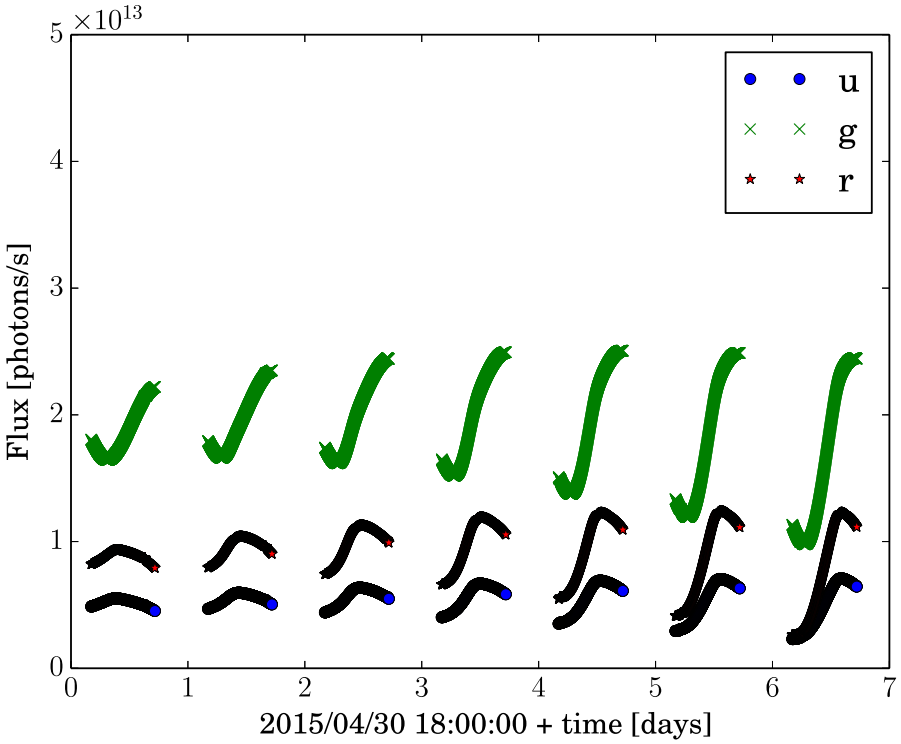


Figure 12.5: u, g, and r-band flux as a function of time for a single point on the sky using data from Table 12.5. Code to produce this plot is available at https://github.com/mcoughlin/skybrightness for public download. This shows in general the differences in flux for a single observation throughout the night.

As motivation for future work, Figure 12.5 shows u, g, and r-band flux as a function of time for a single point on the sky using the measurements described in this paper. We can use these measurements to prioritize observations throughout a given night. In the future, we intend to improve on these measurements by designing the apparatus to take simultaneous measurements. With such an apparatus, we will be able to, for example, measure the color of clouds. We will also be able to take significantly more observations, allowing for refinement of this model, continuing to make it

more useful for observers and those exploring scheduling strategies.

13

A collimated beam projector for precise telescope calibration

Photometry is currently limited by precise broadband photometric calibration at the few percent level[289]. In particular, photometric calibration issues currently dominate the uncertainty budget for type Ia supernova cosmology[55,286]. Photometric calibration of objects in images often still relies on observations of reference fields which lie outside the current field of view. This makes traditional calibration techniques sensitive to systematic errors arising from the temporal and spatial variability of the atmosphere's optical transmission, as well as time-varying instrumental changes. This is

important for research areas that require sub-percent level photometric calibration such as exoplanet surveys, which search for small photometric perturbations, and cosmological supernova surveys, which require detailed knowledge of the relative instrumental response as a function of wavelength.

The primary goal for the majority of calibration systems is to measure the dimensionless system transmission function $R_i(\lambda)$, where λ is the wavelength of the light and i is the pixel index. In general, this function is time-dependent and includes the effects of the atmosphere, optics, filter, and detector. The time-dependent effects of the atmosphere can be directly measured by independent systems. The transmission properties of the atmosphere are determined by a combination of Rayleigh scattering in the atmosphere, small particle scattering from aerosols, and molecular absorption[169,278]. In addition, the atmosphere has significant narrowband emission at wavelengths longer than 750 nm. It is $R_i(\lambda)$ combined with the spectral photon distributions (SPDs) and the effective aperture of the pixels that determines the signal measured from a source. The transmission function is affected by variations in internal interference giving rise to fringing, non-uniform interference filters, and water spots on detector anti-reflective coatings. "Flat-fielding" is traditionally used to normalize the variation in the pixels due to this function. Because both the SPDs and the transmission function jointly determine the measured flux levels, there is no unique flat-field which can be used to normalize this variation, which is important for consistent analysis across visits.

Calibration is typically performed using flat-field screens, which are illuminated with light that fills the telescope aperture. These over-fill the cone of angles which illuminates the telescope's focal plane. Although flat-field screens are often exposed with lamps with sharp spectral features, one method[289], which is used by both the

Pan-STARRS1 Survey[287,301], SNLS[251], and the Dark Energy Survey[186,216], is to use monochromatic light with a monitoring photodiode to determine each pixel's spectral aperture as a function of wavelength. A limitation of this method, however, is that it does not account for "scattered light," and its performance depends on the illumination pattern from the flat-field screen and the geometry of light scattering paths in the telescope and optics. Spatial non-uniformity of the flat-field illumination can masquerade as photometric non-uniformity due to obscuration, dust on optics, degraded mirror coatings, or vignetting. In addition, the scattered light from a flat-field screen has a scattering pattern which is very different from that from celestial objects. There are therefore significant short-comings to relying on flat-field screens for accurate calibration, and thus alternate techniques are worth exploring.

One such technique is a collimated beam projector (CBP) which can be used to determine the instrumental response function and does not suffer from the same systematic scattered light effects. In this design, a projector sends a beam of light with a diameter restricted by the size of the projector's aperture through the system. This is one component of the calibration system for the Large Synoptic Survey Telescope (LSST), which will rapidly and repeatedly survey one half of the sky with high-quality deep imaging and photometry[334]. It has a three-mirror design with a f/1.2 beam, and will take rapid 15 s exposures in optical photometric bands (u,g,r,i,z,y) similar to those used in the Sloan Digital Sky Survey (SDSS)[145]. Photometric calibration is an essential component for achieving the survey's scientific goals, as LSST is likely to reach limits on systematic rather than statistical error in nearly all cases. LSST has a number of particular advantages in achieving more accurate calibration. The survey's rapid cadence allows for the use of celestial sources to monitor stability and uniformity of the photometric data, as each visit is exposed for significantly less time than

the timescale on which the atmospheric extinction changes. It has also been proposed that the Gaia mission could supply data to improve the photometric calibration of LSST[44]. Spectroscopic measurements of atmospheric extinction and emission will be made continuously which will allow the broad-band optical flux observed in the instrument to be corrected to flux at the top of the atmosphere[288]. On-sky photometric measurements will be used in conjunction with instrumental and atmospheric calibrations to calibrate the wavelength-dependence of the entire telescope and camera system throughput.

In this paper, we describe the design, implementation, and first tests of a collimated beam projector system. The goals for the system are enumerated in section 13.1. We describe the apparatus in section 13.2. Measurements and analysis are presented in section 13.3. Section 13.4 concludes with a discussion of topics for further study.

13.1 Goals

The goal of the collimated beam projector is to determine the relative response of the telescope system with respect to wavelength over medium to large spatial scales. This is analagous to the determination of the "illumination correction" (low-order spatial sensitivity variations) that is often accomplished on-sky by rastering sources across the focal plane or through the übercal process[235,264]. The collimated beam projector acts as an artificial star field, and enables the measurement of the relative system throughput in each filter, and allows the determination of instrumental zeropoints. This system can be used in conjunction with the more conventional flat-field screen approach, which is used to determine the high-spatial-frequency pixel-to-pixel quan-

tum efficiency (QE) variations. Furthermore, this device can be used to explore the effectiveness of the telescope system's baffling as well as to measure the ghosting in the optical train. The evolution of the ghosting intensity can be used to monitor any degradation in the quality of the AR coatings on the corrector optics and to measure any changes in filter transmission. The analysis goals of the collimated beam projector which drive the projector design are as follows:

Ghosting. The collimated beam projector can distinguish between the direct and scattered light paths. Light is projected through one or more pinholes onto the telescope focal plane. Images are taken with a variety of filters with enough dynamic range so as to see both primary and secondary spots. Source extraction is performed on each image to determine the fluxes and positions for both the primary and secondary spots. Subsequently, the ratio of these spots is measured to determine the relative flux of the ghosts. The design requirement is that the spot size on the charge-coupled device (CCD) must be smaller than the closest ghost spot.

Cross-talk. The collimated beam projector can be used to allow calculation of the cross-talk coefficients for the CCDs in the system, which are non-zero due to the undesired coupling of signals owing to the proximity of their read-out electronics and cabling. In general, this coupling occurs during the simultaneous read out of amplifiers, causing the imaged source in one amplifier to appear as a faint, mirror-symmetric ghost in another. Images from light projected through multi-spot masks can be used to quantify this effect. By using a single filter with a variety of exposure times, we can measure measure cross-talk at various levels of CCD exposure. We can determine cross-talk in pixels (from baseline reset imperfections) by measuring the ratio of fluxes in nearby pixels.

Throughput measurements. A throughput measurement can be performed using a single pinhole projected at a single angle of illumination and placement on the filter, with the throughput measured by taking the ratio of the flux seen on the focal plane to the flux emanating from the beam projector. Measurements on other parts of the filter can be accomplished by repointing the projector. To characterize the filter's transmission alone, the projector can be re-pointed, keeping the illuminated area on the focal plane fixed, allowing the filter's throughput as a function position to be measured by taking the ratio of the fluxes seen on the focal plane, thus allowing the detector's sensitivity to cancel out. This measurement can be multiplexed by using a mask containing multiple pinholes which allows for illumination of multiple CCDs. A raster scan can be performed by repointing the projector. These measurements can be compared to flat-fields performed on the dome screen.

This single-ray illumination approach described has the disadvantage that the full pupil is not illuminated. This, in turn, means that not all angles will be illuminated; however, it is possible to take a set of data that probes the full phase space. Taking, for example, the size of the collimated beam that illuminates a single pixel to be 180 mm, we would require a total of $N = \frac{\text{LSST effective aperture}}{\text{Beam Area}} = \left(\frac{6.5\,m}{0.18\,m}\right)^2 = 1300$ "pointings." At a nominal imaging cadence of 20 seconds per frame, this would take about 7 hours (or about one cloudy night of time). In addition, the full scan described above is unlikely to be necessary. To the extent that the system is axisymmetric, a radial scan which probes the entire illumination cone through the optical train would suffice. This radial scan would only require $N = \left(\frac{3\,m}{0.18\,m}\right) = 17$ pointings. The radial scans would then be weighted in proportion to the effective collection area at each respective radius.

Sensor characterization. Sensor effects such as tree rings, the "brighter-fatter" ef-

fect, and other effects resulting in astrometric and photometric perturbations can also be measured[250,285,311].

Rotation about collimated beam projector pupil. In order to use the multi-aperture masks to tie together the response across different parts of the focal plane, we need to know the relative flux being broadcast by each pinhole. We have arranged the most recent version of the prototype collimated beam projector to allow us to rotate the projector about the pupil of the collimating optic. This allows us to issue the beam from each pinhole through the same path in the optical train of the main telescope, placing each spot in turn on the same portion of the primary mirror and on the same location of the focal plane. This therefore allows us to measure (using the integrating sphere's monitoring photo-diode to ensure flux stability) each spot's intensity relative to the others. We achieved this by constructing a custom alt-az mount with the intersection of the rotation axes placed at the lens pupil.

Melding dome flats with collimated beam projector data. The information provided by monochromatic dome flats and the collimated beam projector images are, in many respects, complementary. The dome flats provide full-field illumination over the entire input pupil, but are contaminated by illumination from non-focusing light paths. The collimated beam projector spots are free from stray light, but only achieve partial pupil-illumination at discrete locations. Moreover, even without stray light problems, using dome flats to establish flux calibration across the focal plane is limited by the uniformity of the integrated surface brightness over different regions of the screen, since it does not reside at the input pupil of the system.

We plan to use a combination of the collimated beam projector spot images and monochromatic dome flats to exploit the desirable attributes of each data set. At a given wavelength, we will generate a set of collimated beam projector images that

appropriately sample the input pupil of the system, by rastering the portion of the primary mirror that is illuminated by the collimated beam projector beam, while adjusting the orientation of the collimated beam projector and the telescope so as to keep the spot locations fixed on the focal plane. This will ensure, for example, that we appropriately sample the cone of rays incident on the interference filters. This pupil-averaged collimated beam projector spot image will then be used to produce a ghost-corrected monochromatic dome flat. In effect, we will use the dome flats to interpolate the system response function measurements for regions of the focal plane that lie between the collimated beam projector spots. This amounts to making an in-dome illumination correction using virtual stars from the collimated beam projector. Of course, one could supplement this using actual stars on the sky, but the advantage of this approach is that we can use the in-dome systems to do this in narrow-band light, whereas rastered sky images can only be obtained in the relatively broad survey passbands, combined with the object's intrinsic "spectral energy distribution."

13.2 Apparatus

The instrument projects a collimated beam of light of known shape, wavelength, and intensity onto the telescope focal plane. Figure 13.1 shows the basic design concept. An optical fiber brings light (monochromatic or any other desired spectral distribution) from a source through a shutter to an integrating sphere. This homogenizes any wavelength-dependence in the angular distribution from the source. The light then travels to a filter wheel containing a set of ten filters/masks which allows for a choice between a variety of spatial patterns. After the light has been modified it travels through the collimating telescope and out of the system. The light is then re-imaged

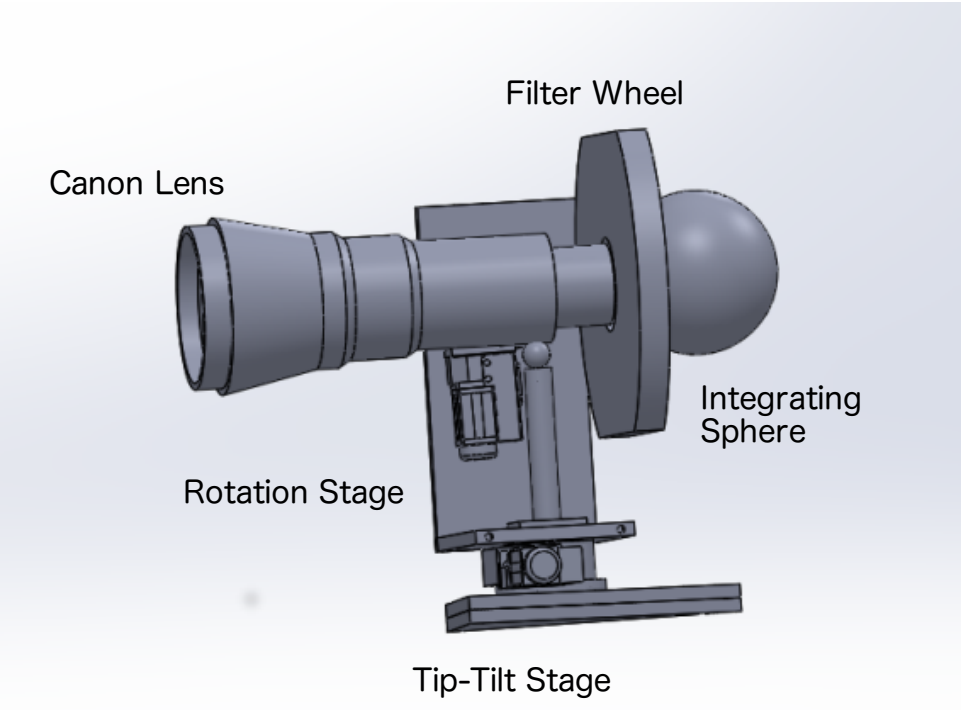


Figure 13.1: Sketch of the apparatus. The apparatus is mounted on a alt-az rotation stage and includes a light source, an integrating sphere, a mask/filter wheel, and the collimating optic. For the sake of scale, the lens diameter is 5 in.

onto the telescope focal plane. The collimator optic will reside inside the enclosure on an alt-az mount so that the collimated beam can be re-imaged onto any location on the focal plane. With the additional freedom of moving the telescope, the collimated beam can achieve any desired position within the input pupil. Consequently, the entire 4-d phase space of input ray positions and angles can, in principle, be scanned.

Our prototype collimated beam projector system has undergone significant evolution, with three phases. The first was used for the calibration of the PanSTARRS system, with results described in Stubbs et al.[287] and Tonry et al.[301]. The second iteration used a Takahashi ED-180 astrograph as the collimating optic, with an f/2.8

beam and a 500 mm focal length, placed on a commercial Paramount MX+ mount with a Thorlabs PDA200C pre-amplifier used to monitor the CBP integrating sphere photocurrent. The most recent iteration uses a Canon EF 500mm f/4 lens as the collimating optic, on a custom alt-az mount which pivots about the lens pupil. We also improved the precision of the photodiode monitoring electronics, with a Keithley 6514 Programmable Electrometer used to monitor the collimated beam projector integrating sphere photocurrent. Lastly, the most recent version uses a monochromator (Newport part number 74125) as the light source, rather than a white light source and narrowband filters. The experience gained with these systems has informed the design of the collimated beam projector that will be used for the LSST project, and has also produced a portable prototype system that we are using to characterize various existing telescope/instrument combinations.

We now describe each component in turn, following the light path. The light source used with the collimated beam projector is not restricted; one could use a white light source, tunable laser, monochromator, or laser diode. In the second version, we use a white light source with both narrowband (10 nm) and broadband Sloan Digital Sky Survey filters (to approximate the LSST filters). In the third version, we use a monochromator as the light source. A shutter is placed on the output ports of the light sources. The most important design consideration for the light source is that it results in a sufficient surface brightness projecting onto the telescope's CCD focal plane.

The light then leaves the light source by way of broadband (340-800 nm and 420-2000 nm) Newport light-guides, to direct the light into the integrating sphere. The integrating sphere ensures that the aperture mask has uniform surface brightness and that the calibration light retains no history from the upstream illumination system. It

contains a photodiode to monitor the output light, which determines the flux from the source onto the telescope focal plane. This can be used to correct for variations in the light intensity masquerading as variations in the throughput. As calibrated photodiodes with National Institute of Standards and Technology (NIST)-traceable metrology standards with spectral response known at the 0.1% level over the wavelengths relevant for CCD instruments exist, it is possible to map the sensitivity of the apparatus as a function of wavelength at this level.

Filter Wheel Slot	Filter	Mask
1	568 nm	$200\mu m$ slit
2	700 nm	$20\mu m$ pinhole
3	671 nm	Ronchi grating
4	2.2° field stop	$20\mu m$ multi-pinhole
5	680 nm	USAF target

Table 13.1: Masks and filters available for the collimated beam projector. The narrowband filters have 10 nm widths.

Light passes from the integrating sphere to a filter wheel, which can accommodate ten 50 mm × 50 mm filters or masks. It will be useful to have the ability to illuminate the entire 3.5 degree diameter LSST field, and this corresponds to a 30.55 mm × 30.55 mm square aperture at the focus of the f/2.8 collimated beam projector. The aperture mask in the filter wheel determines the shape of the light distribution on the focal plane of the telescope.

In the analysis that follows, we will use single and multi-precision pinhole arrays of $20\mu m$ circles. The available masks and filters in the following analysis are described in Table 13.1. The physical size of the mask holes are determined by a balance of needing enough light to emerge from a single pinhole to measure with high signal-to-noise ratio on the focal, plane and not having spots so large as to have difficulty discrim-

inating between the direct light path and the ghosted/scattered light paths. The aperture mask at the focus of the projector is re-imaged onto the instrument with a magnification that is given by the ratio of the focal lengths. Both the first and second collimated beam projector optical systems used for this demonstration had a 500 mm focal length, and therefore the Blanco 4 m, with a 10 m focal length, has a magnification factor of 20×. Similarly, the NOFS 1.3 m with a 5.2 m focal length has a magnification factor of 10.4×.

The use of an aperture mask consisting of an array of pinholes allows for multiplexing throughput measurements. We elect to place a spot onto the center of each detector in the focal plane because differences in silicon lots and between device AR coatings can produce chip-dependent changes in QE. This corresponds to a rectilinear array of pinholes on a grid with spacing corresponding to the spacing between the detectors on the focal plane. The LSST CCD detectors consist of ~4000×4000 10μm pixels. Placing a spot on each detector would then require a 15×15 array of pinholes with a spacing of 40 mm / 20.4 = 1.96 mm. Repointing the collimated beam detector can shift this pattern on each detector.

After the light passes through the mask, the light continues through the collimating optical system. We have used two such collimators, the first a commercial Takahashi wide field astrograph, which is a f/2.8 hyperbolic Newtonian system (plus corrector) that provides excellent optical quality over a 5 degree flat focal plane. The collimator has a focal length of 0.5 m, a diameter of 180 mm, and a 5 deg FOV diameter. The second is a Canon EF 500mm f/4 lens. This compares to the LSST specifications of a 10.2 m focal length, a plate scale of 0.02 arcsec per μm, f/# of 1.2, and a 3.5 deg FOV diameter.

The procedure for performing measurements is as follows. To align the collimated

beam projector, the telescope is first pointed directly at the platform on which the projector is mounted. A digital level is then used to point the projector at the same altitude as the telescope. Then, with the mirror covers closed, a laser pointer is used to determine where the light from the projector will fall on the primary mirror. Afterwards, a Ronchi grating is placed in the mask position, which allows a significant fraction of the light through and contains structure that can be seen by eye in the images. At a light level significantly below the camera's full-well, the collimated beam projector is rotated in azimuth until the pattern can be identified in the telescope images. At this point, the mask is changed to the multi-pinhole array, which, as described above, is designed to place a spot on each CCD. This mask was designed to maximize the number of resolvable spots without creating overlapping ghosts in any given frame, which makes it difficult to disentangle their effects. Small adjustments in both altitude and azimuth, in addition to rotations of the mask, are performed iteratively in order to center as many spots as possible.

13.3 Demonstration

13.3.1 Collimated Beam Projector calibration

The first goal is to measure the relative throughput of the collimated beam projector system. In this analysis, we use the third version of the collimated beam projector. The monochromator is connected to a shutter and light-pipe entering the integrating sphere. The light in the integrating sphere of the collimated beam projector is measured with a photodiode installed in the integrating sphere. This gives a measure of the amount of light entering the system. The light then passes through the optical system. It is projected into another (larger) integrating sphere which captures the

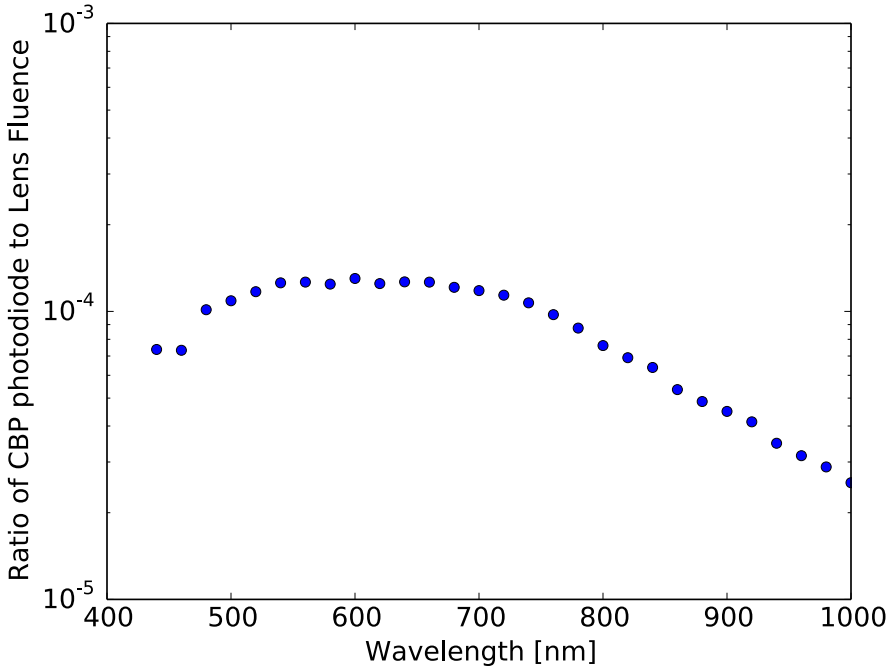


Figure 13.2: Ratio between the collimated beam projector integrating sphere monitoring photodiode flux and the output fluence from the system. This allows for the mapping of the collimated beam projector monitoring photodiode to the number of photons emerging from the system, measured with a NIST-calibrated photodiode.

entire beam, and is equipped with a second monitoring NIST-calibrated photodiode. We measure the (dark-current subtracted) photocurrent from both photodiodes. At a single wavelength, we measure the dilution factor from measuring the output at an integrating sphere port. Combining these measurements, we determine the fluence emerging from the collimated beam projector system, which can be monitored by the photodiode installed in the integrating sphere. Figure 13.2 shows the system flux calibration, which is calculated from the ratio of these currents.

13.3.2 Dark Energy Camera Measurements

Figure 13.3 shows an example of a Dark Energy Camera image with a collimated beam projector multi-pinhole array, using the second version of the projector. The multi-pinhole images show a number of interesting features. Each pinhole appears as a bright source on an individual CCD, and these spots have several novel applications.

Optical and cross-talk ghosting

Optical ghosts and cross-talk ghosts, though arising from fundamentally different origins, can result in similar effects, which are often hard to disambiguate. Cross-talk ghosts always appear at fixed pixel-coordinate offsets with respect to their aggressor, due to their production by couplings in the readout electronics, whereas optical ghosts and glints arise from multiple reflections in the optical system, and therefore move with respect to their aggressor as a function of the location of the aggressor on the focal plane (or, more accurately, their path through the optical train). The end result, however, is a faint, secondary image of a bright star at some unknown offset.

The collimated beam projector plays a critical role in the characterization of the cross-talk and optical ghosting in the system, as well as allowing disambiguation of these two effects. To measure cross-talk ghosts, and thus determine the coupling coefficients of the cross-talk matrix used for their removal, a sparse array of small, bright spots is dithered around the focal plane, and the faint ghosts which arise are measured. Performing these measurements on-sky using stars involves disentangling real sources from fake ones, and this is hard, if not impossible, to do. The collimated beam projector allows for the placement of an arbitrarily sparse array; a single spot can be moved around the focal plane, and the cross-talk ghosts which arise can be

measured. This spot can then be kept in a fixed position on the focal plane, whilst changing its path through the optical train. Ghosts which don't move are known to arise from cross-talk, whereas ghosts which do move are known to be optical in nature. In practice, most of the coupling matrix elements will be small, and so the measurement can be sped up with multiplexing, *i.e.* putting one or more spots down on each CCD simultaneously, as illustrated in Figure 13.3.

Throughput measurements

The collimated beam projector is also used to measure the throughput of the system, with the analysis proceeding as follows. After overscan subtraction, we fit the local background around each spot, computed from the pixels in the CCD which contains the spot in question. Due to the irregularity of the holes in the mask and the imperfect alignment of the mirrors within the collimated beam projector, PSF fluxes cannot be used, and the flux is calculated by simply summing the pixels over threshold in the spot. We note that while this procedure works well for the bright spots, it can be problematic for measuring the ghosts which have significantly less flux, as peak signal levels can be barely above background despite being visible to the eye. We have verified by eye that the automated centroiding and flux measurement gives sensible results, but this tends to fail for ghosts, which usually require special treatment "by hand."

The goal is a relative throughput measurement in the broadband filters, sampled at each of the narrowband filter passbands available. This is a proxy for when a monochromator will be available to measure filter transmission in small steps across the passband. For a given pointing in a DECam broadband filter (taking the r-band filter here as an example), images are taken in each narrowband filter, and the flux mea-

surements from each spot in the different passbands are compared. The flux values in the narrowband filters differ by factors of 42, 12, 15 and 14 for the 568 nm, 671 nm, 680 nm and 700 nm filters respectively when compared to the flux with no narrowband filter in the CBP. The three closely spaced filters sit in the flattop region of the DECam broadband filter, and therefore all have similar throughput, whereas the 568 nm filter sits on the band-edge, leading to much lower transmission.

Due to the ability to tune the spot brightness on the focal plane, the statistical error on measurements can be made relatively small. Therefore, understanding the systematic uncertainty in these measurements is important. One source of systematic error arises from the potential for out-of-band light leak across the different filter bands. This is due to a combination of quantum efficiency variation across a filter (i.e. efficiency near 100% in the passband and near 0.1% out-of-band) and variation in flux with respect to wavelength from the light source, as the one used emitted more at the red wavelengths than at blue wavelengths. Due to the fact that we used narrow-band filters (10 nm FWHM) at 568, 671, 680, and 700 nm, the variation due to red leak, which is due to light from wavelengths longer than the measurement wavelength, in this case is relatively small. Other potential sources of error include imperfect baffling of off-axis light, glow from electronic components such as LEDS on the telescope mount, or scattered light not produced by optical ghosts. Due to the high signal-to-noise ratio of these measurements, these are expected to have minimal effect.

13.4 Conclusion

We have designed and characterized an initial implementation of a collimated projector that can be used for the determination of the telescope instrumental response

function. We have demonstrated success on both the Dark Energy Camera wide field imager on the 4 meter Blanco telescope and United States Naval Observatory Flagstaff Station's 1.3 m reflector. This design serves as the basis for the LSST collimated beam projector described in Ingraham et al[237].

In the future, we will need to demonstrate the ability to combine collimated beam projector data with dome flats. This will require making measurements similar to the Dark Energy Camera data but at many pupil positions and at multiple wavelengths. We also need to coordinate collimated beam projector measurements with on-the-sky calibration measurements.

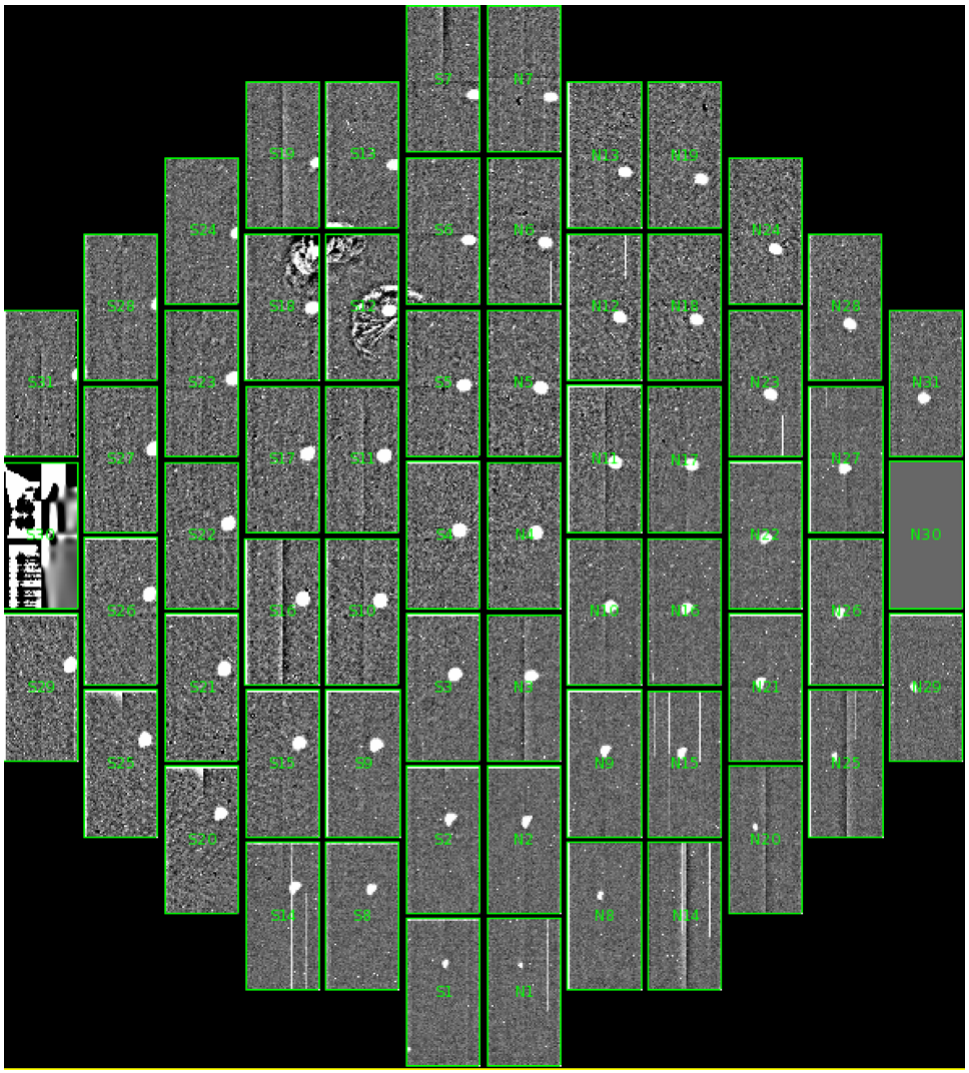


Figure 13.3: An example r-band image of the Dark Energy Camera focal plane with each of the CCDs illuminated with a spot from the CBP multi-pinhole mask.

14

Conclusion

In this thesis, a variety of techniques for the optimization of the use of astronomical observatories are explored. The most obvious example is in the detection of GW signals, which have been discussed in many forms, both with interferometric gravitational-wave detectors and seismometer arrays. In addition, methods for precise telescope calibration and optimal allocation of telescope time for follow-up of gravitational-wave events are also discussed.

There are a number of common threads which tie this work together. First of all, the lines between signal and noise are easily blurred. The typical story is that the problems associated with non-Gaussian frequency behavior of GW detectors and techniques for their mitigation create difficulties to ensure gravitational-wave detections.

Typically, data transients and lines are removed from the data and techniques for fitting both a potential gravitational-wave signal and the noise are used. The first few chapters, on the other hand, turn the typical discussion of seismic noise as a hindrance to gravitational-wave detection on its head and use the seismic data itself to place limits on gravitational-wave signals. In addition, we discuss sky brightness measurements which we treat as signal in our analysis but will be the noise for telescopes such as LSST.

The second is the use of multi-core CPUs and GPUs to make other-wise unfeasible analyses possible. As described above, seedless clustering uses banks of parametrized frequency-time tracks. Because of their parameterization, calculations for many templates can be carried in parallel, which facilitates rapid calculations on multi-core devices such as graphical processor units (GPUs). Using these machines allows for up to an order of magnitude improvement over single-core CPUs, which allows for an order of magnitude more templates used in the analysis.

In summary, the future of GW astronomy is bright. It has been previously demonstrated that the interferometers are capable of detecting gravitational-wave signals. From this thesis, it is clear that there is much work needed to maximize their detection efficiency and the science that can be ascertained from them. Similar optimization will be important for telescopes such as LSST, where calibration and scheduling will be essential for maximizing its science. Many of these improvements will be made in the coming years of the advanced detector era.

References

[1] A., R. V. & Uman, M. A. (2003). *Lightning Physics and Effects*. Cambridge University Press.

[2] A. Walker (1987). Noao newsletter. *NOAO Newsletter*, 10, 16.

[3] Aasi, J., Abadie, J., Abbott, B., Abbott, R., Abbott, T., Abernathy, M., Adams, C., Adams, T., Addesso, P., Adhikari, R., et al. (2014a). Improved Upper Limits on the Stochastic Gravitational-Wave Background from 2009-2010 LIGO and Virgo Data. *Submitted to PRL*.

[4] Aasi, J. et al. (2013a). Prospects for Localization of Gravitational Wave Transients by the Advanced LIGO and Advanced Virgo Observatories.

[5] Aasi, J. et al. (2013b). Search for long-lived gravitational-wave transients coincident with long gamma-ray bursts. *Physical Review D*, 88, 122004.

[6] Aasi, J. et al. (2014b). Improved upper limits on the stochastic gravitational-wave background from 2009˘2010 ligo and virgo data. *Phys. Rev. Lett.*, 113, 231101.

[7] Aasi, J. e. a. (2014). Search for gravitational radiation from intermediate mass black hole binaries in data from the second ligo-virgo joint science run. *Phys. Rev. D*, 89, 122003.

[8] Abadie, J., Abbott, B., Abbott, R., Abbott, T., Abernathy, M., Accadia, T., Acernese, F., Adams, C., Adhikari, R., Affeldt, C., et al. (2012a). Search for gravitational waves from low mass compact binary coalescence in ligos sixth science run and virgos science runs 2 and 3. *Physical Review D*, 85(8), 082002.

[9] Abadie, J., Abbott, B., Abbott, R., Abernathy, M., Accadia, T., Acernese, F., Adams, C., Adhikari, R., Ajith, P., Allen, B., et al. (2010). Predictions for the rates of compact binary coalescences observable by ground-based gravitational-wave detectors. *Classical and Quantum Gravity*, 27(17), 173001.

[10] Abadie, J., Abbott, B. P., Abbott, R., Abbott, T. D., Abernathy, M., Accadia, T., Acernese, F., Adams, C., Adhikari, R., Affeldt, C., & others (2012b). Upper limits on a stochastic gravitational-wave background using LIGO and Virgo interferometers at 600–1000 Hz. *Phys. Rev. D*, 85, 122001.

[11] Abadie, J. et al. (2011). Directional limits on persistent gravitational waves using ligo s5 science data. *Phys. Rev. Lett.*, 107, 271102.

[12] Abadie, J. et al. (2012c). Search for gravitational waves from intermediate mass binary black holes. *Physical Review D*, 85, 102004.

[13] Abadie J. et al. (2010). Predictions for the rates of compact binary coalescences observable by ground-based gravitational-wave detectors. *Classical and Quantum Gravity*, 27(17), 173001.

[14] Abadie J. et al. (2012a). Implementation and testing of the first prompt search for gravitational wave transients with electromagnetic counterparts. *Astronomy and Astrophysics*, 539, A124.

[15] Abadie J. et al. (2012b). Parameter Estimation for Compact Binary Coalescence events with first-generation ground-based Gravitational-Wave Interferometers. *In preparation.*

[16] Abadie J. et al. (2012c). Search for gravitational waves associated with gamma-ray bursts during ligo science run 6 and virgo science runs 2 and 3. *The Astrophysical Journal*, 760(1), 12.

[17] Abbott, B., Abbott, R., Acernese, F., Adhikari, R., Ajith, P., Allen, B., Allen, G., Alshourbagy, M., Amin, R., Anderson, S., et al. (2009a). An upper limit on the stochastic gravitational-wave background of cosmological origin. *Nature*, 460(7258), 990–994.

[18] Abbott, B. et al. (2009b). An upper limit on the stochastic gravitational-wave background of cosmological origin. *Nature*, 460, 990–994.

[19] Abbott, B. P. e. a. (2016a). Characterization of transient noise in advanced ligo relevant to gravitational wave signal gw150914. *Submitted to Classical and Quantum Gravity.*

[20] Abbott, B. P. e. a. (2016b). Gw150914: Implications for the stochastic gravitational-wave background from binary black holes. *Phys. Rev. Lett.*, 116, 131102.

[21] Abbott, R., Adhikari, R., Allen, G., Baglino, D., Campbell, C., Coyne, D., Daw, E., DeBra, D., Faludi, J., Fritschel, P., Ganguli, A., Giaime, J., Hammond, M., Hardham, C., Harry, G., Hua, W., Jones, L., Kern, J., Lantz, B., Lilienkamp, K., Mailand, K., Mason, K., Mittleman, R., Nayfeh, S., Ottaway, D., Phinney, J., Rankin, W., Robertson, N., Scheffler, R., Shoemaker, D. H., Wen, S., Zucker, M., & Zuo, L. (2004). Seismic isolation enhancements for initial and Advanced LIGO. *Classical and Quantum Gravity*, 21(5), S915.

[22] Abbott, R., Adhikari, R., et al. (2002). Seismic isolation for advanced ligo. *Classical and Quantum Gravity*, 19(7), 1591.

[23] Abbott B. et al. (2009). LIGO: The Laser Interferometer Gravitational-Wave Observatory. *Reports on Progress in Physics*, 72, 076901.

[24] Abbott, B. P. et al. (2016). Observation of gravitational waves from a binary black hole merger. *Phys. Rev. Lett.*, 116, 061102.

[25] Accadia, T., Acernese, F., Antonucci, F., Astone, P., Ballardin, G., Barone, F., Barsuglia, M., Basti, A., Bauer, T. S., Bebronne, M., et al. (2011). Status of the Virgo project. *Classical and Quantum Gravity*, 28(11), 114002.

[26] Acernese F. et al. (2008). Status of Virgo. *Classical and Quantum Gravity*, 25, 114045.

[27] Ade, P. A. R. et al. (2014). "detection of b-mode polarization at degree angular scales by bicep2". *Phys. Rev. Lett.*, 112, 241101.

[28] Adhikari, R. (2004). *Sensitivity and noise analysis of 4 km laser interferometric gravitational wave antennae*. PhD thesis, Massachusetts Institute of Technology.

[29] Agathos, M., Del Pozzo, W., Li, T. G. F., Van Den Broeck, C., Veitch, J., & Vitale, S. (2014). Tiger: A data analysis pipeline for testing the strong-field dynamics of general relativity with gravitational wave signals from coalescing compact binaries. *Phys. Rev. D*, 89, 082001.

[30] Aguiar, O. D., Andrade, L. A., Barroso, J. J., Bortoli, F., Carneiro, L. A., Castro, P. J., Costa, C. A., Costa, K. M. F., de Araujo, J. C. N., de Lucena, A. U., de Paula, W., de Rey Neto, E. C., de Souza, S. T., Fauth, A. C., Frajuca, C., Frossati, G., Furtado, S. R., Magalhes, N. S., Jr, R. M. M., Melo, J. L., Miranda, O. D., Jr, N. F. O., Ribeiro, K. L., Stellati, C., Jr, W. F. V., & Weber, J. (2006). The Brazilian gravitational wave detector Mario Schenberg: status report. *Classical and Quantum Gravity*, 23(8), S239.

[31] Allen, B. (2005). chi^2 time-frequency discriminator for gravitational wave detection. *Phys. Rev. D*, 71, 062001.

[32] Allen, B., Hua, W., & Ottewill, A. (1999). Automatic cross-talk removal from multi-channel data. *arXiv preprint gr-qc/9909083*.

[33] Allen, B. & Romano, J. D. (1999). Detecting a stochastic background of gravitational radiation: Signal processing strategies and sensitivities. *Phys. Rev. D*, 59, 102001.

[34] Amaro-Seoane, P., Aoudia, S., Babak, S., Bintruy, P., Berti, E., Boh, A., Caprini, C., Colpi, M., Cornish, N. J., Danzmann, K., Dufaux, J.-F., Gair, J., Jennrich, O., Jetzer, P., Klein, A., Lang, R. N., Lobo, A., Littenberg, T., McWilliams, S. T., Nelemans, G., Petiteau, A., Porter, E. K., Schutz, B. F., Sesana, A., Stebbins, R., Sumner, T., Vallisneri, M., Vitale, S., Volonteri, M., & Ward, H. (2012). Low-frequency gravitational-wave science with eLISA/NGO. *Classical and Quantum Gravity*, 29(12), 124016.

[35] Anderson, W. G., Brady, P. R., Creighton, J. D. E., & Flanagan, É. É. (2001). An excess power statistic for detection of burst sources of gravitational radiation. *Physical Review D*, 63, 042003.

[36] Ando, M., Ishidoshiro, K., Yamamoto, K., Yagi, K., Kokuyama, W., Tsubono, K., & Takamori, A. (2010). Torsion-Bar Antenna for Low-Frequency Gravitational-Wave Observations. *Phys. Rev. Lett.*, 105(16), 161101.

[37] Antolini, E. & Heyl, J. S. (2016). Using the 2-mass photometric redshift survey to optimize ligo follow-up observations. *Submitted to MNRAS*.

[38] Antonini, F. & Perets, H. B. (2012). Secular evolution of compact binaries near massive black holes: Gravitational wave sources and other exotica. *The Astrophysical Journal*, 757(1), 27.

[39] Aoyama, S., Tazai, R., & Ichiki, K. (2014). Upper limit on the amplitude of gravitational waves around 0.1 Hz from the Global Positioning System. *Phys. Rev. D*, 89, 067101.

[40] Archinal, B.A. et al. (2011). Report of the iau working group on cartographic coordinates and rotational elements: 2009. *Celestial Mechanics and Dynamical Astronomy*, 109(2), 101–135.

[41] Armstrong, J. W., Iess, L., Tortora, P., & Bertotti, B. (2003). Stochastic Gravitational Wave Background: Upper Limits in the 1e-6 to 1e-3 Hz Band. *The Astrophysical Journal*, 599(2), 806.

[42] Aso, Y., Michimura, Y., Somiya, K., Ando, M., Miyakawa, O., Sekiguchi, T., Tatsumi, D., & Yamamoto, H. (2013). Interferometer design of the kagra gravitational wave detector. *Phys. Rev. D*, 88, 043007.

[43] Astrodon (2015). Astrodon photometrics sloan filters. *http://www.astrodon.com/sloan.html*. Accessed: 2016-01-09.

[44] Axelrod, T. & Miller, C. (2014). Improving lsst photometric calibration with gaia data. *Publications of the Astronomical Society of the Pacific*, 126(946), pp. 1102–1111.

[45] Babak, S., Biswas, R., Brady, P. R., Brown, D. A., Cannon, K., Capano, C. D., Clayton, J. H., Cokelaer, T., Creighton, J. D. E., Dent, T., Dietz, A., Fairhurst, S., Fotopoulos, N., González, G., Hanna, C., Harry, I. W., Jones, G., Keppel, D., McKechan, D. J. A., Pekowsky, L., Privitera, S., Robinson, C., Rodriguez, A. C., Sathyaprakash, B. S., Sengupta, A. S., Vallisneri, M., Vaulin, R., & Weinstein, A. J. (2013). Searching for gravitational waves from binary coalescence. *Phys. Rev. D*, 87, 024033.

[46] Balser, M. & Wagner, C. (1960). Observations of earth-ionosphere cavity resonances. *Nature*, 188(4751), 638–641.

[47] Barausse, E., Palenzuela, C., Ponce, M., & Lehner, L. (2013). Neutron-star mergers in scalar-tensor theories of gravity. *Phys. Rev. D*, 87, 081506.

[48] Barnes, J. & Kasen, D. (2013). Effect of a high opacity on the light curves of radioactively powered transients from compact object mergers. *The Astrophysical Journal*, 775(1), 18.

[49] Bartos, I., Crotts, A. P. S., & Marka, S. (2015a). Galaxy survey on the fly: Prospects of rapid galaxy cataloging to aid the electromagnetic follow-up of gravitational wave observations. *The Astrophysical Journal Letters*, 801(1), L1.

[50] Bartos, I., Huard, T., & Marka, S. (2015b). James webb space telescope can detect kilonovae in gravitational wave follow-up search. *http://arxiv.org/abs/1502.07426*.

[51] Beccaria, M., Bernardini, M., Braccini, S., Bradaschia, C., Bozzi, A., Casciano, C., Cella, G., Ciampa, A., Cuoco, E., Curci, G., D'Ambrosio, E., Dattilo, V., Carolis, G. D., Salvo, R. D., Virgilio, A. D., Delapierre, A., Enard, D., Errico, A., Feng, G., Ferrante, I., Fidecaro, F., Frasconi, F., Gaddi, A., Gennai, A., Gennaro, G., Giazotto, A., Penna, P. L., Losurdo, G., Maggiore, M., Mancini, S., Palla, F., Pan, H. B., Paoletti, F., Pasqualetti, A., Passaquieti, R., Passuello, D., Poggiani, R., Popolizio, P., Raffaelli, F., Rapisarda, S., Viceré, A., & Zhang, Z. (1998). Relevance of Newtonian seismic noise for the VIRGO interferometer sensitivity. *Classical and Quantum Gravity*, 15(11), 3339.

[52] Beker, M., Cella, G., DeSalvo, R., Doets, M., Grote, H., Harms, J., Hennes, E., Mandic, V., Rabeling, D., van den Brand, J., & van Leeuwen, C. (2011). Improving the sensitivity of future GW observatories in the 1 - 10Hz band: Newtonian and seismic noise. *General Relativity and Gravitation*, 43(2), 623–656.

[53] Ben-Menahem, A. (1983). Excitation of the earth's eigenvibrations by gravitational radiation from astrophysical sources. *Il Nuovo Cimento C*, 6(1), 49–71.

[54] Benesty, J., Huang, Y., & Chen, J. (2008). Wiener and Adaptive Filters. In J. Benesty, M. Sondhi, & Y. Huang (Eds.), *Springer Handbook of Speech Processing* (pp. 103–120). Springer Berlin Heidelberg.

[55] Betoule, M. et al. (2014). Improved cosmological constraints from a joint analysis of the SDSS-II and SNLS supernova samples. *Astronomy and Astrophysics*, 568, A22.

[56] Bilicki, M., Jarrett, T. H., Peacock, J. A., Cluver, M. E., & Steward, L. (2014). Two micron all sky survey photometric redshift catalog: A comprehensive three-dimensional census of the whole sky. *The Astrophysical Journal Supplement Series*, 210(1), 9.

[57] Blanchet L. (2006). Gravitational radiation from post-newtonian sources and inspiralling compact binaries. *Living Reviews in Relativity*, 4(9).

[58] B.N. Holben et al (1998). Aeronet - a federated instrument network and data archive for aerosol characterization. *Remote Sensing of Environment*, 66(1), 1 – 16.

[59] Brevik, J. A., Aikin, R. W., Amiri, M., Benton, S. J., Bock, J. J., Bonetti, J. A., Burger, B., Dowell, C. D., Duband, L., Filippini, J. P., Golwala, S. R., Halpern, M., Hasselfield, M., Hilton, G., Hristov, V. V., Irwin, K., Kaufman, J. P., Keating, B. G., Kovac, J. M., Kuo, C. L., Lange, A. E., Leitch, E. M., Netterfield, C. B., Nguyen, H. T., Ogburn IV, R. W., Orlando, A., Pryke, C., Reintsema, C., Richter, S., Ruhl, J. E., Runyan, M., Sheehy, C., Staniszewski, Z., Sudiwala, R., Tolan, J. E., Turner, A. D., Wilson, P., & Wong, C. L. (2010). Initial performance of the BICEP2 antenna-coupled superconducting bolometers at the South Pole. In *Proc. SPIE*, volume 7741 (pp. 77411H–77411H–10).

[60] Brown, D. A., Harry, I., Lundgren, A., & Nitz, A. H. (2012). Detecting binary neutron star systems with spin in advanced gravitational-wave detectors. *Phys. Rev. D*, 86, 084017.

[61] Brown, D. A., Kumar, P., & Nitz, A. H. (2013). Template banks to search for low-mass binary black holes in advanced gravitational-wave detectors. *Phys. Rev. D*, 87, 082004.

[62] Brown, D. A. & Zimmerman, P. J. (2010). Effect of eccentricity on searches for gravitational waves from coalescing compact binaries in ground-based detectors. *Phys. Rev. D*, 81, 024007.

[63] Bse, M., Allen, R., Brown, H., Gua, G., Fischer, M., Hauksson, E., Heaten, T., Hellweg, M., Liukis, M., Neuhauser, D., Maechling, P., Solanki, K., Vinci, M., Henson, I., Khainovski, O., Kuyuk, S., Carpio, M., Meier, M.-A., & Jordan, T. (2014). Cisn shakealert: An earthquake early warning demonstration system for california. In F. Wenzel & J. Zschau (Eds.), *Early Warning for Geological Disasters*, Advanced Technologies in Earth Sciences (pp. 49–69). Springer Berlin Heidelberg.

[64] Brgmann, R. (2014). Earth science: Warning signs of the iquique earthquake. *Nature*, 512, 258–259.

[65] Cannon, K., Hanna, C., & Keppel, D. (2013). Method to estimate the significance of coincident gravitational-wave observations from compact binary coalescence. *Phys. Rev. D*, 88, 024025.

[66] Canton T. et al (2014). Implementing a search for aligned-spin neutron star – black hole systems with advanced ground based gravitational wave detectors.

[67] Cella, G. (2000). Off-line Subtraction of Seismic Newtonian Noise. In *Recent Developments in General Relativity* (pp. 495–503). Springer.

[68] Chen, W. & Molnar, P. (1975). Short-period rayleigh-wave dispersion across the tibetan plateau. *Bulletin of the Seismological Society of America*, 65(5), 1051–1057.

[69] Christensen, N. (1992). Measuring the stochastic gravitational-radiation background with laser-interferometric antennas. *Phys. Rev. D*, 46, 5250–5266.

[70] Christensen, N., the LIGO Scientific Collaboration, & the Virgo Collaboration (2010). Ligo s6 detector characterization studies. *Classical and Quantum Gravity*, 27(19), 194010.

[71] Christensen N. for the LIGO Scientific Collaboration and the Virgo Collaboration (2010). Ligo s6 detector characterization studies. *Class. Quantum Grav.*, 27(19), 194010.

[72] Chung, J.-K. & Yeh, Y. T. (1997). Shallow crustal structure from short-period rayleigh-wave dispersion data in southwestern taiwan. *Bulletin of the Seismological Society of America*, 87(2), 370–382.

[73] Chreau, F. (2014). Stellarium. *http://www.stellarium.org/*. Accessed: 2016-01-09.

[74] Cochran E., Lawrence J., Christensen C., and Chung A. (2009). A novel strong-motion seismic network for community participation in earthquake monitoring. *IEEE Inst and Meas*, 12(6), 8–15.

[75] Cochran E., Lawrence J., Christensen C., and Jakka R. (2009). The quake-catcher network: Citizen science expanding seismic horizons. *Seismological Research Letters*, 80, 26–30.

[76] Collaboration, B., Ade, P., Aikin, R., et al. (2014). Bicep2 i: Detection of b-mode polarization at degree angular scales. *arXiv preprint arXiv:1403.3985*.

[77] Collaboration, P., Ade, P., Aghanim, N., Armitage-Caplan, C., Arnaud, M., Ashdown, M., Atrio-Barandela, F., Aumont, J., Baccigalupi, C., Banday, A., et al. (2013). Planck 2013 results. i. overview of products and scientific results. *arXiv preprint arXiv:1303.5062*.

[78] Collaboration, T. L. S. & Collaboration, T. V. (2009). An upper limit on the stochastic gravitational-wave background of cosmological origin. *Nature*, 460, 990.

[79] Comte, D., Roecker, S. W., & Surez, G. (1994). Velocity structure in northern chile: evidence of subducted oceanic crust in the nazca plate. *Geophysical Journal International*, 117(3), 625–639.

[80] Cooper, M. R., Kovach, R. L., & Watkins, J. S. (1974). Lunar near-surface structure. *Reviews of Geophysics*, 12(3), 291–308.

[81] Cornell, C. A. (1968). Engineering seismic risk analysis. *Bulletin of the Seismological Society of America*, 58(5), 1583–1606.

[82] Cornish, N. J. & Littenberg, T. B. (2015). Bayeswave: Bayesian inference for gravitational wave bursts and instrument glitches. *Classical and Quantum Gravity*, 32(13), 135012.

[83] Corsi, A. & Mészáros, P. (2009). Gamma-ray burst afterglow plateaus and gravitational waves: multi-messenger signature of a millisecond magnetar? *The Astrophysical Journal*, 702, 1171.

[84] Coughlin, M., Claver, C. F., Stubbs, C., & Tonry, J. L. (2014). Optical All-Sky Camera for the Large Synoptic Survey Telescope. In *American Astronomical Society Meeting Abstracts #224*, volume 224 of *American Astronomical Society Meeting Abstracts* (pp. #122.17).

[85] Coughlin, M. & Harms, J. (2012a). Seismic topographic scattering in the context of GW detector site selection. *Classical and Quantum Gravity*, 29, 075004.

[86] Coughlin, M. & Harms, J. (2014a). Constraining the gravitational-wave energy density of the Universe in the range 0.1 Hz to 1 Hz using the Apollo Seismic Array. *Phys. Rev. D*, 90, 102001.

[87] Coughlin, M. & Harms, J. (2014b). Constraining the gravitational wave energy density of the universe using earth's ring. *Phys. Rev. D*, 90, 042005.

[88] Coughlin, M. & Harms, J. (2014c). Upper Limit on a Stochastic Background of Gravitational Waves from Seismic Measurements in the Range 0.05 - 1 Hz. *Phys. Rev. Lett.*, 112, 101102.

[89] Coughlin, M., Harms, J., Christensen, N., Dergachev, V., DeSalvo, R., Kandhasamy, S., & Mandic, V. (2014a). Wiener filtering with a seismic underground array at the sanford underground research facility. *Classical and Quantum Gravity*, 31(21), 215003.

[90] Coughlin, M., Meyers, P., Kandhasamy, S., Thrane, E., & Christensen, N. (2015a). Prospects for searches for long-duration gravitational-waves without time slides. *Phys. Rev. D*, 92, 043007.

[91] Coughlin, M., Meyers, P., Thrane, E., Luo, J., & Christensen, N. (2015b). Detectability of eccentric compact binary coalescences with advanced gravitational-wave detectors. *Phys. Rev. D*, 91, 063004.

[92] Coughlin, M., Meyers, P., Thrane, E., Luo, J., & Christensen, N. (2015c). Detectability of eccentric compact binary coalescences with advanced gravitational-wave detectors. *Phys. Rev. D*, 91, 063004.

[93] Coughlin, M., Stubbs, C., Barrientos, S., Claver, C., Harms, J., Chris Smith, R., & Warner, M. (2015d). Real-time earthquake warning for astronomical observatories. *Experimental Astronomy*, (pp. 1–18).

[94] Coughlin, M., Stubbs, C., & Claver, C. (2016). A daytime measurement of the lunar contribution to the night sky brightness in lsst's ugrizy bands–initial results. *Experimental Astronomy*, (pp. 1–16).

[95] Coughlin, M., Thrane, E., & Christensen, N. (2014b). Detecting compact binary coalescences with seedless clustering. *Phys. Rev. D*, 90, 083005.

[96] Coughlin, M., Thrane, E., & Christensen, N. (2014c). Detecting compact binary coalescences with seedless clustering. *Phys. Rev. D*, 90, 083005.

[97] Coughlin, M. W. & Harms, J. (2012b). Global characterization of seismic noise with broadband seismometers. *arXiv preprint arXiv:1202.4826*.

[98] Cowperthwaite, P. & Berger, E. (2015). A comprehensive study of detectability and contamination in deep rapid optical searches for gravitational wave counterparts. *http://arxiv.org/abs/1503.07869*.

[99] Creighton, T. (2008). Tumbleweeds and airborne gravitational noise sources for LIGO. *Classical and Quantum Gravity*, 25(12), 125011.

[100] Crossley, D. & Hinderer, J. (2010). GGP (Global Geodynamics Project): An International Network of Superconducting Gravimeters to Study Time-Variable Gravity. In S. P. Mertikas (Ed.), *Gravity, Geoid and Earth Observation*, volume 135 of *International Association of Geodesy Symposia* (pp. 627–635). Springer Berlin Heidelberg.

[101] Crossley, D., Hinderer, J., & Riccardi, U. (2013). The measurement of surface gravity. *Reports on Progress in Physics*, 76(4), 046101.

[102] Crowder, J. & Cornish, N. J. (2007). Solution to the galactic foreground problem for lisa. *Phys. Rev. D*, 75, 043008.

[103] Csizmadia P. et al. (2012). Gravitational waves from spinning eccentric binaries. *Classical and Quantum Gravity*, 29, 245002.

[104] Cutler, C. & Lindblom, L. (1996). Gravitational helioseismology? *Phys. Rev. D*, 54, 1287–1290.

[105] Dahlen, F., , & Tromp, J. (1998). *Theoretical global seismology*. Princeton university press.

[106] Dahlen, F. A. (1968). The Normal Modes of a Rotating, Elliptical Earth. *Geophysical Journal of the Royal Astronomical Society*, 16(4), 329–367.

[107] Danzmann, K. & the LISA study team (1996). Lisa: laser interferometer space antenna for gravitational wave measurements. *Classical and Quantum Gravity*, 13(11A), A247.

[108] Dark Energy Camera (2015). DECam Exposure Time Calculator.

[109] de Waard, A., Gottardi, L., van Houwelingen, J., Shumack, A., & Frossati, G. (2003). MiniGRAIL, the first spherical detector. *Classical and Quantum Gravity*, 20(10), S143.

[110] Delgado, F., Saha, A., Chandrasekharan, S., Cook, K., Petry, C., & Ridgway, S. (2014). The LSST operations simulator. In *Society of Photo-Optical Instrumentation Engineers (SPIE) Conference Series*, volume 9150 of *Society of Photo-Optical Instrumentation Engineers (SPIE) Conference Series* (pp. 915015).

[111] Dergachev, V. e. a. (2014). A high precision, compact electromechanical ground rotation sensor. *Review of Scientific Instruments*, 85(5).

[112] DeRosa, R., Driggers, J. C., Atkinson, D., Miao, H., Frolov, V., Landry, M., Giaime, J. A., & Adhikari, R. X. (2012). Global feed-forward vibration isolation in a km scale interferometer. *Classical and Quantum Gravity*, 29(21), 215008.

[113] Dickerson, S. M., Hogan, J. M., Sugarbaker, A., Johnson, D. M. S., & Kasevich, M. A. (2013). Multiaxis Inertial Sensing with Long-Time Point Source Atom Interferometry. *Phys. Rev. Lett.*, 111, 083001.

[114] Driggers, J. C., Evans, M., Pepper, K., & Adhikari, R. (2012a). Active noise cancellation in a suspended interferometer. *Review of Scientific Instruments*, 83(2), 024501–024501–6.

[115] Driggers, J. C., Harms, J., & Adhikari, R. X. (2012b). Subtraction of Newtonian noise using optimized sensor arrays. *Phys. Rev. D*, 86, 102001.

[116] Dyson, F. J. (1969). Seismic Response of the Earth to a Gravitational Wave in the 1-Hz Band. *The Astrophysical Journal*, 156, 529.

[117] Dziewonski, A. M. & Anderson, D. L. (1981). Preliminary reference Earth model. *Physics of the Earth and Planetary Interiors*, 25(4), 297 – 356.

[118] Eagle, D. (2013). Selenocentric Coordinates and Transformations. *Mathworks File Exchange*.

[119] East, W., McWilliams, S., Levin, J., & Pretorius, F. (2013). Observing complete gravitational wave signals from dynamical capture binaries. *Phys. Rev. D*, 87, 043004.

[120] East, W. E., Pretorius, F., & Stephens, B. C. (2012). Eccentric black hole-neutron star mergers: effects of black hole spin and equation of state. *Phys.Rev.*, D85, 124009.

[121] Ekström, G. (2011). A global model of Love and Rayleigh surface wave dispersion and anisotropy, 25-250s. *Geophysical Journal International*, 187(3), 1668–1686.

[122] Essick, R., Vitale, S., Katsavounidis, E., Vedovato, G., & Klimenko, S. (2015). Localization of short duration gravitational-wave transients with the early advanced ligo and virgo detectors. *The Astrophysical Journal*, 800(2), 81.

[123] et al, A. J. (2010). Predictions for the rates of compact binary coalescences observable by ground-based gravitational-wave detectors. *Classical and Quantum Gravity*, 27(17), 173001.

[124] et al, A. J. (2012a). Search for gravitational waves associated with gamma-ray bursts during ligo science run 6 and virgo science runs 2 and 3. *The Astrophysical Journal*, 760(1), 12.

[125] et al, A. J. (2012b). Search for gravitational waves from binary black hole inspiral, merger and ringdown in ligo-virgo data from 2009-2010. *In preparation*.

[126] et al, A. J. (2012c). Search for gravitational waves from low mass compact binary coalescence in ligo's sixth science run and virgo's science runs 2 and 3. *Physical Review D*, 85, 082002.

[127] et al, B. S. (2014a). Gradual unlocking of plate boundary controlled initiation of the 2014 iquique earthquake. *Nature*, 512, 299–302.

[128] et al, C. B. (2015). Parameter estimation for binary neutron-star coalescences with realistic noise during the advanced ligo era. *http://arxiv.org/abs/1411.6934*.

[129] et al, G. H. (2014b). Continuing megathrust earthquake potential in chile after the 2014 iquique earthquake. *Nature*, 512, 295–298.

[130] et al., L. P. S. (2016). Going the distance: Mapping host galaxies of ligo sources in three dimensions using local cosmography and targeted follow-up. *Submitted to ApJL.*

[131] et al., M. P. (2010). The einstein telescope: a third-generation gravitational wave observatory. *Classical and Quantum Gravity*, 27(19).

[132] et al., T. E. (2011). Long gravitational-wave transients and associated detection strategies for a network of terrestrial interferometers. *Physical Review D*, 83, 083004.

[133] F, K. & J, A. (2008). Seismic hazard: analysis and design of large ground-based telescopes. *Proc. SPIE*, 7012, 70122E–70122E–10.

[134] F Acernese et al (2015). Advanced virgo: a second-generation interferometric gravitational wave detector. *Classical and Quantum Gravity*, 32(2), 024001.

[135] F. L. Vernon and D. Harvey and J. A. Eakins and R. W. Busby and L. Astiz and R. L. Newman and J. Reyes (2009). Calibration Response of the NSF Earthscope USArray Transportable Array. *calibration of USArray.*

[136] F. R. Chromey and D. A. Hasselbacher (1996). The Flat Sky: Calibration and Background Uniformity in Wide Field Astronomical Images. *Publications of the Astronomical Society of the Pacific*, 108, 944.

[137] Fairhurst, S. (2009). Triangulation of gravitational wave sources with a network of detectors. *New Journal of Physics*, 11(12), 123006.

[138] Fairhurst, S. (2011). Source localization with an advanced gravitational wave detector network. *Class. Quantum Grav.*, 28(10), 105021.

[139] Farin, G. (1996). *Curves and Surfaces for CAGD, Fourth Edition: A Practical Guide*. Academic Press.

[140] Farmer, A. J. & Phinney, E. S. (2003). The gravitational wave background from cosmological compact binaries. *MNRAS*, 346, 1197.

[141] Flanagan, E. E. (1993). Sensitivity of the laser interferometer gravitational wave observatory to a stochastic background, and its dependence on the detector orientations. *Physical Review D*, 48(6), 2389.

[142] follow-up of LIGO-Virgo events using rapid sky localization, F. (2015). Hsin-yu chen and daniel e. holz. *Submitted to ApJ*.

[143] Foster, I. (1995). *Designing and Building Parallel Programs: Concepts and Tools for Parallel Software Engineering*. Addison Wesley.

[144] Fouch M et al (2010). Small aperture lunar seismic arrays (salsas). *Ground-Based Geophysics on the Moon*.

[145] Fukugita, M., Yasuda, N., Doi, M., Gunn, J. E., & York, D. G. (2011). Characterization of sloan digital sky survey stellar photometry. *The Astronomical Journal*, 141(2), 47.

[146] Galuk, Y., Nickolaenko, A., & Hayakawa, M. (2015). Knee model: Comparison between heuristic and rigorous solutions for the schumann resonance problem. *Journal of Atmospheric and Solar-Terrestrial Physics*, 135, 85 – 91.

[147] Giaime, J. A., Daw, E. J., Weitz, M., Adhikari, R., Fritschel, P., Abbott, R., Bork, R., & Heefner, J. (2003). Feedforward reduction of the microseism disturbance in a long-base-line interferometric gravitational-wave detector. *Review of Scientific Instruments*, 74(1), 218–224.

[148] Gilbert, F. & Dziewonski, A. M. (1975). An Application of Normal Mode Theory to the Retrieval of Structural Parameters and Source Mechanisms from Seismic Spectra. *Phil. Trans. Roy. Soc. London. Series A, Mathematical and Physical Sciences*, 278(1280), 187–269.

[149] Goins, N. R., Dainty, A. M., & Toksoz, M. N. (1981). Seismic energy release of the moon. *Journal of Geophysical Research: Solid Earth*, 86(B1), 378–388.

[150] Gold, R., Bernuzzi, S., Thierfelder, M., Brugmann, B., & Pretorius, F. (2012). Eccentric binary neutron star mergers. *Phys.Rev.*, D86, 121501.

[151] Grote H. for the LIGO Scientific Collaboration (2010a). The GEO 600 status. *Class. Quantum Grav.*, 27, 084003.

[152] Grote H. for the LIGO Scientific Collaboration (2010b). The GEO 600 status. *Class. Quantum Grav.*, 27, 084003.

[153] Grover, K., Fairhurst, S., Farr, B. F., Mandel, I., Rodriguez, C., Sidery, T., & Vecchio, A. (2014). Comparison of gravitational wave detector network sky localization approximations. *Physical Review D*, 89(4), 042004.

[154] Gutenberg, B. & Richter, C. F. (1944). Frequency of earthquakes in California. *Bull. Seism. Soc. Am.*, 34, 185.

[155] H. Winkler, F. van Wyk, and F. Marang (2013). South African night sky brightness during high aerosol epochs. *South African Institute of Physics 2013 annual conference*.

[156] Harms, J. (2015). Terrestrial Gravity Fluctuations. *Living Reviews in Relativity*, 18(3).

[157] Harms, J., Acernese, F., Barone, F., Bartos, I., Beker, M., van den Brand, J., Christensen, N., Coughlin, M., DeSalvo, R., Dorsher, S., et al. (2010). Characterization of the seismic environment at the Sanford Underground Laboratory, South Dakota. *Classical and Quantum Gravity*, 27(22), 225011.

[158] Harms, J., DeSalvo, R., Dorsher, S., & Mandic, V. (2009). Simulation of underground gravity gradients from stochastic seismic fields. *Phys. Rev. D*, 80, 122001.

[159] Harms, J. & OReilly, B. (2011). Velocity and Attenuation Characterization of the LIGO Site near Livingston, Louisiana. *Bulletin of the Seismological Society of America*, 101(4), 1478–1487.

[160] Harms, J., Slagmolen, B. J. J., Adhikari, R. X., Miller, M. C., Evans, M., Chen, Y., Müller, H., & Ando, M. (2013). Low-frequency terrestrial gravitational-wave detectors. *Phys. Rev. D*, 88, 122003.

[161] Harry, G. M. & the LIGO Scientific Collaboration (2010). Advanced LIGO: the next generation of gravitational wave detectors. *Classical and Quantum Gravity*, 27(8), 084006.

[162] He, X. & Tromp, J. (1996). Normal-mode constraints on the structure of the Earth. *Journal of Geophysical Research: Solid Earth*, 101(B9), 20053–20082.

[163] High, F. W., Stubbs, C. W., Stalder, B., Gilmore, D. K., & Tonry, J. L. (2010). Sky Variability in the y Band at the LSST Site. *Publications of the Astronomical Society of the Pacific*, 122, 722–730.

[164] Hinder, I., Herrmann, F., Laguna, P., & Shoemaker, D. (2010). Comparisons of eccentric binary black hole simulations with post-Newtonian models. *Physical Review D.*, 82.

[165] Hobbs, G. (2005). Pulsars and Gravitational Wave Detection. *Publications of the Astronomical Society of Australia*, 22, 179–183.

[166] Hopman, C. & Alexander, T. (2006). The effect of mass segregation on gravitational wave sources near massive black holes. *The Astrophysical Journal Letters*, 645(2), L133.

[167] Horvath, P., Latham, G. V., Nakamura, Y., & Dorman, H. J. (1980). Lunar near-surface shear wave velocities at the apollo landing sites as inferred from spectral amplitude ratios. *Journal of Geophysical Research: Solid Earth*, 85(B11), 6572–6578.

[168] Hoshiba, M., Kamigaichi, O., Saito, M., Tsukada, S., & Hamada, N. (2008). Earthquake early warning starts nationwide in japan. *Eos, Transactions American Geophysical Union*, 89(8), 73–74.

[169] Houghton, J. (1977). The Physics of Atmospheres.

[170] Huerta, E. A. & Brown, D. A. (2013). Effect of eccentricity on binary neutron star searches in advanced ligo. *Phys. Rev. D*, 87, 127501.

[171] Huerta, E. A., Kumar, P., McWilliams, S. T., O'Shaughnessy, R., & Yunes, N. (2014). Accurate and efficient waveforms for compact binaries on eccentric orbits. *Phys. Rev. D*, 90, 084016.

[172] Hughes, S. A. & Thorne, K. S. (1998). Seismic gravity-gradient noise in interferometric gravitational-wave detectors. *Phys. Rev. D*, 58, 122002.

[173] Ingber, L. (2000). Adaptive simulated annealing (ASA): lessons learned. *CoRR*, cs.MS/0001018.

[174] Irving, J. C. E., Deuss, A., & Woodhouse, J. H. (2009). Normal mode coupling due to hemispherical anisotropic structure in Earth's inner core. *Geophysical Journal International*, 178(2), 962–975.

[175] Ishidoshiro, K., Ando, M., Takamori, A., Takahashi, H., Okada, K., Matsumoto, N., Kokuyama, W., Kanda, N., Aso, Y., & Tsubono, K. (2011). Upper Limit on Gravitational Wave Backgrounds at 0.2 Hz with a Torsion-Bar Antenna. *Phys. Rev. Lett.*, 106(16), 161101.

[176] Isogai, T., the Ligo Scientific Collaboration, & the Virgo Collaboration (2010). Used percentage veto for ligo and virgo binary inspiral searches. *Journal of Physics: Conference Series*, 243(1), 012005.

[177] Ivezic, Z., Tyson, J. A., Abel, B., Acosta, E., Allsman, R., AlSayyad, Y., Anderson, S. F., Andrew, J., Angel, R., Angeli, G., Ansari, R., Antilogus, P., Arndt, K. T., Astier, P., Aubourg, E., Axelrod, T., Bard, D. J., Barr, J. D., Barrau, A., Bartlett, J. G., Bauman, B. J., Beaumont, S., Becker, A. C., Becla, J., Beldica, C., Bellavia, S., Blanc, G., Blandford, R. D., Bloom, J. S., Bogart, J., Borne, K., Bosch, J. F., Boutigny, D., Brandt, W. N., Brown, M. E., Bullock, J. S., Burchat, P., Burke, D. L., Cagnoli, G., Calabrese, D., Chandrasekharan, S., Chesley, S., Cheu, E. C., Chiang, J., Claver, C. F., Connolly, A. J., Cook, K. H., Cooray, A., Covey, K. R., Cribbs, C., Cui, W., Cutri, R., Daubard, G., Daues, G., Delgado, F., Digel, S., Doherty, P., Dubois, R., Dubois-Felsmann, G. P., Durech, J., Eracleous, M., Ferguson, H., Frank, J., Freemon, M., Gangler, E., Gawiser, E., Geary, J. C., Gee, P., Geha, M., Gibson, R. R., Gilmore, D. K., Glanzman, T., Goodenow, I., Gressler, W. J., Gris, P., Guyonnet, A., Hascall, P. A., Haupt, J., Hernandez, F., Hogan, C., Huang, D., Huffer, M. E., Innes, W. R., Jacoby, S. H., Jain, B., Jee, J., Jernigan, J. G., Jevremovic, D., Johns, K., Jones, R. L., Juramy-Gilles, C., Juric, M., Kahn, S. M., Kalirai, J. S., Kallivayalil, N., Kalmbach, B., Kantor, J. P., Kasliwal, M. M., Kessler, R., Kirkby, D., Knox, L., Kotov, I., Krabbendam, V. L., Krughoff, S., Kubanek, P., Kuczewski, J., Kulkarni, S., Lambert, R., Le Guillou, L., Levine, D., Liang, M., Lim, K., Lintott, C., Lupton, R. H., Mahabal, A., Marshall, P.,

Marshall, S., May, M., McKercher, R., Migliore, M., Miller, M., Mills, D. J., Monet, D. G., Moniez, M., Neill, D. R., Nief, J., Nomerotski, A., Nordby, M., O'Connor, P., Oliver, J., Olivier, S. S., Olsen, K., Ortiz, S., Owen, R. E., Pain, R., Peterson, J. R., Petry, C. E., Pierfederici, F., Pietrowicz, S., Pike, R., Pinto, P. A., Plante, R., Plate, S., Price, P. A., Prouza, M., Radeka, V., Rajagopal, J., Rasmussen, A., Regnault, N., Ridgway, S. T., Ritz, S., Rosing, W., Roucelle, C., Rumore, M. R., Russo, S., Saha, A., Sassolas, B., Schalk, T. L., Schindler, R. H., Schneider, D. P., Schumacher, G., Sebag, J., Sembroski, G. H., Seppala, L. G., Shipsey, I., Silvestri, N., Smith, J. A., Smith, R. C., Strauss, M. A., Stubbs, C. W., Sweeney, D., Szalay, A., Takacs, P., Thaler, J. J., Van Berg, R., Vanden Berk, D., Vetter, K., Virieux, F., Xin, B., Walkowicz, L., Walter, C. W., Wang, D. L., Warner, M., Willman, B., Wittman, D., Wolff, S. C., Wood-Vasey, W. M., Yoachim, P., Zhan, H., & for the LSST Collaboration (2008). LSST: from Science Drivers to Reference Design and Anticipated Data Products. *ArXiv e-prints*.

[178] J, M. & G, R. (2008). Normal modes of the earth. *Journal of Physics: Conference Series*, 118(1), 012004.

[179] J Aasi et al. (2012). The characterization of Virgo data and its impact on gravitational-wave searches. *Classical and Quantum Gravity*, 29(15), 155002.

[180] J Aasi et al. (2015). Advanced ligo. *Classical and Quantum Gravity*, 32(7), 074001.

[181] J. Abadie et al. (2012). All-sky search for gravitational-wave bursts in the second joint ligo-virgo run. *Phys. Rev. D*, 85, 122007.

[182] Jenet, F. A., Hobbs, G. B., van Straten, W., Manchester, R. N., Bailes, M., Verbiest, J. P. W., Edwards, R. T., Hotan, A. W., Sarkissian, J. M., & Ord, S. M. (2006). Upper Bounds on the Low-Frequency Stochastic Gravitational Wave Background from Pulsar Timing Observations: Current Limits and Future Prospects. *The Astrophysical Journal*, 653(2), 1571.

[183] Jensen, O. (1979). Seismic detection of gravitational radiation. *Reviews of Geophysics*, 17(8), 2057–2069.

[184] Jones, A., Noll, S., Kausch, W., & Kimeswenger, S. (2014). An Advanced Scattered Moonlight Model. In *American Astronomical Society Meeting Abstracts #224*, volume 224 of *American Astronomical Society Meeting Abstracts* (pp. #405.03).

[185] Jones, A., Noll, S., Kausch, W., Szyszka, C., & Kimeswenger, S. (2013). An advanced scattered moonlight model for Cerro Paranal. *Astronomy and Astrophysics*, 560, A91.

[186] Joseph J. Mohr et al (2012). The dark energy survey data processing and calibration system. *http://arxiv.org/abs/1207.3189*.

[187] J.W. Baker (2008). An introduction to probabilistic seismic hazard analysis. *Report for the US Nuclear Regulatory Commission*, (pp. Version 1.3).

[188] Kalmus, P., Cannon, K., Márka, S., & Owen, B. (2009). Stacking gravitational wave signals from soft gamma repeater bursts. *Phys. Rev. D*, 80, 042001.

[189] Kieffer, H. H. & Stone, T. C. (2005). The Spectral Irradiance of the Moon. *The Astronomical Journal*, 129, 2887–2901.

[190] Kirkpatrick, S., Gelatt, C. D., & Vecchi, M. P. (1983). Optimization by simulated annealing. *Science*, 220(4598), 671–680.

[191] Kiuchi, K., Shibata, M., Montero, P. J., & Font, J. A. (2011). Gravitational waves from the papaloizou-pringle instability in black hole-torus systems. *Physical Review Letters*, 106, 251102.

[192] Klimenko, S., Yakushin, I., Mercer, A., & Mitselmakher, G. (2008). A coherent method for detection of gravitational wave bursts. *Classical and Quantum Gravity*, 25(11), 114029.

[193] Klimenko S., Yakushin I., Mercer A., and Mitselmakher G. (2008). Coherent method for detection of gravitational wave bursts. *Class. Quant. Grav.*, 25, 114029.

[194] Kocsis, B. & Levin, J. (2012). Repeated bursts from relativistic scattering of compact objects in galactic nuclei. *Phys. Rev. D*, 85, 123005.

[195] Kokeyama, K., Izumi, K., Korth, W. Z., Smith-Lefebvre, N., Arai, K., & Adhikari, R. X. (2014). Residual amplitude modulation in interferometric gravitational wave detectors. *J. Opt. Soc. Am. A*, 31(1), 81–88.

[196] Kopparapu, R. K., Hanna, C., Kalogera, V., OShaughnessy, R., Gonzlez, G., Brady, P. R., & Fairhurst, S. (2008). Host galaxies catalog used in ligo searches for compact binary coalescence events. *The Astrophysical Journal*, 675(2), 1459.

[197] Krisciunas, K. & Schaefer, B. E. (1991). A model of the brightness of moonlight. *Astronomical Society of the Pacific*, 103, 1033–1039.

[198] Kulak, A., Kubisz, J., Klucjasz, S., Michalec, A., Mlynarczyk, J., Nieckarz, Z., Ostrowski, M., & Zieba, S. (2014). Extremely low frequency electromagnetic field measurements at the Hylaty station and methodology of signal analysis. *Radio Science*, 49(6), 361–370. 2014RS005400.

[199] Kulak, A. & Mlynarczyk, J. (2013). ELF propagation parameters for the ground-ionosphere waveguide with finite ground conductivity. *IEEE Trans. Antennas Propag*, 61(4), 2269–2275.

[200] Kulak, A., Mlynarczyk, J., Zieba, S., Micek, S., & Nieckarz, Z. (2006). Studies of ELF propagation in the spherical shell cavity using a field decomposition method based on asymmetry of schumann resonance curves. *J. Geophys. Res.*, 111(A10304).

[201] Kuyuk, H.S. and RM. Allen (2013a). A global approach to provide magnitude estimates for earthquake early warning. *Geophysical Research Letters*, 40.

[202] Kuyuk, H.S. and RM. Allen (2013b). Optimal seismic network density for earthquake early warning: A case study from california. *Seismological Research Letters*, 84(6), 946–954.

[203] Kuyuk, H.S. et al (2014). Designing a network-based earthquake early warning system for california: Elarms-2. *Bulletin of Seismological Society of America*, 104(1).

[204] Lai, D. (2012). Dc circuit powered by orbital motion: Magnetic interactions in compact object binaries and exoplanetary systems. *The Astrophysical Journal Letters*, 757, L3.

[205] Large Synoptic Survey Telescope (2015). LSST Exposure Time Calculator.

[206] Larose, E., Khan, A., Nakamura, Y., & Campillo, M. (2005). Lunar subsurface investigated from correlation of seismic noise. *Geophysical Research Letters*, 32(16), n/a–n/a.

[207] Lee, W. H., Ramirez-Ruiz, E., & van de Ven, G. (2010). Short gamma-ray bursts from dynamically assembled compact binaries in globular clusters: Pathways, rates, hydrodynamics, and cosmological setting. *The Astrophysical Journal*, 720(1), 953.

[208] LIGO Scientific Collaboration (2007a). First Cross-Correlation Analysis of Interferometric and Resonant-Bar Gravitational-Wave Data for Stochastic Backgrounds. *arXiv*.

[209] LIGO Scientific Collaboration (2007b). Upper limit map of a background of gravitational waves. *Phys. Rev. D*, 76, 082003.

[210] Lognonne, P. & Mosser, B. (1993). Planetary seismology. *Surveys in Geophysics*, 14(3), 239–302.

[211] Logue, J., Ott, C. D., Heng, I. S., Kalmus, P., & Scargill, J. H. C. (2012). Inferring core-collapse supernova physics with gravitational waves. *Phys. Rev. D*, 86, 044023.

[212] LSST Collaboration (2012). Large synoptic survey telescope: Dark energy science collaboration. *http://arxiv.org/abs/1211.0310*.

[213] Lück, H., Affeldt, C., Degallaix, J., Freise, A., Grote, H., Hewitson, M., Hild, S., Leong, J., Prijatelj, M., Strain, K. A., Willke, B., Wittel, H., & Danzmann, K. (2010). The upgrade of GEO600. *J. Phys.: Conf. Series*, 228, 012012.

[214] Macleod, D. M., Fairhurst, S., Hughey, B., Lundgren, A. P., Pekowsky, L., Rollins, J., & Smith, J. R. (2012). Reducing the effect of seismic noise in ligo searches by targeted veto generation. *Classical and Quantum Gravity*, 29(5), 055006.

[215] Majcher, A. et al. (2015). Status of the pi of the sky telescopes in spain and chile. *Proc. SPIE*, 9662, 966219–966219–9.

[216] Marshall, J. L., Rheault, J.-P., DePoy, D. L., Prochaska, T., Allen, R., Behm, T. W., Martin, E. C., Veal, B., Villanueva, Jr., S., Williams, P., & Wise, J. (2013). DECal: A Spectrophotometric Calibration System For DECam. *ArXiv e-prints*.

[217] Mast, T. S., Nelson, J. E., & Saarloos, J. (1972). Search for seismic signals from gravitational radiation of pulsar cp1133. *Nature*, 240, 140–142.

[218] Meadors, G. D., Kawabe, K., & Riles, K. (2014). Increasing ligo sensitivity by feedforward subtraction of auxiliary length control noise. *Classical and Quantum Gravity*, 31(10), 105014.

[219] Medina, M. A. (1998). Anlisis comparativo de mtodos de regresin de atenuacin de aceleracin mxima. *Memoria Ttulo Ing. Civil*, (pp. 196).

[220] Meeus, J. H. (1991). *Astronomical Algorithms*. Willmann-Bell, Incorporated.

[221] Metzger, B. D., Bauswein, A., Goriely, S., & Kasen, D. (2014). Neutron-powered precursors of kilonovae. *arXiv:1409.0544*.

[222] Metzger, B. D. & Berger, E. (2012). What is the most promising electromagnetic counterpart of a neutron star binary merger? *The Astrophysical Journal*, 746(1), 48.

[223] Moritz Beyreuther, Robert Barsch, Lion Krischer, Tobias Megies, Yannik Behr and Joachim Wassermann (2010). Obspy: A python toolbox for seismology. *Seismological Research Letters*, 81(3), 530–533.

[224] Nakamura, Y. (2011). Timing problem with the lunar module impact data as recorded by the lspe and corrected near-surface structure at the apollo 17 landing site. *Journal of Geophysical Research: Planets*, 116(E12), n/a–n/a.

[225] Nakar, E. (2007). Short-hard gamma-ray bursts. *Physics Reports*, 442(16), 166 – 236. The Hans Bethe Centennial Volume 1906-2006.

[226] Neill, D. R. (2012). Seismic analysis of the LSST telescope. *Proc. SPIE*, 8444, 84440T–84440T–15.

[227] Neill, D. R., Warner, M., & Sebag, J. (2012). Seismic design accelerations for the LSST telescope. *Proc. SPIE*, 8444, 84440R–84440R–15.

[228] Neumeyer, J. (2010). Superconducting Gravimetry. In G. Xu (Ed.), *Sciences of Geodesy - I* (pp. 339–413). Springer Berlin Heidelberg.

[229] Noll, S., Kausch, W., Barden, M., Jones, A. M., Szyszka, C., Kimeswenger, S., & Vinther, J. (2012). An atmospheric radiation model for Cerro Paranal. I. The optical spectral range. *Astronomy and Astrophysics*, 543, A92.

[230] Ohanian, H. & Ruffini, R. (1976). *Gravitation and Spacetime*. W.W. Norton and Company, 2nd edition.

[231] O'Leary, R. M., Kocsis, B., & Loeb, A. (2009). Gravitational waves from scattering of stellar-mass black holes in galactic nuclei. *MNRAS*, 395, 2127.

[232] Oth, A., Bse, M., Wenzel, F., Khler, N., & Erdik, M. (2010). Evaluation and optimization of seismic networks and algorithms for earthquake early warning the case of istanbul (turkey). *Journal of Geophysical Research: Solid Earth*, 115(B10), 2156–2202.

[233] Ott, C. D., Abdikamalov, E., Mösta, P., Haas, R., Drasco, S., O'Connor, E. P., Reisswig, C., Meakin, C. A., & Schnetter, E. (2013). General-relativistic simulations of three-dimensional core-collapse supernovae. *The Astrophysical Journal*, 768(2), 115.

[234] Oxley, P., Ade, P., Baccigalupi, C., deBernardis, P., Cho, H.-M., et al. (2004). The EBEX experiment. *Proc.SPIE Int.Soc.Opt.Eng.*, 5543, 320–331.

[235] Padmanabhan, N., Schlegel, D. J., Finkbeiner, D. P., Barentine, J. C., Blanton, M. R., Brewington, H. J., Gunn, J. E., Harvanek, M., Hogg, D. W., eljko Ivezi, Johnston, D., Kent, S. M., Kleinman, S. J., Knapp, G. R., Krzesinski, J., Long, D., Eric H. Neilsen, J., Nitta, A., Loomis, C., Lupton, R. H., Roweis, S., Snedden, S. A., Strauss, M. A., & Tucker, D. L. (2008). An improved photometric calibration of the sloan digital sky survey imaging data. *The Astrophysical Journal*, 674(2), 1217.

[236] Pasko, V. P. (2010). Recent advances in theory of transient luminous events. *Journal of Geophysical Research: Space Physics*, 115(A6), n/a–n/a. A00E35.

[237] Patrick Ingraham et al. (2016). Obtaining precise relative photometric calibration with LSST. *SPIE 2016*.

[238] Peters, P. C. (1964). Gravitational radiation and the motion of two point masses. *Phys. Rev.*, 136, B1224–B1232.

[239] Peters, P. C. & Mathews, J. (1963). Gravitational radiation from point masses in a keplerian orbit. *Phys. Rev.*, 131, 435–440.

[240] Peterson, J. (1993). Observation and modeling of seismic background noise. *Open-file report*, 93-322.

[241] Picozzi, M., Bindi, D., Pittore, M., Kieling, K., & Parolai, S. (2013). Real-time risk assessment in seismic early warning and rapid response: a feasibility study in bishkek (kyrgyzstan). *Journal of Seismology*, 17(2), 485–505.

[242] Piro, A. L. & Ott, C. D. (2011). Supernova fallback onto magnetars and propeller-powered supernovae. *The Astrophysical Journal*, 736, 108.

[243] Piro, A. L. & Pfahl, E. (2007). Fragmentation of collapsar disks and the production of gravitational waves. *The Astrophysical Journal*, 658, 1173.

[244] Piro, A. L. & Thrane, E. (2012). Gravitational waves from fallback accretion onto neutron stars. *The Astrophysical Journal*, 761, 63.

[245] Piro, T. (2012). Magnetic interactions in coalescing neutron star binaries. *The Astrophysical Journal*, 755, 80.

[246] Prestegard, T., Thrane, E., et al. (2012). Identification of noise artifacts in searches for long-duration gravitational-wave transients. *Classical and Quantum Gravity*, 29, 095018.

[247] Privitera, S. (2014). The importance of spin for observing gravitational waves from coalescing compact binaries with LIGO and Virgo.

[248] Privitera, S., Mohapatra, S. R. P., Ajith, P., Cannon, K., Fotopoulos, N., Frei, M. A., Hanna, C., Weinstein, A. J., & Whelan, J. T. (2014). Improving the sensitivity of a search for coalescing binary black holes with nonprecessing spins in gravitational wave data. *Phys. Rev. D*, 89, 024003.

[249] Punturo, M., Abernathy, M., Acernese, F., Allen, B., Andersson, N., Arun, K., Barone, F., Barr, B., Barsuglia, M., Beker, M., et al. (2010). The einstein tele-

scope: a third-generation gravitational wave observatory. *Classical and Quantum Gravity*, 27(19), 194002.

[250] Rasmussen, A. (2014). Pixel area variations in sensors: a novel framework for predicting pixel fidelity and distortion in flat field response. *Journal of Instrumentation*, 9(04), C04027.

[251] Regnault, N., Guyonnet, A., Schahmanèche, K., Le Guillou, L., Antilogus, P., Astier, P., Barrelet, E., Betoule, M., Bongard, S., Cuillandre, J.-C., Juramy, C., Pain, R., Rocci, P.-F., Tisserand, P., & Villa, F. (2015). The DICE calibration project Design, characterization, and first results. *Astronomy and Astrophysics*, 581, A45.

[252] RM. Allen (2012). Transforming earthquake detection? *Science*, 335, 297–298.

[253] Roelofs, G. H. A., Rau, A., Marsh, T. R., Steeghs, D., Groot, P. J., & Nelemans, G. (2010). Spectroscopic Evidence for a 5.4 Minute Orbital Period in HM Cancri. *The Astrophysical Journal Letters*, 711(2), L138.

[254] Rollins, J. (2011). Multimessenger Astronomy with Low-Latency Searches for Transient Gravitational Waves.

[255] Romanowski, Z. & Krukowski, S. (2007). Transformation of complex spherical harmonics under rotations. *Journal of Physics A: Mathematical and Theoretical*, 40(50), 15071.

[256] Rosat, S. & Hinderer, J. (2011). Noise Levels of Superconducting Gravimeters: Updated Comparison and Time Stability. *BSSA*, 101, 1233–1241.

[257] Röver, C. (2011). Student-t based filter for robust signal detection. *Phys. Rev. D*, 84, 122004.

[258] Ruiz, S. & Saragoni, R. (2005). Frmulas de atenuacin para la subduccin de chile considerando los dos mecanismos de sismognesis y los efectos del suelo. *Congreso ACHISINA, Concepcin.*

[259] Sadeh, D. & Meidav, M. (1972). Periodicities in seismic response caused by pulsar cp1133. *Nature*, 240, 136–138.

[260] Sadowski, A., Belczynski, K., Bulik, T., Ivanova, N., Rasio, F. A., & OShaughnessy, R. (2008). The total merger rate of compact object binaries in the local universe. *The Astrophysical Journal*, 676(2), 1162.

[261] Samsing, J., MacLeod, M., & Ramirez-Ruiz, E. (2014). The formation of eccentric compact binary inspirals and the role of gravitational wave emission in binary-single stellar encounters. *The Astrophysical Journal*, 784(1), 71.

[262] Saulson, P. R. (1984). Terrestrial gravitational noise on a gravitational wave antenna. *Phys. Rev. D*, 30, 732–736.

[263] Sayed, A. H. (2003). *Fundamentals of Adaptive Filtering*. John Wiley & Sons.

[264] Schlafly, E. F., Finkbeiner, D. P., Juri, M., Magnier, E. A., Burgett, W. S., Chambers, K. C., Grav, T., Hodapp, K. W., Kaiser, N., Kudritzki, R.-P., Martin, N. F., Morgan, J. S., Price, P. A., Rix, H.-W., Stubbs, C. W., Tonry, J. L., & Wainscoat, R. J. (2012). Photometric calibration of the first 1.5 years of the pan-starrs1 survey. *The Astrophysical Journal*, 756(2), 158.

[265] Schlegel, D. J., Finkbeiner, D. P., & Davis, M. (1998). Maps of dust infrared emission for use in estimation of reddening and cosmic microwave background radiation foregrounds. *The Astrophysical Journal*, 500(2), 525.

[266] Schofield, R., Ito, M., Mauceli, E., Radkins, H., Gray, C., Moreno, G., & Gonzalez, G. (2000). Source and Propagation of the Predominant 1-50 Hz Seismic Signal From Off-Site at LIGO-Hanford. *LIGO DCC*, G000262.

[267] Schumann, W. (1952). Über die strahlungslosen eigenschwingungen einer leitenden kugel, die von einer luftschicht und einer ionosphärenhülle umgeben ist. *Zeitschrift für Naturforschung A*, 7(2), 149–154.

[268] Sens-Schönfelder, C. & Larose, E. (2008). Temporal changes in the lunar soil from correlation of diffuse vibrations. *Phys. Rev. E*, 78, 045601.

[269] Sens-Schonfelder, C. & Larose, E. (2010). Lunar noise correlation, imaging and monitoring. *Earthquake Science*, 23(5), 519–530.

[270] Sentman, D. D. (1996). Schumann resonance spectra in a two-scale-height earth-ionosphere cavity. *J. Geophys. Res.*, 101(D5), 9479–9487.

[271] Seto, N. (2013). Highly eccentric kozai mechanism and gravitational-wave observation for neutron-star binaries. *Phys. Rev. Lett.*, 111, 061106.

[272] Shibata, M., Taniguchi, K., Okawa, H., & Buonanno, A. (2014). Coalescence of binary neutron stars in a scalar-tensor theory of gravity. *Phys. Rev. D*, 89, 084005.

[273] Shoda, A., Ando, M., Ishidoshiro, K., Okada, K., Kokuyama, W., Aso, Y., & Tsubono, K. (2014). Search for a stochastic gravitational-wave background using a pair of torsion-bar antennas. *Phys. Rev. D*, 89, 027101.

[274] Sidery, T., Aylott, B., Christensen, N., Farr, B., Farr, W., Feroz, F., Gair, J., Grover, K., Graff, P., Hanna, C., Kalogera, V., Mandel, I., O'Shaughnessy, R., Pitkin, M., Price, L., Raymond, V., Röver, C., Singer, L., van der Sluys, M., Smith, R. J. E., Vecchio, A., Veitch, J., & Vitale, S. (2014). Reconstructing the sky location of gravitational-wave detected compact binary systems: Methodology for testing and comparison. *Physical Review D*, 89(8), 084060.

[275] Siegel, D. M. & Roth, M. (2014). An upper bound from helioseismology on the stochastic background of gravitational waves. *arXiv preprint arXiv:1401.6888*.

[276] Singer, L. P., Price, L. R., Farr, B., Urban, A. L., Pankow, C., Vitale, S., Veitch, J., Farr, W. M., Hanna, C., Cannon, K., Downes, T., Graff, P., Haster, C.-J., Mandel, I., Sidery, T., & Vecchio, A. (2014). The first two years of electromagnetic follow-up with advanced ligo and virgo. *The Astrophysical Journal*, 795(2), 105.

[277] Singer, L. P., Price, L. R., & Speranza, A. (2012). Optimizing optical follow-up of gravitational-wave candidates. *http://arxiv.org/abs/1204.4510*.

[278] Slater, P. (1980). Remote sensing, optics and optical systems.

[279] Snoke J.A. (2009). Traveltime tables for iasp91 and ak135. *Seismological Research Letters*, 80(2), 260–262.

[280] Somiya, K. (2012). Detector configuration of kagra-the japanese cryogenic gravitational-wave detector. *Classical and Quantum Gravity*, 29(12), 124007.

[281] Sperhake, U., Berti, E., Cardoso, V., González, J. A., Brügmann, B., & Ansorg, M. (2008). Eccentric binary black-hole mergers: The transition from inspiral to plunge in general relativity. *Phys. Rev. D*, 78, 064069.

[282] Stankiewicz, J., Bindi, D., Oth, A., & Parolai, S. (2013). Designing efficient earthquake early warning systems: case study of almaty, kazakhstan. *Journal of Seismology*, 17(4), 1125–1137.

[283] Stephens, B. C., East, W. E., & Pretorius, F. (2011). Eccentric Black Hole-Neutron Star Mergers. *Astrophys.J.*, 737, L5.

[284] Stochino, A., Abbot, B., Aso, Y., Barton, M., Bertolini, A., Boschi, V., Coyne, D., DeSalvo, R., Galli, C., Huang, Y., Ivanov, A., Marka, S., Ottaway, D., Sannibale, V., Vanni, C., Yamamoto, H., & Yoshida, S. (2009). The seismic attenuation system (sas) for the advanced {LIGO} gravitational wave interferometric detectors. *Nuclear Instruments and Methods in Physics Research Section A: Accelerators, Spectrometers, Detectors and Associated Equipment*, 598(3), 737 – 753.

[285] Stubbs, C. W. (2014). Precision astronomy with imperfect fully depleted ccds an introduction and a suggested lexicon. *Journal of Instrumentation*, 9(03), C03032.

[286] Stubbs, C. W. & Brown, Y. J. (2015). Precise astronomical flux calibration and its impact on studying the nature of the dark energy. *Modern Physics Letters A*, 30, 1530030.

[287] Stubbs, C. W., Doherty, P., Cramer, C., Narayan, G., Brown, Y. J., Lykke, K. R., Woodward, J. T., & Tonry, J. L. (2010). Precise Throughput Determination of the PanSTARRS Telescope and the Gigapixel Imager Using a Calibrated Silicon Photodiode and a Tunable Laser: Initial Results. *The Astrophysical Journal Supplements*, 191, 376–388.

[288] Stubbs, C. W., High, F. W., George, M. R., DeRose, K. L., Blondin, S., Tonry, J. L., Chambers, K. C., Granett, B. R., Burke, D. L., & Smith, R. C. (2007). Toward More Precise Survey Photometry for PanSTARRS and LSST: Measuring Directly the Optical Transmission Spectrum of the Atmosphere. *Publications of the Astronomical Society of the Pacific*, 119, 1163–1178.

[289] Stubbs, C. W. & Tonry, J. L. (2006). Toward 1% photometry: End-to-end calibration of astronomical telescopes and detectors. *The Astrophysical Journal*, 646(2), 1436.

[290] Survey, U. S. G. (2012). Product distribution user guide. *ehppdl1.cr.usgs.gov*.

[291] Sutton P. et al. (2010). X-pipeline: An analysis package for autonomous gravitational-wave burst searches. *New Journal of Physics*, 12, 053034.

[292] T, P. & E, T. (2012). Burstegard: a hierarchical clustering algorithm. *https://dcc.ligo.org/LIGO-L1200204-v1*.

[293] Tai, K. S., McWilliams, S. T., & Pretorius, F. (2014). Detecting gravitational waves from highly eccentric compact binaries. *Phys. Rev. D*, 90, 103001.

[294] Tanaka, S., Shiraishi, H., Kato, M., & Okada, T. (2008). Range science objectives of the selene ii mission as the post selene mission. *Adv. Space Res.*, 42, 394–401.

[295] The Virgo Collaboration (2009). Advanced Virgo Baseline Design.

[296] Thrane, E., Christensen, N., & Schofield, R. (2013). Correlated magnetic noise in global networks of gravitational-wave detectors: Observations and implications. *Physical Review D*, 87(12), 123009.

[297] Thrane, E., Christensen, N., Schofield, R. M. S., & Effler, A. (2014). Correlated noise in networks of gravitational-wave detectors: Subtraction and mitigation. *Phys. Rev. D*, 90, 023013.

[298] Thrane, E. & Coughlin, M. (2013a). Searching for gravitational-wave transients with a qualitative signal model: Seedless clustering strategies. *Phys. Rev. D*, 88, 083010.

[299] Thrane, E. & Coughlin, M. (2013b). Searching for gravitational-wave transients with a qualitative signal model: seedless clustering strategies. *Physical Review D*, 88, 083010.

[300] Thrane, E. & Coughlin, M. (2014). Seedless clustering in all-sky searches for gravitational-wave transients. *Phys. Rev. D*, 89, 063012.

[301] Tonry, J. L., Stubbs, C. W., Lykke, K. R., Doherty, P., Shivvers, I. S., Burgett, W. S., Chambers, K. C., Hodapp, K. W., Kaiser, N., Kudritzki, R.-P., Magnier, E. A., Morgan, J. S., Price, P. A., & Wainscoat, R. J. (2012). The Pan-STARRS1 Photometric System. *The Astrophysical Journal*, 750, 99.

[302] Trampert, J. & Woodhouse, J. H. (1995). Global phase velocity maps of love and rayleigh waves between 40 and 150 seconds. *Geophysical Journal International*, 122(2), 675–690.

[303] Troja, E., King, A. R., O'Brien, P. T., Lyons, N., & Cusumano, G. (2008). Different progenitors of short hard gamma-ray bursts. *Monthly Notices of the Royal Astronomical Society: Letters*, 385(1), L10–L14.

[304] Tuman, V. (1971). Observation of Earth Eigen Vibrations Possibly Excited by Gravity Waves. *Nature*, 230(13), 101–106.

[305] Unnikrishnan, C. S. (2013). Indigo and ligo-india: Scope and plans for gravitational wave research and precision metrology in india. *International Journal of Modern Physics D*, 22(01), 1341010.

[306] Ursin, B. & Toverud, T. (2002). Comparison of seismic dispersion and attenuation models. *Studia Geophysica et Geodaetica*, 46(2), 293–320.

[307] van Putten, M. (2001). Proposed Source of Gravitational Radiation from a Torus around a Black Hole. *Physical Review Letters*, 87(9), 091101.

[308] van Putten, M. (2008). Gravitational Waveforms of Kerr Black Holes Interacting with High-Density Matter. *The Astrophysical Journal Letters*, 684, 91.

[309] Vaseghi, S. V. (2001). *Wiener Filters*, (pp. 178–204). John Wiley & Sons, Ltd.

[310] Vitale, S. (2014). Space-borne gravitational wave observatories. *General Relativity and Gravitation*, 46(5), 1–19.

[311] Walter, C. (2015). The brighter-fatter and other sensor effects in ccd simulations for precision astronomy. *Journal of Instrumentation*, 10(05), C05015.

[312] Wang J., Tilmann F. J., White R. S., Soosalu H., and Bordoni P. (2008). Application of multi-channel wiener filters to the suppression of ambient seismic noise in passive seismic arrays. *Leading Edge*, 27(2), 232–238.

[313] Was, M., Bizouard, M.-A., Brisson, V., Cavalier, F., Davier, M., Hello, P., Leroy, N., Robinet, F., & Vavoulidis, M. (2010a). Limitations of the time slide method of background estimation. *Classical and Quantum Gravity*, 27(19), 194014.

[314] Was, M., Bizouard, M.-A., Brisson, V., Cavalier, F., Davier, M., Hello, P., Leroy, N., Robinet, F., & Vavoulidis, M. (2010b). On the background estimation by time slides in a network of gravitational wave detectors. *Classical and Quantum Gravity*, 27(1), 015005.

[315] Wathelet, M. (2005). *Array recordings of ambient vibrations: surface-wave inversion*. PhD thesis, Université de Liège.

[316] Wathelet, M. (2013). Geopsywiki.

[317] Weber, J. (1960). Detection and generation of gravitational waves. *Phys. Rev.*, 117(1), 306–313.

[318] Weber, R. C., Lin, P.-Y., Garnero, E. J., Williams, Q., & Lognonn, P. (2011). Seismic detection of the lunar core. *Science*, 331(6015), 309–312.

[319] Weisberg, J. & Taylor, J. (2004). Relativistic binary pulsar b1913+16: Thirty years of observations and analysis. *Binary Radio Pulsars, Proc. Aspen Conference, ASP Conf. Series*.

[320] Weisberg, J. M., Nice, D. J., & Taylor, J. H. (2010). Timing Measurements of the Relativistic Binary Pulsar PSR B1913+16. *The Astrophysical Journal*, 722(2), 1030.

[321] Weiss, R. & Block, B. (1965). A gravimeter to monitor the ${}_0\mathrm{s}_0$ dilational mode of the earth. *Journal of Geophysical Research*, 70(22), 5615–5627.

[322] Wen, L. (2003). On the eccentricity distribution of coalescing black hole binaries driven by the kozai mechanism in globular clusters. *The Astrophysical Journal*, 598(1), 419.

[323] Wen, L. & Chen, Y. (2010). Geometrical expression for the angular resolution of a network of gravitational-wave detectors. *Physical Review D*, 81(8), 082001.

[324] Wen, L. & Schutz, B. F. (2005). Coherent network detection of gravitational waves: the redundancy veto. *Classical and Quantum Gravity*, 22(18), S1321.

[325] White, D. J., Daw, E. J., & Dhillon, V. S. (2011). A list of galaxies for gravitational wave searches. *Classical and Quantum Gravity*, 28(8), 085016.

[326] Wiggins, R. A. & Press, F. (1969). Search for seismic signals at pulsar frequencies. *Journal of Geophysical Research*, 74(22), 5351–5352.

[Wilcoxon Research] Wilcoxon Research. 731-207 low frequency seismic accelerometer.

[328] Woodhouse, J. (1988). The Calculation of Eigenfrequencies and Eigenfunctions of the Free Oscillations of the Earth and the Sun. In D. Doornbos (Ed.), *Seismological Algorithms, Computational Methods and Computer Programs*. Academic Press, London, UK, 321-370.

[329] Workshop, M. K. O. E. (2007). Mauna kea observatories earthquake workshop. *Keauhou Beach Resort, Kailua-Kona, Hawaii*.

[330] Xu, Y., Crossley, D., & Herrmann, R. B. (2008). Amplitude and Q of 0S0 from the Sumatra Earthquake as Recorded on Superconducting Gravimeters and Seismometers. *Seismological Research Letters*, 79(6), 797–805.

[331] Y. Nakamura (2005). Far side deep moonquakes and the deep interior of the moon. *Journal of Geopysical Research*, 110, E0100.

[332] Yamada, R., Garcia, R. F., Lognonne, P., Feuvre, M. L., Calvet, M., & Gagnepain-Beyneix, J. (2011). Optimisation of seismic network design: Application to a geophysical international lunar network. *Planetary and Space Science*, 59(4), 343 – 354.

[333] Yunes, N., Arun, K. G., Berti, E., & Will, C. M. (2009). Post-circular expansion of eccentric binary inspirals: Fourier-domain waveforms in the stationary phase approximation. *Phys. Rev. D*, 80, 084001.

[334] Z. Ivezic et al (2014). LSST: from science drivers to reference design and anticipated data products. *http://arxiv.org/abs/0805.2366*.

[335] Zandt, G. & Ammon, C. J. (1995). Continental crust composition constrained by measurements of crustal poisson's ratio. *Nature*, 374(6518), 152–154.

[336] Zhang, H., Thurber, C., & Rowe, C. (2003). Automatic p-wave arrival detection and picking with multiscale wavelet analysis for single-component recordings. *Bulletin of the Seismological Society of America*, 93(5), 1904–1912.